CRANFIELD UNIVERSITY

Bidur Khanal

A Numerical Investigation of the Aerodynamic Noise Generation Mechanism in Transonic Cavity Flows

Department of Engineering Systems & Management,
Aeromechanical Systems Group

PhD

CRANFIELD UNIVERSITY

Defence Academy - College of Management and Technology

Department of Engineering Systems & Management,
Aeromechanical Systems Group

PhD Thesis
2010

Bidur Khanal

A Numerical Investigation of the Aerodynamic Noise Generation Mechanism in Transonic Cavity Flows

Supervisors:
Professor Kevin Knowles and Dr Alistair Saddington

December 2010

Abstract

An overview of the progress of research work on the aerodyamics and aeroacoustics of three-dimensional cavities at transonic speeds is presented with special attention to identify the flow structures responsible for resonant tones. The cavity length to depth (L/D) ratio values were chosen to focus the investigations mainly in the open cavity flow regime. The cavity geometries considered also included the cavities with stores.

In the first part of this project, a two-step computational solver which involves the solution of the Navier-Stokes equations in the first step, and an integral surface solution of the Ffowcs-Williams and Hawkings equation in the subsequent step, is developed especially for the accurate capturing of aeroacoustic phenomena. The solver developed is validated using a wide range of test cases and it also used to study an empty cavity unsteady flow problem at transonic speed. In addition, the solver was tested for its robustness by computing flow around an isolated landing gear.

In the second part of the thesis, a general purpose CFD solver was used to tackle complex geometry problems which included cavities with missiles and spoilers. The flow field within the cavities investigated is shown to be dominated by highly unsteady periodic phenomena. The oscillation mechanism and the internal flow structures are found to remain largely unaffected by the presence of stores, however, the spanwise variation on the flow is limited.

Dedicated to my loving parents ...

Acknowledgements

I am very grateful to my supervisors, Professor Kevin Knowles and Dr. Alistair Saddington for their invaluable guidance, encouragement and enthusiasm throughout the course of this research without them I would not have been able to conduct this research.

I would also like to thank Dr Simon Richie for providing with literature review materials and kindly letting me use his experimental data.

Finally, I could not have completed this work without the continuous love and support of my wife, to whom this thesis is also dedicated.

Contents

List of Figures

List of Tables

Nomenclature

All units are in SI unless otherwise stated

Alphanumeric

a_0	Speed of sound in ambient air
C_p	Pressure coefficient; $(p - p_\infty)/\frac{1}{2}\rho_\infty U_\infty^2$
c_p	Specific heat capacity at constant pressure
c_v	Specific heat capacity at constant volume
D	Cavity Depth
e_t	Specific Internal Energy
f	Frequency
$H()$	Heavy-side function
J	Jacobian
L	Cavity Length
L_i	Aeroacoustic loading term
M	Mach number
p	Static pressure
p_{gauge}	Gauge pressure
p_{ij}	Compressive stress tensor
Pr	Prandtl number
Prt	Turbulent Prandtl number
St	Strouhal number
T	Static temperature
t	Time
T_{ij}	Lighthill's stress tensor

U	Velocity in x-direction
u, v, w	Velocity components in Cartesian coordinates
u_i	Velocity vector components in Cartesian coordinates $(u_1, u_2, u_3) \equiv (u, v, w)$
U_n	Aeroacoustic thickness term
W	Cavity Width
x, y, z	Cartesian coordinate system
x_i	Coordinate directions in Cartesian coordinates $(x_1, x_2, x_3) \equiv (x, y, z)$
y^+	Non-dimensional wall distance, $y^+ = y\sqrt{\tau_w/\rho}/\nu$
$\mathbf{s}$	Displacement vector
$\mathbf{v}$	Velocity vector
$\mathbf{x}$	Observer position vector with components x_i
$\mathbf{y}$	Source position vector with components y_i
$\hat{\mathbf{n}}$	Unit outward normal vector to surface with components $\hat{n}_i$
$\hat{\mathbf{r}}$	Unit vector in propagation direction $\hat{\mathbf{r}} = (\mathbf{x} - \mathbf{y})/\mathbf{r}$
V	Surface area of fluid
V	Volume of fluid
Re	Reynolds number

Greek Symbols

$\delta()$	Dirac delta function
δ_{ij}	Kronecker delta
$\frac{\nu_t}{\nu}$	Freestream turbulence viscosity ratio
γ	Ratio of specific heats, $\gamma = c_p/c_v$
μ	Coefficient of molecular viscosity
μ_t	Coefficient of turbulent viscosity
ν	Kinematic viscosity

Ω	Vorticity magnitude
ρ	Fluid density
τ^*	Retarded time
τ_w	Wall shear stress
τ	Source time
ξ, η, ζ	Generalized coordinate system

Symbols

$\langle\rangle$	Time averaged quantity

Subscripts

$()'$	Perturbation value
$()_0$	Reference value
$()_\infty$	Freestream value
$()_{rms}$	Root mean square value

Abbreviations

2D	Two-dimensional
3D	Three-dimensional
AIAA	American Institute of Aeronautics and Astronautics
CAA	Computational Aeroacoustics
CFD	Computational Fluid Dynamics
CFL	Courant-Friedrichs-Levy
DDES	Delayed Detached Eddy Simulation
DES	Detached Eddy Simulation
DRP	Dispersion Relation Preserving
FFT	Fast Fourier Transform
FW-H	Ffowcs Williams-Hawkings

LES	Large Eddy Simulation
MPI	Message Passing Interface
NASA	National Aeronautics and Space Administration
PPW	Points per Wavelength
RANS	Reynolds-Averaged Navier-Stokes
SA	Spalart-Allmaras
SPL	Sound Pressure Level
URANS	Unsteady Reynolds-Averaged Navier-Stokes

Chapter 1

Introduction

The purpose of this chapter is to provide an outline of the relevant past research works which places the research work presented in this thesis into context. The aims and objectives of the research are stated at the end of the chapter.

1.1 Overview

Aerodynamically-generated noise is a small undesirable by-product of unsteady fluid motion which is apparent in all modern means of transportation. From ground vehicles (road vehicles, high-speed trains) to commercial and military aircraft, aerodynamic noise emission is posing a major environmental problem. In the context of air transport, the pressing environmental challenge the world is facing due to aerodynamic noise has long been identified. Although significant progress has been made in the reduction of noise from individual aircraft, continued growth in civil air traffic has outstripped these efforts. The tremendous growth in air traffic in recent years is, therefore, increasing the pressure from the public to control the noise from aircraft, such that aerodynamic noise now represents a potential barrier to future air traffic growth. Hence, noise reduction technology is critical to the future development, expansion, and operation, of the world air transportation system. It is anticipated that with the projected increase in air travel aeroacoustics research will be more critical for the certification of future aircrafts.

In addition, noise issues are also known to be important on account of structural concerns, especially, it cannot be ignored for the world's ageing aircraft fleet. Higher acoustic loads on aircraft translates to more expense and more weight for reinforced aircraft structures [Raman & McLaughlin (2000)]. Especially in aerospace applications, cavities or surface cutouts are common and are also well documented in aerodynamic noise studies. Flow over a simple cavity geometry produces complex flow features such as flow-induced resonant tones, multiple flow and acoustic instabilities and wave interactions. The effects of these flow features are found to be severe in applications such as wheel wells, weapons bays, and other fuselage openings. Internal weapons bays on military aircraft, in particular, have several design advantages. Reduced aerodynamic drag, low radar cross-section and avoidance of aerodynamic heating of the store are a few examples of these. However, once the weapons bay doors are opened, the resultant flowfield in the cavity is dependent on the cavity geometry and the freestream flow

conditions. The resultant flowfield then interacts with the stores at the beginning of the store release leading to several undesirable aerodynamic effects. Firstly, the self-sustaining pressure fluctuations in the cavity cause cavity resonance which in turn leads to structural fatigue of the aircraft and the store. Secondly, the interaction of the store with the unsteady shear layer formed over the cavity can lead to unpredictable motion of the store.

To address these issues, an efficient technique to control and reduce the noise emissions is required, and the obvious choice to achieve this is by reducing the noise at source. This means that a detailed understanding of the nature of the source responsible, its noise generation mechanisms and the noise radiation characteristics, is required. Hence, a computational solver which is capable of accurately modelling the flow physics responsible is essential. Computational techniques can also be used as a tool for the development of flow control. This project is also motivated by the structural and environmental challenges posed by acoustic fluctuations in cavity geometries. It also includes the computational study of the effects of the store on the aerodynamic and the aeroacoustic characteristics of a cavity. The ultimate aim is to propose a suitable flow control and/or design change to reduce the acoustic signature of aircraft with minimum aerodynamic penalty.

1.2 Literature Review

A literature review relevant to current research is presented in this section. This includes introductory background, advances in cavity research, computational methodologies and computational solver developments.

1.2.1 Cavity Aeroacoustics

Cavity flow research has been evolving continuously for more than 100 years with work dating back to as early as 1875. Helmholtz (1875) developed an analytical expression for the flow resonance process. Helmholtz's work was further developed by Rayleigh (1896) who, using energy equations for compressible fluids, made adjustments for different mouth geometries over the resonant chambers. Rayleigh's studies, which he modelled as an equivalent spring-mass system for oscillating compressible fluid in the chamber, showed that the kinetic energy of the fluid in the cavity mouth was stored by the compressibility of the fluid in the cavity chamber. These early works, although relevant to cavity flow studies, were not explicit studies of cavity flow characteristics. The study of the aerodynamic properties of cavity flowfields did not start until the mid 20th century.

One of the early works to study cavity flow physics was carried out by Owen (1958) during 1952 and 1953 at the Royal Aircraft Establishment. His investigation, which involved low speed wind tunnel experiments, found the pressure fluctuations to be random for shallow and moderately deep bomb bays. He also found that for a given bay geometry the fluctuating pressure was proportional to free-stream kinetic energy. Similar studies by Norton (1952) carried out in America at the time on a B-47 aircraft at rather higher speeds showed that, in addition to the random pressure fluctuation, strong periodic fluctuations may occur in the flow over bomb bays. The nature of these periodic fluctuations was studied by Krishnamurty (1955) and Plumblee et al. (1962). Krishnamurty found, experimentally, that the periodic pressure fluctuations are accompanied by strong acoustic radiation from the cavity and that their frequency increases with the airspeed and decreases with increasing cavity length. On the other hand, Plumblee *et al.* proposed, analytically, that the periodic fluctuations in the cavity were due to an acoustic resonance excited by the unsteadiness in the boundary layer approaching the cavity. But this conjecture fails when the boundary layer approaching the cavity is laminar because the periodic pressure fluctuations exist even in the case of laminar flow. Wind tunnel experiments were also conducted on flow over cavities at subsonic and transonic speeds by Rossiter (1966) to better understand the cavity flow characteristics. Rossiter's study showed that unsteady pressures in cavities exposed to subsonic and transonic flows may contain both

random and periodic components. However, generally, the random component predominated in shallow cavities ($L/D > 4$) and the periodic component predominated in deep cavities ($L/D < 4$). In his experiment, a resonance mechanism similar to the mechanism devised by Powell (1953) of edge tones within the cavity appeared to be responsible for the periodic component of pressure fluctuation. The measured periodic components were found to be as high as 35% of the free-stream dynamic pressure. These works of Krishnamurty (suggesting strong acoustic radiation from the cavity) and of Rossiter (on the presence of a resonance mechanism responsible for the periodic pressure fluctuation in the cavity) were early breakthroughs in the description of flow oscillation mechanisms based on acoustic resonance specifically for cavity flows. They will serve as the starting point for the subsequent sections in this literature review.

1.2.2 Cavity Flow Types

Early studies based on the analysis of wake flows by Charwat et al. (1961a,b) led to the characterisation of three distinct types of cavity flows based on the cavity floor pressure distributions, which are primarily dependent on the geometry of the cavity. These were categorized as open, closed and intermediate flows. In the 1980s, Stallings & Wilcox (1987) studied cavity pressure distributions at supersonic speeds experimentally. Their work led to a more detailed classification of the flow types and the intermediate flow type was further explained and divided into transitional open and transitional closed flow.

Cavity flows are usually classified by the length-to-depth ratio (L/D) of the cavity and four different types of cavity flows are categorized depending on the value of this ratio. Cavity flows, however, exhibit a wide variety of phenomena whose precise nature depends sensitively on a number of parameters including the value of L/D. In the literature, vastly different values of L/D have been quoted to define the flow types. For instance: $L/D < 7$ for open and $L/D > 13$ for closed cavity flow is reported in Stallings & Wilcox (1987) whereas $L/D < 10$ for open and $L/D > 13$ for closed cavity flow is reported in the work of Plentovich (1992). Similarly, Dix & Bauer (2000) quote $L/D < 9$ for open and $L/D > 13$ for closed cavity flow whereas Srinivisan & Baysal (1991) quote $L/D < 3$ for open and $L/D > 10$ for closed cavity flowfields. Tracy & Plentovich (1992) investigated the variations in the values of L/D and concluded that the vast disagreements in the literature were due to the dependence of the cavity flow type on Mach number as well as L/D. The other important of parameters that affect cavity flow types are incoming boundary layer thickness (δ), ambient density (ρ), viscosity (μ), and speed of sound (a_0). Although the underlying physical mechanisms vary, it is known that self-sustaining oscillations develop over a wide range of these parameters.

Open Cavity Flows

Open cavity flows are found to have, compared to all flow types, a more organized character and are often dominated by highly periodic phenomena. Such flow types are widely present in many aerospace applications, such as wheel wells, weapons bays, and other fuselage openings for sensors. Unsteady flow approaching such a cavity forms an oscillating free shear layer when the flow separates from the upstream edge of the cavity. The shear layer bridges the cavity and re-attaches at a point on the downstream wall, thus forming a large captive eddy within the cavity. When the cavity flow is stable a nearly uniform longitudinal static pressure distribution is established. This is desirable for safe store separation. However, strong acoustic tones can develop due to the strong interactions between instabilities in the shear layer and the vortices present in the cavity. These high intensity acoustic tones which occur at specific frequencies, can lead to structural vibration of aircraft components and the surrounding structure (including the separating store) leading further to structural fatigue.

Numerous investigations have been conducted to gain insight into cavity flow dynamics e.g. Krishnamurty (1955); Rossiter (1966); Charwat et al. (1961a,b); Rockwell & Naudascher (1978, 1979) and there is now an understanding that open cavity flows can produce self-sustained oscillations and interactions between the shed vortices inside and outside the cavity. These oscillations are undesirable as they can induce structural vibration and fatigue, noise radiation and substantial increases in mean drag. A detailed account of the oscillation mechanism based on past studies will be given in a later section. Figure 1.1(a) shows a basic representation of the open cavity flowfield model for subsonic and supersonic speeds. This research project is also concerned with the investigation of open cavity flow regimes.

Closed Cavity Flows

Closed cavity flows are associated with cavities having L/D ratios typically greater than 13. In this type of flow regime, the shear layer which forms as the incoming boundary layer separates at the cavity leading edge, reattaches along the floor of the cavity, before separating again ahead of the downstream wall. This creates two distinct separation regions, one downstream of the leading face and one upstream of the trailing face. Such flows are characterized by adverse static-pressure gradients along the cavity floor. The closed cavity flow at subsonic speeds is also characterized as responding in the wake mode as it exhibits a bluff body wake behaviour resulting in pressure fluctuations that are generally broadband in nature. Gharib & Roshko (1991) studied the closed cavity

flowfields and found it similar to bluff body wakes, hence the name. In this class of cavity flows, self oscillations cease (unlike in open cavity flows) and the cavity flow becomes unstable on a macro scale which results in greatly increased drag. The pressure distribution in this class of flow consists of three separate stages associated with the flow dynamics. The sharp longitudinal static pressure gradient present within the cavity can cause dangerously large pitching moments on any separating stores. A typical closed cavity flowfield for both subsonic and supersonic speeds can be seen in Figure 1.1(d).

Transitional Cavity Flows

An experimental study of cavity flow behaviour at supersonic speeds by Stallings & Wilcox (1987) led to classification of cavity flow types into transitional closed and transitional open cavity flows, and these types of flow occur for values of L/D that lie in the range between open and closed cavity flows i.e. typically $7 < L/D < 13$. Detailed investigations of the cavity flowfield were carried out by varying the cavity length (and, hence, L/D). Firstly, with the cavity flowfield being of the closed type, the cavity length was decreased until the flowfield changed to open flow. Secondly, the length of a cavity, with the flowfield well inside the open flowfield regime, was gradually increased until the flow changed to closed type. In this way, two critical L/D ratios were recorded corresponding to the change of flowfield types. The data showed that the critical L/D ratio obtained by increasing the cavity length was greater than that obtained by decreasing cavity length. This hysteresis effect on the value of L/D ratios increased with increasing Mach number. The transitional cavity flow type occurs in between the two values of the critical L/D ratios.

Transitional closed cavity flow occurs at the lower L/D boundary of the closed cavity flow. In this case the impingement and exit shocks that normally occur for the closed cavity flow types at supersonic speeds coincide to form a single shock. Large longitudinal pressure gradients, as in the case for closed cavity flows, are present in the cavity and can cause large pitching moments to exist on any store being released from the cavity. With a further small reduction in L/D value from transitional closed cavity flow, the impingement and exit shock waves transform abruptly into a series of compression wavelets. This suggests that the shear layer still enters the cavity but it does not impinge on the cavity floor. This type of flow is referred to as transitional open cavity flow. Longitudinal pressure gradients are present within the cavity, though they are not as severe as for the transitional closed cavity flow. Hence, pitching moments on the stores are also less severe. Figure 1.1(b-c) shows typical flow characteristics of transitional open and transitional closed cavity flows, respectively, at supersonic speeds.

1.2.3 Physics behind Cavity Flow Oscillations

Many studies have been conducted to understand the fundamental fluid mechanics associated with open cavity flow oscillations e.g. Krishnamurty (1955); Plumblee et al. (1962); Rossiter (1966); Gharib & Roshko (1991). Open cavity flow fields can exhibit a number of different flow oscillation characteristics depending on the flow conditions and cavity geometry. The study of Rockwell & Naudascher (1978) defined these oscillation characteristics and categorized them into three different oscillation types which are described below.

Fluid Dynamic Oscillations

Fluid dynamic oscillations occur in cavities with a short length compared to the acoustic wavelength. The frequencies of such oscillations can be traced to the selective amplification of the vorticity fluctuations inside the cavity shear layer. The primary mechanism for the existence of these oscillations is the amplification of unstable disturbances in the cavity shear layer and this process is strongly enhanced by the presence of the downstream edge of the cavity. The cavity downstream edge enhances the upstream propagation of disturbances which is the feedback condition. Two parameters can, therefore, be emphasized for the existence of these oscillations: the selective amplification condition of the shear layer and the feedback process. Selective amplification of shear layer instabilities, which causes some disturbances to be amplified more than others, is necessary for the generation of large amplitude oscillations. But this is not a sufficient condition because, without the existence of an effective feedback mechanism, the oscillations would eventually die.

Fluid-Resonant Oscillations

Fluid-resonant cavity oscillations occur when the oscillation is strongly coupled with resonant wave effects within the cavity. For this class of oscillations, the frequencies are sufficiently high such that the acoustic wavelength is typically of the same order of magnitude as the cavity characteristic length e.g. L or W. Within the context of the open-flow regime, the nature of the flow oscillations is further dependent on the L/D. According to Tracy & Plentovich (1993) if the value of L/D is sufficiently large, longitudinal standing waves may exist and the cavity is termed a shallow cavity. Similarly according to East (1966), transverse waves may exist in the the cavity if the value of L/D is sufficiently small, and such a cavity is, then, called a deep cavity. Although the values of L/D which define these two classes have not been precisely identified, shallow cavity behaviour

is usually found to occur for $L/D > 1$, while deep cavity behaviour usually occurs for $L/D < 1$ according to Rockwell & Naudascher (1978). The development of either of these two resonant modes of oscillation is dependent upon several interacting events. For deep cavities at low Mach number it was found in the work of East (1966) that discrete frequency oscillations exist only over a limited velocity range, indicating an effective discrete feedback mechanism in the shear layer rather than broadband disturbance energy from the shear layer that is mainly responsible for the resonance. For the range of geometries and flow conditions investigated the resonant frequency was found to decrease as either length or depth was increased.

Fluid-Elastic Oscillations

If one or more of the cavity walls deform elastically to an extent such that the feedback mechanism of the shear layer instabilities is established, then fluid-elastic oscillations occur. In fact, it can be assumed that the vibrating structure has the same effects as the resonating wave does in fluid resonant oscillations. Amplification of the shear instabilities is via a resonant-type process as in fluid-resonant oscillations and the frequency response of the system is the same as the natural frequency curves of a structural oscillator. This type of oscillation is very complex and more challenging than the previous two because there is an inherent flow-structure interaction in the system. This interaction requires an account for inertial, elastic and structural damping characteristics and their mutual interactions while describing the mechanism for self-sustained oscillations.

Cavity Flow Control Techniques

In the previous sections, it was highlighted that the flow approaching a simple cavity produces a rich variety of complex flow phenomena including resonant tones, multiple flow and acoustic instabilities, and complex wave interactions. A wide spectrum of research activities [Vakili & Gauthier (1994); Raman et al. (1999); Huang & Weaver (1991); Cattafesta et al. (2008); Lawson & Barakos (2009)] to control these complex cavity flow behaviours is ongoing across the globe. Although initially the solution might seem simple enough such that any scheme that disrupts the resonance mechanism can be used to suppress resonant tones, finding a practical solution is not straightforward. There are currently three main approaches which are being used to vary the way the flow behaves in the cavity. They are: passive, active open-loop, and closed-loop flow controls. Passive methods involve manipulating the cavity geometry by either modifying the cavity walls slanting angle or adding mechanical devices to deliberately alter the flow inside the cavity.

The other two methods involve manipulating the flow inside the cavity by devices that require external energy input e.g. jets or oscillating flaps. They can be either of the open- or closed-loop types. Closed-loop control requires the implementation of a feedback loop in the control system allowing it to continuously monitor and update the control parameters to match the changing flow conditions. Hence, closed-loop control systems are more suitable for time-varying and off-design situations. The closed loop system developed by Cattafesta et al. (1999) to suppress the resonant modes from a weapons-bay was not very successful, although this was blamed on the poor performance of the actuators. Active open-loop methods have been found to be limited by actuator bandwidth, and they require large actuator power to be effective [Cattafesta et al. (1999)] whereas closed-loop techniques introduce greater complexity and are not mature enough yet. At this point, it is important to point out that passive and active open-loop schemes break the resonance cycle in a fundamentally different way to the closed-loop counterparts. Because the dynamics of a linear system cannot be changed with open-loop control, any open-loop method used to modify the cavity resonance cycles must do so at finite amplitudes, typically at amplitudes comparable to the tones being suppressed. By contrast, closed-loop control can act by changing the dynamics of the linear system, which implies that low-power actuators can be used effectively. A classification of various flow control schemes is depicted in Fig 1.2 [Cattafesta et al. (2003)]. In this research thesis, passive devices are considered for cavity acoustic suppression.

1.2.4 Cavity Flow Modelling and Developments

An important and common phenomenon associated with all classes of cavity flow is increased noise radiation. Far-field noise measurements presented by Yu (1977) indicate the acoustic power is proportional to the sixth power of the freestream velocity for shallow cavities, and is proportional to the 4.7th power for deep cavities. The published data for the amplitudes of oscillation exhibit considerable scatter even for similar Mach numbers and cavity geometry. Colonius (2001) suggests that this may be primarily due to the influence of differences in the nature of the boundary layers at separation on the instability characteristics of shear layers that span the cavities.

The first description of the phenomena governing shallow cavity oscillations dates back to earlier experimental work conducted by Rossiter (1966). The Rossiter model is based on the idea of an acoustic feedback cycle, similar to that put forward by Powell (1953) in his work on edge-tones. The theory may be summarized as follows: vortical disturbances originating at the leading edge of the cavity travel downstream and impinge on the downstream cavity corner, generating acoustic disturbances. These acoustic waves

then propagate upstream to the region near the shear layer separation point where they induce localized vortical fluctuations, thereby closing the feedback loop. Realising that these events must be synchronized, Rossiter derived the following semi-empirical formula to predict the resonant frequencies

$$f_n = \frac{U_\infty}{L}\left(\frac{n-\alpha}{M_\infty + \frac{1}{K}}\right) \tag{1.1}$$

where f_n is the frequency corresponding to the n_{th} mode, M_∞ is the freestream Mach number, K is the ratio of disturbance velocity in the shear layer to the freestream velocity and α is an empirical constant employed to account for the phase lag between the passage of a vortical disturbance past the cavity trailing edge and the formation of an upstream travelling disturbance. The value of α depends on the L/D and is evaluated as : $\alpha = 0.062(L/D)$.

Rossiter's model is generally found to agree well with experimental results at moderate subsonic Mach numbers. Heller et al. (1971) found that the temperature recovery within the cavity was important at transonic and supersonic Mach numbers and hence it was essential to account for the increased speed of sound within the cavity. To accommodate these high Mach number ranges, various alternative semi-empirical models have been developed by several authors, e.g. Heller et al. (1971), Tam & Block (1978). Heller et al. (1971) proposed a modification to Rossiter's equation (1.1) to account for the higher speed of sound within the cavity for cavity flows at high Mach numbers thus:

$$f = \frac{U_\infty}{L}\left(\frac{n-\alpha}{M_\infty\left[1+\frac{(\gamma-1)}{2}M_\infty^2\right]^{-\frac{1}{2}} + \frac{1}{K}}\right) \tag{1.2}$$

where γ is the ratio of specific heats of the test fluid ($\gamma = 1.4$ for air).

The linear analysis of Tam & Block (1978) merits some discussion as it is the most sophisticated approach of all, offering a more complete and physical explanation of noise generation by shallow cavities. In this model, sound generation at the downstream edge is modelled as a simple line source along the trailing edge, that alternately produces compression and rarefraction waves as the shear layer is deflected into and out of the cavity. The effects of reflection from the cavity walls are incorporated through image sources. At the upstream edge of the cavity, the phase difference between the pressure waves, within and outside the cavity, results in a pressure difference that excites the shear

layer and completes the feedback mechanism. By including the effects of finite shear layer thickness in their model, Tam and Block were able to obtain good agreement with their experimental data. Apart from the prediction of the possible modes of resonance using the above mentioned semi-empirical models, the inherent complexity of cavity flows has, to date, stalled the further development of more complete analytical models. Numerical models have, therefore, played an important role in the development of our understanding of cavity flow physics. Although computational resources have increased, so too has the complexity and sophistication of numerical models. To date, the majority of work has been based on time-dependent Reynolds-averaged Navier-Stokes simulations e.g. Srinivisan & Baysal (1991); Grace (2001); Henderson et al. (2000); Takeda & Shieh (2004), although more recent works have shown promise with the Large Eddy Simulations of Rizzetta & Visbal (2003) and, more importantly, hybrid RANS/LES methods of Arunajatesan & Sinha (2003); Xiao et al. (2003, 2004).

1.2.5 Overview of Aeroacoustic Research

The study of aeroacoustics is mainly concerned with noise produced by aerodynamic sources including turbulence and moving aerodynamic surfaces. An integral component of the acoustic analysis of these sources is the aerodynamic field generated by them which, in essence, acts as the source of noise. Also, aeroacoustics is concerned essentially with a small by-product of fluid flows whose internal dynamics can generally be assumed to be negligibly small. This initially gives rise to hope that the flow dynamics will be more or less decoupled from the wave motion and hence an assumed knowledge of the flow can be used to predict the wave motion. However, flow variables defining a turbulent flow cannot be defined with any degree of confidence which suggests that aeroacoustic theory should be formulated in such a way that it demands the minimum information from the flow. Hence, great care is needed while approximating the aerodynamically generated noise. Firstly, it is a small by-product of the aerodynamic flow field. Secondly, even though the approximations regarding the aerodynamic field may be safe enough, they can be fatal for the by-product. Large errors are, therefore, likely even with reasonable approximations.

Aerodynamic Noise Theory

Aerodynamic noise research is a relatively new subject and the modern theory of aerodynamic noise did not come to light until the pioneering work of Sir James Lighthill (1952) in early 1950s. Lighthill established the theory of aerodynamic noise, which was based

on the exact Navier-Stokes equations. Considering the idealized problem of predicting the sound produced by a finite region of turbulent flow embedded in an otherwise homogenous fluid with constant speed of sound, a_0, and density, ρ_0, and assuming that the density fluctuations at large distances from such a turbulent region behave like acoustic waves, Lighthill demonstrated that the exact equations of continuity and momentum could be rearranged into an inhomogeneous wave equation, now known as Lighthill's equation:

$$\frac{\partial^2 \rho}{\partial t^2} - a_0^2 \nabla^2 \rho = \frac{\partial^2 T_{ij}}{\partial x_i \partial x_j}. \tag{1.3}$$

where T_{ij} is Lighthill's stress tensor, given by $T_{ij} = (\rho u_i u_j + p_{ij} - a_0^2 \rho \delta_{ij})$ and a_0 is the speed of sound in ambient air. This rearrangement of the Navier-Stokes equations introduced the concept of the acoustic analogy (popularly known as Lighthill's acoustic analogy), which simply states that there is an analogy between the density fluctuations in any real flow and the small fluctuations in density that would result from a distribution of quadrupole-type acoustic sources in a fictitious non-moving medium with sound speed a_0. Lighthill solved the above wave equation using properties of generalised functions (see the work of Farassat (1994) for details), and obtained the final solution presented below:

$$\rho - \rho_0 = \frac{1}{4\pi a_0^2} \frac{\partial^2}{\partial x_i \partial x_j} \int_V \frac{T_{ij}(y, t - \frac{r}{a_0})}{r} dy. \tag{1.4}$$

The application of Lighthill's acoustic analogy to any aerodynamic noise problem is dependent upon being able to specify Lighthill's stress tensor (T_{ij})[1] to sufficient accuracy. In actual fact, Lighthill's equation is a coupled integro-differential equation for density, since this appears as the independent variable and also in the source term. The evaluation of the noise source, therefore, requires a complete knowledge of the flowfield, including the sound field. This, however, is rarely available and so in practical applications of Lighthill's acoustic analogy it is necessary to assume that the sound waves present in the flow do not modify the flow itself. Lighthill's stress tensor can then be approximated by replacing the fluctuating instantaneous density by the ambient density and the remaining flow variables estimated from aerodynamic principles. This is the virtue of Lighthill's

[1]Tensorial suffices used are for representing the vector components. Both the suffix form and the bold face symbols are used to denote vectors, the choice being made either in accordance with convention or conciseness of the formulae. With the usual convention of vector and tensor analysis, therefore, the terms with a repeated suffix are to be regarded as summed over all possible values of the suffix.

approach; it is capable of producing a good approximation of the order of magnitude of the sound radiated from a turbulent flow, even when the actual unsteady flow field itself is only available in very approximate detail. In fact, Lighthill's celebrated eighth-power law is a result of an early exploitation of this very feature. Assuming only that the quadrupole sources scaled with the variables defining the hydrodynamic mean field, Lighthill was able to show that the acoustic power radiated from a jet at low Mach number scaled with the eighth power of the jet velocity, establishing the turbulence of the jet mixing layer as the main source of noise and showing jet speed to be the principal parameter determining the overall noise.

Hence, although Lighthill's theory is based on the exact Navier-Stokes equations, the answer obtained from Lighthill's theory is only as accurate as the equivalent acoustic source terms, which must be calculated or measured for the given unsteady or turbulent flow. In Lighthill's equation, the acoustic sources are treated as a distribution of equivalent point sources, whose strengths are obtained from Lighthill's stress tensor T_{ij}, where T_{ij} is derived from the properties of the unsteady or turbulent flowfield. The theory also assumes the absence of a solid boundary and hence insignificant back reaction of the sound produced on the flowfield itself (i.e. the sound produced is so weak relative to the motions producing it that no significant flow-acoustic interaction can be expected unless there is such a resonator present to amplify the sound). However, when the source mean flow is non-uniform, the propagation of sound waves through it involves flow-acoustic interaction. This has been discussed by Renaut & Rosemary (1997) in detail. Also, this theory accounts only for the energy which escapes in the form of sound from the flow and its directional distribution, and is confined in its application to completely subsonic flows.

Curle (1955) extended Lighthill's theory to account for the effect of solid boundaries. He pointed out that the presence of solid boundaries can affect the acoustic propagation in two ways. Firstly, the sound produced by quadrupole sources in Lighthill's theory will be reflected and diffracted by the solid boundary. Secondly and most importantly, the quadrupoles will no longer be distributed over the whole of the space but only the region external to the solid boundary. It is, therefore, possible to have a resultant distribution of dipoles (or monopole sources) at the boundaries. Dipoles are especially likely since in acoustics they correspond to the externally applied forces and such forces are present between the fluid and the solid boundary. The modified version of Lighthill's solution proposed by Curle, which now consists of a volume as well as a surface integral, is

$$\rho - \rho_0 = \frac{1}{4\pi a_0^2}\frac{\partial^2}{\partial x_i \partial x_j}\int_V \frac{T_{ij}(y, t - \frac{r}{a_0})}{r} dy - \frac{1}{4\pi a_0^2}\frac{\partial}{\partial x_i}\int_S \frac{P_i(y, t - \frac{r}{a_0})}{r} dS(y). \tag{1.5}$$

where,

$$P_i = -\ell_j P_{ij}.$$

and ℓ_j is the direction cosine of the outward normal to the fluid. In Curle's solution, an extra surface integral is included which is equivalent to the sound generated by a distribution of dipoles of strength P_i per unit area in a medium at rest (P_i is exactly the force per unit area exerted on the fluid by the solid boundaries in the x_i direction). Also, the volume integral in Curle's equation is different from that in Lighthill's equation. The difference arises from the effect of the impact (on a solid boundary) of sound waves from the quadrupoles. Curle proposed the sound field as the sum of that generated by a volume distribution of quadrupoles and by the source distribution of dipoles.

Ffowcs-Williams & Hawkings (1969) extended the Lighthill-Curle theory to evaluate the density field radiated by turbulence in the presence of arbitrarily moving surfaces which, when expressed in terms of generalised functions (as illustrated in the work of Farassat (1994)), is:

$$\left(\frac{\partial^2}{\partial t^2} - a_0^2\nabla^2\right)(\rho H(f)) = \frac{\partial^2}{\partial x_i \partial x_j}\left(T_{ij}H(f)\right) - \frac{\partial}{\partial x_i}\left(L_i\delta(f)\right) + \frac{\partial}{\partial t}\left(U_n\delta(f)\right). \tag{1.6}$$

where,

$$\begin{aligned} T_{ij} &= \rho u_i u_j - \tau_{ij} + \left[(p - p_0) - a_0^2(\rho - \rho_0)\right]\delta_{ij}. \\ L_i &= L_{ij}\hat{n}_j = \left[\rho u_i(u_j - v_j) + p'_{ij}\right]\hat{n}_j. \\ U_n &= U_i\hat{n}_i = \left[\rho(u_i - v_i) + \rho_0 v_i\right]\hat{n}_i. \\ p'_{ij} &= (p - p_0)\delta_{ij} - \tau_{ij}. \end{aligned}$$

In aeroacoustic literature, the three terms on the right hand side of the Eq.B.24 are known as quadrupole, loading and thickness source terms, respectively. The thickness and loading source terms are surface distributions of sources as indicated by $\delta(f)$. When the control surface encloses a physical surface, the thickness source accounts for the displacement of fluid produced by the body and the loading source accounts for the unsteady loading exerted by the body on the fluid. The quadrupole source, a volume source distribution as indicated by $H(f)$, accounts for all the non-linearity in the region external to the control surface. Solutions to the above equation can be presented in various forms. Below is one of the frequently used forms (a detailed derivation is given by Farassat & Succi (1983)).

$$
\begin{aligned}
a_0^2(\rho-\rho_0)H(f) &= \frac{\partial^2}{\partial x_i \partial x_j}\int_V \left[\frac{T_{ij}}{r|1-M_r|}\right]_{\tau^*} \mathrm{d}V + \int_S \left[\frac{Q_r \dot{+} Q_r}{r(1-M_r)^2}\right]_{\tau^*} \mathrm{d}S \\
&+ \frac{1}{a_0}\int_S \left[\frac{F_r}{r(1-M_r)^2}\right]_{\tau^*} \mathrm{d}S + \int_S \left[\frac{F_r+F_m}{r^2(1-M_r)^2}\right]_{\tau^*} \mathrm{d}S \\
&+ \frac{1}{a_0}\int_S \left[\frac{F_r\left(r\dot{M}_r \dot{+} a_0 M_r - a_0 M^2\right)}{r^2(1-M_r)^2}\right]_{\tau^*} \mathrm{d}S \\
&+ \int_S \left[\frac{Q_r\left(r\dot{M}_r \dot{+} c_0 M_r - a_0 M^2\right)}{r^2(1-M_r)^3}\right]_{\tau^*} \mathrm{d}S. \qquad (1.7)
\end{aligned}
$$

1.2.6 Acoustic Analogy

Acoustic analogies are reformulations of the governing fluid flow equations (compressible Navier-Stokes equations). In this method, the Navier-Stokes equations are rearranged in the form of an inhomogeneous wave equation with source terms on the right hand side. Source terms are then made independent of the fluctuating acoustic variables with some assumptions. Such a formulation represents a linear wave problem at rest with equivalent acoustic sources (monopoles, dipoles and quadrupoles) derived from an unsteady flow. Hence, an aeroacoustic problem (based on instability in fluid flow), can essentially be converted into a problem of classical acoustics. This is the reason why the formulations based on this approach are widely known as acoustic analogies. The methods based on these acoustic analogies (first pioneered by Lighthill and then later extended by Curle (1955) and Ffowcs-Williams & Hawkings (1969)) require only the information on the near-field flow to predict farfield noise, and hence provide a viable alternative to computational aeroacoustics (CAA - see Section 1.2.7). This, therefore, means that a farfield noise data at a very large distance can be calculated using a nearfield CFD results, i.e. it avoids the requirement to have a CFD domain which covers source and observer locations. This is the method most widely used in current aeroacoustic simulations. Some of these techniques will be explained in subsequent sections. One of the interesting aspects of integral methods is that the required computational time is independent of the observer distance. However, increasing the observer distance means an increased amount of analysis data, and hence a higher storage requirement. Integral methods require knowledge of the aerodynamic flowfield around the body surface, which then permits one to evaluate the acoustic pressures at any point in the field by executing a certain number of integrals. A typical aerodynamic noise calculation, therefore, is performed in two steps, popularly

known as a hybrid method. In the first step, CFD calculations are performed to retrieve the necessary flowfield variables demanded by the integral formulations in the second step. Then an integral formulation is applied to propagate the disturbances to the farfield. It is necessary to comment on the finding of Tam (2002) that the acoustic analogy should not be taken as the absolute answer by acoustic researchers. Tam pointed out that the acoustic analogy fails to identify correct acoustic sources in turbulent flows, and may not be a suitable tool for noise problems where large turbulent structures and fine-scale turbulence define radiated sound fields (e.g. high Mach number flow, jet noise problems). This is not always true. There should be no dispute over the fact that the acoustic analogy can be used to predict the radiated noise as long as the nature of turbulence is known in sufficient detail. Hence, it is not the acoustic analogy which fails to identify the correct acoustic sources in turbulent flows but the choice of turbulence model which determines the accuracy of the noise prediction. As there is no absolute answer to the best choice of turbulence model (which in itself depends on the individual problem), so is the case for aeroacoustic simulations.

Ffowcs Williams-Hawkings (FW-H) Formulation

This formulation is the most widely used for noise radiation studies and was derived by Ffowcs-Williams & Hawkings (1969). It is based on an exact rearrangement of the continuity equation and the Navier-Stokes equations into the form of an inhomogeneous wave equation with two surface source terms (monopole and dipole) and a volume source term (quadrupole). This formulation embodies the most general form of the acoustic analogy. It permits the use of both impenetrable walls as well as permeable interior surfaces off the wall as integration surfaces. Therefore, it is able to deal with much broader classes of acoustic problems than can Curle's integral formulation, as reported in the work of Kim et al. (2003). It is linear when the quadrupole distribution is neglected, which is valid in the case of many subsonic applications. Taking into account quadrupole source terms requires substantially more computational resources due to the need for volume integration. It is, however, necessary to take into account the volume source term when calculating the noise radiated in high-speed flow conditions (e.g. transonic and supersonic flows). Another advantage is that the three source terms present in this method each have physical meaning. This was demonstrated in the study by Brentner (1986) in the case of helicopter rotor noise. The monopole source term in Eq. B.24 represents the thickness noise and is determined completely by the geometry and the kinematics of the body. The second term (dipole source), on the other hand, represents the loading noise and is generated by the forces that act on the fluid as a result of the presence

of the body (i.e. rotor in this case). Finally, the volumetric source term represented by Lighthill's stress tensor accounts for the nonlinear effects, e.g. nonlinear wave propagation and steepening, variations in the local speed of sound, and the noise generated by shocks, vorticity, and turbulence in the flowfield. This is helpful in understanding the noise-generation mechanism and designing quieter airframe components. The derivation and solution of the FW-H equation is set out in in Appendix B.

Kirchhoff's Formulation

This is another integral formulation which, unlike the FW-H formulation, does not require volume integration because it has only a surface source term. This is the reason why this method has been particularly popular in the past in the prediction of transonic noise generated by the advancing rotor tip of helicopters. To adapt the FW-H scheme in this situation would be computationally expensive, the reason being that the quadrupole source term is no longer negligible, thus requiring a computationally-demanding volume integration. However, Kirchhoff's formulation requires the integration surface to be chosen in the linear flow region (i.e. away from the region where significant velocity gradients exist), but the linear region itself may not be well defined and is problem-dependent. It is necessary, therefore, to specify the integration surface well away from the body surface (e.g. aerofoil surface). Specification of an integration surface well away from the body surface (at least one aerofoil chord away from the wall surface in the case of high-lift noise simulation) has negative effects as CFD solutions may not be well resolved away from the wall surfaces. Hence, the placement of Kirchhoff's integration surface is a compromise. Due to this shortfall, Manoha et al. (2002) had to use discretized linearised Euler equations (LEE) governing acoustic propagation in the non-linear region (i.e. the region between wall surface and the Kirchoff surface) before using Kirchhoff's formulation to propagate the acoustic disturbances to the farfield. Hence, Manoha's study involved a three step procedure. The use of LEE, however, increases the computational cost significantly since the propagation domain must be meshed with an adequate resolution with respect to the smallest acoustic wavelength, and also because finite difference higher-order schemes are needed to ensure numerical accuracy and low dispersion of the propagation of acoustic waves. However, the domain where LEE is used is strictly limited to the area of significant velocity gradients, normally small in most airframe noise problems so that a viable solution can be obtained. Although this avoids the evaluation of the volume integral, it requires knowledge of the derivative of pressure in the direction normal to the surface. This can impose difficulty, especially when there are discontinuities on the surface. In the case of the FW-H equation, it requires

values of pressure, density and flow-velocity perturbations, which are available from CFD solutions.

FW-H vs Kirchhoff's Formulation

Brentner & Farassat (1998) studied the FW-H and Kirchhoff formulation comparatively to address the superiority between the two in airframe noise prediction. The first clear advantage of the FW-H formulation is that it gives insight into the acoustic field in that the predicted noise is explicitly separated into physical components, i.e., thickness, loading and quadrupole terms. Also, the FW-H method can include non-linear effects of volume quadrupoles in its surface integral without having to perform volume integration if the usual assumption of an impenetrable surface is relaxed. This can be achieved by lifting the integration surface to enclose all the intense volume quadrupole terms usually present near the body surface. Kasper et al. (2004) assessed the radiated noise from volumetric sources in the case of a two-dimensional, three-element aerofoil by comparing a permeable surface integration with the sum of solid body surface integration and a volume integral. Their study resulted in different spectra for a body-aligned integration surface and an off-body surface. Also, the result of the off-body integration surface was in good agreement with the sum of the result of the solid-body integration surface and volume integral. This indicated that the volumetric sources were not negligible, and the off body integration surface was found to take account of the volumetric sources.

Ffowcs Williams has pointed out several implications of the permeable surface ($f = 0$) in Section 11.10 of the book by Crighton et al. (1992). The placement of the integration surface for the FW-H method is a matter of convenience as long as the quadrupole source term is utilized. The predicted acoustic pressure field by the Kirchhoff method can incur serious errors if the integration surface is placed in the non-linear region e.g. wake of an aerofoil. This was experienced in the work of Manoha et al. (2002) for the case where the integration surface intersected the wake behind the trailing edge of a slat; the result was conflicting with experiment. A final advantage of the FW-H approach is that it is relatively mature and has robust algorithms that have been validated for a variety of industrial problems. Recently, Kim et al. (2003) implemented the FW-H formulation in Fluent, a general purpose commercial CFD code, for aeroacoustic analysis. This implementation accounts only for stationary integration surfaces yet also allows for permeable integration surfaces. It is based on advanced-time formulation for better computational efficiency. The accuracy and suitability of the results from these general-purpose commercial codes, however, can be limited mainly because they are implemented in a lower-order scheme.

1.2.7 Computational Methods in Aeroacoustics

Computational methods have advanced the evolution of modern engineering analysis techniques, and aeroacoustics is no exception. Much of the advancement in acoustic analysis has arisen from the availability of large computational resources. So far, computational fluid dynamics has been the main tool in the development of new designs in the aeronautics sector, advances in both numerical techniques and increased power of computers being the key. The trend to apply powerful and effective computational fluid dynamics (CFD) methods is on the increase, due to the complexity of the flow physics engineers have to deal with in aeronautics. Computational aeroacoustics (CAA), as with the field of CFD, encompasses a wide variety of physical models and solution philosophies. CAA is different from CFD in the sense that it involves the development of schemes to approximate spatial and temporal derivatives in a way that preserves the physics of wave propagation, a phenomenon of little significance in typical aerodynamic computations because aerodynamic noise is a fractional by-product of fluid flows. Also, generally, aerodynamic problems can sometimes be modelled as time independent whereas aeroacoustics problems are, by their very nature, time dependent. The numerical modelling of such phenomena is very demanding and poses challenges distinct from those present in the more developed field of CFD.

Generally, CAA includes a number of constituents, e.g. nearfield flow and source modelling, integral formulations. For source modelling, CAA involves solving both the aerodynamic and aeroacoustic problems simultaneously and is based on the solution of the fluid motion equations by classical field methods (e.g. finite volume, finite element, finite difference). In other words, CAA attempts to resolve directly wave propagation to the far-field. Because of the classical field methods employed in solving fluid equations in CAA, it requires large computational resources in order to avoid excessive dissipation in solution. The requirement in computational resources increases as the observer distance is increased. According to Francescantonio (1997), due to this drawback, an acceptable solution could only be obtained at a reasonable cost for observers at a distance of about 3 times the rotor radius in the case of helicopter noise (this figure is based on present computational capability available). In practical situations, however, the observer distance usually required is about two to three orders of magnitude greater than the reference length used (e.g. cavity length, wing chord etc). Therefore, the problem of direct numerical simulation of airframe noise is still beyond the capabilities of CAA based on currently available computing power. Some of these issues and practical limitations which exist in CAA are discussed in the subsequent section.

Modelling Issues and Limitations in CAA

The numerical modelling of aeroacoustic phenomena is demanding for several reasons. Foremost is the fact that aeroacoustic problems are, by definition, time-dependent. They must, therefore, be treated time-accurately with appropriate consideration of all relevant time-scales. Since the human ear is sensitive to a wide range of frequencies (typically 20 Hz to 20 kHz), simulations dealing with such problems must also span this broad spectrum. An equally important consideration is the disparity between the energy levels of the unsteady flow fluctuations and the acoustic signals. A fairly intense acoustic wave of 100dB contains pressure fluctuations which are three orders of magnitude smaller than the pressure fluctuations in a typical turbulent flow. This large disparity between acoustic and flow variables presents a severe challenge to direct numerical simulation and has prompted many researchers to question whether it is more prudent to solve for the perturbations after the mean flow has been determined. For nonlinear problems in which the interaction between the acoustic and hydrodynamic fields is important, there is no alternative but to face the large magnitude disparity.

A numerical simulation attempting to simulate noise problems must resolve both the source evolution and sound propagation phenomena accurately enough so that sound fields are not contaminated by numerical errors. In practice, however, possible problems exist due to error accumulation in numerical methods when the numerical schemes are not optimized for low dissipation and dispersion characteristics. Numerical schemes approximate the non-dispersive, non-dissipative systems of governing equations through discretisation, which has numerical dissipation and dispersion, and introduces errors that may significantly affect the accuracy of the calculation. This has been the main challenge in aeroacoustics ever since computational methods were first employed. When the acoustic waves are part of the source mechanisms, as in cases involving acoustic/flow feedback, Singer & Guo (2004) find numerical dispersion to be the most harmful because it corrupts the phase information of the waves affecting the interaction between flow and sound. Furthermore, as one is often interested in the farfield characteristics of a given sound field, the computed sound fields need to be propagated over large distances comprising many wavelengths. This causes the dissipation to accumulate over the propagation length, resulting in significant changes in wave amplitude. Dispersion and dissipation errors are thus significant when numerical techniques such as finite difference and finite element methods are used for spatial discretisation in solving propagation problems when the propagation length is a distance of many wavelengths. Hence, to ensure that the computed solution is uniformly accurate over such long distances, a numerical scheme must be almost free of numerical dispersion, dissipation, and anisotropy.

As mentioned above, the radiation of acoustic energy to the far field is a defining feature of many aeroacoustic problems. The domains of interest in such cases are essentially unbounded. As it is impossible to solve directly a problem posed on an unbounded domain, the numerical modelling of such phenomena requires the introduction of artificial boundaries to make the computational domain finite. The boundary conditions imposed along these artificial boundaries need to closely approximate the free space solution that exists in the absence of these boundaries. Although such exact non-reflecting or farfield boundary conditions are known for several specific problems, the derivation of more general, efficient and suitably accurate boundary conditions remains an active area of research.

1.2.8 Numerical Schemes

The emergence of CAA as a viable research tool in aeroacoustics is testament not only to the proliferation of powerful computer resources, but also the development and improvement of numerical schemes more capable of meeting the challenges laid out in the preceding paragraphs. The advances in the development of high-order accurate schemes has been central to this success. High-order methods are available in a variety of forms, but researchers have favoured high-order finite difference schemes in CAA development. Such schemes have come to popularity as they represent a good compromise between high-order accuracy, increased complexity and available computing resources. Both explicit and implicit finite difference spatial discretization schemes are widely used e.g. Tam & Webb (1993); Kim & Lee (1996); Hixon (2000); Gaitonde & Visbal (1999). Explicit schemes employ large computational stencils for accuracy, whereas implicit schemes achieve high-order accuracy by solving for the spatial derivatives implicitly using relatively compact stencils. Traditionally, the coefficients of these finite difference schemes are chosen to give the highest order of formal accuracy.

The overwhelming majority of finite difference schemes employed in CAA have symmetric stencils because such schemes contain no inherent dissipation. While this property is desirable for wave propagation it does leave such schemes susceptible to uncontrolled growth of numerical instabilities. To overcome these difficulties, Visbal & Gaitonde (2001, 2000) proposed filtering methods and Kim & Lee (2000a) suggested damping schemes whose spectral characteristics can be optimized to reduce the filter's (or damping function's) impact on the resolved signal. For this reason, central differencing is preferred in CAA applications. With reference to integral formulations used in aeroacoustics, numerical dispersion has not been a matter of great concern. This is because the numerical dispersion and dissipation issue may be avoided (as Singer & Guo (2004) explain) when

using unsteady CFD and integral surface solution, e.g. the FW-H equation, whereby the propagation of the acoustic waves to the farfield is handled by an integral formulation that exactly preserves the non-dispersive and non-dissipative nature of the sound waves; no numerical discretisation is involved in the formulation and the wave characteristics are exactly computed. However, increases in accuracy requirements and the development of aircraft with fewer localized noise sources will drive the need for improved dispersion and dissipation characteristics. Hence, the desire for increased accuracy will always be present. Kurbatskii & Mankbadi (2004) presented a collective overview of the numerical tools currently available in aeroacoustic research and on-going developments. Subsequent sections below discuss a few of the popular, low dispersion, higher order schemes available currently.

Dispersion-Relation-Preserving (DRP) Scheme

Tam & Webb (1993) proposed a higher order finite difference scheme (widely known as a Dispersion-Relation-Preserving (DRP) scheme) to reduce dispersion so that the wave number of the original differential equations are replicated by the solution of the finite difference equations. The numerical solution of a higher-order finite difference scheme will have the same number of wave modes as the original differential equation if both systems have the same dispersion relations. They found that it was possible to achieve the same dispersion relation between the numerical and exact solutions as long as points-per-wavelength greater than four were maintained for the system under consideration. But there will always be the truncation error depending on the order of the discretization scheme. The derivation of the method uses Fourier-Laplace transforms rather than the usual truncated Taylor series. The use of Fourier analysis offers great flexibility including stability investigations, specification of acceptable errors from numerical calculations, etc. The authors used asymptotic solutions to develop the radiation and outflow boundary conditions for the DRP scheme. The transform method allows one to construct the asymptotic solution of the finite difference equations. The study shows the superior performance of the proposed higher-order explicit finite difference scheme over standard finite difference schemes. The numerical study was performed unidiagonally instead of multidiagonally. It, however, requires a large number of stencils (i.e. seven stencils for fourth order spatial accuracy).

Compact Scheme

Kim & Lee (1996) proposed a weighted optimization technique for the optimization of the

compact finite difference scheme. The DRP scheme of Tam and Webb, as explained above, was developed to minimise the dispersive errors in the wave number domain but it was a unidiagonal scheme. Therefore, the work of Kim and Lee is essentially an extension of Tam's unidiagonal DRP scheme to a multidiagonal (tridiagonal and pentadiagonal) compact scheme with high order and high resolution. It is obvious that the overall error of a numerical computation is determined by both the resolution and the order of truncation, and actual error characteristics of the compact schemes are dependent on their multidiagonality (usually, expansion from unidiagonality to multidiagonality results in improved resolution and truncation order). They found that the optimized sixth-order tridiagonal and the optimized fourth-order pentadiagonal scheme performed the best of all.

Kim (2007) also proposed a set of optimised boundary closure schemes for use with compact central finite difference schemes in non-periodic domains. The boundary schemes are given in a form of non-central compact finite differences. They maintain fourth-order accuracy, a pentadiagonal matrix system and a seven-point stencil which the main interior scheme employs. The coefficients of the scheme were optimized for improved resolution characteristics at boundary points by making use of polynomial-trigonometric blended extrapolation functions. The increased performance and accuracy of the new boundary schemes coupled with the main interior scheme of Kim & Lee (1996) at interior stencils have been effectively demonstrated through their applications to single- and multi-dimensional benchmark problems.

Prefactored Compact Scheme

Hixon (2000) proposed a small stencil compact scheme of prefactored type. The main feature of the method is that the tridiagonal matrices found in higher order compact schemes, which otherwise require an LU-decomposition technique, are reduced to two independent upper and lower bidiagonal matrices. These then can be solved in parallel. Also, the stencil size is reduced from five points to three for sixth order accuracy and, due to the smaller stencil size, only one boundary stencil is required instead of two. Hixon also showed that the stability and accuracy of the proposed scheme was much more dependent on the performance of the boundary stencils than in the case of equivalent explicit schemes. This is because the error from the boundary stencil derivatives can propagate many points into the computational domain.

Optimized Prefactored Compact Scheme

Ashcroft & Zhang (2003) proposed new optimized prefactored compact schemes in an effort to reduce dispersion and dissipation errors in aeroacoustic problems. This, in a sense, was the improved extension to the scheme developed by Hixon (2000). This method used Fourier analysis similar to the one used by Kim & Lee (1996), rather than the Taylor series expansion used by Hixon, and performs optimization to achieve the best possible accuracy and range factor. An obvious benefit in using a Fourier series is that it allows one to optimize the dispersive scheme by quantifying the dispersive errors. This method also used a weighting function and optimization range factor. The study showed a reduction in grid resolution requirements when compared to Tam's DRP and Hixon's prefactored compact schemes. It was also concluded that a fourth-order three point scheme provided the best overall performance in terms of resolution versus computational cost. Although the computational cost in this scheme is relatively low compared to other implicit compact differencing schemes, the boundary derivatives calculation (which is the most important for complex geometries) can have increased errors compared to the scheme of Kim (2007).

At this point it is necessary re-iterate that the problems in aeroacoustics are, by their very nature, time-dependent. Hence, just ensuring high spatial accuracy in isolation does not ensure good results in aeroacoustic simulations. DeBonis & Scott (2002) studied the consequences of disparate temporal and spatial descritizations. Their computational study found that for schemes with lower order time-stepping, the truncation error caused by time-stepping dominated the solution, reducing the overall error of the scheme to the order of time-stepping and eliminating the benefit gained from higher-order spatial discretization. The study included Gottlied-Turkel 2-4 predictor-corrector scheme and two-stage Runge-Kutta schemes (4-4 and 4-6). The Gottlied-Turkel method is fourth order accurate in space and second order accurate in time. Reducing the time step was found to increase the order of accuracy but with an increase to computational cost. The Runge-Kutta 4-4 scheme was found to perform best of all computationally.

Patched Grid Methods

Computational analysis of complex configurations using structured grids almost always (apart from geometrically simple cases) requires multiple blocks of grids. Even so, one-to-one matching at block interfaces while generating multi-block grids can cause significant difficulty depending on the complexity of the configuration. Also, an attempt to create a structured grid for a complex geometry causes highly-skewed cells which, in turn, results in inaccurate calculations. Another factor which can cause major problems in generating

a structured grid is the necessity to cluster grid points in regions where the flow variables and their gradients change rapidly. These issues are relevant to this research project as the configuration being considered is complex and a structured grid is used in the project.

The grid-generation issue mentioned above can be improved by the use of a zonal or patched, grid methods. The patched grid method allows one to generate the grid in each block independently i.e. it does not require one-to-one matching. Then, inter-block communication is established by using suitable interpolation at the block interface. Rai (1986a,b) proposed a patched-grid algorithm for Euler equations based on linear interpolation at the inter-block interface. Conservation is ensured at the grid interface using one-sided flux interpolation at the boundary. The interface condition for one subdomain is defined from the conservative variables while for the adjacent subdomain the interface condition is defined from the numerical flux. Rai's method of achieving conservation at the boundary can be difficult to achieve and implement in higher-order schemes. Lerat & Wu (1996) proposed a stable and conservative patched-grid algorithm for compressible flows. They demonstrated that their scheme was able to predict discontinuities in high-speed flow. They also pointed out that they were unable to achieve general stability for the scheme proposed by Rai (1986a,b). But Lerat and Wu's scheme is conservative and stable for dissipative difference schemes. Similarly, Benkenida et al. (2002) proposed a splitting and dividing approach, similar to the work of Lerat & Wu (1996), to maintain conservation at the block interfaces. The main issue in patched-grid methods is achieving conservation and overall stability of the schemes. It will not be an issue in the case of dissipative difference schemes such as that of Lerat & Wu (1996). But achieving stability for high-order accurate, non-dissipative, centered schemes (i.e. compact schemes) can be impossible by employing simple interpolation at the boundary.

1.3 Aims and Objectives

The main aims of the research work in this thesis are to develop a computational research programme capable of resolving cavity flowfields accurately, and investigate and describe the cavity flowfields for a range of truly three-dimensional (3D) cavity geometries which fall into the open flow category. Upon establishing the flow behaviour within the empty cavity geometries, the presence of generic missile bodies in the cavity will be investigated in order to quantify and describe their effects on the time-averaged and unsteady flowfields. The final aim of this project is to assess numerically the suitability and effectiveness of passive flow control devices for the suppression of cavity tones. The objectives of the research work are set out as follows:

- A high-order accurate CFD solver based on a fourth-order optimized compact scheme will be developed for the purpose of capturing acoustic sources. The high-order solver will be validated and then used for the computation of various aerodynamic noise problems.
- Computational simulations will be performed on various empty cavity and cavity-with-missile geometries to quantify and describe the mean and unsteady flow behaviour in the cavity.
- The presence of a missile inside the cavity means that the unsteady flow in the cavity interacts with the missile. This may, therefore, modify the flow structure which originally existed in a clean cavity. Hence, computations will be performed to study these interaction phenomena and their contributions to noise generation.
- The final stage will be spent assessing a suitable noise reduction treatment for the tone noise from cavities.

1.4 Structure of Thesis

This thesis describes the research work performed to study the unsteady aerodynamics and resulting aeroacoustic effects of unsteady flowfields. The thesis is structured into chapters. Chapter 1 has reviewed the fundamentals of cavity flows, aerodynamic noise generation and computational aeroacoustics; and the existing methods for their suppression. Chapters 2 is concerned with the computational methodologies employed including the development of a higher-order aeroacoustic solver. Chapters 3 and 4 are devoted to the analysis of the computational results obtained. Conclusions and a discussion on the scope of future work are presented in Chapter 5.

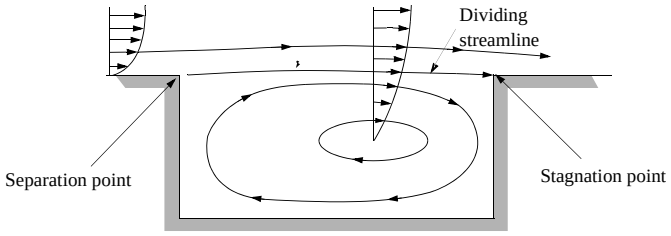

(a) Open cavity flow.

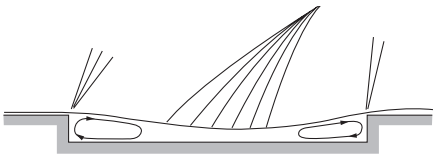

(b) Transitional-open cavity flow.

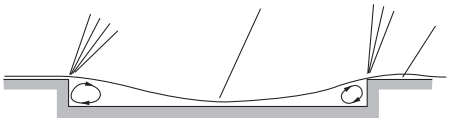

(c) Transitional-closed cavity flow.

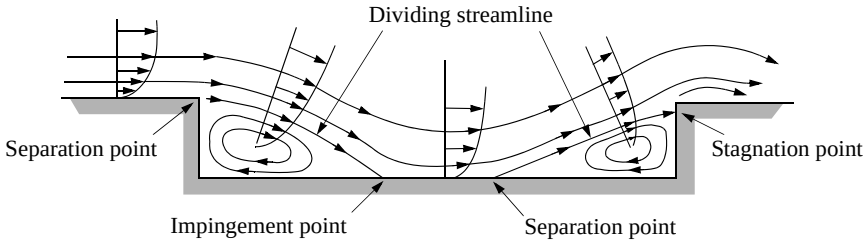

(d) Closed cavity flow.

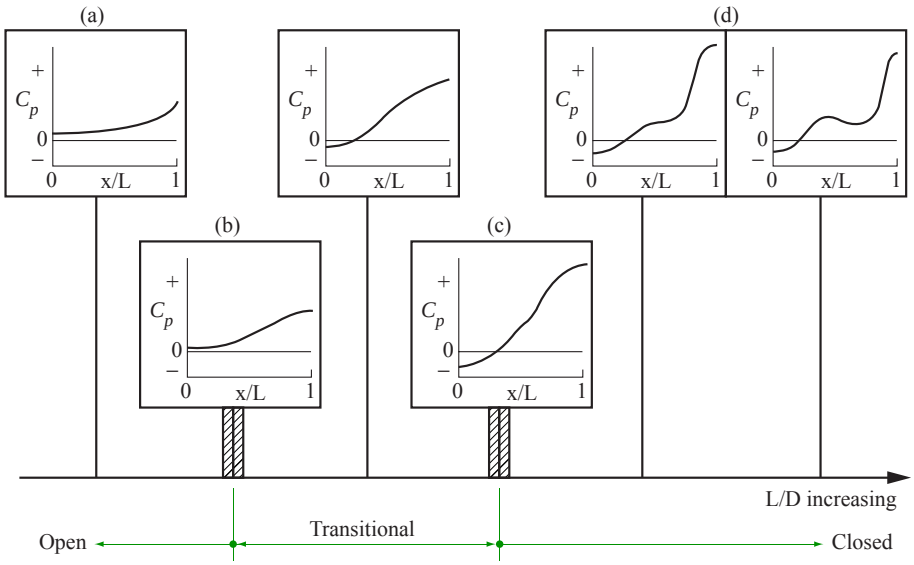

(e) Cavity flow type classification, based on floor pressure distributions.

Figure 1.1: Cavity flow types and corresponding pressure distributions ESDU (2004).

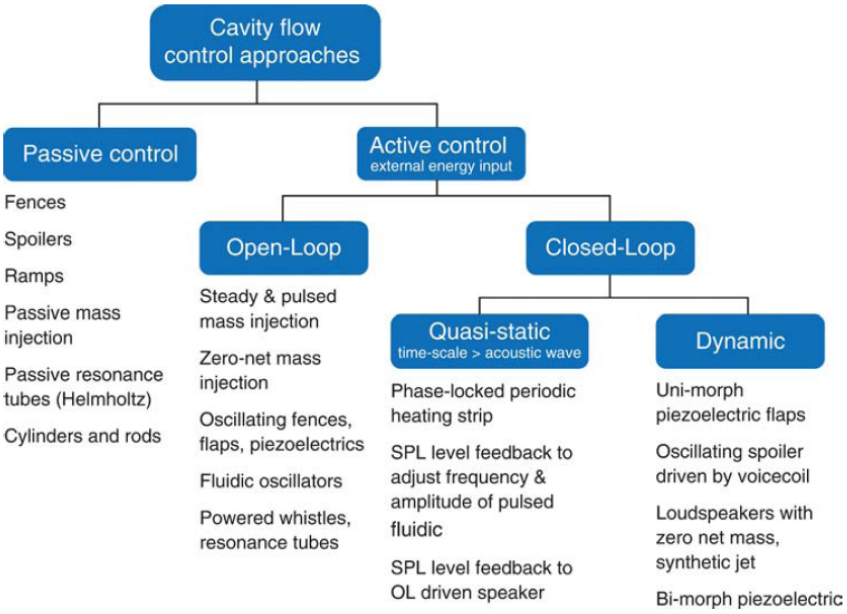

Figure 1.2: Classification of flow control methods, from Cattafesta et al. (2003).

Chapter 2

Computational Methodologies

The computational methodologies used in this project are outlined in this chapter. The chapter is broken into three main sections. The first provides an account of the high-order CAA solver developed by the author, the second deals with the general purpose low-order CFD solver Fluent and the final section describes the Radiation Solver, based on the integral formulation of Ffowcs-Williams & Hawkings (1969), for farfield noise prediction.

2.1 Introduction

The aim of the research work undertaken in this project is to investigate the acoustic tones produced by transonic cavities with missiles. The review of the literature indicated that a direct numerical simulation of an aeroacoustic problem was still beyond the capabilities of CAA based on currently-available computing power. A hybrid approach based on the use of near-field CFD computations coupled with solutions of the FW-H equation is a more practical alternative. Hence, the computational approach adapted in this research is also a two-step hybrid method. Three main numerical solvers were used for this purpose: a general purpose Reynolds-Averaged Navier-Stokes flow solver, a high-order accuracy Navier-Stokes flow solver and an integral formulation for farfield propagation based on the Ffowcs Williams and Hawkings equation.

Firstly, the Navier-Stokes-based solvers are used to solve the flow around a chosen geometry using a computational grid. This provides the information on the time-dependent flow dynamics in the noise source regions. These flow results can then be used as input to the FW-H solver to yield the acoustic information. This two-step method is illustrated in Figure 2.1. Detailed accounts of the computational solvers used are presented in the following sections.

2.2 High-order CFD Solver

The solver, based on a finite difference scheme, is a high-order computational aeroacoustics code developed by the author which solves the Navier-Stokes equations in conservative form. A high-order, optimized, compact finite difference scheme in space and fourth

order explicit temporal differencing is used to minimise the dissipation and dispersion errors. The time-dependent, three-dimensional Navier-Stokes equations can be expressed, in Cartesian coordinates as:

$$\frac{\partial \mathbf{Q}}{\partial t} + \frac{\partial \mathbf{E}}{\partial x} + \frac{\partial \mathbf{F}}{\partial y} + \frac{\partial \mathbf{G}}{\partial z} = \mathbf{S}_v \tag{2.1}$$

where the conservative variables and the inviscid flux variables are represented as

$$\mathbf{Q} = \begin{bmatrix} \rho \\ \rho u \\ \rho v \\ \rho w \\ \rho e_t \end{bmatrix}, \quad \mathbf{E} = \begin{bmatrix} \rho u \\ \rho u^2 + p \\ \rho uv \\ \rho uw \\ (\rho e_t + p)u \end{bmatrix}, \quad \mathbf{F} = \begin{bmatrix} \rho v \\ \rho uv \\ \rho v^2 + p \\ \rho vw \\ (\rho e_t + p)v \end{bmatrix}, \quad \mathbf{G} = \begin{bmatrix} \rho w \\ \rho uw \\ \rho vw \\ \rho w^2 + p \\ (\rho e_t + p)w \end{bmatrix}$$

For air as an ideal gas, the total energy term is given by $\rho e_t = \frac{p}{\gamma - 1} + \frac{1}{2}\rho(u^2 + v^2 + w^2)$. where $\gamma = c_p/c_v$ is the ratio of specific heat coefficients under constant pressure and constant volume.

The right hand term $\mathbf{S}_v$ in Eq. 2.1 is the source term containing the viscous flux derivatives and is represented as:

$$\mathbf{S}_v = \frac{\partial \mathbf{E}_v}{\partial x} + \frac{\partial \mathbf{F}_v}{\partial y} + \frac{\partial \mathbf{G}_v}{\partial z}.$$

$$\text{where } \mathbf{E}_v = \begin{bmatrix} 0 \\ \tau_{xx} \\ \tau_{xy} \\ \tau_{xz} \\ u\tau_{xx} + v\tau_{xy} + w\tau_{xz} + q_x \end{bmatrix}, \quad \mathbf{F}_v = \begin{bmatrix} 0 \\ \tau_{yx} \\ \tau_{yy} \\ \tau_{yz} \\ u\tau_{yx} + v\tau_{yy} + w\tau_{yz} + q_y \end{bmatrix}$$

$$\text{and } \mathbf{G}_v = \begin{bmatrix} 0 \\ \tau_{zx} \\ \tau_{zy} \\ \tau_{zz} \\ u\tau_{zx} + v\tau_{zy} + w\tau_{zz} + q_z \end{bmatrix}$$

The viscous stress tensor components are related to the Cartesian velocity components by the following equations:

$$\tau_{xx} = \frac{1}{\mathrm{Re}_\infty}\left(2\mu\frac{\partial u}{\partial x} + \lambda\nabla.\mathbf{v}\right), \quad \tau_{xy} = \tau_{yx} = \frac{\mu}{\mathrm{Re}_\infty}\left(\frac{\partial u}{\partial y} + \frac{\partial v}{\partial x}\right)$$
$$\tau_{yy} = \frac{1}{\mathrm{Re}_\infty}\left(2\mu\frac{\partial v}{\partial y} + \lambda\nabla.\mathbf{v}\right), \quad \tau_{yz} = \tau_{zy} = \frac{\mu}{\mathrm{Re}_\infty}\left(\frac{\partial v}{\partial z} + \frac{\partial w}{\partial y}\right)$$
$$\tau_{zz} = \frac{1}{\mathrm{Re}_\infty}\left(2\mu\frac{\partial w}{\partial z} + \lambda\nabla.\mathbf{v}\right), \quad \tau_{xz} = \tau_{zx} = \frac{\mu}{\mathrm{Re}_\infty}\left(\frac{\partial w}{\partial x} + \frac{\partial u}{\partial z}\right) \tag{2.2}$$

where μ is molecular viscosity and λ and μ are related by Stokes' hypothesis :$\lambda + 2\mu/3 = 0$.

The heat flux terms are evaluated as:

$$q_x = \frac{\mu}{(\gamma-1)\,\mathrm{Pr}\,\mathrm{Re}_\infty M_\infty^2}\frac{\partial T}{\partial x} \quad , \quad q_y = \frac{\mu}{(\gamma-1)\,\mathrm{Pr}\,\mathrm{Re}_\infty M_\infty^2}\frac{\partial T}{\partial y} \quad ,$$
$$q_z = \frac{\mu}{(\gamma-1)\,\mathrm{Pr}\,\mathrm{Re}_\infty M_\infty^2}\frac{\partial T}{\partial z} \tag{2.3}$$

Eq. 2.1 is expressed in Cartesian coordinates. For the study of flow around complex geometries, the governing equations must be solved in an orthogonal curvilinear coordinate system, also known as a body-fitted coordinate system. This allows the complex geometry problem to be transformed into, and simulated using, a uniform computational domain, which is also easier to handle with finite difference schemes. The equations in the curvilinear system are obtained after a transformation from the physical coordinate system to the computational coordinate system using Eqns. 2.4.

$$\xi = \xi(x, y, z), \qquad \eta = \eta(x, y, z), \qquad \zeta = \zeta(x, y, z). \tag{2.4}$$

The chain rule can be used to evaluate the spatial derivatives of the governing equation and, hence, the transformation metrics, thus

$$\frac{\partial}{\partial x} = \left(\frac{\partial \xi}{\partial x}\frac{\partial}{\partial \xi} + \frac{\partial \eta}{\partial x}\frac{\partial}{\partial \eta} + \frac{\partial \zeta}{\partial x}\frac{\partial}{\partial \zeta}\right), \quad \frac{\partial}{\partial y} = \frac{\partial \xi}{\partial y}\frac{\partial}{\partial \xi} + \frac{\partial \eta}{\partial y}\frac{\partial}{\partial \eta} + \frac{\partial \zeta}{\partial y}\frac{\partial}{\partial \zeta}$$
$$\textit{and} \quad \frac{\partial}{\partial z} = \frac{\partial \xi}{\partial z}\frac{\partial}{\partial \xi} + \frac{\partial \eta}{\partial z}\frac{\partial}{\partial \eta} + \frac{\partial \zeta}{\partial z}\frac{\partial}{\partial \zeta} \tag{2.5}$$

which then gives the transformation metrics as

$$\begin{aligned}
\xi_x &= \frac{\partial \xi}{\partial x} = J\left(\frac{\partial y}{\partial \eta}\frac{\partial z}{\partial \zeta} - \frac{\partial y}{\partial \zeta}\frac{\partial z}{\partial \eta}\right), \quad \xi_y = \frac{\partial \xi}{\partial y} = J\left(\frac{\partial x}{\partial \zeta}\frac{\partial z}{\partial \eta} - \frac{\partial x}{\partial \eta}\frac{\partial z}{\partial \zeta}\right), \quad \xi_z = \frac{\partial \xi}{\partial z} = J\left(\frac{\partial x}{\partial \eta}\frac{\partial y}{\partial \zeta} - \frac{\partial x}{\partial \zeta}\frac{\partial y}{\partial \eta}\right) \\
\eta_x &= \frac{\partial \eta}{\partial x} = J\left(\frac{\partial y}{\partial \zeta}\frac{\partial z}{\partial \xi} - \frac{\partial y}{\partial \xi}\frac{\partial z}{\partial \zeta}\right), \quad \eta_y = \frac{\partial \eta}{\partial y} = J\left(\frac{\partial x}{\partial \xi}\frac{\partial z}{\partial \zeta} - \frac{\partial x}{\partial \zeta}\frac{\partial z}{\partial \xi}\right), \quad \eta_z = \frac{\partial \eta}{\partial z} = J\left(\frac{\partial x}{\partial \zeta}\frac{\partial y}{\partial \xi} - \frac{\partial x}{\partial \xi}\frac{\partial y}{\partial \zeta}\right) \\
\zeta_x &= \frac{\partial \zeta}{\partial x} = J\left(\frac{\partial y}{\partial \xi}\frac{\partial z}{\partial \eta} - \frac{\partial y}{\partial \eta}\frac{\partial z}{\partial \xi}\right), \quad \zeta_y = \frac{\partial \zeta}{\partial y} = J\left(\frac{\partial x}{\partial \eta}\frac{\partial z}{\partial \xi} - \frac{\partial x}{\partial \xi}\frac{\partial z}{\partial \eta}\right), \quad \zeta_z = \frac{\partial \zeta}{\partial z} = J\left(\frac{\partial x}{\partial \xi}\frac{\partial y}{\partial \eta} - \frac{\partial x}{\partial \eta}\frac{\partial y}{\partial \xi}\right)
\end{aligned} \tag{2.6}$$

where J is the transformation Jacobian relating the geometrical properties of the physical domain to the uniform computational domain, and is expressed as

$$J = \left[\frac{\partial x}{\partial \xi}\left(\frac{\partial y}{\partial \eta}\frac{\partial z}{\partial \zeta} - \frac{\partial y}{\partial \zeta}\frac{\partial z}{\partial \eta}\right) - \frac{\partial x}{\partial \eta}\left(\frac{\partial y}{\partial \xi}\frac{\partial z}{\partial \zeta} - \frac{\partial y}{\partial \zeta}\frac{\partial z}{\partial \xi}\right) + \frac{\partial x}{\partial \zeta}\left(\frac{\partial y}{\partial \xi}\frac{\partial z}{\partial \eta} - \frac{\partial y}{\partial \xi}\frac{\partial z}{\partial \eta}\right)\right]^{-1}. \tag{2.7}$$

The equations above are non-dimensionalised using the following reference values and solved in non-dimensionalised form.

$$\rho^* = \frac{\rho}{\rho_\infty}, \quad \mathbf{v}^* = \frac{\mathbf{v}}{c_\infty}, \quad p^* = \frac{p}{\rho_\infty c_\infty^2}, \quad c^* = \frac{c}{c_\infty}, \quad \mathbf{x}^* = \frac{\mathbf{x}}{L}, \quad t^* = t/(L/c_\infty). \tag{2.8}$$

2.2.1 Turbulence Modelling

Turbulence is a state of fluid motion characterized by random and chaotic three-dimensional vorticity. Turbulence results in increased energy dissipation, mixing, and heat transfer in the flow. Turbulence is of great technological importance because of the large effects it has on the flows in which it occurs. The prediction of these effects in a flow of interest is one of the primary concerns of applied fluid dynamicists, and it is often the case that the uncertainties in a fluid dynamic calculation are dominated by uncertainties in the turbulence models. Therefore, one can argue that for researchers of fluid dynamics, turbulence models, their approximations and limitations are of most relevance in the study of turbulence. Turbulence research is continuously evolving and several turbulence modelling strategies are available today. It is, however, an unfortunate fact that no single turbulence model is universally accepted as being superior for all classes of fluid dynamic problems. The choice of turbulence model depends on several factors such as the physics encompassed in the flow, the established practice for a specific class of problem, the level of accuracy required, the available computational resources, and the amount of

time available for the simulation. To make the most appropriate choice of the model, it is necessary to understand the capabilities and limitations of the various options. In the present study, the one-equation model of Spalart & Allmaras (1992) for 2D simulations and an extension of the same model, Detached-Eddy Simulation (DES) for 3D simulation is used. DES is a hybrid model which behaves as a standard SA RANS model within the attached boundary layer and as a Large-Eddy Simulation (LES) Sub-Grid Scale (SGS) model in the rest of the flow. The one-equation SA model requires the least computational resources and is found to be reliable for aerospace applications. The turbulent transport equation solved in this case is given by,

$$\frac{\partial}{\partial t}\left(\rho\tilde{\nu}\right) + \frac{\partial}{\partial x_i}\left(\rho\tilde{\nu}u_i\right) = G_\nu + \frac{1}{\sigma_\nu}\left[\frac{\partial}{\partial x_j}\left\{\left(\mu + \rho\tilde{\nu}\right)\frac{\partial\tilde{\nu}}{\partial x_j}\right\} + C_{b2}\rho\left(\frac{\partial\tilde{\nu}}{\partial x_j}\right)^2\right] - Y_v \tag{2.9}$$

where G_ν is the production term of turbulent viscosity and Y_ν is the turbulent viscosity destruction term. σ_ν and C_{b2} are constant. Additional details of the turbulence model can be found in Spalart & Allmaras (1992); Krist et al. (1998) and Fluent (2005). The system of partial differential equations in Eq. 2.9 is solved for the transport variable $\tilde{\nu}$ to calculate μ_t using the relation, $\mu_t = \rho\tilde{\nu}f_{\nu 1}$. The turbulent viscosity term (μ_t) is required to close the system of equations in Eq. 2.1. $f_{\nu 1}$ is the viscous damping function. The standard RANS SA turbulence model uses the distance to the nearest wall to define a length scale d that is used to calculate the production and the dissipation terms of turbulent viscosity. In the DES formulation of Spalart & Allmaras (1997), the length scale d is replaced with a DES length scale d_{DES} defined as:

$$d_{DES} = \min(d, C_{DES}\Delta) \tag{2.10}$$

$$\Delta = \max(\delta x, \delta y, \delta z) \tag{2.11}$$

where C_{DES} is a constant for the DES model and Δ is the largest cell dimension in the computational grid. The modified length scale calculated using the relations in Eq. 2.10 ensures a length scale that is the same as the standard SA RANS length scale near the walls where $d << \Delta$ and reduces to the local grid spacing away from the walls where $d >> \Delta$. The effect of this is to activate a hybrid SA turbulence model that behaves as a standard SA RANS model within the attached boundary layers and as a LES Sub-Grid Scale model in the rest of the flow including the separated regions. From Eq. 2.10 it can clearly be said that this model is grid-dependant and, hence, any solution using this model also relies on the grid design i.e. depending on whether the cells in the

attached boundary layer are carefully designed, a local grid spacing will be used as the length scale rather than the standard SA RANS length scale required in the boundary layer. This version of DES is found to work well in thin boundary layers with flattened grid cells where the turbulence model switches to its RANS mode, and in the regions of massive separation where the turbulence model behaviour changes to LES mode with grid cells close to isotropic. However this model can exhibit an incorrect behaviour in thick boundary layers and shallow separation regions. This behaviour begins when the grid spacing parallel to the wall becomes less than the boundary layer thickness (This situation can arise either due to grid refinement or due to the boundary layer thickening). In these situations, the grid spacing is then fine enough in the boundary layer for the DES length scale to switch the turbulence model to the LES mode (but the grid is not sufficiently fine to support resolved velocity fluctuations internal to the boundary layer i.e. LES content) which in turn causes the eddy viscosity to drop below the RANS level. This reduces the modelled Reynolds stresses and the lack of fully resolved LES content mean the resolved stresses cannot restore the balance from the depleted value of the eddy viscosity. This deficiency in modelled stresses results in reduced skin friction leading to a possible premature separation of the boundary layer, which is not a physical behaviour. Spalart et al. (2006) proposed a way of identifying the boundary layer so that switching of the turbulence model to LES mode can be prevented. In the modified form of DES (also known as Delayed DES), the length scale d_{DES} is redefined as:

$$d_{DES} = d - f_d \max(0, d - C_{DES}\Delta) \tag{2.12}$$

where

$$f_d = 1 - \tanh\left\{(8r_d)^3\right\}$$

and

$$r_d = \frac{\nu_t + \nu}{\sqrt{U_{i,j}U_{i,j}}\kappa^2 d^2}$$

where ν is the molecular viscosity, $(U_{i,j})$ the velocity gradients (with usual tensorial convention), κ the Kármán constant. Similar to r (which is the square of the ratio of a model length scale to the wall distance) in the SA model, r_d equals 1 in the log layer, and falls to 0 gradually towards the edge of the boundary layer. The addition of ν in the numerator is to ensure that r_d remains away from 0 very near to the wall. In the SA model, $\tilde{\nu}$ is used instead of $(\nu_t + \nu)$. The parameter f_d is designed to be 1 in the LES region where $r_d \ll 1$, and 0 elsewhere. This model, thus, ensures that the LES mode is prevented

in boundary layers. This version of DES [also known as Delayed DES or DDES] has been incorporated in the high-order solver developed in this thesis to ensure that the DES model is resistant to the ambiguities due to grids and boundary layers.

2.2.2 Numerical Schemes

Conventional low-order CFD schemes used for aerodynamic computations cannot predict acoustic waves propagation accurately. Excessively fine grid systems are required for an acoustic propagation problem over a long distance. Even if the discretization scheme used is high-order, accurate prediction of acoustic waves is dependent on the dispersion and dissipation characteristics of the scheme. Hence, a high-order discretization scheme with low dispersion and dissipation errors is desirable for an acoustic computation.

Spatial discretization

A compact finite differencing approach is used in this work to evaluate the first order spatial derivatives of the governing equations, Eq. 2.1. This approach allows formulation of accurate high-order schemes relatively easily and the high-order accuracy can be maintained for complex geometries through the use of a curvilinear coordinate system. Specifically, a fourth-order pentadiagonal type of central compact finite difference scheme due to Kim (2007) has been used for the spatial discretization in the solver developed in this work. A pentadiagonal system of central finite difference scheme for evaluating the first-order spatial derivative, D, of a scalar function f, at point i can be expressed as:

$$\beta D_{i-2} + \alpha D_{i-1} + D_i + \alpha D_{i+1} + \beta D_{i+2} = \frac{1}{\Delta x} \sum_{m=1}^{3} a_m \left(f_{i+m} - f_{i-m} \right) \tag{2.13}$$

This is a generalization of the seven-point Padé scheme [Lele (1992)] used on the interior nodes and can be solved by inverting a pentadiagonal matrix. The grid spacing Δx is a constant independent of the index i in the computational domain where all the grid points are equally spaced. If α and β equal to zero, an explicit formulation is achieved where the derivative depends only on the values of the function at neighbouring grid points. If either α or β are non-zero, the derivative also depends upon the function's derivative values at neighbouring grid points and is termed an implicit or compact scheme. The resolution characteristics of Eq. 2.13 can be analysed in the spectral domain using a Fourier transform. Taking the Fourier transform of Eq. 2.13 and using Euler's formula, the equation in the spectral domain can be written as:

$$jk^*\Delta x\tilde{f}(k)\left[1+2\alpha\cos\left(k\Delta x\right)+2\beta\cos\left(2k\Delta x\right)\right]=2j\tilde{f}(k)\sum_{m=1}^{3}a_m\sin\left(mk\Delta x\right) \tag{2.14}$$

where

$$\tilde{f}(k)=\int_{-\infty}^{\infty}f\left(x\right)e^{-jkx}dx$$

In Eq. 2.14, k is the true wave number of the partial derivatives and k^* is the numerical wave number which has a certain deviation from the true wave number due to the numerical approximation. Ideally k^* should coincide with k up to as high a value as possible in order to achieve high resolution characteristics. It is impossible to achieve a perfect match between k^* and k over the entire range due to the limitations of numerical schemes. The discrepancy between k^* and k is also referred to as the dispersion error of the scheme. The resolution characteristics of the scheme can be improved by minimising the error over a desired wave number range. Following Kim (2007) (see also the work of Kim & Lee (1996)), the total integrated error function due to the discretization scheme over $0\leq\kappa\leq r\pi$ (where $\kappa=k\Delta x$) can be written as:

$$E=\int_{0}^{r\pi}\left[\left(1+\delta\right)\kappa\left\{1+2\alpha\cos\kappa+2\beta\cos2\kappa\right\}-2\sum_{m=1}^{3}a_m\sin m\kappa\right]^2\left(\frac{\kappa}{r\pi}\right)^{10}d\kappa \tag{2.15}$$

where $r<1$ is a factor to determine the integration range and $(\frac{\kappa}{r\pi})^{10}$ is a weighting function to concentrate the optimization on the high wave number band. The conditions for the integrated error in Eq. 2.15 to be a minimum can be written as:

$$\frac{\partial E}{\partial\alpha}=0,\ \frac{\partial E}{\partial\beta}=0,\ \frac{\partial E}{\partial a_m}=0\ \ (m=1,\ 2,\ 3) \tag{2.16}$$

Solving Eqns 2.16 along with the equation resulting from the matching of the same terms in the Taylor series expansion of Eq. 2.13, optimized values of α, β and $a_m(m=1,\ 2,\ 3)$ can be found. In addition, an optimization strategy based on polynomial-trigonometric blended extrapolation functions has been used by Kim (2007) to maintain the high resolution characteristic at or near the grid boundaries. Details are available in Kim (2007). This optimized compact differencing which maintains fourth-order accuracy throughout the grid block (even at the boundary) is used in this research project for the calculation

of spatial derivatives. The derivatives of the inviscid fluxes are obtained by first forming the fluxes at the grid nodes and subsequently differentiating each component using the above formulae. For the computation of the viscous terms, the primitive variables, u, v, w and T are first differentiated to form the components of the stress tensor and the heat flux vector at each node. The viscous flux derivatives are then computed by a second application of the same scheme. A similar optimization strategy has been applied by the author for the derivation of optimized interpolation schemes with potential application in overset grid methods. The detailed process is presented in Appendix C.

Temporal discretization

In most CFD solvers, multistage Runge-Kutta (R-K) schemes have often been favoured for their low storage requirements and good overall stability response. For CAA solvers, however, the stability consideration alone is not sufficient, since R-K schemes also add both dissipation and dispersion errors to the computation. CAA schemes have to be time-accurate as well as spatially accurate in order to predict wave propagation correctly. To predict the acoustic propagation problems accurately both the temporal as well as spatial discretization schemes must have low dissipation and dispersion characteristics. The fourth-order explicit, low-storage R-K scheme of Hu et al. (1996) is used in the present high-order solver to advance the solution in time. This is a two-step alternating scheme optimized for low dissipation and dispersion errors. The scheme uses four stages in the odd time steps and six stages in the even steps. If the governing equations are written as

$$\frac{\partial \hat{\mathbf{Q}}}{\partial t} = \mathbf{R}(\hat{\mathbf{Q}}) \tag{2.17}$$

where

$$\mathbf{R}(\hat{\mathbf{Q}}) = \hat{\mathbf{S}}_v - \frac{\partial \hat{\mathbf{E}}}{\partial \xi} - \frac{\partial \hat{\mathbf{F}}}{\partial \eta} - \frac{\partial \hat{\mathbf{G}}}{\partial \zeta},$$

then a low storage representation of an explicit p-stage R-K scheme can be represented as:

$$\hat{\mathbf{Q}}^{n+1} = \hat{\mathbf{Q}}^n + \mathbf{K}_p \tag{2.18}$$

with

$$\mathbf{K}_i = \Delta t \mathbf{R}\left(\hat{\mathbf{Q}}^n + g_i \mathbf{K}_{i-1}\right) \quad i = 1,\ 2, ..., p \tag{2.19}$$

In Eqns. 2.18 and 2.19, p denotes the number of R-K stages in each step, and g_i are the coefficients of the particular step. The superscript n indicates the time level. Integration from time step n to time step $n + 2$, is accomplished alternatively by first employing the four-stage scheme to integrate from time level n to time level $n + 1$, and then the six-stage scheme to integrate from time level $n + 1$ to time level $n + 2$. Two stage schemes are favoured over single step schemes as they permit a greater degree of optimization for wave propagation. In this way the dissipation and dispersion errors of the alternating two-step schemes are reduced below those attainable through optimization of either of the individual single steps.

Filtering Scheme

Although high-order schemes are capable of resolving a wider range of wave numbers or frequencies than conventional low-order schemes, these schemes cannot resolve all the wave number or frequency range (especially in the high wave number band). Also, the compact finite differencing used in the high-order solvers are centered schemes, and like any other centered difference schemes contain no inherent dissipation. Whilst this is desirable for acoustic wave propagation problems it does leave such schemes susceptible to numerical instabilities due to the growth of high-frequency modes. These difficulties originate mainly from grid non-uniformity, boundary conditions, poorly specified initial conditions and the non-linearity in the flowfields. Hence, in order for a high-order solver to be robust and accurate in solving complex flowfields with non-uniform grids, a suitable filtering technique is essential to remove the unwanted numerical oscillations that may develop from the unresolved high wave number or frequency range. In the CAA solver developed in this research project, the removal of these very high frequency non-physical waves is achieved by using the low pass eighth-order implicit filtering formula due to Visbal & Gaitonde (2002).

If the solution vector to be filtered is denoted by φ, the filtered values $\hat{\varphi}$ are obtained by solving the tridiagonal system given below:

$$\alpha_f \hat{\varphi}_{i-1} + \hat{\varphi}_i + \alpha_f \hat{\varphi}_{i+1} = \sum_{n=0}^{N} \frac{a_n}{2} \left(\varphi_{i+n} + \varphi_{i-n}\right) \tag{2.20}$$

where the coefficients α_f, a_0, a_1, ...a_n determine the order and spectral response of the filtering scheme. In Eq. 2.20, the filtered variable $\hat{\varphi}$ is an implicit function of the solution variable to be filtered, φ. The spectral function (SF), defined as the ratio of the filtered

and unfiltered fourier coefficients, indicates on which wavelengths the filter acts and is given by:

$$SF(k\Delta x) = \frac{\sum_{n=0}^{N} a_n \cos(nk\Delta x)}{1 + 2\alpha_f \cos(nk\Delta x)} \tag{2.21}$$

where k is the numerical wave number of the spatial discretization. The coefficients a_n are determined by solving the equation $SF(\pi) = 0$ along with matching the Taylor series coefficients of Eq. 2.20 to the desired order. With a proper choice of these coefficients, Eq. 2.20 provides a $2N^{th}$ order formula on a $2N + 1$ point stencil. α_f is a tuning parameter for the wave length characteristics of the filter which satisfies the inequality $-0.5 \leq \alpha_f \leq 0.5$, with higher values of α_f corresponding to a less dissipative filter. Visbal & Gaitonde (2002, 2000) showed that the N + 1 coefficients $a_0, a_1, ...a_n$ can be expressed solely in terms of α_f. For the work presented in this thesis the eighth-order filter with $\alpha_f = 0.495$ has been used. This choice ensures the spectral characteristics of the filter closely match those of the spatial compact discretization, preserving the accuracy.

The eighth-order formula requires a nine point stencil, it is therefore not suitable for use at and near boundary points. In these regions, the order of accuracy of the filter is reduced, as the boundary is approached, to the level for which a centred scheme is available. Values along the boundary points are left unfiltered. The filter is applied sequentially in each coordinate direction to the conserved variables once after the final stage of the explicit R-K time stepping.

Characteristic Boundary Conditions

One major issue with any high-order solver is the sensitivity of the solution to the grid skewness and the boundary conditions used. It is, therefore, desirable to have a boundary formulation which avoids any kind of extrapolation or simplification while solving the governing equations at the boundary. Boundary conditions based on the method of characteristics have been developed to meet these high accuracy requirements and have been continuously evolving for many years [Thompson (1987, 1990); Poinsot & Lele (1992); Kim & Lee (2000b, 2004)]. Characteristic boundary conditions for Navier-Stokes equations (also known as NSCBC) are widely used in reacting flow, high temperature mixtures etc [Sunderland & Kennedy (2003); Yoo et al. (2005); Yoo & Im (2007)]. Another advantage of this method is that it avoids the excessive communication at multi-block interfaces required by other interblock treatments e.g. overlapping grids. Hence this

method has been widely used to treat the block interfaces in multi-block grid domains for efficient parallel computations [Sumi & Kurotaki (2006); Kim & Lee (2003)].

Characteristic interface boundary treatments have been well documented [e.g. Kim & Lee (2003); Sumi & Kurotaki (2006); Sumi et al. (2007)] although these methods are only valid for inviscid and laminar flows. There is also a mathematical consistency issue which exists for multi-dimensional Navier-Stokes equations, when characteristic equations are expressed in the form given in the literature [Kim & Lee (2003); Sumi & Kurotaki (2006); Sumi et al. (2007)]. The characteristic equations in this form do not satisfy Pfaff's condition [Thompson (1987); Whitham (1974); Chen & Zha (2006)]. In addition, all the existing interface treatments based on the method of characteristics lack a satisfactory interface matching of turbulence quantities. To address these issues, the mathematically consistent form of the characteristic equations relevant to interface boundary treatment are derived and a simple and robust technique is proposed to match turbulence quantities at multi-block interfaces for turbulent flow problems. The detailed derivation of the characteristic equations, the interface matching techniques along with the characteristic transformation matrices are given in Appendix A. In the context of the high-order CAA solver, the characteristic boundary treatment involves three steps. In the first step, the spatial derivative is calculated using the fourth-order accurate scheme throughout the grid block including boundaries (as stated in the last paragraph on page 38 and the first paragraph on page 39). In the second step of the characteristic boundary treatment (including interface condition),it involves calculating the characteristic wave amplitudes at the boundaries using the spatial derivatives (which are fourth-order accurate). In the final stage, the characteristics waves calculated in second step are corrected depending on the signs of wave convection speeds (Also see Appendix A). The high-order accuracy, therefore, is maintained because it does not involve any low-order approximation while calculating the wave amplitudes.

Metric Cancellation Errors

The high-order solver developed in this research work solves the strong-conservation form of the Navier-Stokes equations (see Appendix A Eq. A.30) which implies that the metric identities in Eqns. 2.22 to 2.24 have been implicitly invoked. Eq. 2.25, which is only applicable to time-variant coordinate systems (i.e. moving meshes), is derived from the grid volume conservation[1], also widely referred to as the geometric conservation law

[1]Actually Eq. 2.25 can be derived easily by setting $\rho = 1$ and the velocities u, v, w to zero in the first equation of the time-variant form of the Navier-Stokes equations in Appendix A [Eq. A.30].

(GCL) in the literature [Pulliam & Steger (1980); Thomas & Lombard (1979); Chung & Tucker (2003); Visbal & Gaitonde (2001)]. In any finite-difference discretization scheme these identities must be satisfied numerically (Eq. 2.22 to 2.24 for non-moving meshes) in order to ensure freestream preservation.

$$\left(\frac{\xi_x}{J}\right)_\xi + \left(\frac{\eta_x}{J}\right)_\eta + \left(\frac{\zeta_x}{J}\right)_\zeta = 0 \tag{2.22}$$

$$\left(\frac{\xi_y}{J}\right)_\xi + \left(\frac{\eta_y}{J}\right)_\eta + \left(\frac{\zeta_y}{J}\right)_\zeta = 0 \tag{2.23}$$

$$\left(\frac{\xi_z}{J}\right)_\xi + \left(\frac{\eta_z}{J}\right)_\eta + \left(\frac{\zeta_z}{J}\right)_\zeta = 0 \tag{2.24}$$

$$\left(\frac{1}{J}\right)_\tau + \left(\frac{\xi_t}{J}\right)_\xi + \left(\frac{\eta_t}{J}\right)_\eta + \left(\frac{\zeta_t}{J}\right)_\zeta = 0 \tag{2.25}$$

The issues of the freestream preservation and metric cancellation errors, hence, is important and have to be ensured in order to extend high-order schemes to non-trivial 3D generalized curvilinear coordinates. These errors arise in finite difference discretizations of governing equations written in strong conservation form and could easily degrade the accuracy of the high-order calculations. Grid-induced errors may appear, for instance, in regions of large grid variations or near singularities. The straight forward approach of calculating the metrics given in Eq. 2.6 fails to provide metric cancellation for general 3D curvilinear meshes. Evaluation of the y and z derivatives (which are required to calculate ξ_x, η_x and ζ_x) using compact centred schemes in Eq. 2.6 does not satisfy the metric identity in Eq. 2.22 and therefore grid-induced errors appear in regions of large grid variation or near singularities. For curvilinear 2D meshes, Pulliam & Steger (1980) demonstrated that the compact scheme provided metric cancellation when the metrics were evaluated with the same finite difference scheme as those employed for the computation of fluxes. Pulliam & Steger (1980) introduced a simple averaging procedure to guarantee the freestream preservation on 3D curvilinear grids. Although this procedure worked well for a low-order (second-order) scheme, it is not suitable for high-order solvers. An alternative method to enforce the metric identities can be achieved by using the method of Thomas & Lombard (1979) which consists of writing the metric relations in conservative form as follows:

$$\begin{aligned}
\xi_x &= J\left\{\frac{\partial}{\partial\zeta}\left(z\frac{\partial y}{\partial\eta}\right)-\frac{\partial}{\partial\eta}\left(z\frac{\partial y}{\partial\zeta}\right)\right\}, & \xi_y &= J\left\{\frac{\partial}{\partial\zeta}\left(x\frac{\partial z}{\partial\eta}\right)-\frac{\partial}{\partial\eta}\left(x\frac{\partial z}{\partial\zeta}\right)\right\}\\
\xi_z &= J\left\{\frac{\partial}{\partial\zeta}\left(y\frac{\partial x}{\partial\eta}\right)-\frac{\partial}{\partial\eta}\left(y\frac{\partial x}{\partial\zeta}\right)\right\}, & \eta_x &= J\left\{\frac{\partial}{\partial\xi}\left(z\frac{\partial y}{\partial\zeta}\right)-\frac{\partial}{\partial\zeta}\left(z\frac{\partial y}{\partial\xi}\right)\right\}\\
\eta_y &= J\left\{\frac{\partial}{\partial\xi}\left(x\frac{\partial z}{\partial\zeta}\right)-\frac{\partial}{\partial\zeta}\left(x\frac{\partial z}{\partial\xi}\right)\right\}, & \eta_z &= J\left\{\frac{\partial}{\partial\xi}\left(y\frac{\partial x}{\partial\zeta}\right)-\frac{\partial}{\partial\xi}\left(y\frac{\partial x}{\partial\zeta}\right)\right\}\\
\zeta_x &= J\left\{\frac{\partial}{\partial\xi}\left(z\frac{\partial y}{\partial\eta}\right)-\frac{\partial}{\partial\xi}\left(z\frac{\partial y}{\partial\eta}\right)\right\}, & \zeta_y &= J\left\{\frac{\partial}{\partial\eta}\left(x\frac{\partial z}{\partial\xi}\right)-\frac{\partial}{\partial\xi}\left(x\frac{\partial z}{\partial\eta}\right)\right\}\\
& & \zeta_z &= J\left\{\frac{\partial}{\partial\eta}\left(y\frac{\partial x}{\partial\xi}\right)-\frac{\partial}{\partial\xi}\left(y\frac{\partial x}{\partial\eta}\right)\right\}
\end{aligned} \tag{2.26}$$

The conservative differential form of Eq. 2.26 is ideally suited to the strong-conservation form of the flow equations solved in the CAA solver developed in this work and is therefore selected for 3D complex geometry simulations.

2.3 Low-order CFD Solver

In the second part of this research, the CFD solver FLUENT was used to simulate the complex geometry cases which involved 3D cavity geometry with stores and spoilers. FLUENT is a finite-volume solver and the temporal and spatial discretization schemes available in FLUENT provide at most second-order accuracy in space and time. It is, therefore, not ideal for aeroacoustic applications. Nevertheless, many studies e.g. Kim et al. (2003); Mathey et al. (2006) have shown FLUENT to be capable of simulating aeroacoustic problems, and of resolving the flow structures responsible for noise generation when suitably designed computational mesh and time-step sizes are used. Options for both explicit as well as implicit time-stepping are available with the solver. The governing equations are integrated over small finite volumes to yield the equations that conserve the primary variables in each control volume. In Fluent, the governing Navier-Stokes equations [Eq. 2.1] are solved in integral form. The integral form of Eq. 2.1 for a control volume V with a differential surface area S can be expressed as follows:

$$\frac{\partial}{\partial t}\int_V \mathbf{Q}dV + \int_S [\mathbf{E}+\mathbf{F}+\mathbf{G}-\mathbf{S}_v].dS = \int_V \mathbf{H}dV. \tag{2.27}$$

where the vector **H** represents all the source terms such as body forces and energy sources. The vector **H** is zero in absence of external forcing and heat sources. For full details, see Fluent (2005).

2.4 Radiation Solver

In airframe noise, one is often interested in the farfield characteristics of a given sound field. Hence, the computed sound fields need to be propagated over large distances comprising many wavelengths. An acoustic radiation solver based on the integral formulation of Ffowcs-Williams and Hawkings (the FW-H solver is based on a retarded-time formulation) has also been developed to compute noise distribution in the farfield. This formulation embodies the most general form of the acoustic analogy. It permits the use of both impenetrable walls as well as permeable interior surfaces off the wall as integration surfaces. The FW-H equation is an exact rearrangement of the Navier-Stokes equations and is found to be appropriate for computation of the noise field when solid boundaries play a direct role in the generation of sound. The solution of the FW-H equation is obtained in terms of volume and surface integrals and may be used to predict the farfield acoustic signal based solely on nearfield data. The FW-H method has typically been applied by having the integration surface coincide with solid boundaries, but the method is still applicable when the surface is off the body and permeable. A detailed derivation of the FW-H equation, as employed in the radiation solver is given in Appendix B.

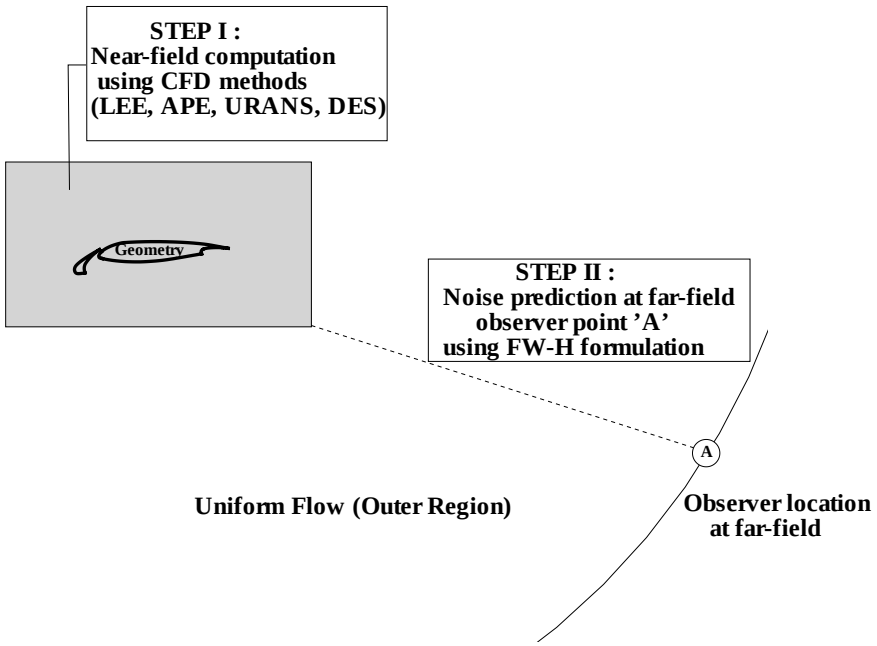

Figure 2.1: Schematic of the two-step computational procedure.

Chapter 3

High-order Solver Simulations

In this chapter, computed results on the source of noise using the high-order CAA solver developed by the author and its validation with available analytical and experimental data is presented. Both 2D and 3D geometries are considered.

3.1 Introduction

In Chapter 1, it was highlighted that the conventional low-order CFD schemes used for aerodynamic computations cannot predict acoustic wave propagation accurately. Excessively fine grid systems are required for an acoustic propagation problem over a long distance. Even if the discretization scheme used is high-order, accurate prediction of acoustic waves is dependent on the dispersion and dissipation characteristics of the scheme. A high-order discretization scheme with low dispersion and dissipation errors is, therefore, essential for accurate computation of aerodynamic noise.

A fourth-order accurate CAA solver based on optimized compact finite differencing was developed by the author to resolve the flow features responsible for aerodynamic noise generation. The purpose of this chapter therefore is to validate the solver and examine its capabilities to resolve the acoustic waves without dispersion and dissipation errors. In addition, its robustness to complex geometries with multi-block curvilinear grids is demonstrated by computing the unsteady flow around a generic landing gear wheel. Finally, the solver was tested for its capability to resolve the flow inside a truly three-dimensional cavity geometry and analyze the influence of the three-dimensional flow features on the oscillation process. All simulations using the CAA solver were run as unsteady flows and the turbulence in the flow was modelled using one-equation model of Spalart & Allmaras (1992) for 2D [URANS simulation] and the DES formulation of Spalart et al. (2006) for the 3D geometries.

3.2 Validation Work

In this section, results from various simulation cases to validate the CAA solver are presented. Several test cases including both inviscid and viscous simulations were performed to validate the CAA solver. One of the test cases was from the typical CAA benchmark problems [Tam et al. (1997)] used in the validation of CAA codes.

3.2.1 Two-Dimensional Acoustic Scattering

To demonstrate the accuracy of the CAA solver in multi-dimensions and illustrate the stability and low dispersive behaviour of the solver, a two-dimensional acoustic scattering problem from the Second CAA workshop [Tam et al. (1997)] is considered. The physical problem is to study the scattering of the sound source (generated by a propeller) from the fuselage of an aircraft. The fuselage is idealized as a circular cylinder and the noise source (propeller) as a line source so that the computational domain is 2D. The geometry therefore is a 2D cylinder of non-dimensional radius $R = 0.5$ placed at the origin of a cylindrical coordinate system. An acoustic pulse with initial conditions is scattered by the cylinder. The initial conditions for this sound scattering problem are given by:

$$p(x, y, 0) = \exp\left[-\ln 2\left(\frac{(x-4)^2 + y^2}{0.04}\right)\right] \tag{3.1}$$
$$u(x, y, 0) = 0$$
$$v(x, y, 0) = 0$$

This benchmark problem has been solved in previous work of Kim & Lee (2000b) on an orthogonal grid generated with an O-topology. In the present work, this case is solved on a non-orthogonal grid domain generated using H-topology to challenge the stability of the solver. The computational domain consists of a square box of $30d$ edge dimension with the cylinder at its centre. The grid domain based on H-topology and the cell distributions near the cylinder surface is shown in Figure 3.1. The number of grid points is 355×220. A snapshot of the computed pressure field at non-dimensional time $t = 5$ is shown in Figure 3.2. From the figure, it can be seen that the acoustic pulse has just reflected off the cylinder at this time. The unsteady pressure history is recorded at three points: A($r = 5; \theta = 90°$), B($r = 5; \theta = 135°$) and C($r = 5; \theta = 180°$) during simulation. Figures 3.3, 3.4 and 3.5 show these computed pressure time histories in comparison with the analytic solution. From the computed result, superior resolution characteristics of the optimized compact finite difference schemes with negligible dispersion and dissipation errors are evident. To verify that the superior accuracy is maintained irrespective of directional position in the domain, acoustic pressure was monitored at three different locations as mentioned above and as may be seen, good agreement is evident at all three locations.

3.2.2 Inviscid flow past a 2D cylinder

An inviscid flow past a circular cylinder is a steady flow without separation and is close to potential flow in the low-Mach-number regime. The grid domain used was the same as the one based on an H-topology used in the acoustic scattering case. A pressure contour plot for a Mach number of 0.1 is presented in Figure 3.6. The pressure coefficient curve is plotted in Figure 3.7 along the cylinder surface in comparison with the potential flow case. From Figures 3.6 and 3.7, it is evident that the computed inviscid solution is in good agreement with the potential field of an ideal flow.

3.2.3 Sound Propagation in 3D Curvilinear Meshes

For the next validation case, propagation of a 3D spherical acoustic pulse in a curvilinear mesh is computed to evaluate the effect of metric cancellation errors on acoustic propagation. A three-dimensional curvilinear grid is generated using the following equations [see Visbal & Gaitonde (2001)]:

$$
\begin{aligned}
x(i,j,k) &= x_{ref} + \delta x\left[(i-1) + \sin\left\{\frac{8\pi\,(j-1)\,\delta y}{L_y}\right\}\sin\left\{\frac{8\pi\,(k-1)\,\delta z}{L_z}\right\}\right] \\
y(i,j,k) &= y_{ref} + \delta y\left[(j-1) + \sin\left\{\frac{8\pi\,(i-1)\,\delta x}{L_x}\right\}\sin\left\{\frac{8\pi\,(k-1)\,\delta z}{L_z}\right\}\right] \\
z(i,j,k) &= z_{ref} + \delta z\left[(k-1) + \sin\left\{\frac{8\pi\,(i-1)\,\delta x}{L_x}\right\}\sin\left\{\frac{8\pi\,(j-1)\,\delta y}{L_y}\right\}\right]
\end{aligned}
\tag{3.2}
$$

with

$$\delta x = \frac{L_x}{n_x - 1};\ \delta y = \frac{L_y}{n_y - 1};\ \delta z = \frac{L_z}{n_z - 1}$$

and

$$i = 1 \ldots n_x;\ j = 1 \ldots n_y;\ k = 1 \ldots n_z.$$

The domain generated using Eqns 3.2 results in a computational grid which does not satisfy the metric identities discussed in Chapter 2 [i.e. Eq. 2.22 to 2.24]. An isometric view of the resulting wavy mesh is shown in Figure 3.8. A 3D spherical acoustic pulse was initiated at the centre of the mesh to study its propagation accuracy in the distorted wavy mesh. An initial spherical acoustic pulse for this case is prescribed by:

$$
\begin{aligned}
p &= p_\infty + \varepsilon e^{-\ln 2\left(\frac{x^2+y^2+z^2}{9}\right)} \\
u(x,y,z,0) &= 0 \\
v(x,y,z,0) &= 0 \\
w(x,y,z,0) &= 0
\end{aligned}
\tag{3.3}
$$

where $\varepsilon = 0.01$.

Figures 3.9a and 3.9b display the calculated pressure contours on a plane through the centre of the spherical pulse at $t = 10$ for the case when the metrics are evaluated using Eqns 2.6 and 2.26 respectively. It is apparent that significant distortion of the acoustic wave occurs due to the lack of freestream preservation (i.e. metric cancellation errors). The acoustic pressure along the grid line $i = j = 31$ is compared in Figure 3.10 for both the calculations with the theoretical solution and poor performance of the standard metric evaluation method is apparent. The results obtained with the metric evaluation procedure of Eq. 2.26 exhibit no acoustic distortions and the computed line pressure is in excellent agreement with the theory. Hence, even for relatively good quality curvilinear grids, errors resulting from the lack of freestream preservation can corrupt the acoustic pressure significantly unless proper metric evaluation procedures are employed. This case has clearly demonstrated that the superior performance of the high-order method can be extended to a complex geometry cases involving general curvilinear grids.

3.2.4 Vortex propagation across a block interface

To further test the accuracy of the interface conditions and demonstrate its transparent behaviour towards acoustic waves, a two dimensional problem of an isentropic vortex convection across a block interface is considered. The Mach number of this case is taken to be 0.3, and the Reynolds number in viscous flow is set to be 10^4. A single convective vortex in an uniform flow is expressed as:

$$p = p_\infty - \frac{\rho C_0^2}{2R_0^2}\exp(-r^2) \tag{3.4}$$

$$u = u_\infty - \frac{C_0\,(y-y_c)}{R_0^2}\exp(-r^2/2) \tag{3.5}$$

$$v = \frac{C_0\,(x-x_c)}{R_0^2}\exp(-r^2/2) \tag{3.6}$$

$$\tag{3.7}$$

where

$$r^2 = \frac{(x-x_c)^2 + (y-y_c)^2}{R_0^2}$$

and C_0 and R_0 are set to 0.167 and 0.2 respectively [Sumi & Kurotaki (2006)]. Figure 3.11 shows the two block grid domain used in the computation and each of the block had grid dimension of 121×241. The vortex is initially released from $(x_c, y_c) = -(1, 0)$ at $t = 0$. The pressure contours of the propagating vortex at four different instances is shown in the Figure 3.12. From the figures it can be seen that the vortex passes through the block interface boundary very smoothly and there is no evidence of the acoustic reflections or any other instabilities at the block interface boundary. The pressure signal along a horizontal line through the centre of the convecting vortex corresponding to the first three instances in Figure 3.12 is plotted in Figure 3.13. As can be seen in the figure, there is no reflection of the signals at the block interface and it is found to pass smoothly. The characteristic boundary condition, therefore, is transparent to the vortex propagation problem.

3.2.5 Laminar flow past a 2D cylinder

Viscous flow past a circular cylinder is found to shed vortices in the well-known Von Kármán vortex street behind the cylinder. It is known experimentally that a regular Von Kármán street exists when the flow Reynolds number (based on cylinder diameter) lies in a range of about 60 to 5000 [Schlichting (1979)] and the Strouhal number depends only on Reynolds number in this range. This regular vortex shedding causes fluctuations in lift and drag forces and the fluctuation of forces results in the radiation of a dipole sound field. The radiated dipole sound is estimated analytically and compared with the computational result. The analytical formula neglects the effects of quadrupole sources due to the convection of vortices. However, the quadrupole source strength is negligibly

small at low subsonic flows compared to the dipole source. The analytical formula, therefore, is well suited for predicting sound directivity for low subsonic flows and is used in this work for comparison with the computed result. The analytical formula used to predict the dipole sound directivity [Kim & Lee (2004)] can be written as,

$$p'_{rms}(r,\theta) = \frac{\rho_\infty a_\infty^2}{4}\left[\left\{\frac{M_\infty^5 Sr}{r/d}\right\}\left\{\overline{C_L^2}\sin^2\theta + 4\overline{\left(C_D - \overline{C_D}\right)^2}\cos^2\theta\right\}\right]^{\frac{1}{2}} \tag{3.8}$$

where Sr is the Strouhal Number, r the distance from the centre of the cylinder, and d is the cylinder diameter.

As with the inviscid case, a non-orthogonal grid generated using an H-topology was used for the viscous flow simulation about a 2D cylinder. The flow Reynolds number based on the cylinder diameter for this case was 300. The number of grid points used was 250×150. The grid points were clustered near the cylinder wall and the boundary layer was resolved by approximately 25 grid points normal to the cylinder surface. The viscous grid domain with the cell distributions near the cylinder surface is shown in Figure 3.14. The simulation was run with a CFL number of 0.5 and was continued until the non-dimensional time reached $t \times a_\infty/d = 400$. Figure 3.15 shows contours of the instantaneous vorticity and velocity fields at the end of the computation; this clearly indicates the existence of a Von Kármán street along with the positions of the vortices. Time-dependent lift and drag coefficients are plotted in Figure 3.16. From the figure, a periodic fluctuation of unsteady forces with constant magnitudes at a constant frequency is evident after initial transients have settled. The frequency of this periodic oscillation was used to evaluate the Strouhal number. The computed values of Strouhal number, mean drag coefficient, and rms fluctuating lift coefficient are compared with experimental data [Schlichting (1979); Kim & Lee (2004)] and listed in Table 3.1. From the results, the mean flow properties computed using the proposed boundary conditions are found to agree well with the experiment. Figure 3.17 compares the computed acoustic directivity with the analytical estimation using Eq. 3.8. From the figure the computed result is in excellent agreement with the analytical approximation demonstrating the low acoustic dispersion and dissipation characteristics of the solver.

3.2.6 Turbulent Flow Past a Backward-Facing Step

Having demonstrated the good accuracy of the solver in computing an acoustic scattering, potential flow past a cylinder and viscous laminar flow, a viscous turbulent calculation is performed to demonstrate the performance of the turbulence matching [see Appendix

Table 3.1: Strouhal Number and Mean Force coefficients

Cases	**Strouhal Number** (St)	**Drag Coefficient** ($\overline{C_d}$)	**RMS Lift Coefficient** $(\overline{C_l^2})^{\frac{1}{2}}$
Experiment	0.21 ± 0.005	1.2 ± 0.1	0.6 ± 0.1
Computed	0.212	1.202	0.612

A for details]. For this case a backward-facing step was chosen, owing to the ready availability of high-quality experimental data. The computational domain was designed using a structured multi-block strategy. The basic topology and block structure of the computational domain and the structured grid are shown in Figure 3.18. Inter-block boundaries are denoted by dashed lines. As indicated, the computational domain consists of eight structured blocks. Along the inflow boundary, the two Cartesian velocity components u, v together with the turbulence quantity ν_t were prescribed to ensure that the computed boundary layer profile matched the experiment [Jovic & Driver (1994)]. These values were determined using Wilcox's EDDYBL boundary layer program [Wilcox (2006)], together with a knowledge of the experimental boundary layer profile upstream of the step. In total the computational grid consisted of approximately 33000 cells. To resolve the shear and boundary layers, grid cells are clustered along all solid walls as well as around the step region using a hyperbolic tangent distribution function. In all cases the meshes were designed to ensure a y^+ of less than or equal to one along all solid walls. Upstream of the step, the boundary layer was resolved with a minimum of 25 mesh points. In the experiment [Jovic & Driver (1994)] the backward-facing step flow was found to be closely represented by a two-dimensional flow in the measurement domain. Hence, in accordance with the experimental observation, a two dimensional simulation was performed in this case. A characteristic outflow boundary with pressure at infinity (ie free stream value) was imposed at the downstream boundary of the domain and an outflow along the upper boundary.

Computations were performed using both the new matching procedure and the existing approaches (based on simple averaging) at the block-interfaces. From the result, a discontinuity was found to exist in turbulence variables (e.g. μ and ν) at block interfaces when the turbulence quantities at the interface were matched using simple averaging. Contours of non-dimensional kinematic viscosity are plotted in Figure 3.19 for the result using standard averaging and a clear discontinuity is found to exist at the three-block-interface junction. This discontinuity, however, is not present in the result from the new treatment (using proposed turbulence matching procedure). Contours of non-dimensional kinematic viscosity are again plotted in Figure 3.20 for the result from the new interface treatment and a smooth and continuous solution is found to exist at all the block

interfaces. Comparisons of mean streamwise velocity profiles with experiment at two different locations are plotted in Figure 3.21. A reasonably good agreement between the experiment and the computed result is evident. Hence, the proposed method to match turbulence quantities at the block interfaces completes the extension of characteristic-based interface matching methods for turbulent flow simulation with improved accuracy and robustness.

3.3 Cavity Flow Simulations

After validating the CAA solver for a wide range of flow types, it is utilized for 2D and 3D cavity flow simulations, which is also the main focus of this thesis. Although geometrically simple, cavity flowfields exhibit complex flow behaviours and therefore can be taken as benchmark cases representative of geometrically more complex flows. This section therefore is devoted to investigating computationally the aerodynamic noise generation mechanism in cavities using the CAA solver. In particular the flow physics responsible for the tonal noise generation are emphasized in this section. For comparison with experiment, two specific cavity geometries are considered. The first type is an automobile door cavity and the second is a plane cavity.

3.3.1 Flow over a 2D Automobile Door Cavity

In this section the results of a two-dimensional viscous turbulent simulation of the flow over an automobile door cavity are presented and analyzed. This geometry represents the gap between a closed car door and car body; it has a narrow opening, which is exposed to the external flow, and a relatively deep main cavity with $L/D \leq 1$.

Geometry and Flow Conditions

The geometrical details of the cavity investigated are shown in Figure 3.22(a). The 2D geometry, which is representative of an automobile door gap, comprises a simple rectangular surface cutout with a lip or overhang extending from the upstream edge. The basic cavity dimensions in this case are taken from the experimental work of Henderson (2000). The computational domain was designed using a structured multi-block strategy. For this case, ten structured grid blocks were used to construct the computational domain. Figure 3.22(b) shows a view of the nearfield computational grid for the case. Along the inflow boundary, the two Cartesian velocity components u, v together with

the turbulence quantity ν were prescribed to ensure that the computed boundary layer thickness matched the experiment [Henderson (2000)]. These values were determined using Wilcox's EDDYBL boundary layer program [Wilcox (2006)] assuming a one-seventh power-law for the boundary layer. In total the computational grid consisted of approximately 55000 cells. To resolve the shear and boundary layers, grid cells were clustered along all solid walls, and notably along the cavity mouth using a hyperbolic tangent distribution function. In all cases the meshes were designed to ensure a y^+ of less than or equal to one along all solid walls. Upstream of the cavity lip, the boundary layer was resolved with a minimum of 25 mesh points. Grid stretching within the cavity was kept to a minimum, but outside the cavity grid stretching was used to create a coarse buffer region near the outflow to damp disturbances before they encountered the characteristic non-reflecting boundary. Adiabatic, no-slip boundary conditions are imposed on all solid walls in the computation.

Computed Results

Figure 3.23 shows a sequence of vorticity contours demonstrating the vortex shedding from the lower edge of the cavity lip. The nature of the flow in the vicinity of the cavity opening can be analysed by examining these sequences. The images correspond to times in the oscillation cycle, and highlight the unsteadiness in the resulting shear layer as the boundary layer separates from the lip of the cavity. The oscillations develop as a consequence of shear layer instabilities which amplify small pressure disturbances in a feedback loop. The convective growth of these instabilities results in the unsteady impingement of the shear layer on the downstream face of the cavity. As a consequence of this unsteady shear layer behaviour, the pressure in the vicinity of the downstream wall fluctuates in a quasi-periodic manner. The resulting cyclic oscillation process near the cavity neck can be described as follows. As the pressure at the cavity downstream face increases due to the impingement of the shear layer, a mass flux from the neck into the main body of the cavity results. During this phase the density and pressure increase within the main body. As the shear layer continues to evolve with time the pressure in the downstream wall region is reduced when the shear layer is deflected over the corner. As this occurs mass flows out from the cavity resulting in the reduction of density and pressure inside the main body. The feedback loop is closed, as the density and pressure perturbations radiate together as sound from the cavity, perturbing the shear layer. When the frequency of the disturbance is suitably in phase with the developing shear layer, resonance occurs. At resonance, sound pressure levels (SPL) in excess of 130dB have been observed in experiments. The spectral content of the computed pressure at a

point on the downstream-facing edge of the cavity lip is compared with the experimental data of Henderson (2000) in Figure 3.24. The computed results show that a strong tonal component at just over 1800 Hz ($St = 0.315$) dominates the acoustic spectrum, which is in good agreement with the experimental data. The computed tone amplitude also closely matches that in experiment, lying within 3dB. The nature of the oscillations observed may be described to have similarity with a classic Helmholtz resonator. In order to verify the hypothesis that the cavity was indeed behaving as a Helmholtz resonator, the following theory for a Helmholtz resonator was used to estimate the oscillating frequency of the resonator:

$$f_{Helmholtz} = \frac{a}{2\pi}\sqrt{\frac{A_O}{d_O V_{in}}} \tag{3.9}$$

where d_O is the equivalent depth of the neck, A_O is the area of the opening, V_{in} is the volume of the cavity and a is the speed of sound. The equivalent depth of the neck was calculated using the approximation of Rayleigh (1896) on a piston in a baffle. The estimated resonant frequency using the simple relation of Eq. 3.9 was found to be $f = 1850$ Hz, which is in good agreement with the numerical and experimental values. This clearly indicates that the mode of oscillation is that of a Helmholtz resonator.

3.3.2 3D Clean Cavity, $L/D = 4$, $W/D = 1$

The CAA solver is now employed to study the tonal noise produced by a 3D cavity geometry at transonic speed. Fully 3D numerical simulations are performed with the CAA code. Both the mean and unsteady flowfields inside the cavity are examined in detail and comparisons are made with available experimental data [Tracy & Plentovich (1997)].

Geometry and Flow Setup

The cavity configuration investigated is a 3D plane cavity, which comprises a simple rectangular cutout in an otherwise infinite plate and is therefore fully described by its length-to-depth and length-to-width ratios. The geometry considered was 9.6 inches long with $L/D = 4$ and $W/D = 1$ and corresponds to one of the cases in the experimental investigation [Tracy & Plentovich (1997)]. For this study the Mach number of the freestream flow is 0.8. Again, as with the geometry, the flow condition corresponds to a subset of those investigated by Tracy & Plentovich (1997). The computational domain extends $4D$

upstream, 8D downstream, 6D vertically and 4D laterally from the cavity. A sectional view of the multi-block structure of the computational domain and the structured grid is shown in Figure 3.25. In total, the computational domain consisted of 52 structured blocks with approximately 2.9 million grid points. Along the inflow boundary, the two Cartesian velocity components u, v together with the turbulence quantity ν were prescribed so that the computed boundary layer just upstream of the cavity had approximately the same thickness as in the experiment [Tracy & Plentovich (1997)]. These values were determined using Wilcox's EDDYBL boundary layer program [Wilcox (2006)], together with a knowledge of the experimental boundary layer thickness upstream of the cavity. The computed profile was then copied across the span at the inflow boundary and the z-component of velocity (w) was set to zero. To resolve the shear and boundary layers grid cells are clustered along all solid walls using a hyperbolic tangent distribution function. At the cavity leading edge, the boundary layer is resolved with approximately 20 mesh points. A characteristic outflow boundary with pressure at infinity (i.e. free-stream value) was imposed at the downstream boundary of the domain, as well as along the upper and lateral boundaries. To assess the adequacy of the computational domain and demonstrate the suitability of the grid a grid convergence study was undertaken. Due to the excessive computational time involved in 3D unsteady computations, two-dimensional simulations were used to establish grid convergence. For this purpose three meshes were generated with the same basic mesh topology, see Fig. 3.25(c), but with varying grid densities. The details of the grid convergence study are given in Appendix D. The intermediate grid in the 2D grid convergence study was found to be in good agreement with the fine grid and hence was chosen as the basis for the 3D grid generation. The 3D grid thus generated was used for the unsteady flow simulation for this cavity case. At the first stage, a preliminary steady simulation was performed using the commercial, general purpose CFD solver, Fluent. To reduce the computational time, the steady solution was then used to initialize the unsteady simulation in the CAA solver. The results of the computation are presented in the following sections.

Aerodynamic Field

Time-mean flow

The time-mean flowfield is characterized by the mean surface static pressure coefficient (C_p) distribution. The computed mean C_p distribution is presented in Figure 3.26 for the simulated case (the experimental C_p data were not available for comparison). The study of the mean C_p distribution in Figure 3.26 indicates that the flow belongs to the open

cavity flow type and it is found to exhibit many of the global flow features commonly found in open cavity flows. The time-mean flow within the cavity is dominated by a large-scale recirculating flow pattern. The location of the centre of the large structure may be identified from the trough in the mean C_p plot that is mostly evident along the cavity floor and the structure is centred downstream of the middle of the cavity. A careful study of the mean C_p plot also found that the time-mean flowfield is not uniform across the cavity span. This can be concluded from Figure 3.26 which shows the mean C_p plots for various spanwise locations. For this case, the centreline of the cavity is seen to record the greatest variation in the pressure coefficient.

Although the mean C_p plots can be used to identify the cavity flow type, a more detailed study of the flow behaviour and structure inside the cavity is not possible from these plots. Hence visualization of 2D sectional streamlines using line integral convolution (LIC) images [Knowles et al. (2006)] along with 3D flow particle tracking was used to study the flow behaviour further. To study the state of the time-mean flow features inside the cavity, vortex core locations were calculated in the time-averaged CFD data and stream lines were emitted from the calculated locations. The resulting mean flow structure is presented in Figure 3.27. These streamlines represent the time-mean path of unsteady vortical structures inside the cavity. In addition, sectional streamlines of computed time-mean velocity data are visualized using LIC in Figure 3.28. Figure 3.27 reveals a single vortex structure which is seen to travel upward in the upstream third of the cavity, before being swept downstream to merge with the large recirculation near the lip of the cavity. This is also evident from the LIC image in Figure 3.28(h). This observation is consistent in principle with the results presented in Chapter 4 (in Chapter 4, the results show the presence of two contra-rotating vortices, but these are observations on wider cavities, i.e. $W/D \geq 2$). The structures have described in ESDU Item 02008 [ESDU (2004)] as 'tornado-like' vortices which spiral up towards the mouth plane (i.e. the open plane) of the cavity although a description of their subsequent movement is not given. These structures have also been studied by Atvars et al. (2009) with the aid of experiments and CFD visualization. The formation of a single vortex structure can be described as follows. When the flow travelling upstream along the floor of the cavity reaches the upstream wall, the proximity of the cavity sidewall forces the flow to divert in the spanwise direction towards the opposite sidewall. The proximity of the opposite sidewall forces the flow to turn and flow downstream but is prevented from doing so by the flow travelling upstream along the cavity floor. The flow is forced to turn out towards the sidewall of the cavity which forms the vertical 'tornado-like' structures seen on the cavity floor. The presence of only one vortex structure in this case is thought to be due to

the narrow cavity width ($W/D = 1$). The LIC images of sectional streamlines at various spanwise locations (i.e. Figures 3.28[a-f]) also clearly indicate the three-dimensionality in the time-mean flow inside the cavity. Firstly, the most noticeable three-dimensional flow feature is the variation in the position of the core of the main recirculating flow across the span of the cavity. Secondly, secondary recirculating regions are found to appear upstream and downstream of the main recirculating structure in the cavity for $z/W = 0.4$ and $z/W = 0.5$ locations.

Time-dependent flowfield

The basic unsteady flow physics are also in accordance with Rossiter's model. These global unsteady features may be seen in Figure 3.29 which shows the time development of tubular vortical structures in terms of the iso-surfaces of the second invariant of the velocities Joeng & Hussain (1995). The unsteady behaviour of the flow inside the cavity may be analysed by studying the evolution of these structures. The incoming boundary layer separates at the cavity leading edge forming a shear layer. As the shear layer develops downstream, instabilities quickly grow leading to the tubular vortex structures evident (tracked with a blue oval) in Figure 3.29. With time, these structures continue to grow while being convected downstream. At the rear of the cavity, the interaction of the vortical structures with the cavity trailing edge generates disturbances that travel upstream along the cavity floor (shown with a red arrow in Figure 3.29(a)) towards the cavity leading edge, thus closing the feedback loop. The tornado-like vortex observed in the meanflow study is actually the time-averaged path of the tubular vortex structures seen in the unsteady flow.

To study the unsteady flow quantitatively, the frequency content of the nearfield pressure fluctuations was extracted using fast Fourier transforms. Figure 3.30 shows the comparison between experimental [Tracy & Plentovich (1997)] and computed pressure spectra at the leading edge of the cavity (note that experimental data were only available for the leading-edge monitor point). Mode frequency predictions from the modified Rossiter equation are represented by the dashed lines. From the figure, computed mode frequencies are found to agree well with the experimental data, although the magnitude of the tones have small discrepancies. These discrepancies may be due to the lack of sufficient knowledge of experimental test conditions that affect the cavity flowfield e.g. incoming boundary layer characteristics, tunnel turbulence levels, ambient density (ρ) and ambient temperature (T) (or speed of sound, a_0). Also, the computed results are found to agree better with the dominant mode frequency predicted by the modified Rossiter equation. Higher modes, however, are not well captured by the computation.

This may be due to the limitation on the grid size used. Due to the fourth order accuracy of the solver, the computational time is very high and hence this limits the size of the grid domain for a realistic simulation time frame. To tackle this issue, adaption of zonal grid methods (patched and/or overlapped grids) are proposed as an area of future work in the further development of the CAA solver.

To compare the computational accuracy of the CAA solver, an unsteady simulation was also performed for the same cavity geometry using the second order finite volume solver, Fluent. Although a zonal grid with non-matching interfaces could have been used to reduce the number of the overall grid size in the Fluent simulation, the grid domain which was used for the CAA simulation was used to enable like-for-like comparison. The comparison was focused on the accuracy of prediction of resonant modes by both the solvers. Figure 3.31 shows the resonant modes predicted by both the solvers compared to experiment. From the figure, the CAA solver is found to perform better in prediction of acoustic phenomena. Firstly, the first resonant mode is not picked up by the Fluent solver (In Chapter 4, it will be shown that Fluent can offer better accuracy with zonal grid methods). Secondly, the computed resonant frequency of the second mode from the CAA solver is also closer (albeit marginally) to experiment than Fluent. Higher order modes are not picked up by either of the solvers. This may be due to the limitation posed by the number of grid cells in the structured grid domain. This proves that the high order CAA solver can perform better than second order solver under identical conditions. However, the computing costs for the CAA solver was found to be almost 10 times more than that required for the Fluent solver as shown in Table 3.2.

Table 3.2: Required Computational Resources in Simulations

Solver	**No. of cores**	**Simulation time** (days)	**Total CPU hrs**
CAA solver	52 (13 Quad core nodes)	240 (Approx.)	2.99×10^5
Fluent	16 (4 Quad core nodes)	120 (Approx.)	4.6×10^4

3.4 Flow around a Generic Landing Gear

To demonstrate the stability and robustness of the CAA solver for flowfields involving complex geometries (i.e. challenging geometries for the generation of structured grids), the unsteady flowfield around a generic landing gear was computed using the CAA code.

The investigation involves the aerodynamic noise radiation from a single wheel isolated in a freestream.

Aerodynamic noise from landing gear is considered a major component of airframe noise, especially during landing when the engine is operating at low thrust. Numerous experimental as well as computational studies to identify the noise source and its attenuation techniques are being carried out around the globe [Ringshia et al. (2006); Guo (2008)]. The landing gear acoustic spectrum normally has a peak at mid to low frequencies and is considered to be a significant source of noise for modern passenger aircraft such as the Airbus A380 or Boeing 787. Flow over the large elements such as the wheels is found to be responsible for low-frequency noise whilst small components such as axles, struts, wires etc are responsible for the noise at higher frequencies. Streamlined fairings are being proposed to reduce the high frequency noise. However, streamlining the wheel is not practical and hence the wheel is thought to be the most challenging component in airframe noise.

Geometry and Flow Setup

The landing gear geometry considered in this investigation was a single wheel with a diameter of $1.05m$. A multi-block structured grid was created to compute the unsteady flowfield around the wheel. A fully structured computational domain was created using a multi-block domain strategy. The origin of the co-ordinate system coincided with the geometric centre of the wheel. Due to the complexity involved in generating a structured grid around a landing gear geometry, the total number of structured blocks to construct the computational domain was 424. The number of grid points used was 3.15 million. The computational domain extended $7d$ upstream, $15d$ downstream, $5d$ vertically and $4d$ laterally from the centre of the wheel. These dimensions were chosen to be large enough to minimise the influence of the boundaries on the final solution and small enough to minimize the number of grid points. Similar values have previously been found to be sufficient in the simulation of a comparable geometry [Hedges et al. (2002)]. Figure 3.32 shows the 3D computational domain used in this computation. Figure 3.33 shows the wheel geometry and structured grid distributions. The grid points were clustered near the wheel surface to ensure $y^+ = O(1)$. The boundary layer was resolved by approximately 20 grid points normal to the wheel surface. A characteristic outflow boundary with pressure at infinity (i.e. free-stream value) was imposed at the downstream boundary of the domain, as well as along the upper and lateral boundaries whereas a characteristic inflow boundary condition was imposed at the inlet. A preliminary steady simulation

was computed using the commercial CFD solver, Fluent. To reduce the computational time, the steady solution was then used to initialize the unsteady simulation in the CAA solver. The simulation was run with a CFL number of 0.5.

Aerodynamic Field

Time-mean flow

To understand the mean flow structure around the landing gear wheel and to investigate the state of the separated flow in the wheel wake, vortex core locations were calculated in the time-averaged CFD data and mean flow streamlines were then emitted from the calculated vortex core locations. The resulting mean flow structure is presented in Figure 3.34. These streamlines clearly show that the vortex cores are formed at the hub of the wheel. The wheel hubs act as circular cavities and the vortical structures are formed due to the flow separation and formation of an unsteady shear layer. The mean flow structures in Figure 3.34 suggest that the downstream wake is driven by the dominant separated shear layer from the wheel hubs rather than the separated flow from the upper surface of the wheel.

Time-dependant flow

Figure 3.35 shows the instantaneous iso-surfaces of the second invariant of the velocities around the wheel. The large vortex structures can clearly be seen to be shed from the hub cavities. The hub cavity is seen to drive the shedding of the large scale structures with the wheel top surface having a negligible effect on this. The visualization indicates that the separated shear layer in the wheel hub cavities is the most important in landing gear noise generation. To study the unsteady flow quantitatively, the frequency content of the farfield (at a distance of 100m from the centre of the wheel) pressure signals were extracted using fast fourier transforms. Resulting spectra are presented in Figure 3.36. From the figure, it is evident that dominant acoustic peaks occur at low frequencies (less than 200 Hz) for all the cases. Low frequency peaks are expected when there is a flow around large components, in this case the wheel. No peaks are seen to exist at higher frequencies (greater than 200 Hz) which is also expected. This is because the landing gear model in this case did not have any small components e.g. axle, hub cut outs etc which are responsible for the high frequency noise. The farfield sound directivities were obtained at Plane-AA and Plane-BB (see Figure 3.37) for 36 equi-spaced observer locations located around a circle of radius 100m (see Figure 3.38). The directivity in Figure 3.39 shows the

sound distribution in two planes. The directivity distribution at Plane-AA clearly shows the presence of a dipole sound field, whereas the distribution at Plane-BB shows that the sound radiation is approximately uniform in this plane.

3.5 Summary

A CAA solver which utilizes a family of optimized high-order accurate finite-difference compact schemes has been developed to compute aerodynamic noise generation problems accurately. The solver is based on a hybrid strategy which combines nearfield numerical simulations with a farfield radiation model. An extensive set of two-dimensional numerical simulations were performed to validate the solver. In addition, a 3D plane cavity flowfield was also simulated which showed greater complexity, with presence of multiple modes. All the computed results from the CAA solver were found to agree well with experiments (in both the frequency and the magnitude). The solver was also used to study a 3D landing gear geometry to test its robustness and stability for 3D generic curvilinear grids.

The computed results presented in this chapter have demonstrated the capability of the CAA solver to resolve unsteady flowfields accurately for a wide range of geometries and flow conditions. The solver is found to perform robustly with complex multi-block curvilinear structured grid despite having no artificial dissipation in it.

Although the solver has shown great potential in solving complex unsteady flows accurately, it has a few shortfalls when tackling complex geometries and the high speed flow problems. The shortfalls are purely due to the excessively long computation times involved because of the explicit time stepping used, making flow problems at transonic speeds computationally very expensive and time consuming. In addition, the solver's requirement for a structured grid domain means that complex geometries (e.g. cavity with stores and landing gear assembly) cases cannot be solved with the current state of the code. For these reasons, the rest of the computational studies were performed using the commercial CFD solver Fluent. Chapter 4, therefore, presents the computational studies in 3D cavity geometries at transonic speeds using Fluent.

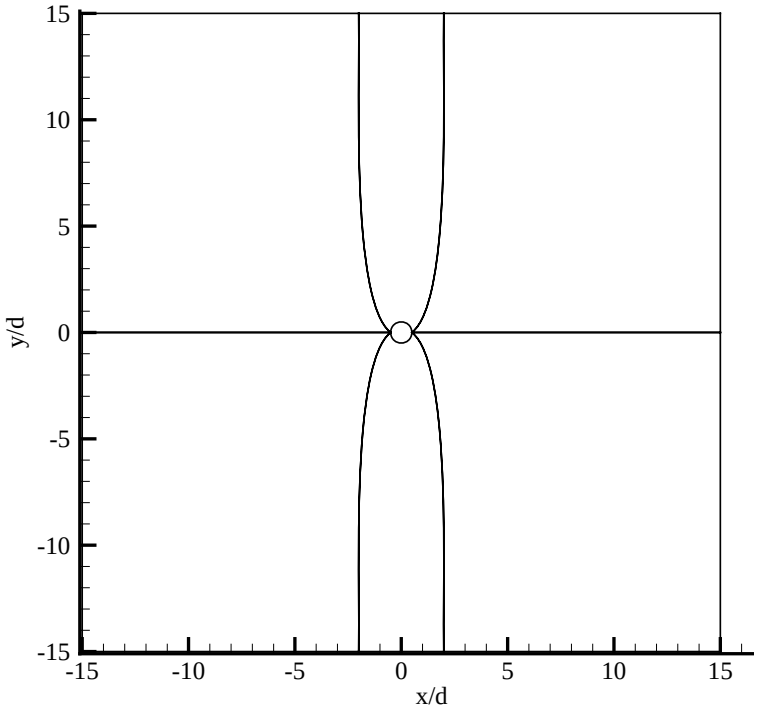

(a) H-topology Grid domain.

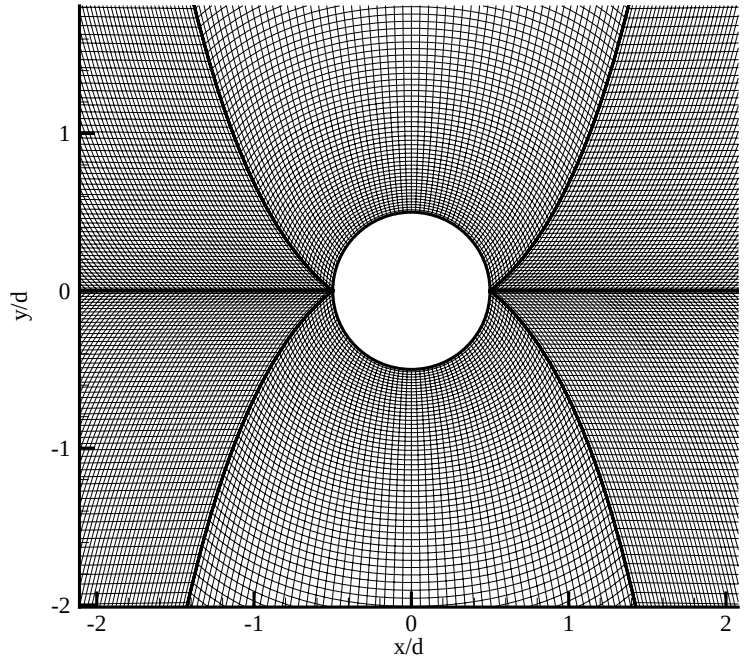

(b) Grid points near the cylinder surface (every other points shown).

Figure 3.1: H-topology domain and grid distribution.

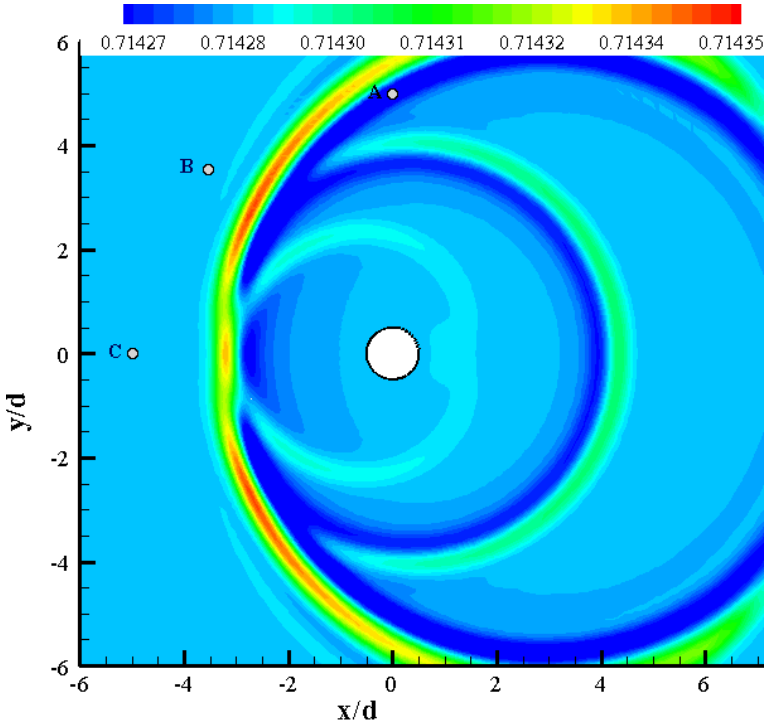

Figure 3.2: Pressure contours showing acoustic scattering off a cylinder.

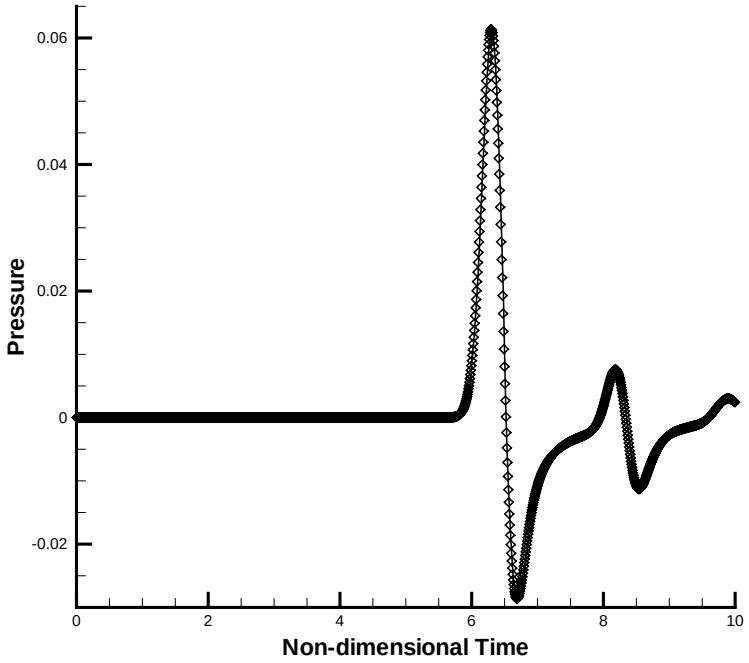

Figure 3.3: Comparison between computed and analytical pressure signals at monitor point A(◊ numerical, — analytical)

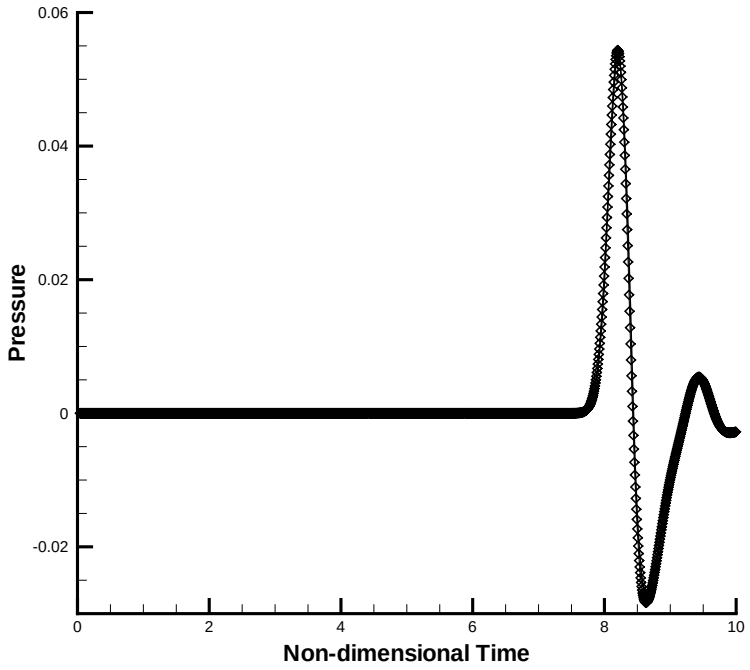

Figure 3.4: Comparison between computed and analytical pressure signals at monitor point B(◊ numerical, — analytical)

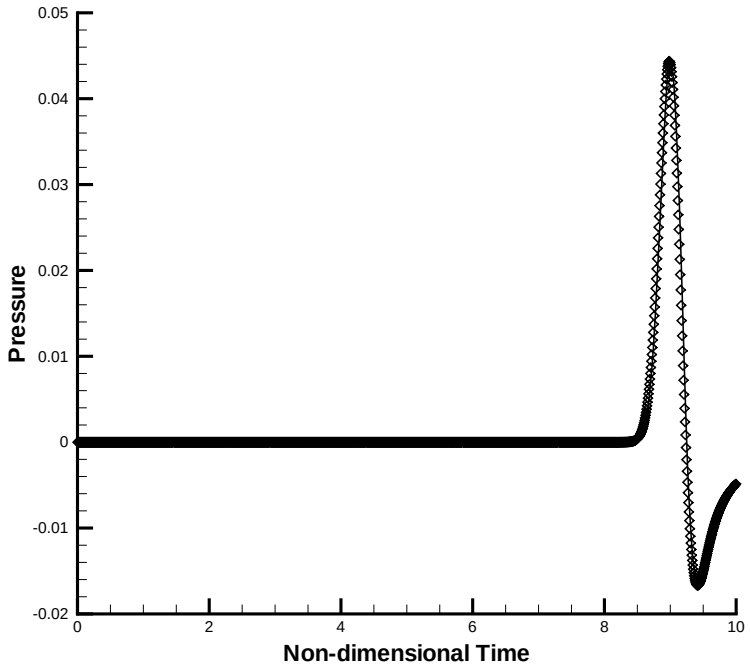

Figure 3.5: Comparison between computed and analytical pressure signals at monitor point C(◊ numerical, — analytical)

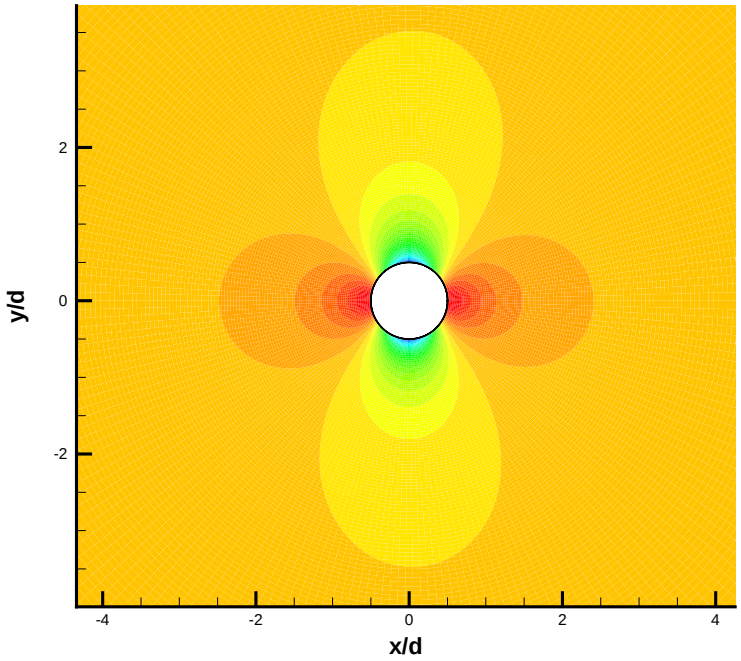

Figure 3.6: Pressure contours from inviscid flow simulation.

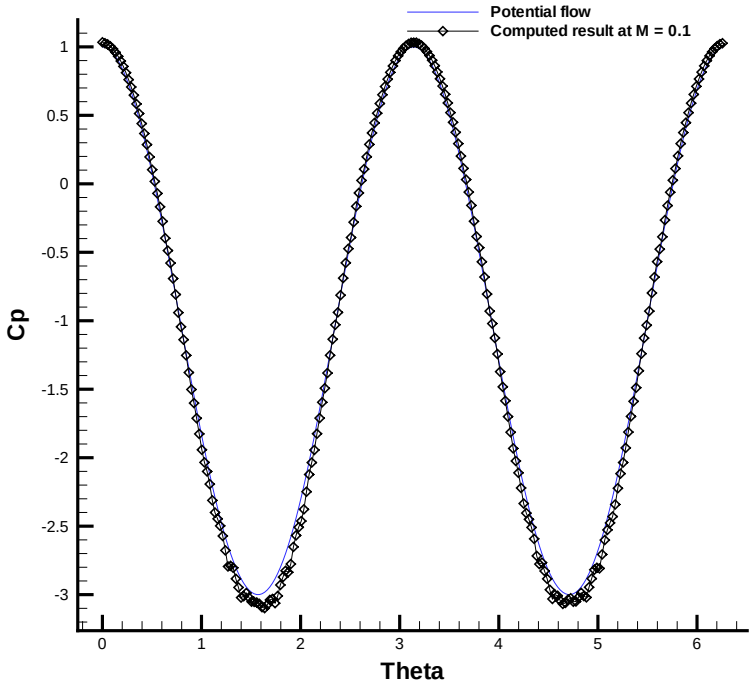

Figure 3.7: Pressure coefficients comparison between potential flow and computation.

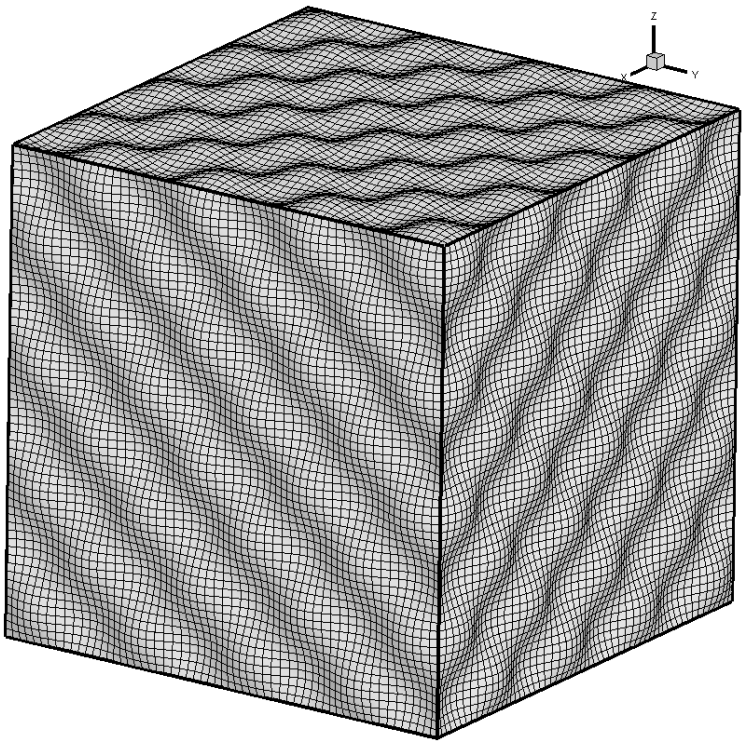

Figure 3.8: Wavy grid to test the metric cancelation errors.

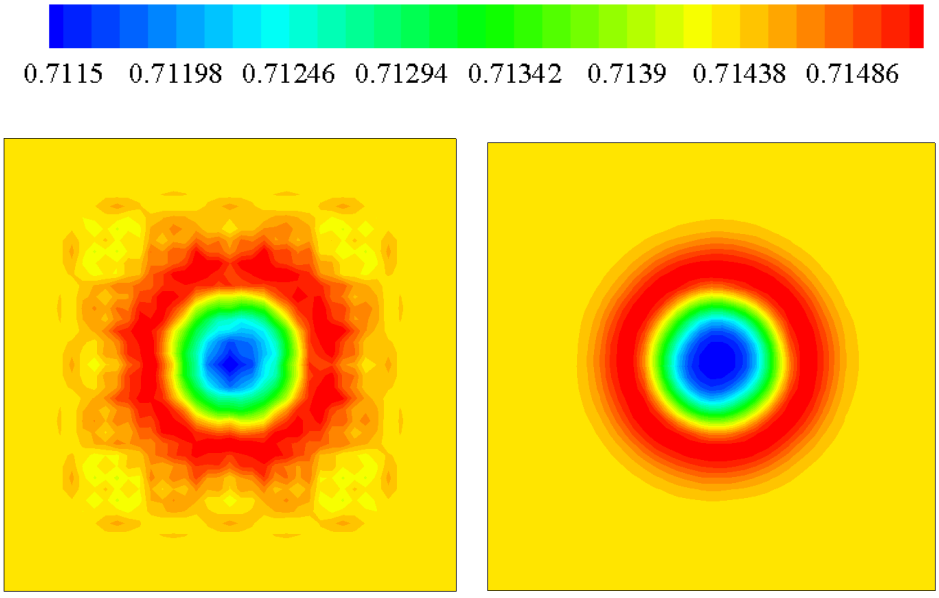

(a) Standard metric formula. (b) New metric formula.

Figure 3.9: Snapshot of acoustic pressure at central plane (2D XY-Plane).

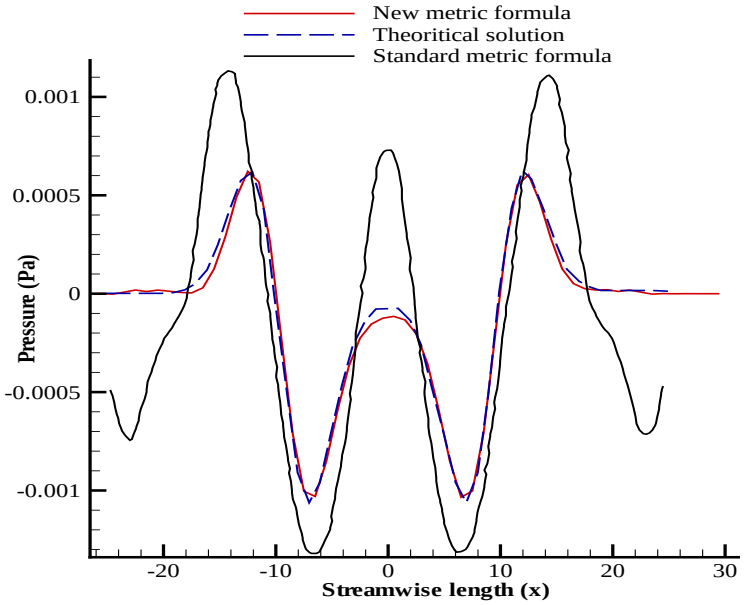

Figure 3.10: Comparison of computed pressure (p/p_∞) with analytical solution.

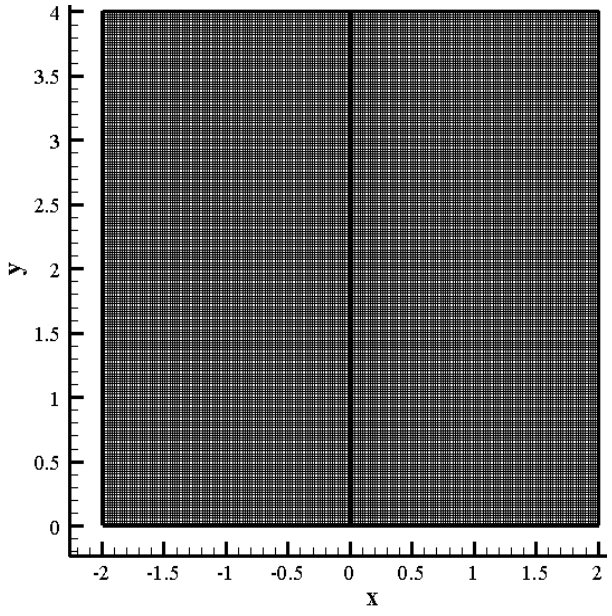

Figure 3.11: Grid domain for vortex propagation.

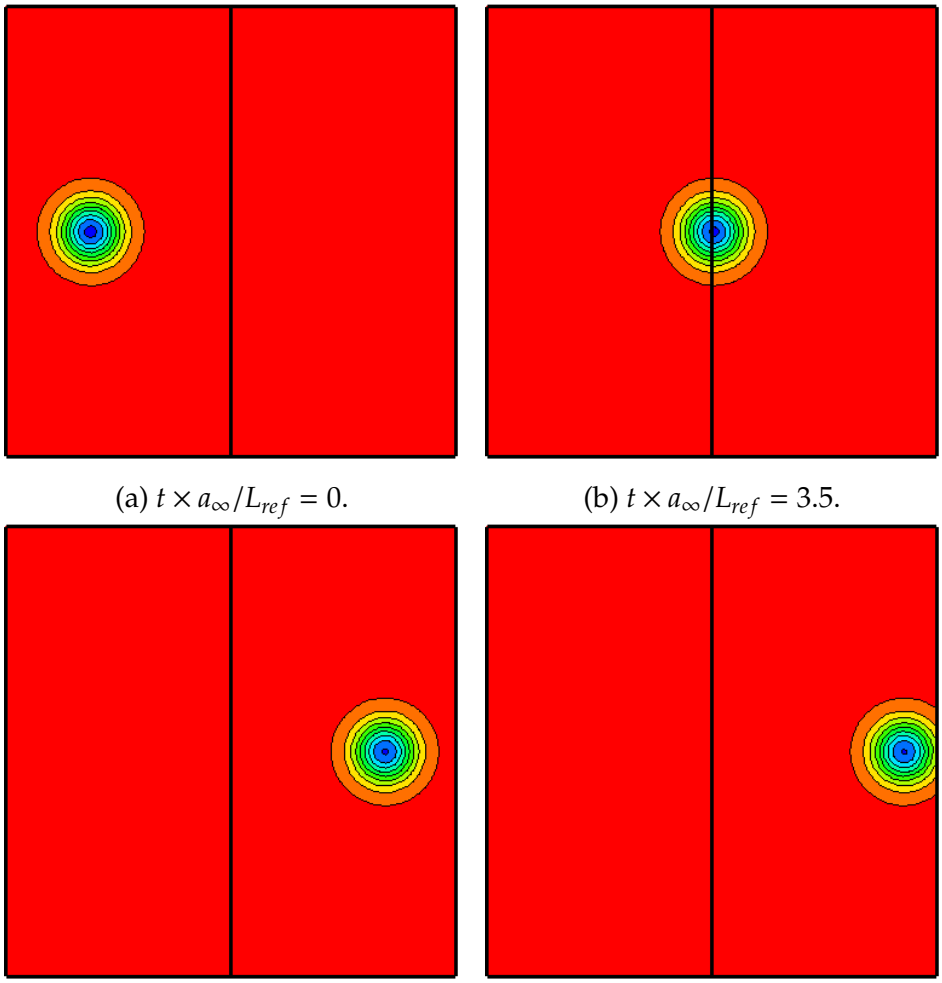

(a) $t \times a_\infty / L_{ref} = 0.$ (b) $t \times a_\infty / L_{ref} = 3.5.$

(c) $t \times a_\infty / L_{ref} = 7.$ (d) $t \times a_\infty / L_{ref} = 7.8.$

Figure 3.12: Pressure contours showing vortex convection.

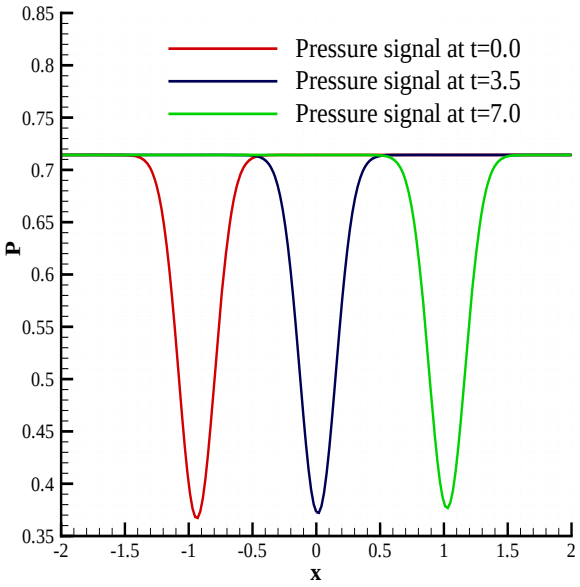

Figure 3.13: Computed pressure signals three different times (corresponding to Figures 4.15(a), 4.15(b) and 4.15(c).

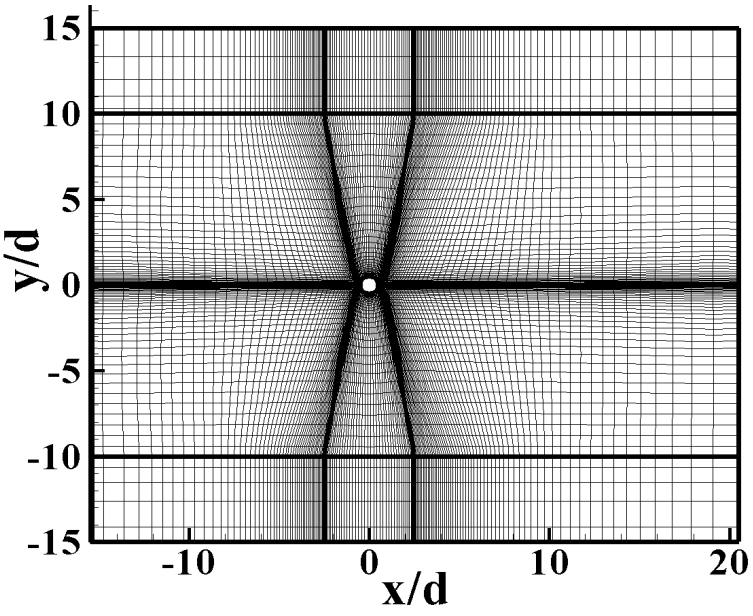

Figure 3.14: Grid domain for viscous computation (every other point shown).

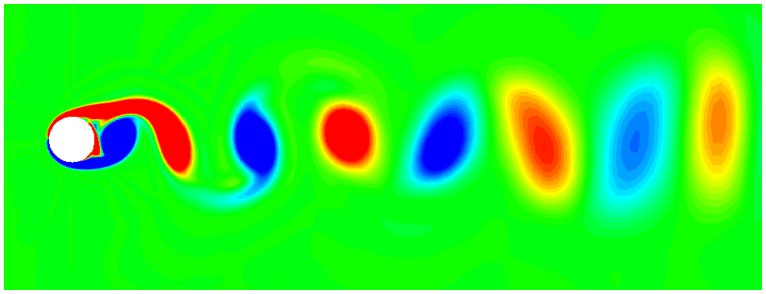

(a) Contours of vorticity magnitude.

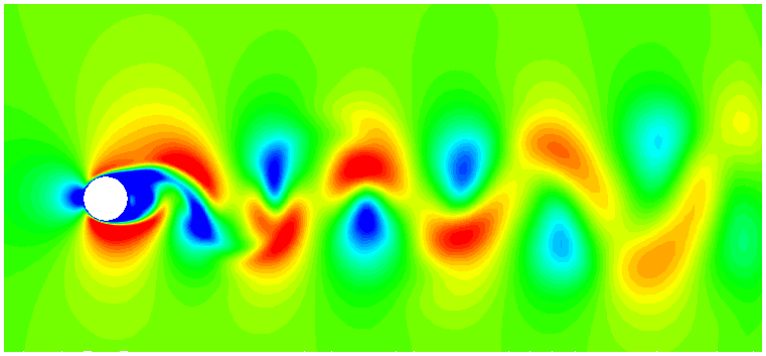

(b) Contours of velocity magnitude.

Figure 3.15: Snapshot of instantaneous flowfield at $t \times a_\infty / d = 400$.

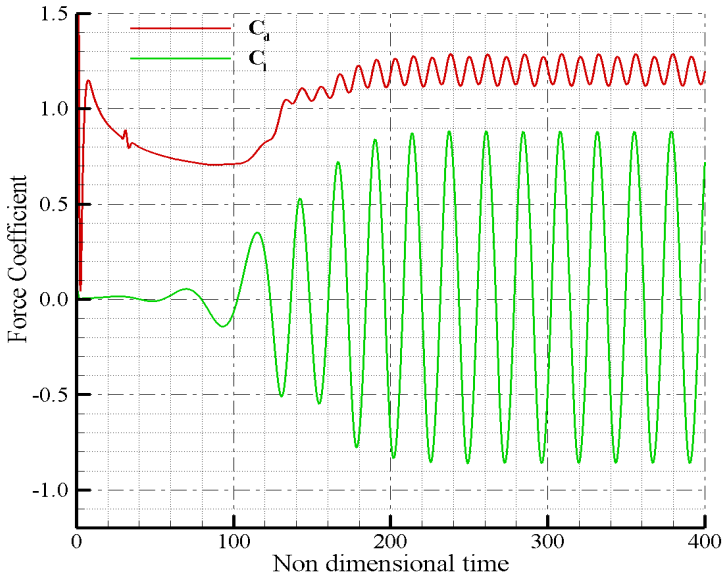

Figure 3.16: Fluctuating force coefficients.

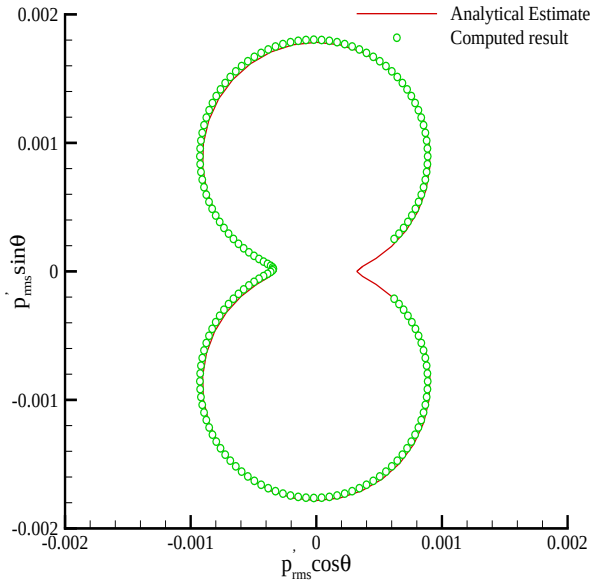

Figure 3.17: Acoustic directivity.

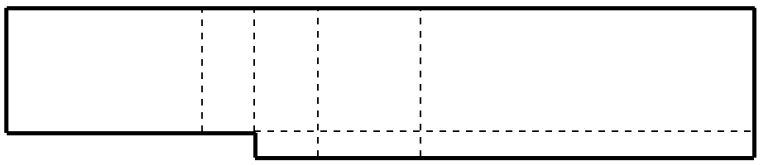

(a) Computational multi-block domain.

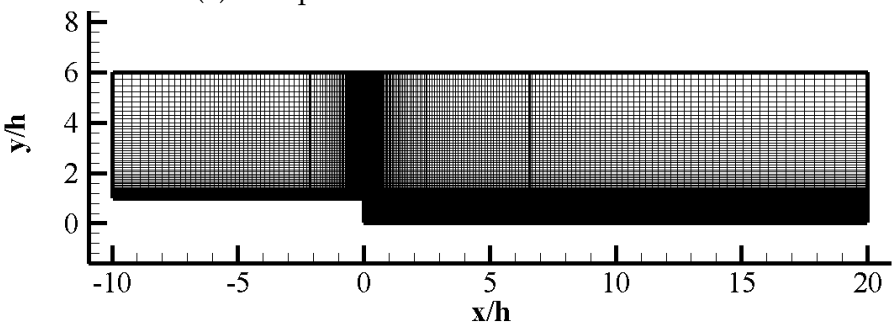

(b) Computational grid.

Figure 3.18: Backward-facing step domain design and grid generation.

(a) Contours of mean kinematic viscosity.

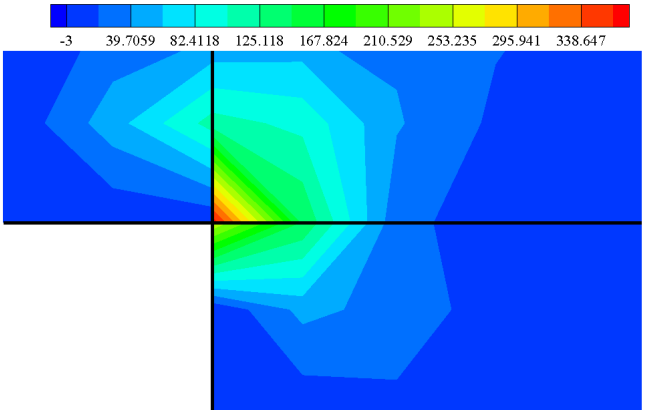

(b) Kinematic viscosity at block interface (zoomed in view).

Figure 3.19: Mean kinematic viscosity (ν/ν_∞) contours using standard block interface treatment.

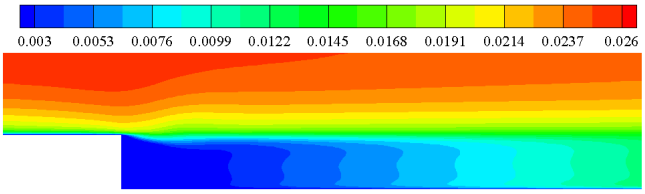

(a) Mean velocity magnitude (U/U_∞).

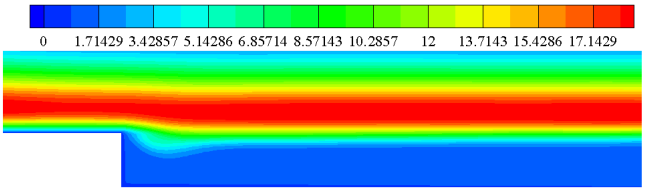

(b) Mean kinematic viscosity.

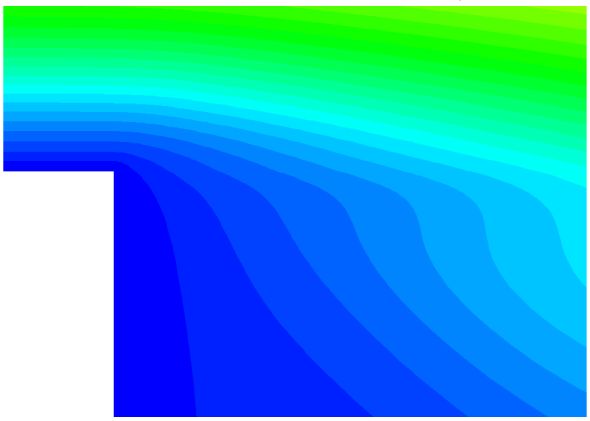

(c) Kinematic viscosity (ν/ν_∞) at block interface (zoomed in view).

Figure 3.20: Mean flow contours using new treatment.

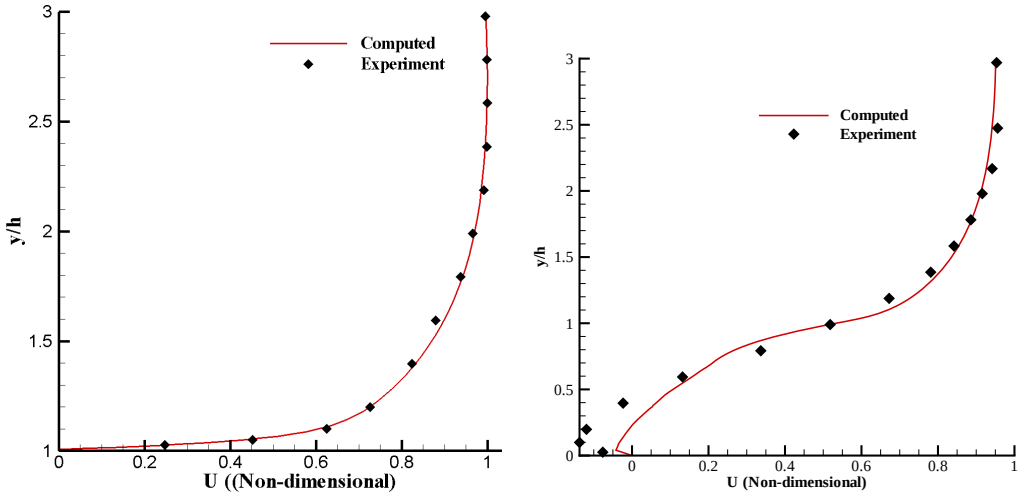

(a) Profile at x/h=-3.12.

(b)Profile at x/h=4.

Figure 3.21: Mean velocity profiles.

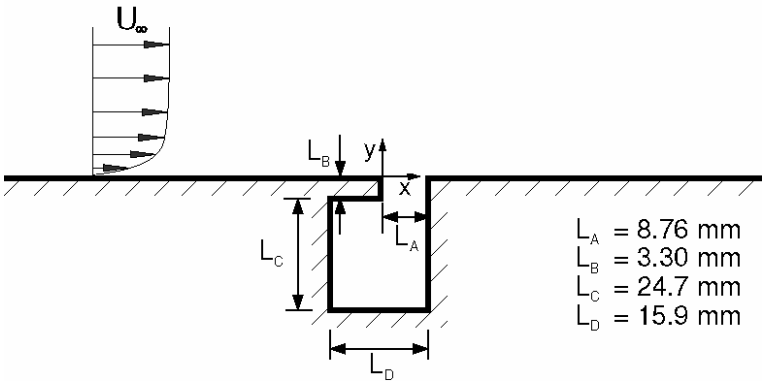

(a) Geometry.

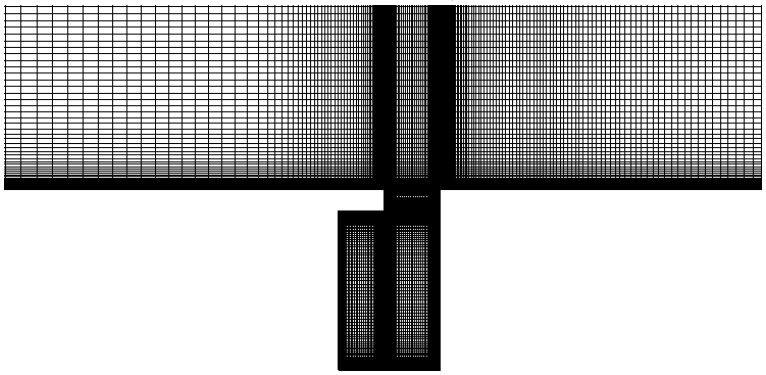

(b) Grid.

Figure 3.22: Geometrical details of automobile door cavity.

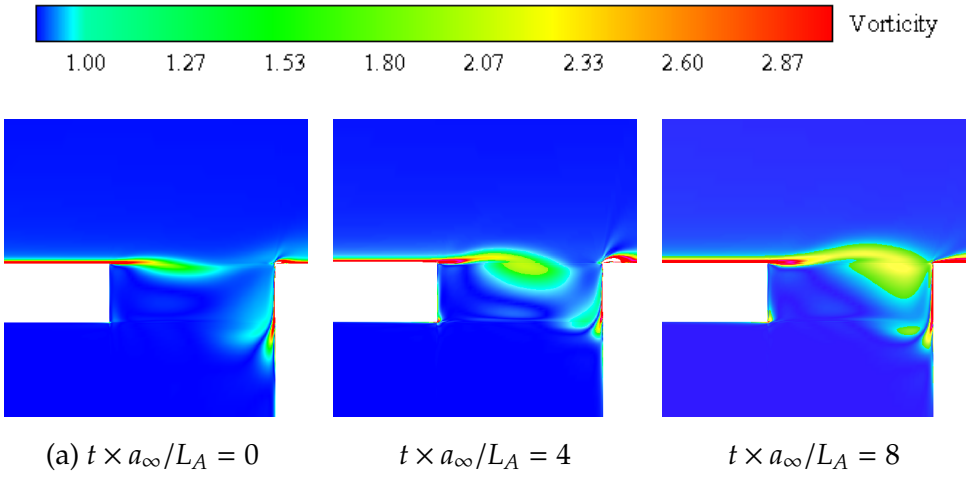

Figure 3.23: Sequence of instantaneous vorticity contours (non-dimensional) for the lip region.

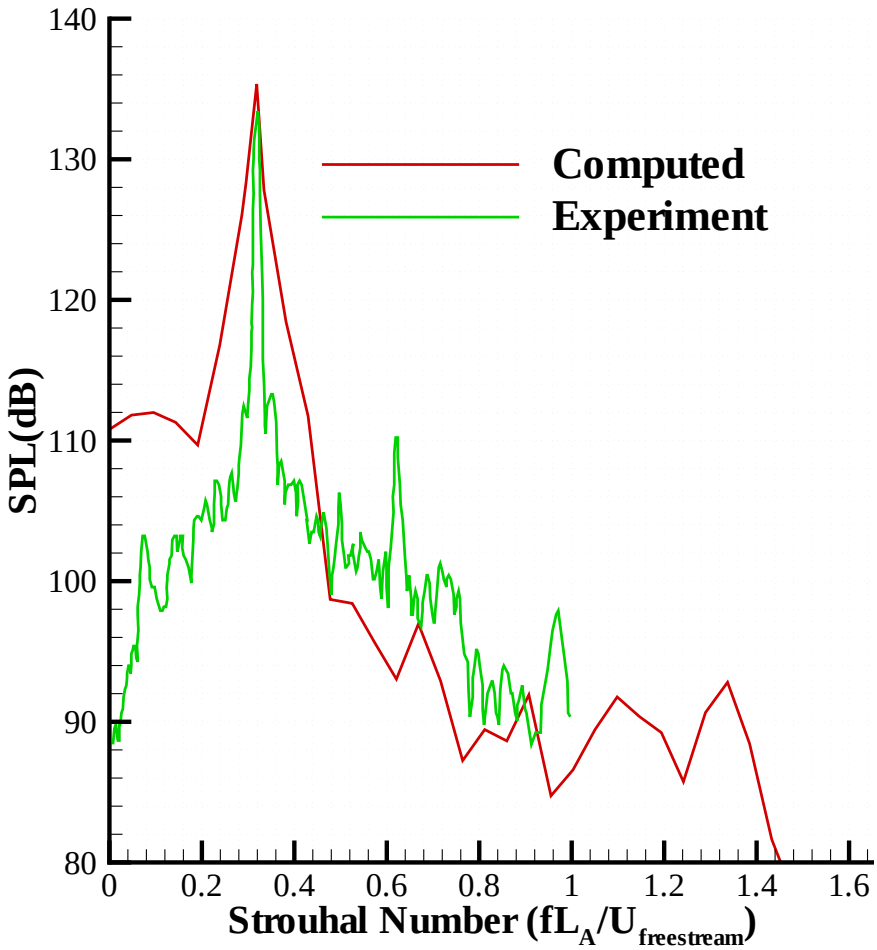

Figure 3.24: Pressure spectra comparison at leading wall.

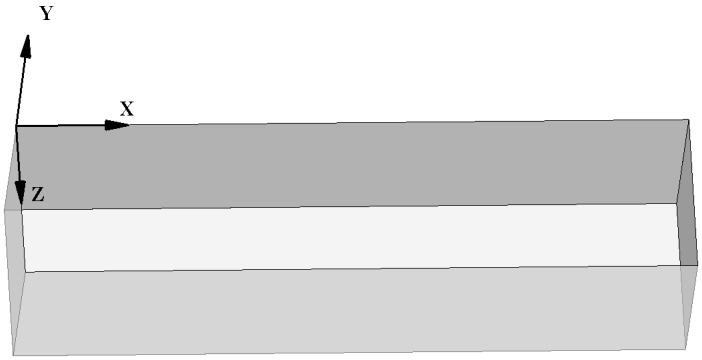

(a) 3D cavity geometry and co-ordinate system.

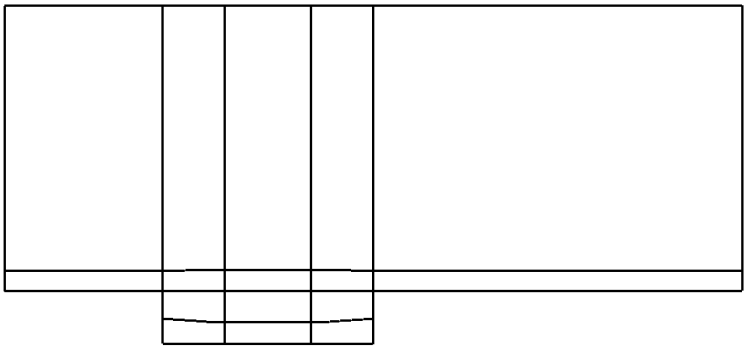

(b) A sectional view of multi-block domain.

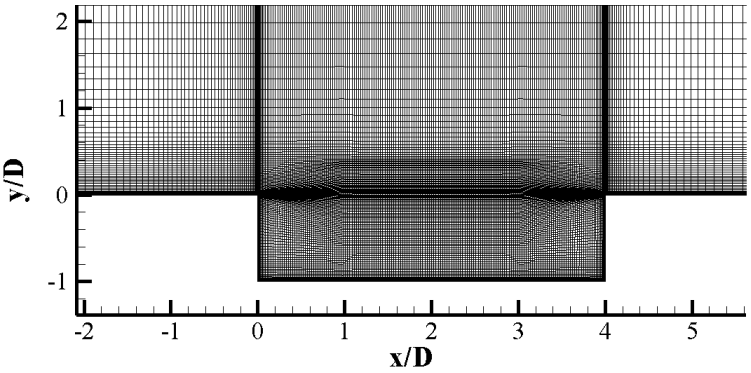

(c) Grid distribution inside the cavity (zoomed in view).

Figure 3.25: Multi-block Domain Design and Grid generation.

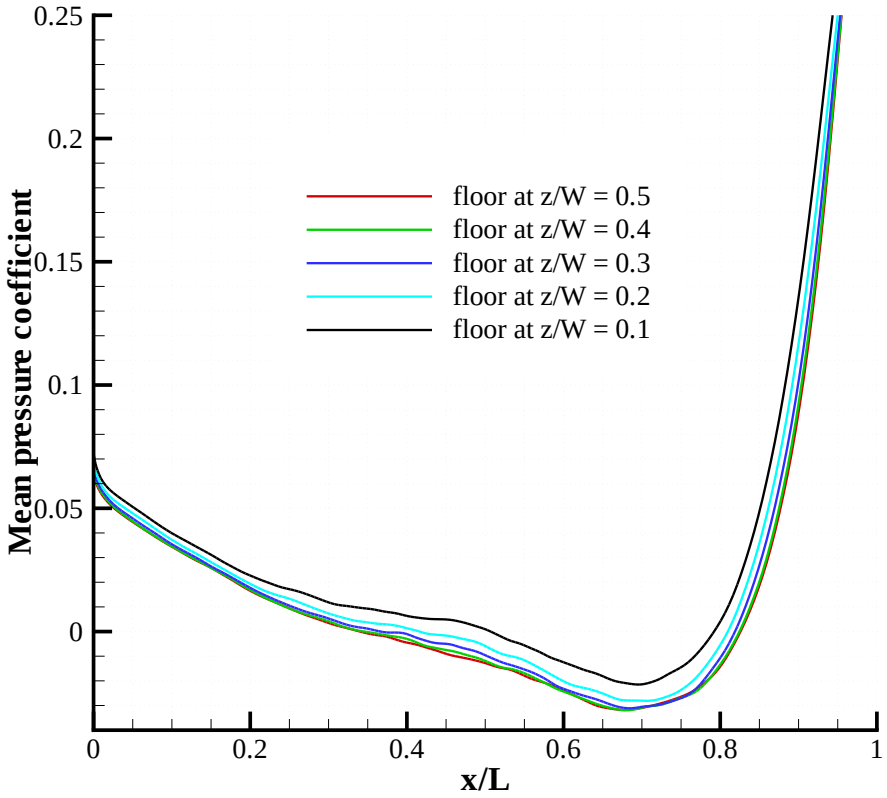

Figure 3.26: Mean C_p along varying spanwise locations, $L/D = 4$ and $W/D = 1$; $M_\infty = 0.8$.

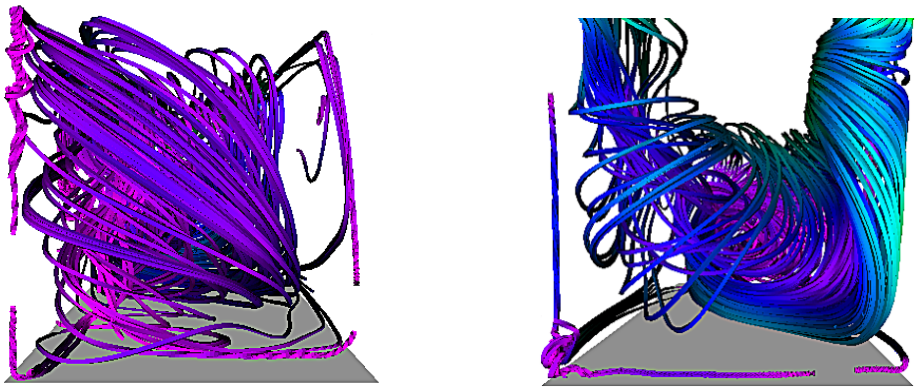

(a) Downstream view from leading edge. (b) Upstream view from trailing edge.

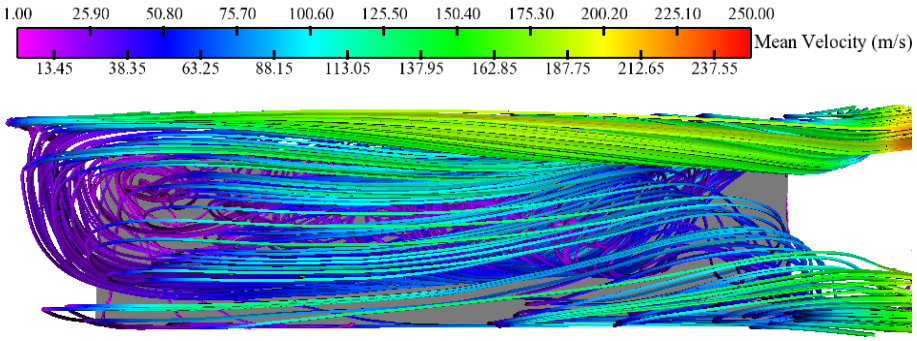

(c) State of the mean flow in the cavity.

Figure 3.27: Time-mean streamlines for 3D cavity, $L/D = 4$ and $W/D = 1$; $M_\infty = 0.8$.

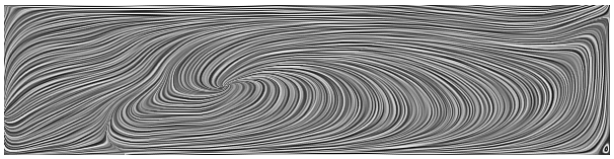

(a) Time mean streamlines in x-y plane at $z/W = 0.1$

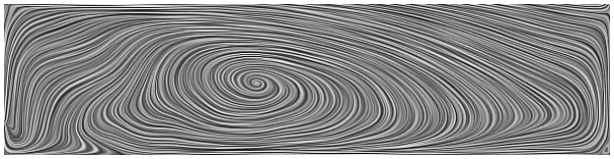

(b) Time mean streamlines in x-y plane at $z/W = 0.2$

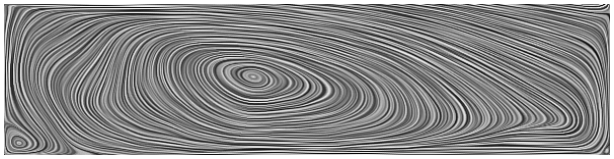

(c) Time mean streamlines in x-y plane at $z/W = 0.3$

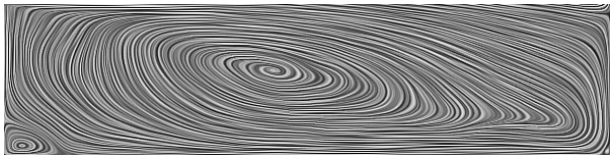

(d) Time mean streamlines in x-y plane at $z/W = 0.4$

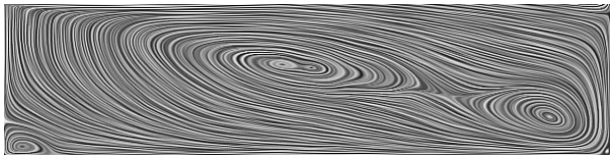

(e) Time mean streamlines in x-y plane at $z/W = 0.5$

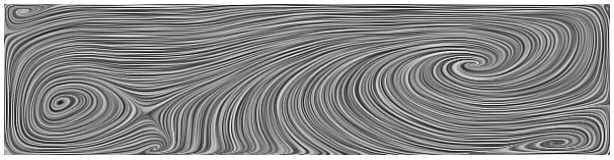

(f) Time mean streamlines in x-z plane at $y/D = 0.5$

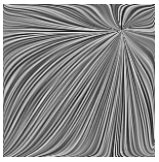

(g) Upstream wall.

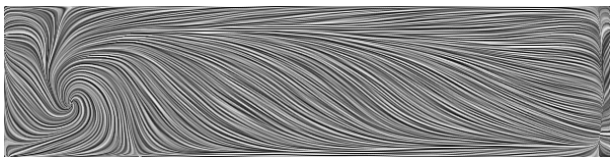

(h) Cavity Floor.

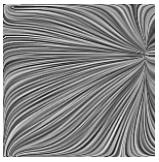

(i) Downstream wall.

Figure 3.28: Mean flow maps on various planes and surfaces in the cavity using LIC, $L/D = 4$ and $W/D = 1; M_\infty = 0.8$.

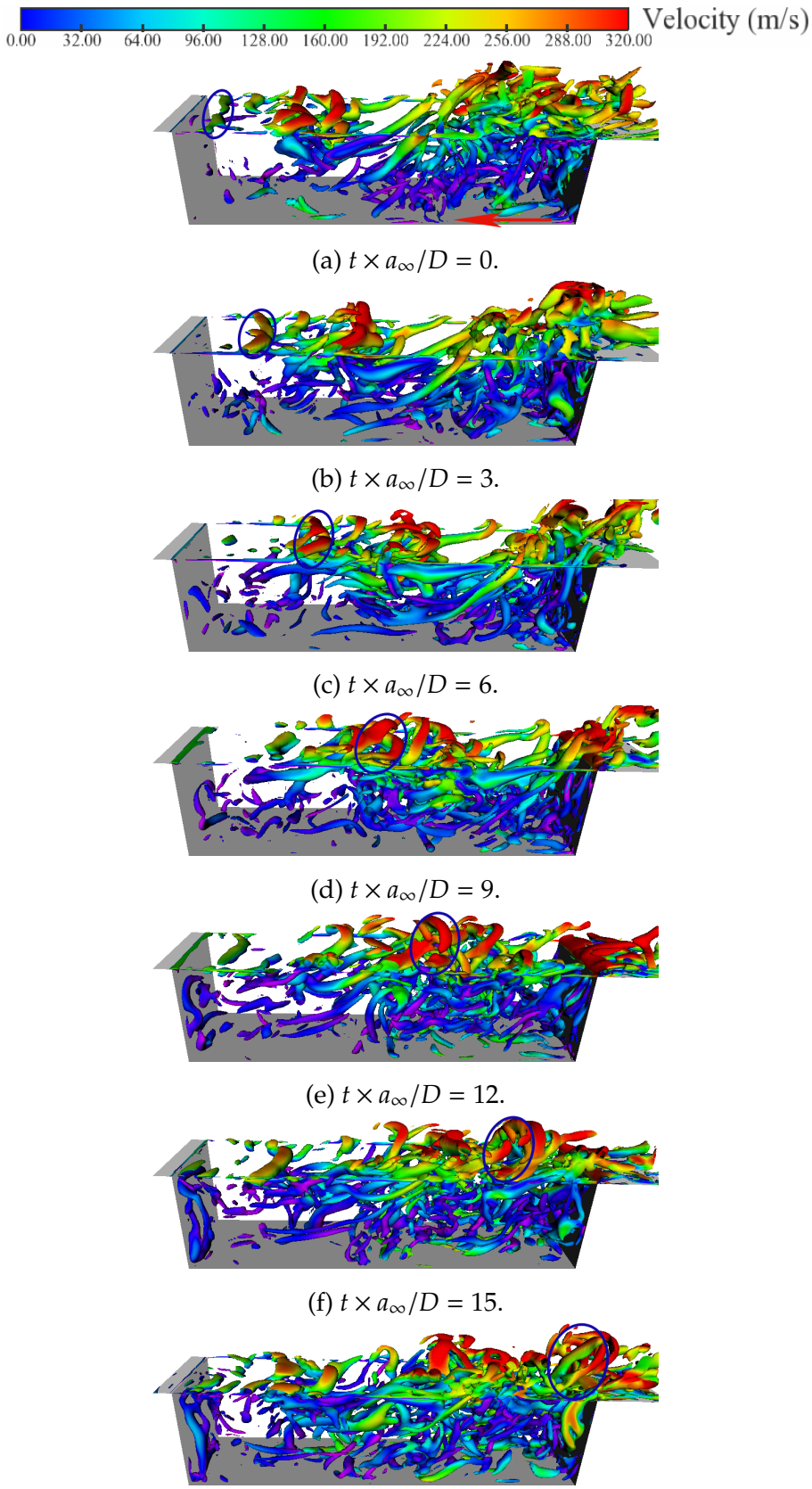

(a) $t \times a_\infty / D = 0$.

(b) $t \times a_\infty / D = 3$.

(c) $t \times a_\infty / D = 6$.

(d) $t \times a_\infty / D = 9$.

(e) $t \times a_\infty / D = 12$.

(f) $t \times a_\infty / D = 15$.

(g) $t \times a_\infty / D = 18$.

Figure 3.29: Shear layer vortex evolution over one cycle of oscillation: iso-contours of the Q-criterion, $L/D = 4$ and $W/D = 1$; $M_\infty = 0.8$ [This cycle equates to an approximate frequency of 289 Hz and hence corresponds to the first resonant mode in Fig. 3.30].

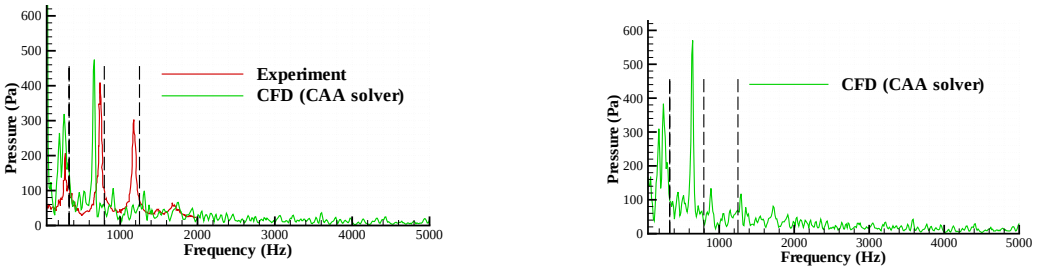

(a) Monitor point near cavity leading wall. Experimental data from Tracy & Plentovich (1997).

(b) Monitor point near cavity rear wall.

Figure 3.30: Cavity pressure spectra, $L/D = 4$ and $W/D = 1$; $M_\infty = 0.8$. Vertical dashed lines indicate Rossiter mode frequencies.

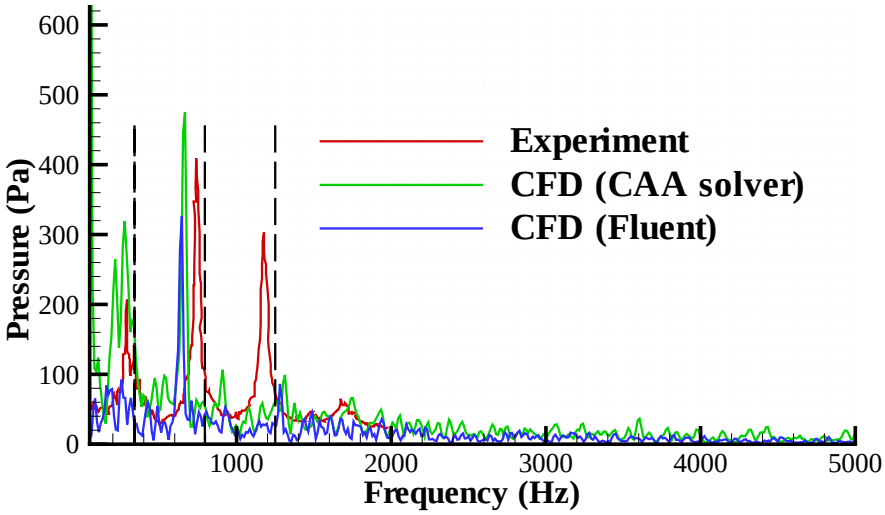

Figure 3.31: Cavity pressure spectra comparison, $L/D = 4$ and $W/D = 1$; $M_\infty = 0.8$. Vertical dashed lines indicate Rossiter mode frequencies.

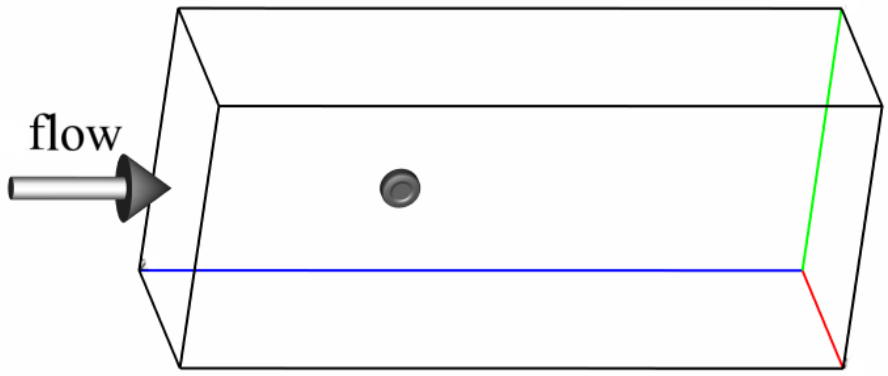

Figure 3.32: Computational domain for landing gear study.

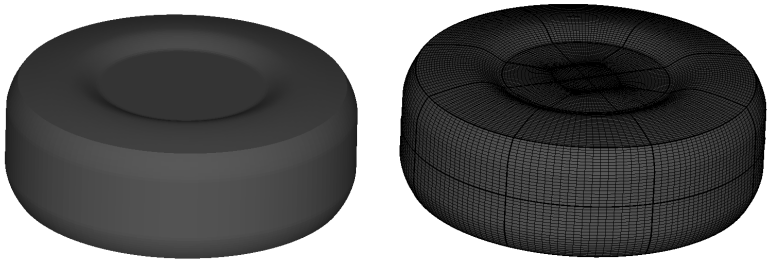

(a) CAD model. (b) Structured surface grid.

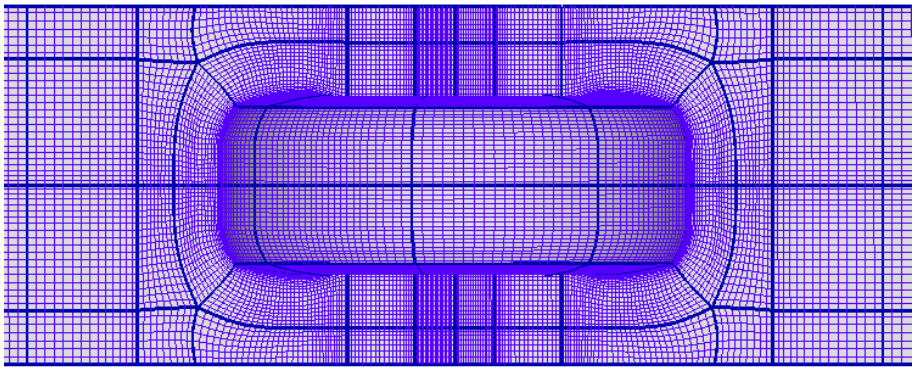

(c) Structured near field grid design.

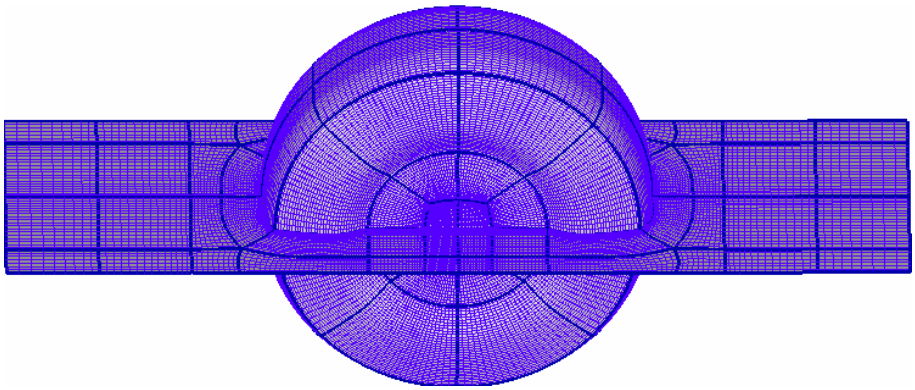

(d) Structured grid distribution around the wheel.

Figure 3.33: Landing gear geometry and grid design; $M_\infty = 0.3$.

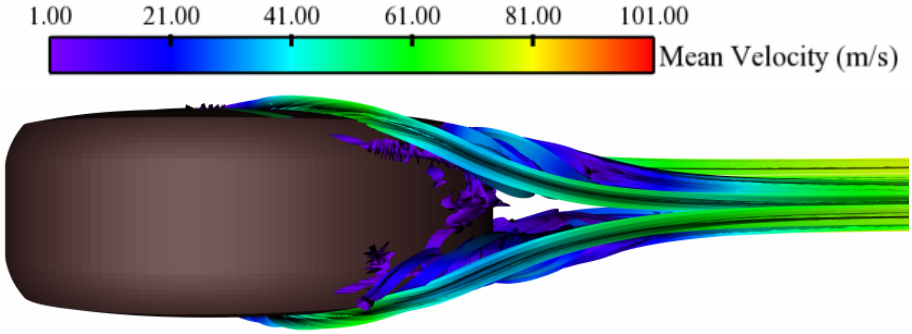

(c) View from the top.

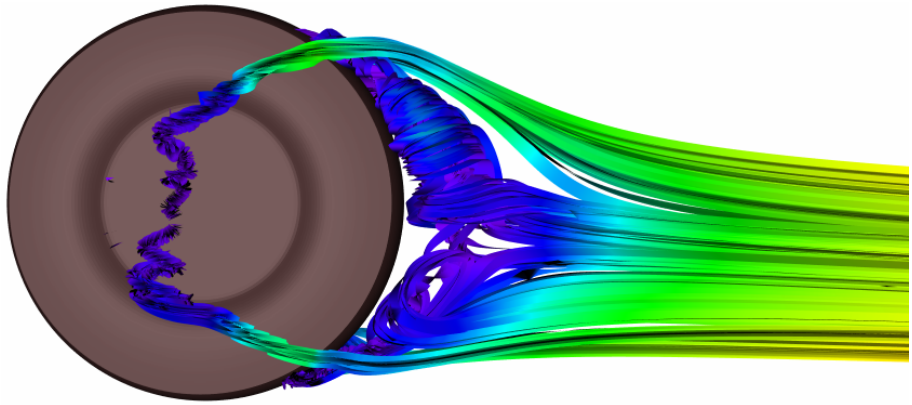

(d) View from the side.

Figure 3.34: Time-mean streamlines around the wheel, $M_\infty = 0.3$.

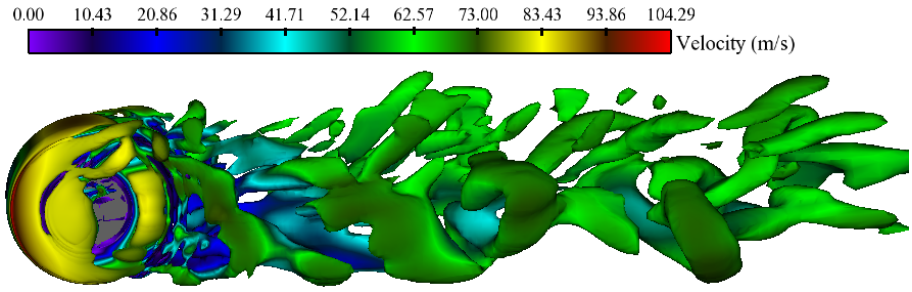

Figure 3.35: Iso-surfaces of the second invariants of velocities.

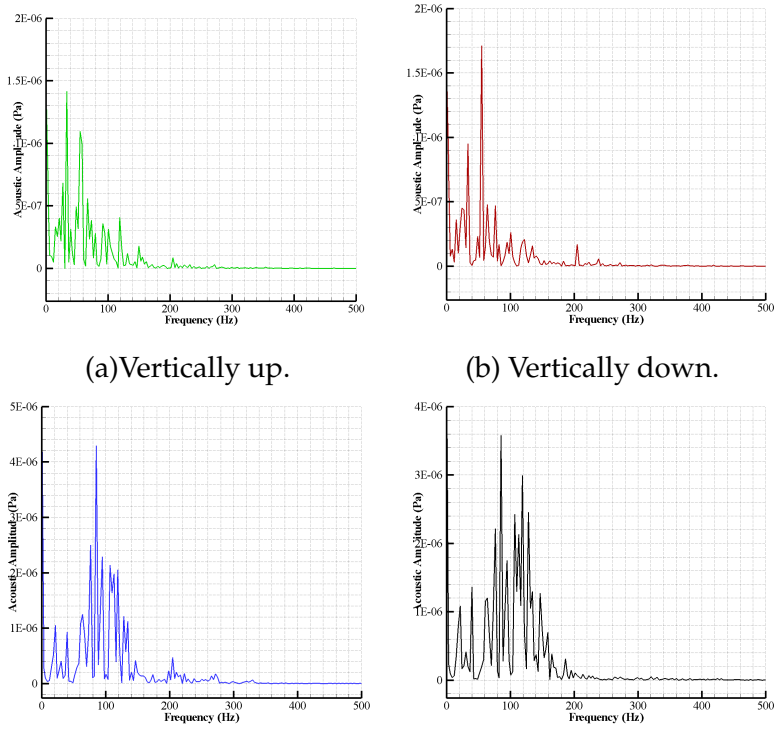

(a)Vertically up. (b) Vertically down.

(c) Upstream side. (d) Downstream side.

Figure 3.36: Farfield acoustic spectra as observed by receivers at a distance of $100m$ *from the centre of the wheel.*

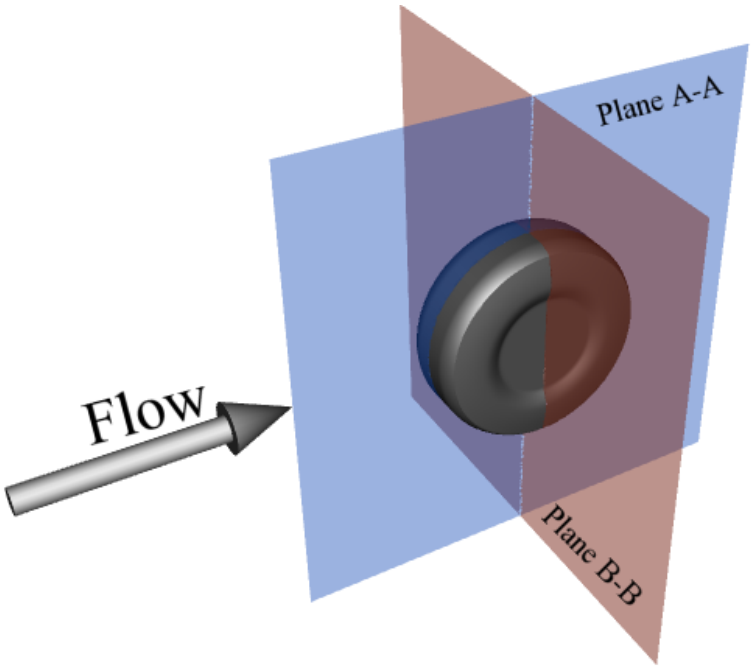

Figure 3.37: Planes used for sound directivity calculations.

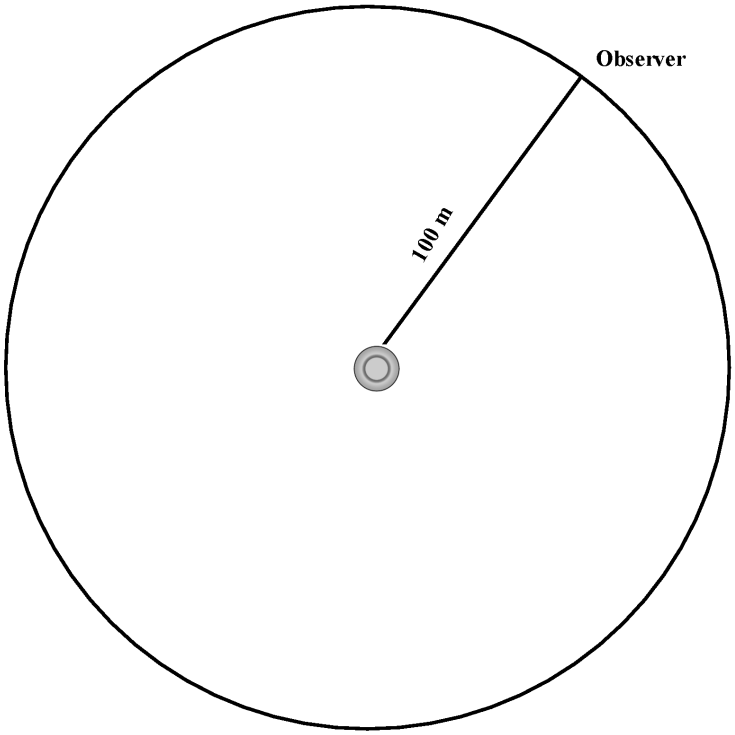

Figure 3.38: Location of observers at farfield.

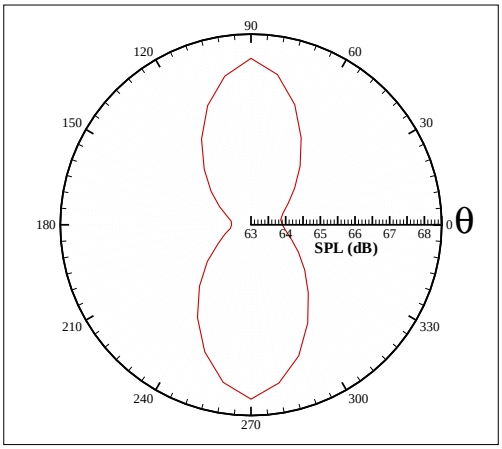

(a) Directivity on plane AA.

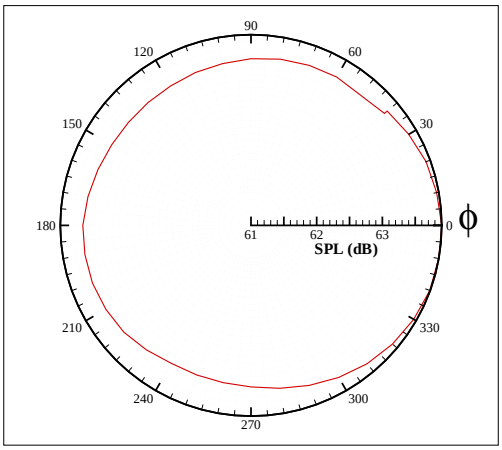

(b) Directivity on plane BB.

Figure 3.39: Sound directivities across different planes.

Chapter 4

Low-order Solver Simulations

In this chapter, the source of noise and its radiation by cavity geometries submerged in transonic turbulent flows is investigated numerically using a general purpose commercial CFD solver. Several 3D cavity geometries are considered to study the unsteady flow behaviour responsible for noise generation. The 3D geometries studied also consisted of stores in the cavity and spoilers in the upstream boundary layer.

4.1 Introduction

Cavities or surface cutouts exist commonly in aerospace applications and are also well documented in studies of aerodynamic noise. Although it is well known that cavity flows often exhibit significant three-dimensional behaviour, such phenomena have generally received little attention in the literature, and cavity flows have often been treated as two-dimensional to simplify analysis. This approach has brought significant insight into the fundamental physics of cavity flow and has resulted in the development of semi-empirical models for the prediction of the modes of oscillation in the cavities [Rossiter (1966); Heller et al. (1971); Tam & Block (1978)]. Nevertheless, experimental observations have long pointed to the presence of 3D flow with strong evidence of span-wise variations in the cavity shear layer, as well as the stretching of the recirculating flow within the cavity [Rockwell & Naudascher (1979)]. Although some might argue that such details are not vital to the prediction of the frequencies of oscillation, one should anticipate a knowledge of such flow features to be of prime importance in the understanding and prediction of the aerodynamic noise radiated from three-dimensional cavity geometries. The purpose of this chapter, therefore, is to examine the flow in a truly three-dimensional cavity geometry and investigate the nature of the three-dimensional flow features; and study its influence on the oscillation process and the nature of the radiated sound field.

4.1.1 Cavity Geometry Types

Three types of 3D geometries were considered in this investigation. The first type is a three-dimensional clean cavity, which comprises a simple rectangular cutout in an otherwise infinite plate and is therefore fully described by its length-to-depth and length-to-width ratios. The second type had stores in the cavity. The stores were either mounted

on a support strut as in the work of Stallings Jr. et al. (2002) or mounted on the cavity trailing edge as in the work of Ritchie (2005). Both types of arrangement are shown in Figure 4.1. The third type of cavity geometry had a vertical spoiler at the cavity leading edge as shown in Figure 4.2(b). All the cavity geometries investigated in this work had the L/D ratio varying between 4.0 and 6.25 and a width-to-depth (W/D) variation of 2.0 to 2.5. In these investigations the Mach number of the flow varied from 0.8 to 0.85. The cavity geometries described correspond to some of the many cases in the experimental investigations of Stallings Jr. et al. (2002), Ritchie (2005) and Geraldes (2005).

The basic design and the extent of the three-dimensional computational domain and mesh density were chosen following preliminary two-dimensional numerical simulations (see Appendix D). The computational domain extends $4L$ upstream, $5L$ downstream, and $3L$ vertically and laterally from the cavity. The overall mesh size for all the 3D cases was maintained approximately between 1.7 million cells and 2.85 million cells. Grid cells were clustered along all solid walls and in the region of the shear layer using hyperbolic-tangent distributions. At the cavity leading edge, the boundary layer is resolved with approximately 20 mesh points. In all the 3D computational results presented in this chapter, Detached-Eddy Simulation (DES) based on a one-equation model of Spalart & Allmaras (1992) has been used to complete the closure of the Navier-Stokes equations. DES is a hybrid model which behaves as a standard SA RANS model within the attached boundary layer and as a Large-Eddy Simulation (LES) Sub-Grid Scale (SGS) model in the rest of the flow. This model has been described in detail in Chapter 2.

4.2 Clean Cavity, $L/D = 4$, $W/D = 2.4$

Geometry and Flow Setup

The cavity geometry studied in this case was a 10cm long clean cavity with $L/D = 4$ and $W/D = 2.4$ (see also Figure 4.2(a)); and it had identical flow and geometrical settings to the experimental study of Geraldes (2005). For this study the Mach number of the freestream flow was maintained at 0.85. A 3D computational domain was generated using a structured meshing strategy. The non-matching grid interfacing techniques were utilized to minimize the number of grids in the structured domain. Figures 4.3, 4.4 and 4.5 show sectional views of the three-dimensional computational domain and its structured grid structure. The grid cells inside the cavity were maintained close to cubic volumes with a minimum amount of stretching (evident from the zoomed views in the figures) so that an LES-type length scale can be invoked inside the cavity. The origin of the coordinate

system is set at the cavity leading edge along the left sidewall of the domain (also shown in Figure 4.2(a)). In total, the computational domain consisted of approximately 2.6 million structured grid points. Along the inflow boundary, the two Cartesian velocity components u, v were prescribed so that the computed boundary layer just upstream of the cavity had approximately the same thickness as in the experiment [Geraldes (2005)]. All the solid surfaces (cavity walls and flat plate) were treated as adiabatic walls with a no-slip condition. The rest of the boundary faces were set as pressure farfield. The spacial discretization used was flux difference splitting based on second-order upwind (default option for compressible flow in Fluent) with a second-order central differencing applied to the modified turbulent viscosity and a second-order implicit scheme adapted for temporal discretization. Due to the transonic speed involved, a coupled solver was chosen to ensure a fully compressible solution and a constant time step of 1×10^{-5}s was maintained for the unsteady simulation.

Aerodynamic Field

Time-mean flow

The time-mean flowfields are characterized by their mean surface static pressure coefficient (C_p) distributions. The C_p plot for this case is presented in Figure 4.6 and compared with the measured data. Study of the mean C_p distribution for this case indicates that the flow belongs to the open cavity type and it is found to exhibit many of the same global open cavity flow behaviours. The time-mean flow within the cavity is dominated by a large-scale recirculating flow pattern. The location of the centre of the large structure may be identified from the trough in the mean C_p plot that is mostly evident along the cavity floor and the structure is centred downstream of the middle of the cavity (approximately at $x/L = 0.58$). The computed C_p showed some discrepancies from the experiment but the global characteristics are similar. Both the CFD and experimental C_p distributions are largely flat across the floor, typical of open cavity flows. Despite the small differences in the C_p distributions (between CFD and experiments), the internal flow structure in the cavity is largely in agreement with the experiment of Geraldes (2005).

To analyze and understand the behaviour of the mean flow inside the cavity further, a more detailed study of the flow inside the cavity using flow visualization techniques is necessary. Hence visualization of 2D sectional streamlines using LIC images [Knowles et al. (2006)] and 3D surface flow particle tracking were used. To study 3D time-mean flow features inside the cavity, vortex core locations were calculated and stream lines were released from the calculated cores. The resulting mean flow structure is presented

in Figure 4.7. In addition, sectional streamlines of the computed time-mean velocity data are visualized using LIC in Figure 4.8. Figure 4.7 reveals the presence of two contra-rotating flow structures in the upstream third of the cavity which merge to a single, large recirculation further downstream. This is also evident from the LIC image in Figure 4.8(g). These structures are described in ESDU Item 02008 [ESDU (2004)] as 'tornado-like' vortices which spiral up towards the mouth plane (i.e. the open plane) of the cavity although speculation on their subsequent movement is not given. This has been further analyzed and discussed by Atvars et al. (2009), with the aid of experiments and CFD visualization, describe that these structures are formed when the flow travelling upstream along the floor of the cavity reaches the upstream wall. The proximity of the cavity sidewall forces the flow to divert in the spanwise direction towards the centreline of the cavity. When the flow reaches the centreline plane, it meets the flow from the other side of the centreline and is forced to turn to flow downstream but is prevented from doing so by the flow travelling upstream along the cavity floor. The flow is forced to turn out towards the sidewall of the cavity which forms the vertical 'tornado-like' structures seen on the cavity floor. Results for a narrower cavity ($W/D = 1$) presented in Chapter 3 showed the presence of only one 'tornado-like' vortex. Also visible in Figure 4.7 are two vortices trailing downstream from the downstream corners of the cavity, which is consistent with the flow visualisation works of Taborda et al. (2001). The meanflow structures captured by CFD in Figure 4.8(f-h) are also in good agreement with the oil flow visualization of Taborda et al. (2001) (see Figure 4.9). Hence, the global features of the mean flowfield captured by CFD agree well with the experimental observations. The LIC images of sectional streamlines at various spanwise locations (i.e. Figures 4.8[a-e]) also clearly indicate the three-dimensionality in the time-mean flow inside the cavity. Firstly, the most noticeable three-dimensional flow feature is the variation in the position of the core of the recirculating flow across the span of the cavity. Secondly, a secondary recirculating region exists in the upstream third of the cavity for all spanwise locations except near the centreline ($z/W = 0.4$ and $z/W = 0.5$).

Time-dependent Flowfield

The unsteady flowfield was also analyzed to study the unsteady structures inside the cavity. From the CFD result, the computed flow inside the cavity was found to be highly unsteady and dominated by periodic phenomena. The unsteady features inside the cavity and the shear layer fluctuation process may be seen in Figure 4.10 which shows the time development of tubular vortical structures in terms of the iso-surfaces of the second invariant of the velocities [Joeng & Hussain (1995)] and their effect on the instability of

the shear layer. The solid red arrow represents the flow direction and the vertical arrow shows the direction of movement of the tubular structures. The presence of large-scale structures can clearly be seen from the figures. The primary effect of the 3D cavity geometry is seen to be the introduction of a warping of the vortex axis across the span of the cavity. This is partly due to the end walls retarding the growth of the vortical structures as they move downstream over the cavity. Overall, the unsteady flowfield is found to be dominated by the time-dependent behaviour of the shear layer spanning the mouth of the cavity. As the incoming boundary layer separates at the cavity leading edge a shear layer is formed. As the shear layer develops downstream, convective instabilities grow leading to the formation of vortex-like structures (see also Figure 3.29 in Chapter 3) which ultimately impinge on the downstream wall of the cavity. At the downstream end of the cavity, the interaction of the vortical structures with the cavity trailing edge generates disturbances that travel upstream along the cavity floor towards the cavity leading edge. Upon reaching the leading edge of the cavity, these tubular structures trigger instabilities in the separated shear layer completing the feedback loop. It is worth noting here that this event does not guarantee shear layer resonance. It all depends on the extent of the instability caused in the shear layer. In other words, it depends on the amount of unsteady turbulent kinetic energy the tubular structures are carrying. In Figure 4.10, the amplification of initial instability in the shear layer caused by the tubular structures are monitored (marked by blue ovals). The figure shows that the shear layer instability grows quickly resulting in the violent flapping of the shear layer as it reaches the trailing edge. It will be shown later (for the same cavity geometry but with a vertical spoiler in the upstream boundary layer) that faintly energized structures are not able to excite strong enough instabilities in the separated shear layer to develop resonance modes.

A more quantitative study of these variations may be obtained by analyzing the frequency content of the nearfield pressure time-history data using fast fourier transforms. Figure 4.11 shows the comparison between experimental and computed pressure spectra. The data correspond to sampling points located at $x/L = 0.90$ on the floor of the cavity. From the comparison, the frequency of the first resonant mode is well predicted by the computation compared to experiment although the CFD under-predicts the magnitude of the tone by $4dB$. Mode frequency predictions from the modified Rossiter equation are represented by the dashed lines. The computed second mode frequency ($1642Hz$) however is lower than the experiment. The computed second mode frequency is found to agree better with the second mode frequency predicted by the modified Rossiter equation. Also, the CFD shows the second-mode dominance whereas the first-mode is dominant in the experiment. These discrepancies may be due to the lack of sufficient knowledge of the

experimental test conditions that affect the cavity flowfield e.g. incoming boundary layer characteristics, tunnel turbulence levels, ambient density (ρ) and ambient temperature (T) (or speed of sound, a_0).

4.3 Clean Cavity, $L/D = 5$, $W/D = 2$

The second cavity case was a 16cm long clean cavity with $L/D = 5$ and $W/D = 2.0$; it had identical flow and geometrical settings to the experimental study of Ritchie (2005) (see also Atvars et al. (2009)) except that $W/D = 2.5$ in the experiment.

Geometry and Flow Setup

For this study the Mach number of the freestream flow was maintained at 0.85 consistent with the experiment [Ritchie (2005)]. The 3D computational domain was again generated using a structured meshing strategy described in the previous empty cavity case (See Section 4.2). The coordinate system and the basic grid topology has been maintained identical for all the clean cavity computational domains. The computational domain for this case consisted of approximately 2.4 million structured grid points. Along the inflow boundary, the two Cartesian velocity components u, v were prescribed using the experimental boundary layer data to emulate the boundary layer thickness upstream of the cavity leading edge measured in the experiment [Ritchie (2005)]. At the cavity leading edge, the boundary layer is resolved with approximately 20 mesh points. All the solid surfaces (cavity walls and flat plate) were treated as adiabatic walls with a no-slip condition. The rest of the boundary faces were set as pressure farfield. The spatial and temporal discretization schemes used were same as those in Section 4.2.

Time-mean flow

To study the time-mean flowfield characteristics, initially the mean surface static pressure coefficient (C_p) distributions are examined. The C_p plots for this case ($L/D = 5$, $W/D = 2$) is presented in Figure 4.12 for a number of different spanwise locations. The study of the mean C_p distribution for this case indicates that the flow belongs to the open cavity flow type and it is found to exhibit many of the same global open cavity flow features. A careful study of the mean C_p plot also found that the time-mean flowfield is not uniform across the cavity span. This can be concluded from Figure 4.12 which shows the variation of mean C_p along with experimental C_p data at floor centreline. For this case, the

centreline of the cavity does not record the greatest variation in the pressure coefficient. Instead, the greatest variation is found at a position 16.7% from the centreline. This is thought to be the result of the significant spanwise flow present in wide 3D cavities. The computed C_p showed significant discrepancies with the experiment in the rear half of the cavity. This difference however is very small, especially when compared to the difference between the CFD and the experimental cavity width. The C_p in the experiment was found to be negative for the first 60% of the cavity floor with a minimum at approximately $x/L = 0.4$. C_p then continues to rise downstream of the $x/L = 0.4$ mark, reaching a maximum value at $x/L = 0.9$ (the most downstream measurement station). The experimental C_p distribution within the cavity is typical of flows on the boundary between open and transitional-open types (see Figure 1.1). The effect of the thick boundary layer in the experiment is consistent with the observations of Plentovich (1992) and Ahuja & Mendoza (1995). In the work of Ahuja & Mendoza (1995), increasing the boundary layer thickness resulted in the disappearance of resonant modes and further increase resulted in pressure spectra of a purely broadband nature (i.e. the pressure spectrum resembled the characteristic of a closed cavity flow). This then implies that increasing the boundary layer thickness has the effect of changing the cavity flow from an open to a closed type.

As in the previous case (Section 4.2), further investigations to understand the mean flow structures inside the cavity were carried out by studying 2D sectional streamlines from LIC images and 3D surface flow visualization. The resulting mean flow structures are presented in Figures 4.13 and 4.14. As in Sec. 4.2, Figure 4.14 clearly indicates the presence of two contra-rotating flow structures in the upstream third of the cavity which merge to a single, large recirculation further downstream. This is also evident from the LIC image in Figure 4.13(g). Also visible in Figure 4.14 are two vortices trailing downstream from the downstream corners of the cavity which is again consistent with the experiment [Taborda et al. (2001)]. The CFD shows a main recirculation which is further downstream than seen in the experiments [Atvars et al. (2009)]. This may be due to the effect of the narrow cavity geometry ($W/D = 2$) compared to experiment ($W/D = 2.5$). The LIC images of sectional streamlines at various spanwise locations (i.e. Figures 4.13[a-e]) also clearly indicate the slight three-dimensionality in the time-mean flow inside the cavity.

Time-dependent flowfield

The unsteady flowfield was also analyzed to study the unsteady structures inside the cavity. From the results, the flows were found to be highly unsteady and dominated by periodic phenomena. Figure 4.15 shows the instantaneous iso-surfaces of vorticity

magnitude and the second invariant of the velocities Joeng & Hussain (1995). The presence of large-scale structures can clearly be seen from the figures. The unsteady flowfield is found to be mainly dominated by the time-dependent behaviour of the shear layer spanning the mouth of the cavity, typical of open cavity flow types. A more quantitative study of these variations may be obtained by analyzing the frequency content of the nearfield pressure time-history data using fast fourier transforms. Figure 4.16 shows the comparison between experimental and computed pressure spectra. The data correspond to sampling points located at $x/L = 0.10$ and $x/L = 0.90$ on the floor of the cavity. From the comparison, the frequency of the dominant mode is well predicted by the computation compared to experiment. But the CFD broadband noise level is found to be higher than the experiment. The reason for the higher broadband noise level is not yet known. Despite these differences, the dominant resonant mode frequencies are in good agreement with the experiment.

4.4 Clean Cavity, $L/D = 5$, $W/D = 2.5$

This cavity case had identical geometrical and flow setting to the cavity in Section 4.3 except the W/D which was set to 2.5 in line with the experiment [Ritchie (2005)]. All the boundary conditions set up were also maintained identical to those in Section 4.3.

Time-mean flow

To study the time-mean flowfield characteristics, firstly the mean surface static pressure coefficient (C_p) distributions are examined. The C_p plot for this case is presented in Figure 4.17. The mean C_p distribution indicates that the flow resembles the behaviour of transitional open cavity flows and the time-mean flow within the cavity is found to be dominated by a large-scale recirculating region. Unlike in Section 4.3, the location of the centre of the large structure (identified from the trough in the mean C_p plot along the cavity floor) is upstream of the middle of the cavity at approximately $x/L = 0.45$. The computed C_p starts positive initially but goes negative after $x/L = 0.1$ and is negative until approximately $x/L = 0.56$. This is similar to the mean flow behaviour in the experiment although the C_p in the experiment was found to be negative for the first 60% of the cavity floor with a minimum at approximately $x/L = 0.4$. However, it is worth noting that the most upstream experimental measurement station was at $x/L = 0.1$. The C_p then continues to rise downstream of the $x/L = 0.4$ mark, reaching a maximum value at $x/L = 0.9$ (the most downstream measurement station). This behaviour is thought to be due to the

thick boundary layer which was present in the experiments and is largely captured by CFD. Both the C_p distributions are typical of flows on the boundary between open and transitional-open types (see Figure 1.1 in Chapter 1). Despite small differences in the C_p distributions (between CFD and experiments), the characteristics of the C_p curves are in good agreement.

As in the previous cases, further investigations to understand the meanflow structures inside the cavity were carried out by studying 2D sectional streamlines and 3D flow visualization. The resulting mean flow structure is presented in Figure 4.18. Also, the sectional streamlines of the computed time-mean velocity data are visualized using LIC in Figure 4.19. As in the previous cases, Figure 4.18 clearly indicates the presence of two contra-rotating, "tornado-like" flow structures in the upstream third of the cavity which merge into the single, large recirculation further downstream. This is also evident from the LIC image in Figure 4.19(g). Also visible in Figure 4.18 are two vortices trailing downstream from the downstream corners of the cavity consistent with the results in Sections 4.2 and 4.3 (and also in the work of Taborda et al. (2001)). The CFD is found to have a generally good agreement with the experimental flow visualization results as shown in Figure 4.20. From the figure the location of the main recirculation from CFD is in good agreement with the oil flow visualization data at $z/W = 0.67$. Also the location of tornado vortices match well with the experimental images. Hence, overall, the global features of the meanflow are well captured by CFD with respect to the experimental observations. The LIC images of sectional streamlines at various spanwise locations (i.e. Figures 4.19[a-f]) also indicate the existence of spanwise variation in the time-mean flow inside the cavity (gradual spanwise variation seen on the location of the core of the main recirculating structure).

Time-dependent flowfield

In previous cases (Sections 4.2 and 4.3), the unsteady flowfield inside the cavity was found to be highly unsteady and dominated by periodic phenomena. Similar behaviour was observed in this case also, with a clear evidence of spanwise flow indicating three-dimensionality. The unsteady features inside the cavity and the shear layer fluctuation process may be seen in Figure 4.21 which shows the time development of tubular vortical structures and their effect on the instability of shear layer. The images are isometric views looking downstream from upstream of the leading edge. The dark solid arrow represents the flow direction and the horizontal blue arrow represents the direction of the movement of the tubular structures with time. In Figure 4.21, the main emphasis is

put on monitoring the movements of vortical structures along the cavity width with time. The unsteady flowfield can be seen to be dominated by the time-dependent behaviour of the shear layer spanning the mouth of the cavity which flaps violently. A red coloured oval is used to track the growth and movement of unsteady vortical structures with time. From the figure, the tubular structures which start at the left side are seen to move gradually towards the right with time. After a non-dimensional time of $t \times a_\infty/D = 5.0$, the structures are seen to have reached the right half of the cavity span. This clearly reaffirms the three-dimensional flow seen in the previous cases and is consistent with the results of the mean flow study. The frequency content of the nearfield pressure time-history is presented in Figure 4.22 which compares CFD and the experiment [Ritchie (2005)]. The data correspond to sampling points along the central plane at $x/L = 0.10$ and $x/L = 0.90$ on the floor of the cavity. From the plots, the frequency of the dominant mode predicted by the computation is found to agree well with experiment. The CFD result, however, is found to show a second mode dominance while the first mode is dominant in the experiment. Also the CFD broadband noise level is found to be higher than the experiment for the sampling location at $x/L = 0.10$. Despite these differences, the resonant mode frequencies are in good agreement with the experiment.

4.5 Cavity with Stores, $L/D = 5$, $W/D = 2.5$

To study the effect of the presence of missile bodies on the cavity mean and unsteady flowfields, two different configurations were simulated on the baseline geometry of Section 4.4. The first of the two configurations had a missile body whose axis was in line with the flat plate and mounted on the trailing edge of the cavity along the central plane as shown in Figure 4.1(b). The second configuration had two missiles mounted at $z/W = 0.25$ and $z/W = 0.75$ as shown in Figure 4.1(c). All the flow set up and boundary conditions were identical to those in Sections 4.3 and 4.4. A 3D computational domain based on a hybrid mesh was used, which consisted of mainly structured cells with a small number of unstructured cells to bridge the missile nose area for easier transition to a structured grid. In addition, non-matching grid interface techniques were utilized to minimize the number of cells in the structured domain. Figures 4.23(a), 4.23(b) and 4.23(c) show the sectional views of the three-dimensional computational domain in the presence of missile bodies. The origin of the coordinate system is set at the cavity leading edge along the left sidewall of the domain (identical to the clean cavity case in Section 4.4).

Time-mean flow

The C_p plots for the cavity with store cases are presented in Figure 4.24. The mean C_p distribution indicates that the flow resembles the behaviour of transitional open cavity flows and the time-mean flow within the cavity is found to be dominated by a large-scale recirculating region. Although the location of the centre of the large structure (identified from the trough in the mean C_p plot) is in the upstream half of the cavity, the result was found to have significant discrepancies from the experiment. Although the mean C_p in the experiment and CFD are negative at identical areas of the floor, the magnitudes differ. The lowest value of C_p in the experiment is -0.06 compared to -0.02 in the computed data of the two missile case. The C_p in the CFD is only just negative. The C_p in the experiment then undergoes a steep rise compared to the very shallow rise in the CFD. The reason for this discrepancy is not known.

3D mean flow streamlines and 2D sectional streamlines were also visualized to understand the nature of the mean flow in the cavity. The mean flow structures for both the cases are presented in Figure 4.25. The figure reveals that the presence of missile bodies in the cavity mouth plane reduces the spanwise flow in the cavity. The strong recirculating flow on either side of the missile however, still exists. The flow structures on either side of the missile (at least for the cavity with one missile case) are found to have similarity with flows in a narrow cavity (see also Section 3.3.2 in Chapter 3). Also, the sectional streamlines of the computed time-mean velocity data are visualized using LIC in Figures 4.26, 4.27 and 4.28. The LIC images indicate the existence of 3D flow at varying spanwise planes (Figures 4.26(a-e)). Also the images in Figure 4.28 confirm that the presence of missile in the cavity causes the mean flow in the cavity to divide in two halves. This is also evident from the streamlines in Figures 4.27. Similarly, LIC images for the cavity with two missiles are presented in Figures 4.29, 4.30 and **??**. These images also reveal that the mean flow has effectively been divided into two halves due to the presence of the missiles. The central inner span of the cavity (the region between the two missiles) is seen to record minimum amount of three dimensionality where the rolled up streamlines (from the gap between the missile and the side wall) from both sides form a curved path around the nose of the missile body and move towards downstream wall in straight line (see Figure 4.25(b)). LIC images of computed profiles on cavity floors are also compared with the oil flow visualization results from the experiment [Ritchie (2005)] in Figure 4.32. Despite the difference in the mean pressure coefficients, the meanflow structures predicted by the CFD is in good agreement with that seen in the experiment.

Time-dependent flowfield

The unsteady features inside the cavity and the shear layer fluctuation process may be seen in Figure 4.33 which shows the time development of tubular vortical structures and their effect on the instability of the shear layer. The images are isometric views looking downstream from the upstream leading edge. In Figure 4.33, the main emphasis is put on monitoring the evolution of the separated shear layer, which is divided in two halves by the missile in the middle. The unsteady flowfield can be seen to be dominated by the time-dependent behaviour of the shear layer which has been broken in two parts and both the parts travel with same speed and reach the trailing edge at the same time. Each halve of the shear layer is seen to behave as if it was a separated shear layer of a narrow cavity. A blue coloured oval is used to track the growth and movement of unsteady vortical structures with time. Also evident in the figure is the tubular structures which start at the left side are seen to move gradually towards centre of the cavity. However these structures do not cross to the right side as seen in the clean cavity case [Section 4.4]. This clearly reaffirms the fact that the three-dimensional flow is limited to each side of the missile but there is negligible activity across the centre. Similar structures were observed in the two missile case. Frequency content of the nearfield pressure time-history is presented in Figure 4.34 for the one missile case which compares CFD and the experiment. The data correspond to sampling points along the central plane at $x/L = 0.10$ and $x/L = 0.90$ on the floor of the cavity. From the plots, the frequency of the dominant mode predicted by the computation is found to agree well with experiment. The CFD result, however, is found to show the second mode dominant while the reverse is true in experiment. Also the CFD broadband noise level is found to be slightly higher than the experiment. Figure 4.35 shows the computed spectrum for the two missiles case along with the experiment. The data correspond to a sampling point along the central plane at $x/L = 0.90$ on the floor of the cavity. The CFD result shows discrepancies with the experiment in terms of the resonant mode frequency and also the magnitudes. The resonant frequencies predicted by the CFD are lower than the experiment.

4.6 Clean Cavity (and Cavity with Store), $L/D = 5.42$, $W/D = 2$

The cavity considered in this case was 12.2cm deep with an L/D of 5.42 and W/D of 2.0. A further investigation was also carried out with a missile body in the cavity. The missile body was mounted on a support strut as shown in Figure 4.1(a). These cases correspond to

some of the many cases in the experimental investigation by Stallings Jr. et al. (2002) and have comparatively thinner incoming boundary layer than those investigated previously (see Sections 4.24.3 and 4.4). Also, the store is mounted on a support strut unlike in Section 4.5. These cases were, therefore, considered to investigate the effect of thin boundary layers and also to study the possible changes in flow characteristics due to strut mounted store. The flow conditions for these cases also correspond to a subset of those investigated by Stallings *et al*.

Time-mean flow

As in the previous cases, the characteristics of the time-mean flowfields were analyzed by studying the mean surface static pressure distributions. The mean C_p distributions for the clean cavity and the cavity-with-store cases are plotted in Figure 4.36. The flow conditions were set to match the experimental study of Stallings Jr. et al. (2002). The study of the mean C_p indicated that the computed C_p was initially positive for the first 17% of the cavity floor. It was negative until $x/L \approx 0.5$ with a minimum at approximately $x/L = 0.5$. The C_p then continued to rise downstream of $x/L = 0.5$, reaching a maximum value at the cavity trailing edge. This behaviour was present in both the computed cases. The influence of the presence of the store in the cavity on the static pressure distributions may be seen in terms of an increase in pressure along the cavity floor and a decrease in the maximum pressure observed along the aft wall of the cavity. In both the cases the point of maximum pressure is seen to lie at the rear end of the floor. In the experiments, however, the C_p is found to have a marginally negative value at the upstream end (first measurement was at $x/L = 0.046$) and the pressure continues to drop until approximately $x/L = 0.45$. The C_p, then, continues to rise downstream of $x/L = 0.45$, reaching a maximum value at the cavity trailing edge. From Figure 4.36, it can be seen that there is a negligible effect on the mean C_p due to the presence of the store in the front half of the cavity length. This is true for both computed and experimental results. The computed results over-predict the experiment by a C_p of no more than 0.025 in the front half. The rear half of the cavity shows a small effect on the C_p distribution due to the presence of the store. The computed result is found to slightly over-predict the experiment. Despite the discrepancy, the computed mean flowfield has captured the essential mean flow behaviour (i.e. the curves have similar slopes). The behaviour of both the computed as well as experimental cavity floor C_p distributions suggests that the flow shares similarity with flows on the boundary between open and transitional-open types.

Figures 4.37 and 4.38 show the time-mean flowfield for the clean cavity. These images

also reaffirm most of the global flow features observed in the previous cases. Figure 4.38 and the LIC image in Figure 4.37(g) reveal the presence of two 'tornado-like' structures in the upstream third of the cavity which merge to a single, large recirculation further downstream. A third recirculating region is found to exist in the downstream end of the main recirculating region for this case from Figure 4.37. The LIC images at various spanwise locations (i.e. Figures 4.37[a-e]) also reveal the three-dimensionality in the time-mean flow inside the cavity. Both the variation in the position of the core of the recirculating structure across the span of the cavity and the appearance of a secondary recirculating region upstream of the main recirculation is evident for all spanwise locations except $z/W = 0.4$ and $z/W = 0.5$.

Time-mean flowfields were also visualised for the cavity-with-store case to understand the time development of the mean flow due to the presence of a store. Figures 4.39 and 4.40 show the state of mean flow features for this case. Most of the global flow features observed in the clean cavity case are seen to exist in this case. However, some noticeable differences can also be seen after careful study of the images. Although Figures 4.40 and the LIC image in Figure 4.39(j) hint at the presence of two recirculating structures on either side of supporting strut upstream of the cavity, these structures are very weak in comparison to the structures seen in Figures 4.38 and 4.37(g). The presence of two strong 'tornado-like' structures, however, is clearly evident in Figure 4.39(g) which is a section view at half the cavity depth. This can be further clarified with the aid of a description of the formation of these structures by Atvars et al. (2009). When the flow travelling upstream along the floor reaches the upstream wall of the cavity, the proximity of the cavity sidewall forces it to divert in the spanwise direction towards the centreline. On reaching the centreline plane, it meets the flow from the other side of the centreline and is forced to turn to flow downstream. Unlike in the clean cavity case, the flow travelling upstream along the cavity floor encounters the flat base of the supporting strut. Hence the downstream travelling flow is able to travel without forming a complete recirculation. At a plane parallel to the floor above the support base, however, the strut cross section is smaller and is more slender. This allows the flow travelling upstream to continue to a large extent, thereby, forcing the downstream travelling flow to turn in a vertical spiral. This explains the reappearance of the 'tornado-like' structures in Figure 4.39(g). Also the variation in the position of the core of the recirculating structure across the span of the cavity is less noticeable from the LIC images in Figure 4.39 (although not immediately noticeable, the centre of the main recirculating core does not shift compared to the Figures 4.37[a-e]). This indicates that the spanwise flow structure off the centre plane shows fewer 3D effects compared to the clean cavity case. However, a secondary recirculating region

upstream of the main recirculation is found to exist at various spanwise locations except $z/W = 0.4$ and $z/W = 0.5$ consistent with the previous observations. The upstream view of the cavity trailing edge in Figure 4.40 reveals that the streamlines are seen to have divided due to the presence of the store and the supporting strut. The upstream view from the rear of the cavity (see Figure 4.40(b)) clearly shows the streamlines rolling up in two halves on either side of the store body.

Time-dependent flowfield

Unsteady flowfields were analyzed for the both clean cavity and cavity-with-store cases to study the unsteady structures inside the cavity and the effects of the store. Figures 4.41(a) and 4.41(b) show the iso-surfaces of the vorticity magnitude for the clean cavity and the cavity with the store respectively. From the figures, the warping of the vorticity iso-surface can be seen to be enhanced (shear layer warping on both sides of the store) due to the presence of the store. As the vortical structures in these regions reach the trailing edge, the vortex axis is aligned with the streamwise direction. Then the 3D flow in the end wall regions leads to the formation of thin streamwise vortices, which is also clear from the study of time-mean streamlines in Figures 4.40 (also Figures 4.14 and 4.38).

Figures 4.42 and 4.43 show the frequency content of the pressure signals for both the cases. Figure 4.44 compares the pressure spectra from the two cases at two different positions along the cavity centreline. Predicted mode frequencies from the two cases along with the calculation using the modified Rossiter formula are presented in Table 4.2. From the results, the first mode frequency from the clean cavity is found to agree well with the modified Rossiter formula. The dominant mode, however, is not the first mode and the dominant peak occurs at 212 Hz. This frequency is significantly lower compared to the second mode of 279 Hz predicted by the modified Rossiter formula. Higher order modes are absent in the computed spectrum. The cavity-with-store case, however, has many peaks in the pressure spectrum and the corresponding mode frequencies agree reasonably well with the Rossiter formula. Five Rossiter modes are clearly present for the store case in contrast to the clean cavity which only had two modes (clearly identifiable) present. High speed cavity flows are characterised by the existence of more than a single dominant mode and these multiple modes are found to couple non-linearly resulting in amplitude modulations at different frequencies. This is most probable for the clean cavity because spanwise flow fluctuations (i.e in the z-axis direction) are dominant compared to the store case which has less pronounced spanwise flow. Hence a coupling between the lateral and longitudinal instabilities may have resulted in a dominant peak (low frequency

modulation) at 212 Hz for the clean cavity case. This is not represented by the Rossiter formula, which is based on a 2D acoustic feedback mechanism. The flow behaviour and parameters which leads to this type of coupling is not clear. This, however, is thought to be due to the thin incoming boundary layer upstream of the leading edge which results in thin separated shear layer. The clean cavity results in the earlier sections (see Sections 4.2, 4.3 and 4.4) do not exhibit this behaviour, which may be due to the relatively thick incoming boundary layer present in those cases which result in a relatively 'stiff' separated shear layer). The thin separated shear layer are found to undergo more enhanced spanwise flapping than those seen in thick boundary layer studies.

The mean flowfield visualisation in the time-mean flow study clearly showed that the flowfield was divided in two halves (for the cavity-with-store case) with little evidence of flow across the store and supporting strut. It is suggested that this blockage effect of store and strut on the spanwise flow may have reduced the possibility of spanwise and streamwise flow fluctuations undergoing non-linear coupling to result in amplitude modulations. This may be the reason for the co-existence of multiple modes without coupling between them.

Table 4.1: Comparison of mode frequencies (Hz) for cavity with $L/D = 5.42$, $W/D = 2$ and $M_\infty = 0.80$

mode	Clean cavity	Cavity with store	Modified Rossiter Formula
1	114	145	111.4
2	212	276.6	279
3	–	424	445
4	–	618	615
5	–	765	782

4.7 Clean Cavity (and Cavity with Store), $L/D = 6.25$, $W/D = 2$

The last two cavity cases considered were 12.2cm deep with an L/D of 6.25 and W/D of 2.0, one of the two had a store in the cavity. The rear end of the store in the previous case (Section 4.6) was very close to the cavity trailing edge. This case, therefore, was considered to study the flow features resulting from increased gap between the rear of the store and the cavity trailing edge. The geometry and flow conditions in these cases also correspond to some of the many cases in the experimental investigation by Stallings Jr. et al. (2002).

Time-mean flow

The mean C_p distributions are plotted for both the cases in Figure 4.45 to analyze the meanflow characteristics. As in the previous cases (Section 4.6), it can be seen that there is negligible effect on mean C_p due to the presence of the store in the front part of the cavity floor until $x/L = 0.2$. Both computed and experimental data show that the C_p starts with a marginally negative value at the upstream end (first floor measurement point was at $x/L = 0.039$ in experiment). The rear half of the cavity shows very little effect on the C_p plot due to the presence of store, in either the experiment or CFD. A reasonable agreement between the computed and experimental mean flowfield is evident from the comparison although, as in Section 4.6, the CFD has generally predicted higher C_p levels than seen experimentally. The behaviour of the computed as well as experimental cavity floor C_p distributions showed that the flow shared similarity with the transitional-closed type.

Figures 4.46 and 4.47 show the state of the time-mean flowfield for both the cases. These images also reaffirm most of the global mean flow features observed in the previous cases (see Sections 4.3 and 4.6). As before, Figures 4.47(a) and the LIC image in Figure 4.46(e) reveal the presence of two 'tornado-like' structures in the upstream third of the cavity which merge to a single, large recirculation further downstream. A third recirculating region is found to exist in the downstream end of the main recirculating region for this case from Figure 4.46. The LIC images at various spanwise locations (i.e. Figures 4.46[a-c]) also reveal the three-dimensionality inside the cavity. The cavity-with-store case also revealed similar mean flow features which were observed in the previous case (see Section 4.6). As in Section 4.6, the upstream view of the cavity trailing edge in Figure 4.47(d) reveals that the streamlines are seen to have divided due to the presence of the store and the supporting strut.

Time-dependent flowfield

Figure 4.48 shows the frequency content of the pressure signals for these cases at one point on the cavity floor centreline, near the upstream wall. Predicted mode frequencies from the two cases are presented in Table 4.2. As in the previous two cases, the first mode frequency from the clean cavity case is found to agree well with modified Rossiter formula (although a difference of 8 Hz in the case of clean cavity). The first mode, however, is not the dominant mode and the dominant peak occurs at 268 Hz. This frequency is different to the second mode of 234 Hz predicted by the modified Rossiter formula. Higher order modes are absent in the computed spectra. The cavity-with-store case, however,

has many peaks in the pressure spectra (consistent with the observations in Section 4.6) and the corresponding mode frequencies show reasonable agreement with the Rossiter formula. Up to five Rossiter modes are clearly present for the store case in contrast to the clean cavity which only had the first and second modes present. These observations are consistent with the results in Section 4.6. The discrepancies on the predicted modes between the CFD and the modified Rossiter formula is greater than those observed in Section 4.6 which may be due to the effect of the increased gap between the base of the store and the cavity downstream wall on the unsteady flowfield.

Table 4.2: Comparison of mode frequencies (Hz) for cavity with $L/D = 6.25$, $W/D = 2$ and $M_\infty = 0.80$

mode	Clean cavity	Cavity with store	Modified Rossiter Formula
1	97	91.7	89
2	268	214.0	234
3	–	360.7	380
4	–	477.0	525
5	–	617.0	670

4.8 Cavity with Spoiler, $L/D = 4$, $W/D = 2.4$

In this section, computational results obtained to study the flow control effects of a passive device (a serrated spoiler in this case) are presented. The main objective of the spoiler is to introduce disturbances in the shear layer in order to disrupt the resonant mechanism that sustains the cavity oscillations. Spoilers have been extensively used as a means of reducing the tones produced by cavities, however the detailed flow physics behind the tone suppression effects of these are not well understood. The main purpose of this section, therefore, is to study and describe the flow features inside the cavities in the presence of a spoiler in the upstream boundary layer and the subsequent reasons behind the tone suppression.

Geometry and Flow Setup

The cavity geometry studied in this case is exactly same as the cavity in Section 4.2, the only difference being the presence of a serrated spoiler immediately upstream of the cavity leading edge. The spoiler geometry is a slightly modified version of one of the sawtooth spoilers used by Geraldes (2005) in his experiments and, therefore, it had identical flow

conditions to the experiment. The spoiler geometry used here is a modified version of the coarsest (also termed the "large" spoiler) of the three spoiler geometries in the experiments of Geraldes (2005). Each of the triangular elements in the experiment measured 7.375*mm* wide and 3.6875*mm* high. In this study, the spoiler geometry was modified to facilitate good quality structured grid generation in the upstream boundary layer where the spoiler is located. To resolve the boundary layer correctly, structured grid cells with low skewness angles are essential and this is crucial for accurate prediction of the flowfield inside the cavity. To ensure consistency with the experiment, the sawtooth profile was modelled as a series of trapezia of identical heights and surface area. The only variable was then the base width. The spoiler profiles are shown in Figure 4.49. The 3D computational domain was generated using a structured meshing strategy. The non-matching grid interface techniques were utilized to minimize the the number of grids in the structured domain. Figures 4.50, 4.51 and 4.52 show sectional views of the three-dimensional computational domain and its structured grid structure. The zoomed in views clearly show the grid topology used to generate the structured cells around the spoiler profile. The grid cells inside the cavity were maintained close to cubical volumes with a minimum amount of stretching (evident from the zoomed views in the figures) to ensure that the LES-type length scale is activated inside the cavity. The origin of the coordinate system is set at the cavity leading edge along the left sidewall of the domain (also shown in Figure 4.2(b)). In total, the computational domain consisted of approximately 2.79 million structured cells. Along the inflow boundary, the two Cartesian velocity components u, v were prescribed so that the computed boundary layer just upstream of the cavity had approximately the same thickness as in the experiment of Geraldes (2005).

Aerodynamic Field

Time-mean flow

The effect of spoilers on the cavity mean flowfields are investigated first by studying the mean surface static pressure coefficient (C_p) distributions and then by mean flow visualization. The C_p plots for the clean cavity and cavity with spoiler cases are presented in Figure 4.53, which clearly indicates the heavy pressure loss due to the presence of the spoiler. The mean C_p distribution is negative for the most of the cavity length, positive only after $x/L = 0.93$. The dissipation (at Kolmogorov scale) and self-regeneration of turbulent kinetic energy all takes place in the boundary layer and the spoiler acts as an external device that extracts energy from the flow resulting in the heavy pressure loss. To analyze and understand the behaviour of the mean flow inside the cavity further, a

more detailed study of the flow behaviour and structure inside the cavity was performed using flow visualization techniques. The resulting mean flow structure is shown in Figure 4.54. The mean flow streamlines do not show any evidence of spanwise flow. Also the 'tornado-like' vortices normally seen in empty cavities are absent. The 'tornado-like' vortices were described as the mean flow path of unsteady tubular structures responsible for sustaining resonance mechanisms in earlier sections. It was also highlighted (in Section 4.2) that the sustained resonant fluctuation of the shear layer was dependant on the amount of energy the vortical structures were carrying. The dissipation of turbulent kinetic energy by the spoiler means that the structures are weakly energized and therefore are unable to sustain the spanwise flow. This also explains the absence of 'tornado-like' vortices. Also absent in Figure 4.54(b) are the two vortices trailing downstream from the downstream corners of the cavity which is normally found in clean cavities. Instead, uniformly spaced streamwise vortices are seen to exit from the trailing wall. This also reinforces the statement that the flow inside the cavity is unable to sustain 3D behaviour and resonant modes due to extraction of energy by the spoiler. This will be explained further while analyzing the unsteady results. In addition, sectional streamlines of the computed time-mean velocity data are visualized using LIC in Figure 4.55. The sectional streamlines at various spanwise locations (i.e. Figures 4.55[b-f]) also indicate that the spanwise flow is not present. The position of the core of the recirculating region across the span of the cavity is approximately constant including the secondary recirculating region which exists in the upstream third of the cavity for all spanwise locations. The main feature of the mean flow pattern on the cavity floor is also consistent with the oil flow visualization of Geraldes (2005), who observed a massive separation region located in the region of $x/L = 0.25$ to 0.3 where all the streamlines converge (in the CFD, streamlines are seen to converge approximately at $x/L = 0.3$).

Time-dependent Flowfield

The unsteady flowfield was also analyzed to study the effect of the spoiler on the flow oscillations. From the result, the computed flow inside the cavity was found to be highly unsteady and dominated by periodic phenomena. The unsteady features inside the cavity and the shear layer fluctuation process may be seen in Figure 4.56 which shows the time development of tubular vortical structures and their effect on the instability of the shear layer. The solid red arrow represents the flow direction and the vertical arrow shows the direction of movement of the tubular structures. The shear layer spanning the cavity width is found to be more stable in this case. To explain this, first the origin of spanwise fluctuations in a 3D clean cavity needs to be explained. The shear layer in clean cavities

undergoes warping which is partly due to the slowing down of the flow by the side walls. But the main reason can be described as follows.

The wall shear stress due to the three-dimensional flat plate boundary layer upstream of the leading edge of a 3D cavity results in a component of viscous force in the spanwise direction. When the flow separates at the cavity leading edge, this spanwise force acts as an initial trigger for the spanwise oscillation of the separated shear layer. The oscillation gets energized by the presence of unsteady turbulent energy in the flow. In the case of the spoiler, however, the spoiler flowfield acts as a barrier against the spanwise instability. In addition, the loss of turbulent kinetic energy due to the presence of the spoiler means the shear layer instabilities do not get enough energy to amplify. This is thought to be the reason for the stable separated shear layer. The tubular structures are seen to arrive at the cavity leading edge in Figure 4.56 but these structures do not have sufficient energy to cause the violent flapping of the streaks of the separated shear layer. Therefore the sustained fluctuation of the shear layer does not occur. In other words, the resonant modes are absent. Frequency contents of the nearfield unsteady pressure signal was extracted using fast fourier transforms for comparison with experiment. The resulting spectra are shown in Figure 4.57. From the figure, the CFD result is found to record the complete suppression of the dominant tones in the presence of the spoiler, consistent with the experiment. The computed broadband noise level has some discrepancies with the experiment which may be due to the lack of sufficient knowledge of the experimental test conditions that affect the cavity flowfield e.g. incoming boundary layer characteristics, tunnel turbulence levels, ambient density (ρ) and ambient temperature (T) (or speed of sound, a_0). Overall, the computed result is found to capture the global characteristics well when compared to experiment.

4.9 Summary

This chapter presented the results of computational studies in 3D cavity geometries at transonic speeds using the commercial CFD solver, Fluent. Various 3D cavity geometries were considered which also consisted of stores in the cavity and spoilers in the upstream boundary layer. The CFD results for all the empty cavity cases showed the presence of a strong oscillation feedback mechanism. The overall effect of the presence of a store in the cavity was found to be to divide the cavity flow such that the resulting flowfield behaves similarly to two narrow cavity flowfields. The CFD results for a cavity with a spoiler showed the complete suppression of resonant modes, consistent with the experiment. The results indicated the spoiler to act as an energy-extracting device, thus dissipating

the turbulent energy from the approaching boundary layer. This then was found to reduce the widely-occurring phenomenon in clean cavities, of cross-stream warping of transverse vortical structures in the free shear layer.

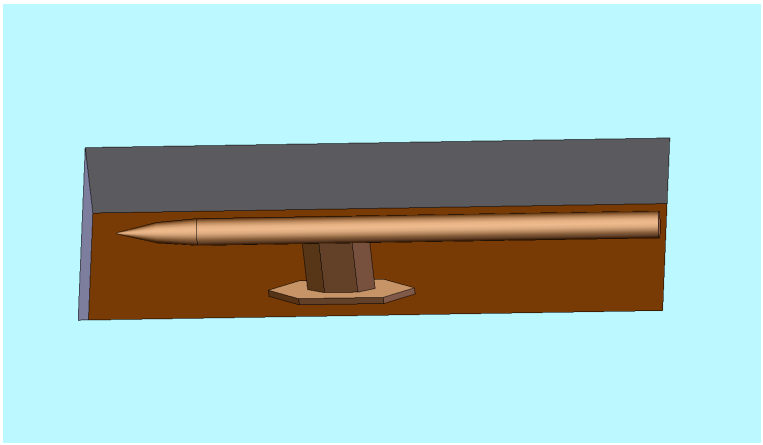

(a)Missile mounted on a support strut.

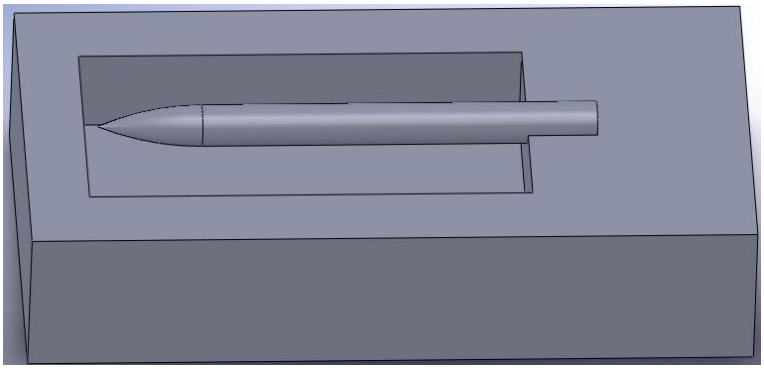

(b)Missile mounted on cavity trailing edge.

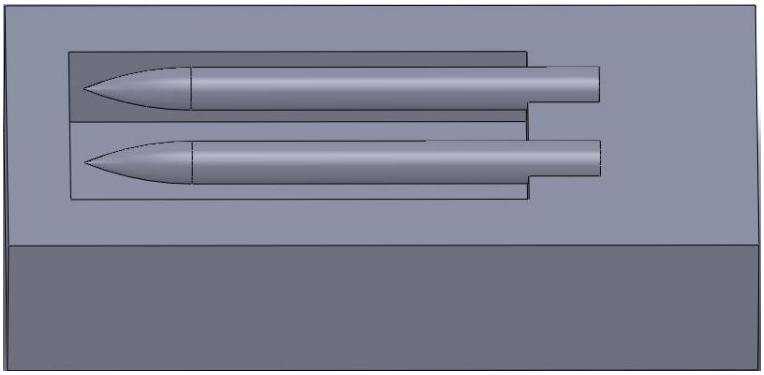

(c) Missiles (Two) mounted on cavity trailing edge.

Figure 4.1: Isometric views of the stores in cavity.

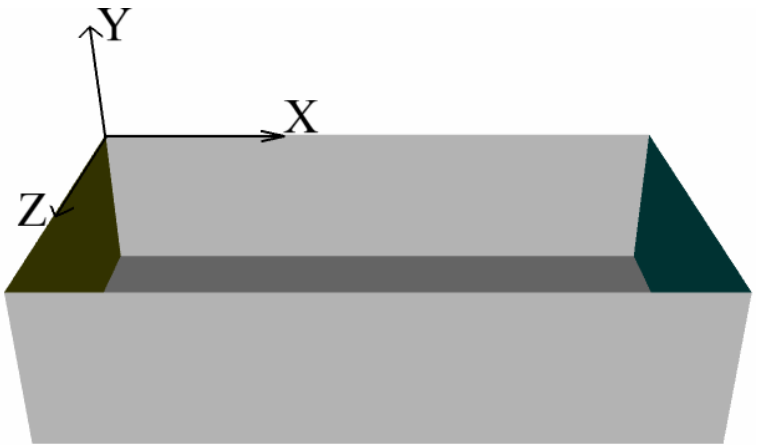

(a)Clean Cavity.

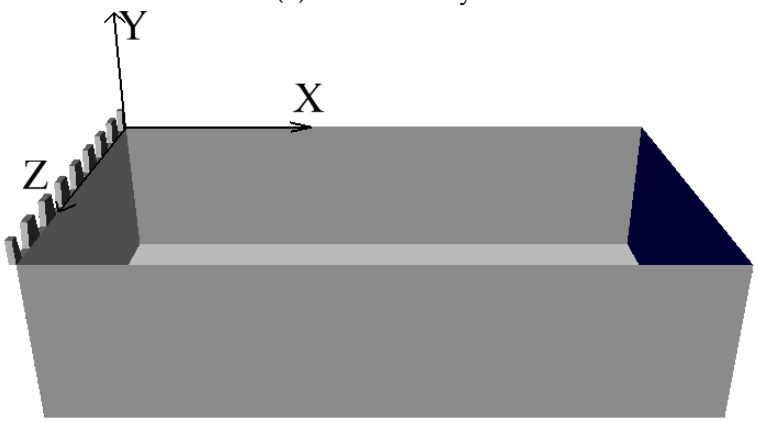

(b)Cavity with Spoiler.

Figure 4.2: Isometric views of the clean cavity and cavity with spoiler.

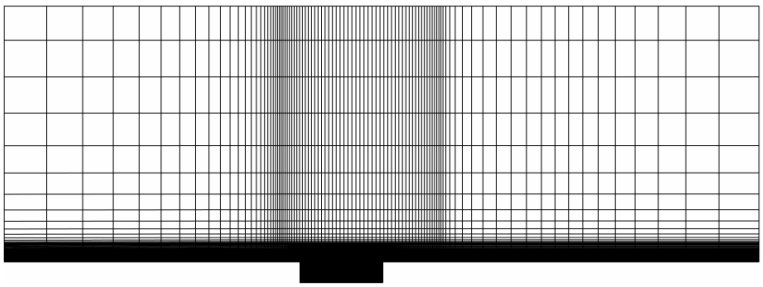

(a) Section view of grid in empty cavity.

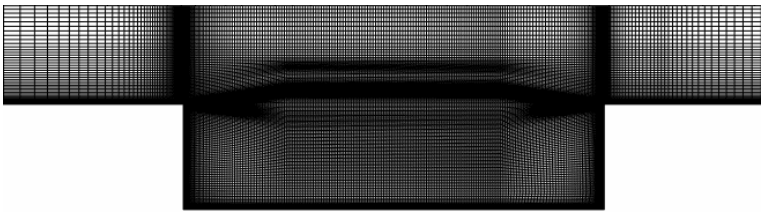

(b) Section view of grid (zoomed in).

Figure 4.3: Structured grid distribution across XY-plane.

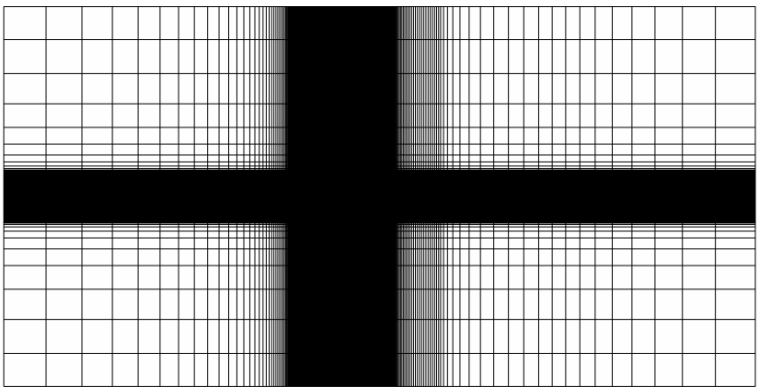

(a) Section view of grid in empty cavity.

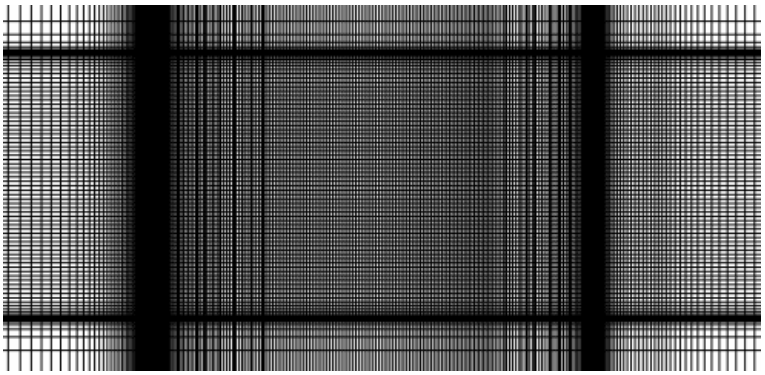

(b) Section view of grid (zoomed in).

Figure 4.4: Structured grid distribution across XZ-plane.

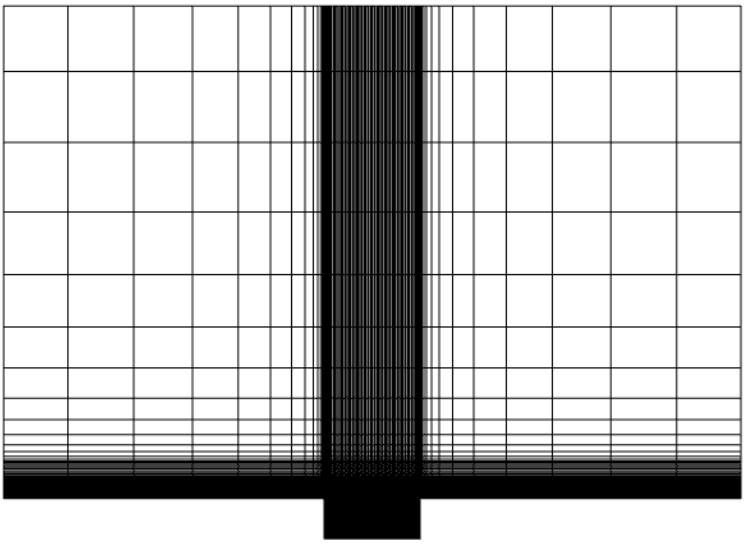

(c) Section view of grid in empty cavity.

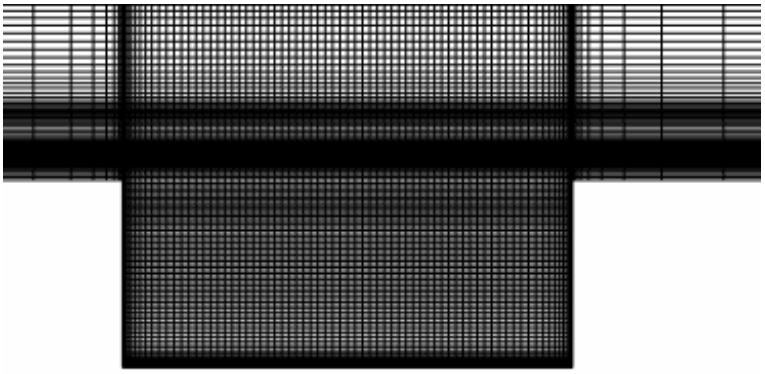

(d) Section view of grid (zoomed in).

Figure 4.5: Structured grid distribution across YZ-plane.

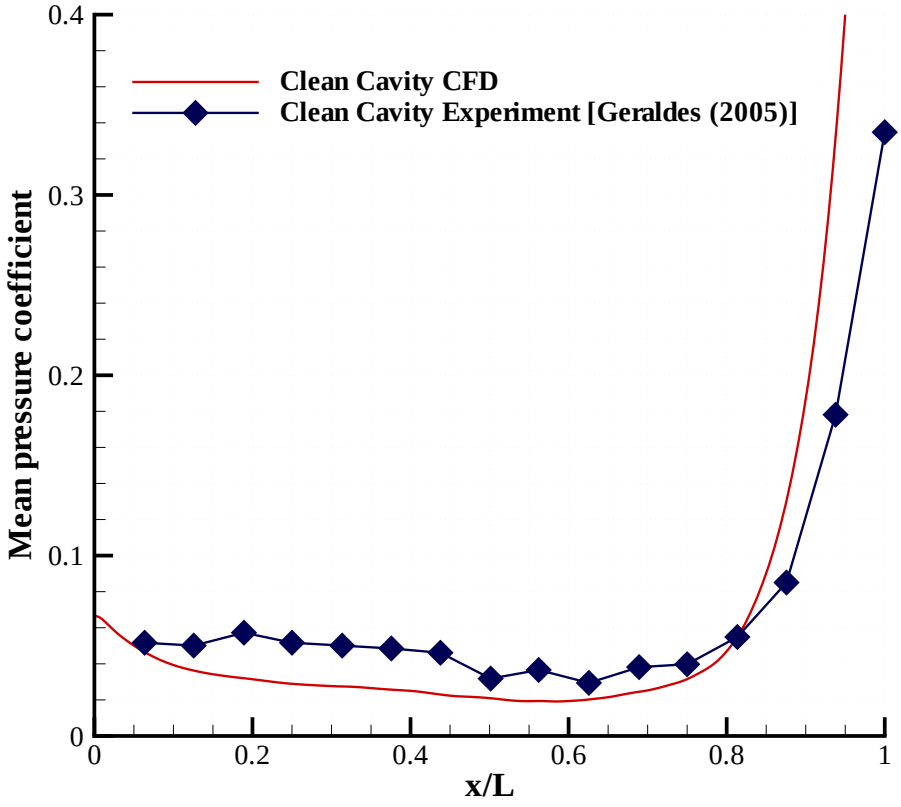

Figure 4.6: Centre line mean C_p along the cavity floor, $L/D = 4$ and $W/D = 2.4$.

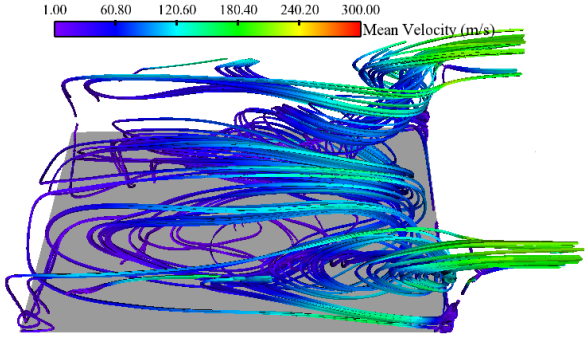

(a) 'Tornado-like' vortices in the cavity.

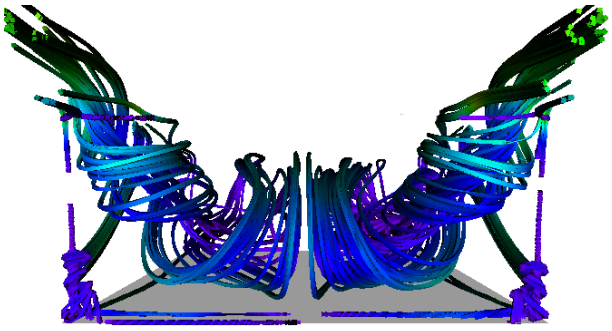

(b) View from the cavity rear wall.

Figure 4.7: Time-mean streamlines for 3D cavity, $L/D = 4$*,* $W/D = 2.4$ *and* $M_\infty = 0.85$*.*

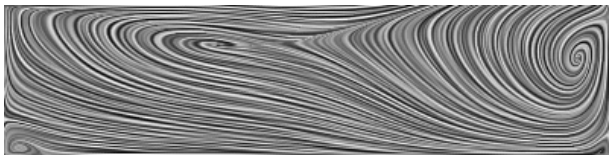

(a) Time mean streamlines in x-y plane at $z/W = 0.1$

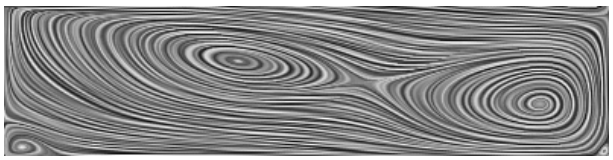

(b) Time mean streamlines in x-y plane at $z/W = 0.2$

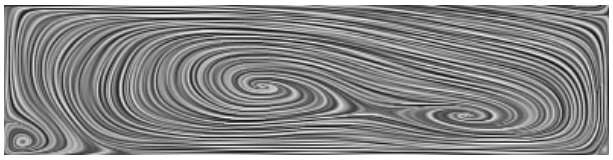

(c) Time mean streamlines in x-y plane at $z/W = 0.3$

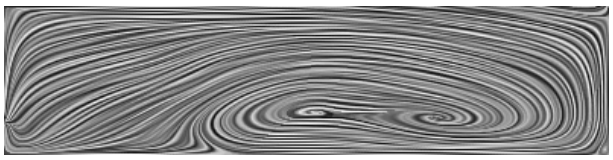

(d) Time mean streamlines in x-y plane at $z/W = 0.4$

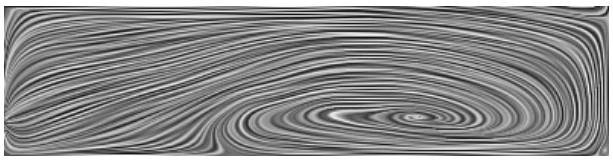

(e) Time mean streamlines in x-y plane at $z/W = 0.5$

(f) Upstream wall.

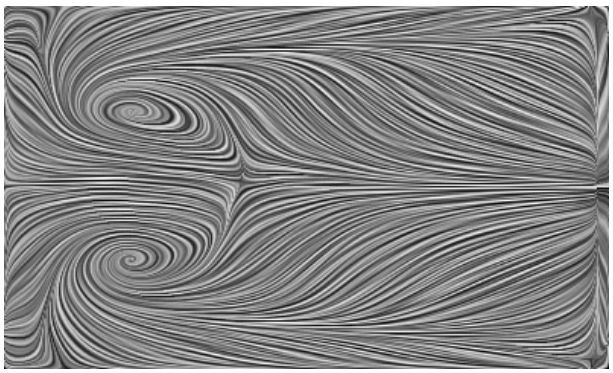

(g) Cavity Floor.

(h) Downstream wall.

Figure 4.8: Mean flow map for clean cavity using Line Integral Convolution, $L/D = 4$, $W/D = 2.4$ and $M_\infty = 0.85$.

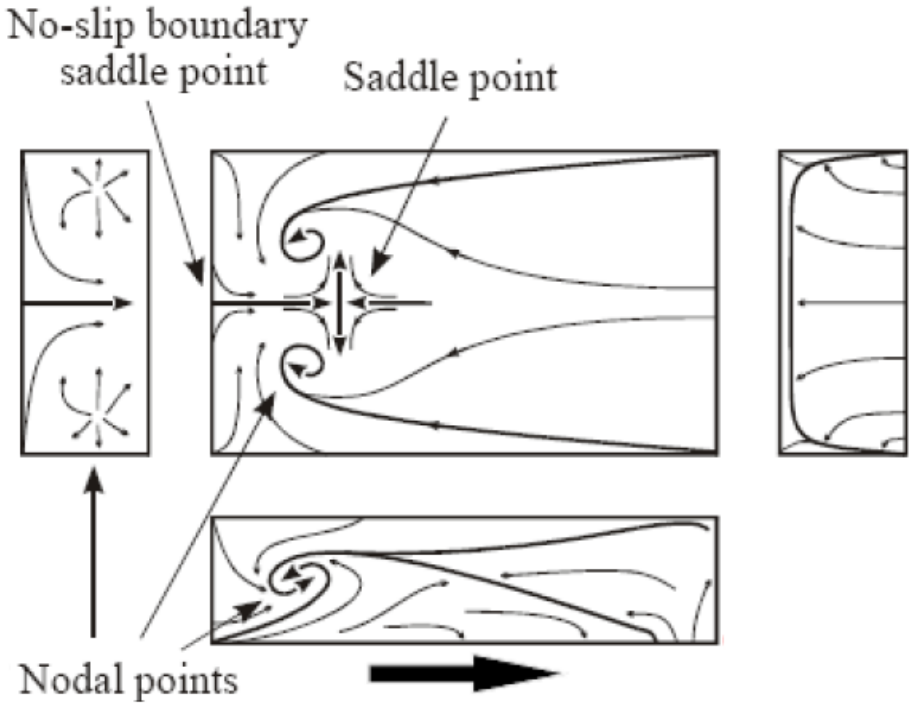

Figure 4.9: Oil flow visualization for an L/D=4 cavity [Taborda et al. (2001)].

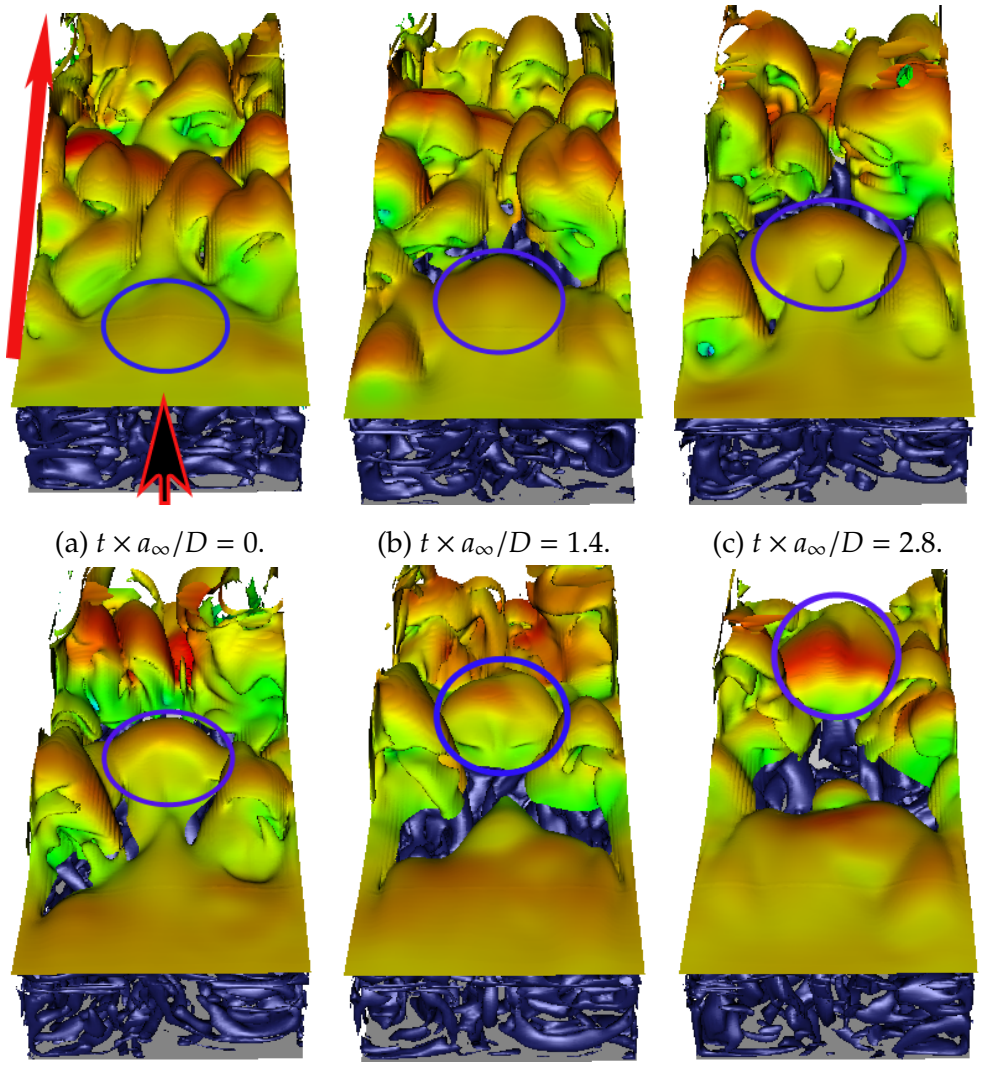

(a) $t \times a_\infty/D = 0$. (b) $t \times a_\infty/D = 1.4$. (c) $t \times a_\infty/D = 2.8$.

(c) $t \times a_\infty/D = 4.2$. (c) $t \times a_\infty/D = 5.6$. (c) $t \times a_\infty/D = 7.0$.

Figure 4.10: Shear layer vortex evolution over one cycle of oscillation: iso-contours of the Q-criterion and vorticity sheet, $L/D = 4$ and $W/D = 2.4$; $M_\infty = 0.85$.

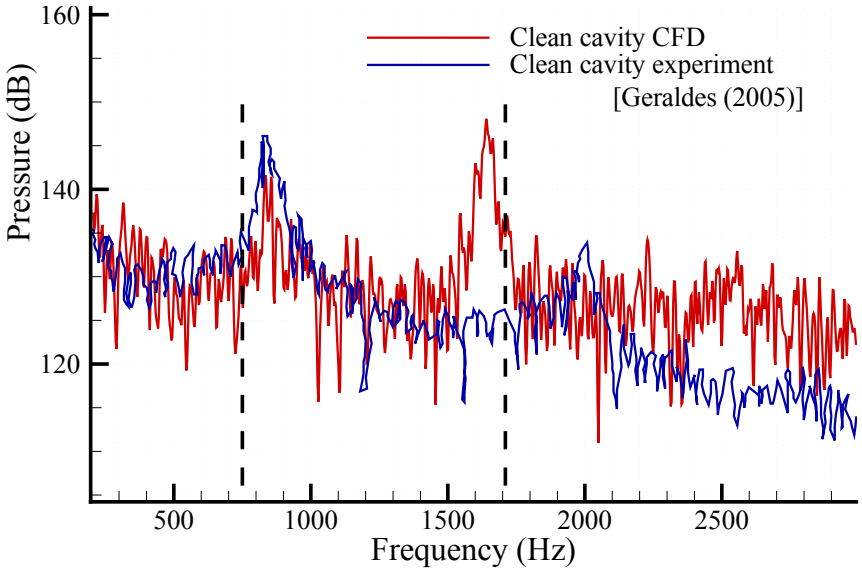

Figure 4.11: Pressure spectra at floor centreline, $x/L = 0.9$.

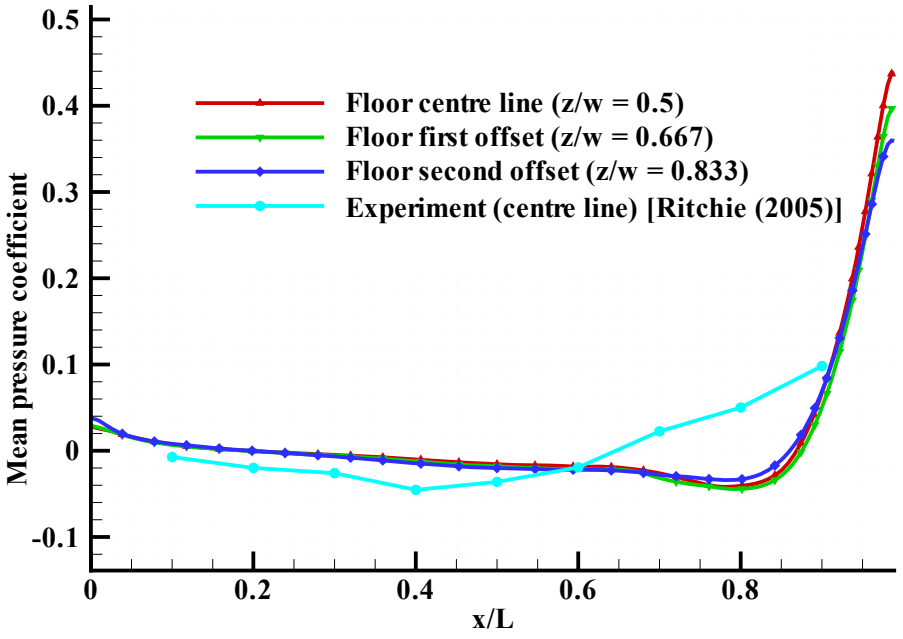

Figure 4.12: Mean C_p along varying spanwise locations, $L/D = 5$, $W/D = 2$ and $M_\infty = 0.85$.

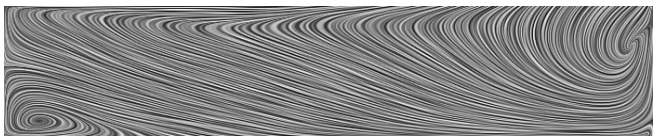

(a) Time mean streamlines in x-y plane at $z/W = 0.01$

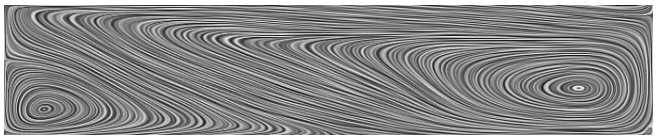

(b) Time mean streamlines in x-y plane at $z/W = 0.2$

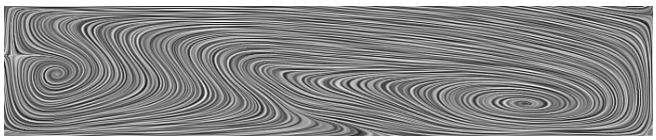

(c) Time mean streamlines in x-y plane at $z/W = 0.3$

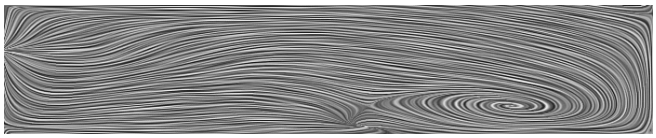

(d) Time mean streamlines in x-y plane at $z/W = 0.4$

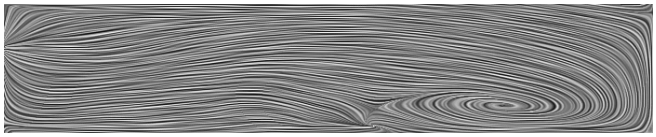

(e) Time mean streamlines in x-y plane at $z/W = 0.5$

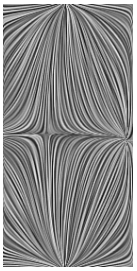

(f) Upstream wall.

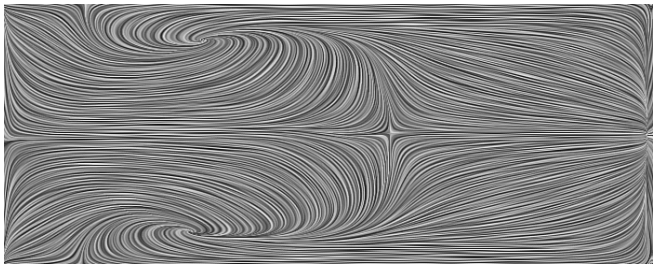

(g) Cavity Floor.

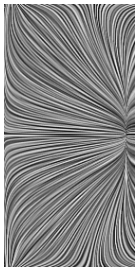

(h) Downstream wall.

Figure 4.13: Mean flow map in cavity using Line Integral Convolution, $L/D = 5$, $W/D = 2$ and $M_\infty = 0.85$.

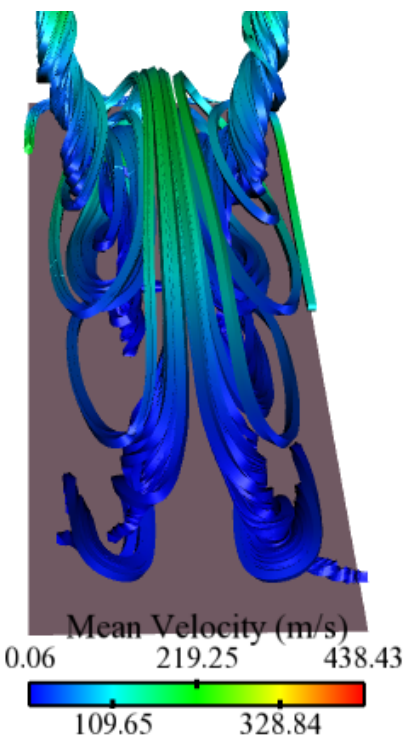

(a) 'Tornado-like' vortices in the cavity.

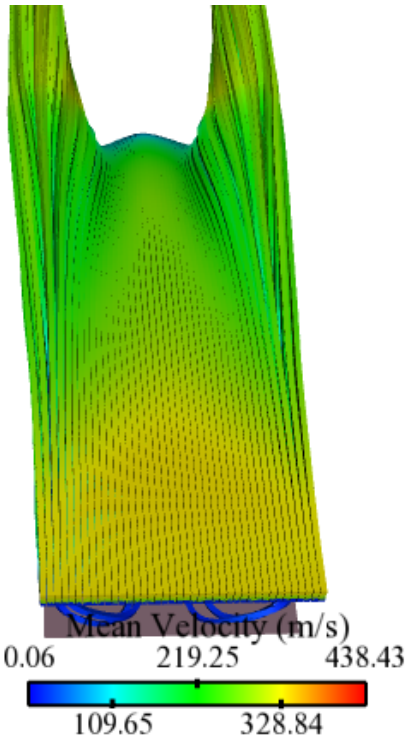

(b) Streamlines released from upstream of cavity leading edge.

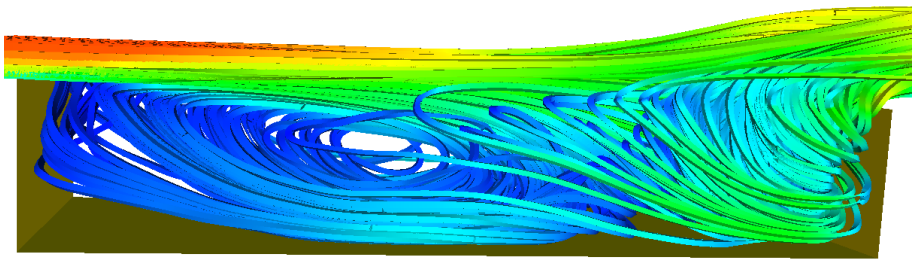

(c) View from the cavity side wall.

Figure 4.14: Time-mean streamlines for 3D cavity, $L/D = 5$, $W/D = 2$ and $M_\infty = 0.85$.

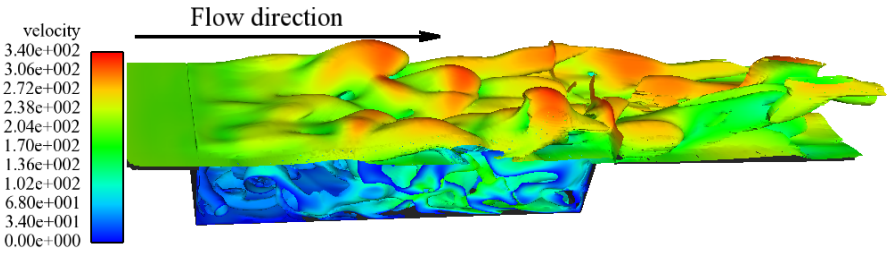

(a) Vorticity magnitude.

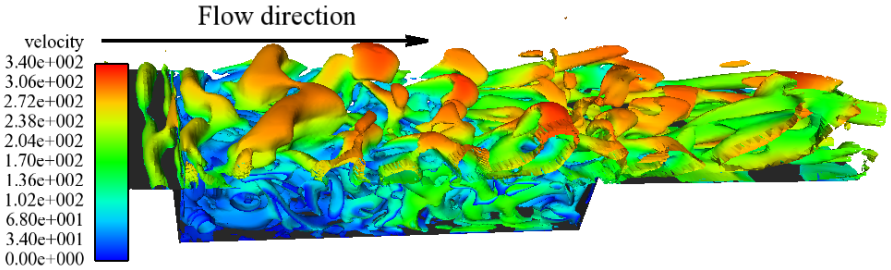

(b) Second invariant of the velocities.

Figure 4.15: Iso-surfaces showing flow structure in the cavity for Case 1 (L/D = 5, W/D = 2 and M_∞ = 0.85).

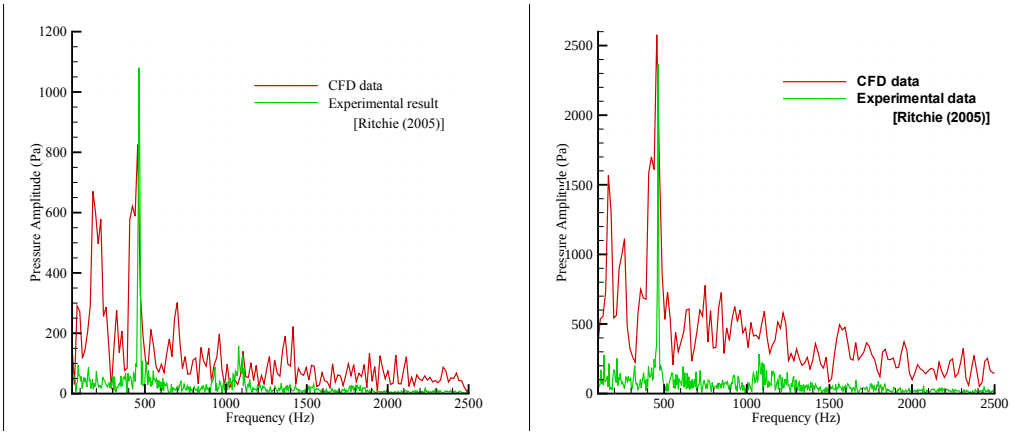

(a) Floor at x/L=0.10.

(b) Floor at x/L=0.90.

Figure 4.16: Empty cavity pressure spectra at floor centreline, L/D = 5, W/D = 2 and M_∞ = 0.85.

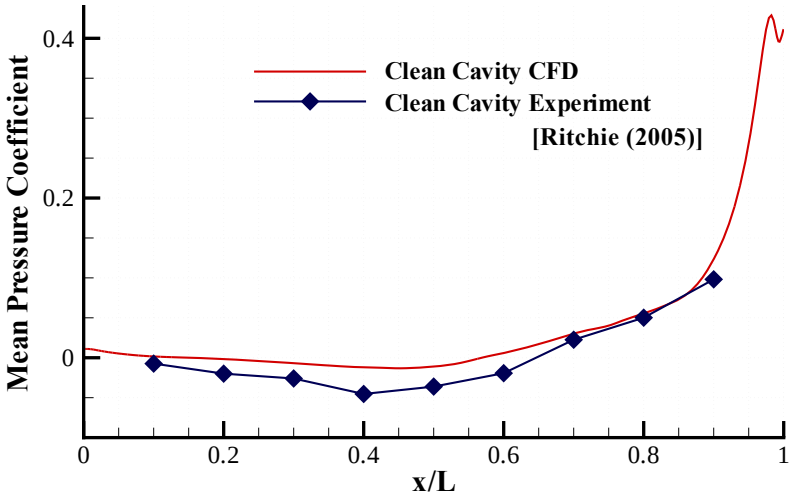

Figure 4.17: Mean C_p along the cavity centreline, $L/D = 5$ and $W/D = 2.5$.

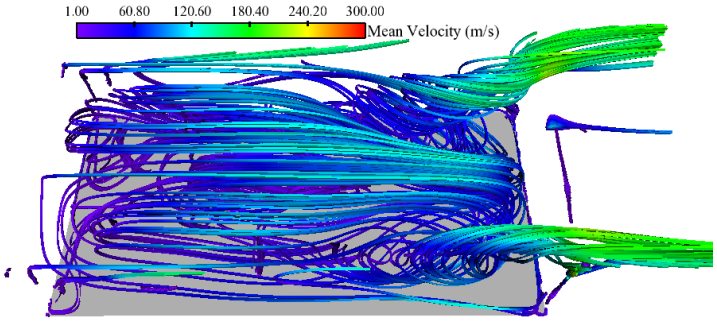

(a) 'Tornado-like' vortices in the cavity.

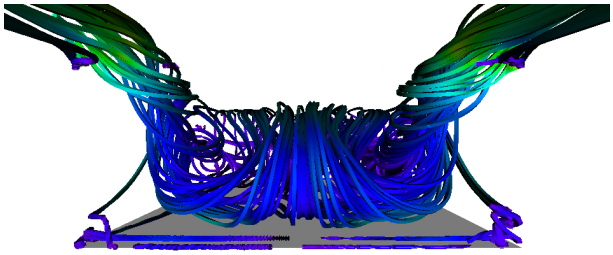

(b) View from the cavity rear wall.

Figure 4.18: Time-mean streamlines for 3D cavity, $L/D = 5$, $W/D = 2.5$ and $M_\infty = 0.85$.

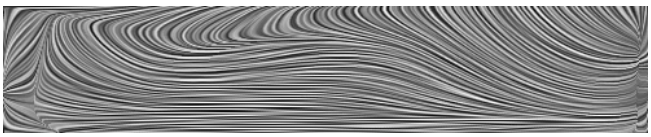

(a) Streamlines at side wall

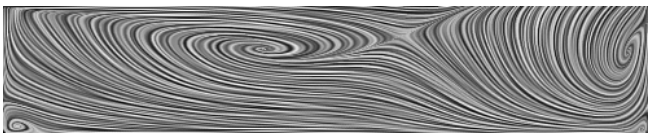

(b) Streamlines in x-y plane at $z/W = 0.1$

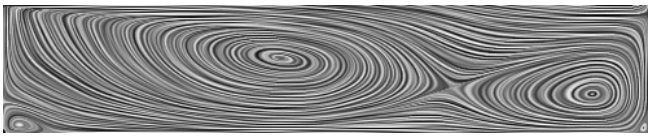

(c) Streamlines in x-y plane at $z/W = 0.2$

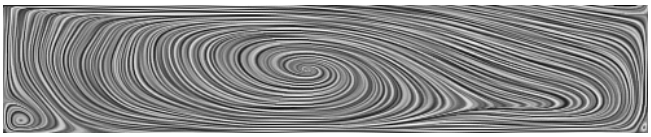

(d) Streamlines in x-y plane at $z/W = 0.3$

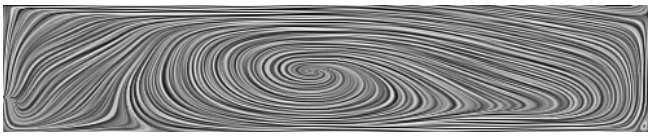

(e) Streamlines in x-y plane at $z/W = 0.4$

(f) Streamlines in x-y plane at $z/W = 0.5$

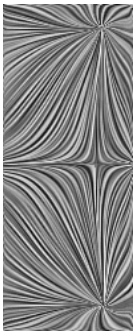

(g) Upstream wall.

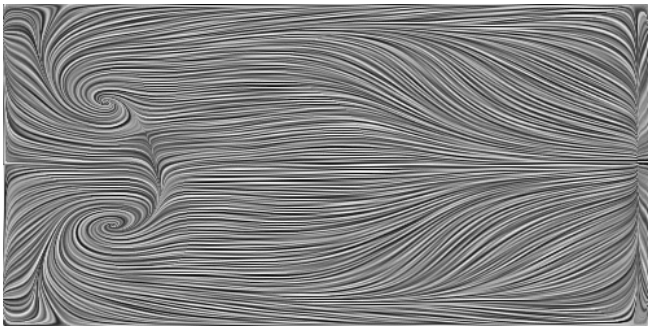

(h) Cavity Floor.

(i) Downstream wall.

Figure 4.19: Mean flow map for clean cavity using Line Integral Convolution, $L/D = 5$, $W/D = 2.5$ and $M_\infty = 0.85$.

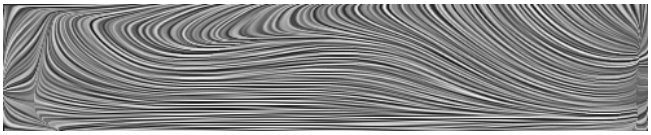

(a) Side wall, CFD result.

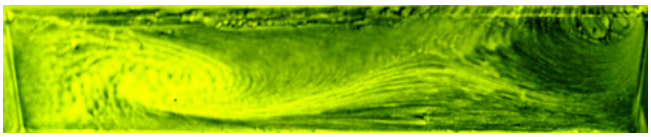

(b) Side wall, experiment (Oil flow).

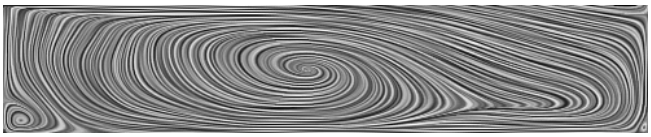

(c) x-y plane at $z/W = 0.67$, CFD.

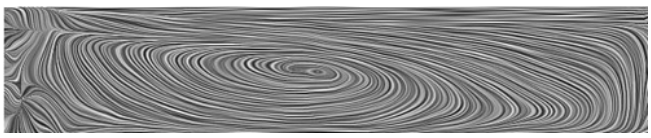

(d) x-y plane at $z/W = 0.67$, experiment (LIC of PIV data).

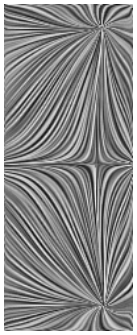

(e) Upstream wall.

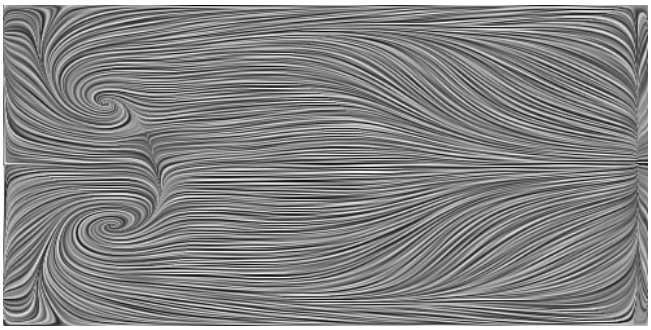

(f) Cavity Floor.

CFD result

(g) Downstream wall.

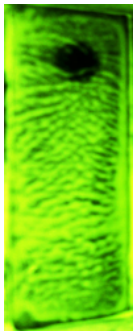

(h) Upstream wall.

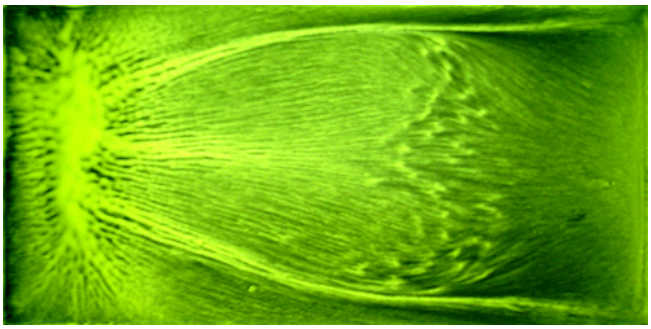

(i) Cavity Floor.

Oil flow Visualization

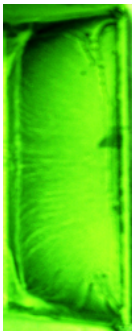

(j) Downstream wall.

Figure 4.20: Mean flow map Comparison, $L/D = 5$, $W/D = 2.5$ and $M_\infty = 0.85$.

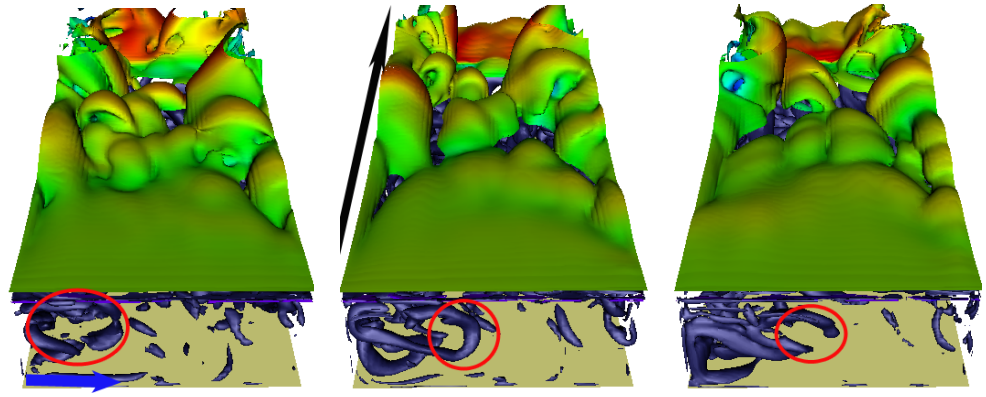

(a) $t \times a_\infty/D = 0.$ (b) $t \times a_\infty/D = 1.0.$ (c) $t \times a_\infty/D = 2.0.$

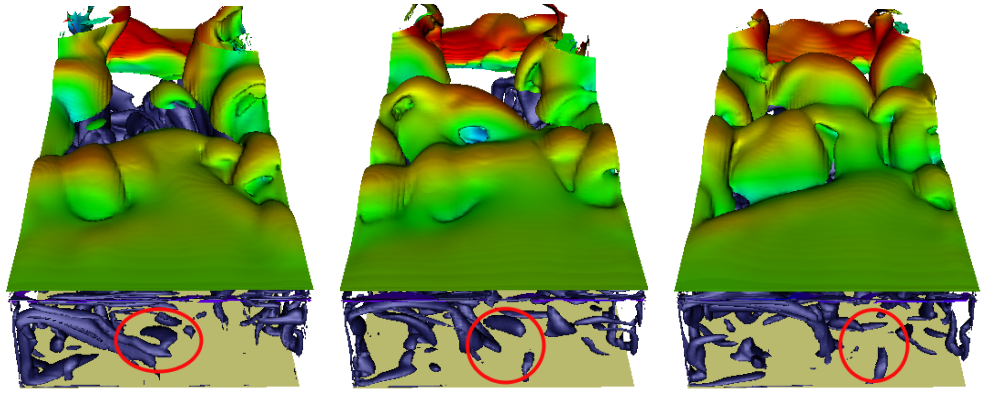

(c) $t \times a_\infty/D = 3.0.$ (c) $t \times a_\infty/D = 4.0.$ (c) $t \times a_\infty/D = 5.0.$

Figure 4.21: Shear layer vortex evolution over one cycle of oscillation: iso-contours of the Q-criterion (tubular structures in dark blue) and vorticity sheet (coloured by velocity), $L/D = 5$ and $W/D = 2.5$; $M_\infty = 0.85$.

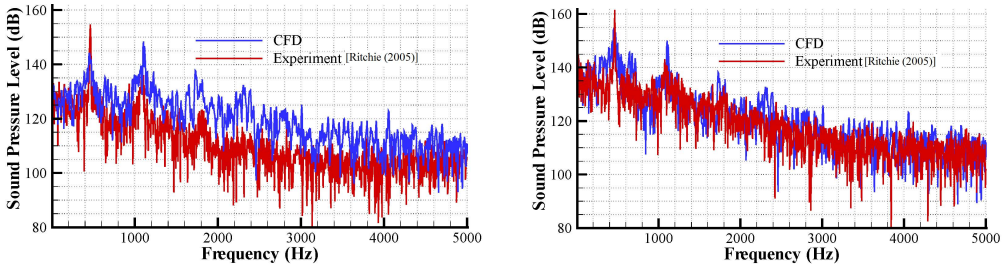

(a) Floor at x/L=0.10. (b) Floor at x/L=0.90.

Figure 4.22: Clean cavity pressure spectra at floor centreline, $L/D = 5$, $W/D = 2.5$ and $M_\infty = 0.85$.

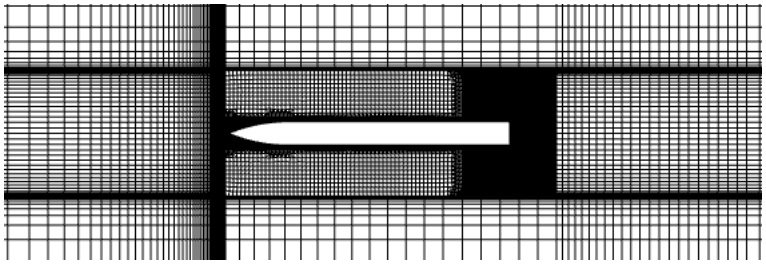

(a) Section view of grid in cavity with a missile body (XZ-plane).

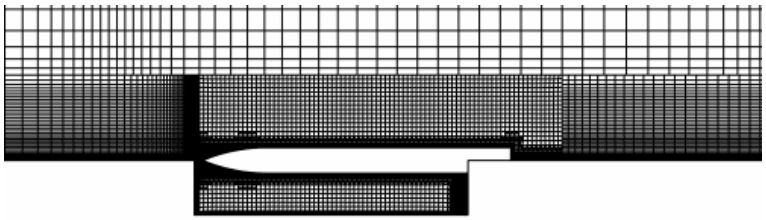

(b) Section view of grid in cavity with a missile body (XY-plane).

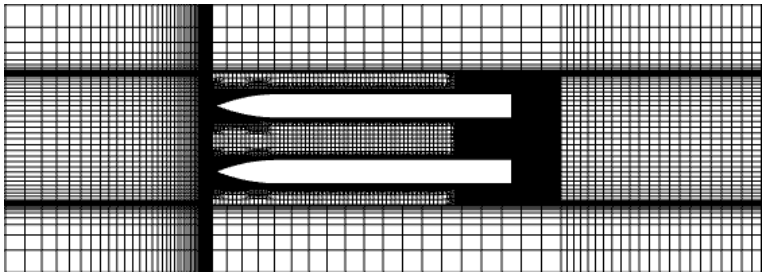

(c) Section view of grid in cavity with two missiles (XZ-plane).

Figure 4.23: Structured grid distribution across XY-plane.

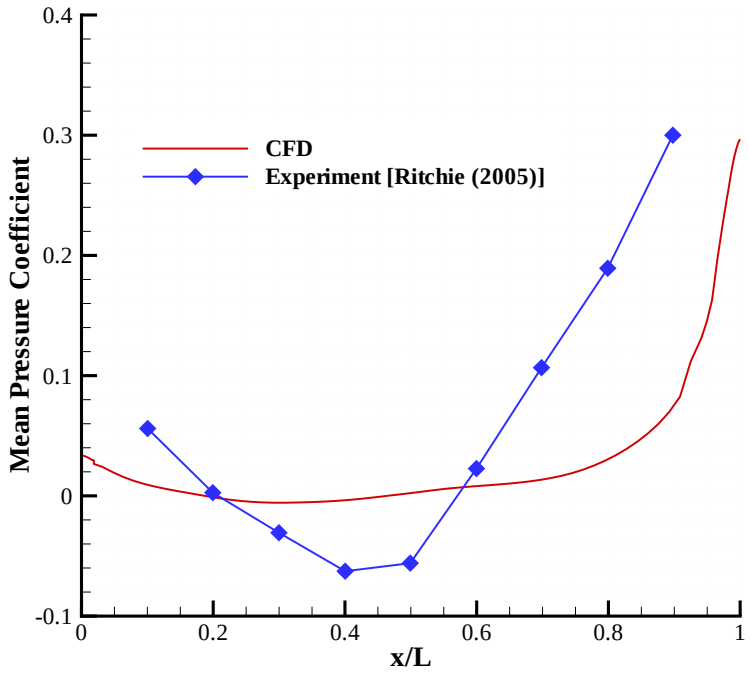

(a) Cavity with one missile body.

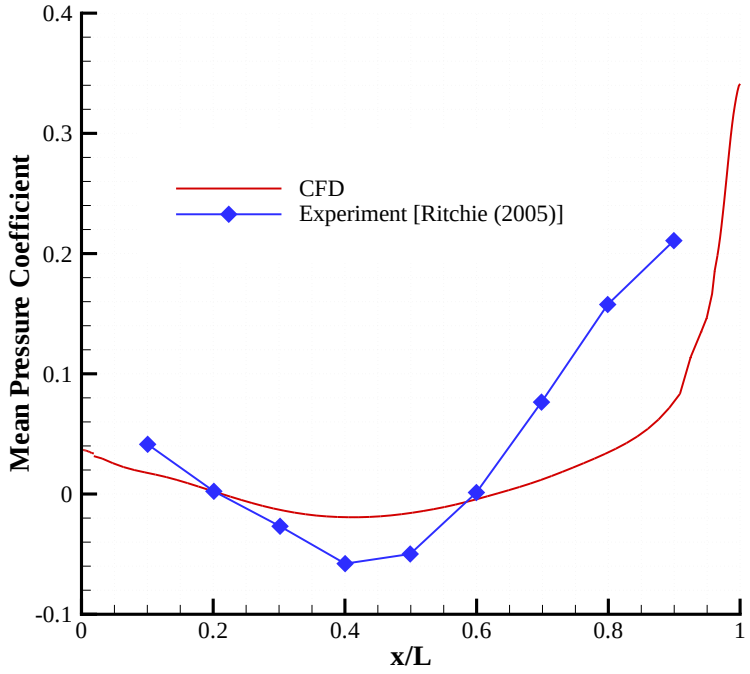

(b) Cavity with two missile bodies.

Figure 4.24: Mean C_p along the floor centreline, $L/D = 5$ and $W/D = 2.5$.

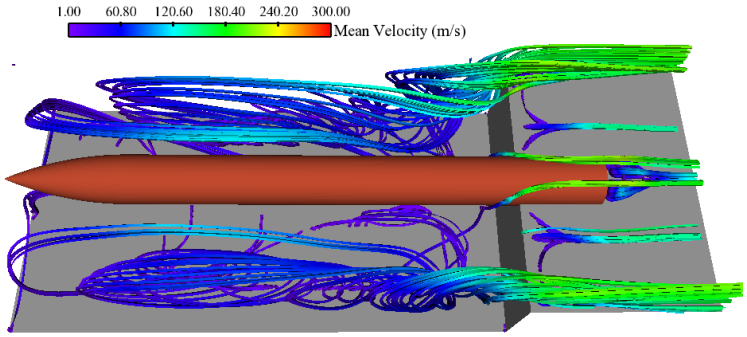

(a) Cavity with one missile body.

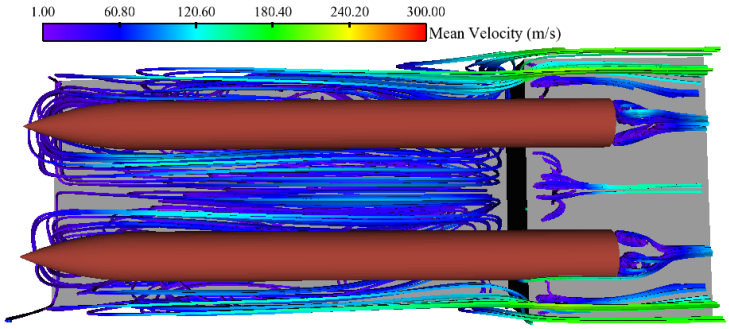

(b) Cavity with two missile bodies.

Figure 4.25: Meanflow streamlines, $L/D = 5$ *and* $W/D = 2.5$.

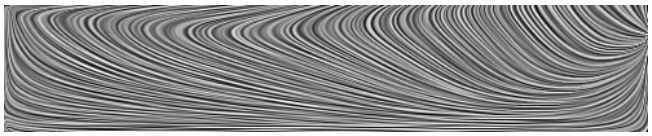

(a) Time mean streamlines at side wall

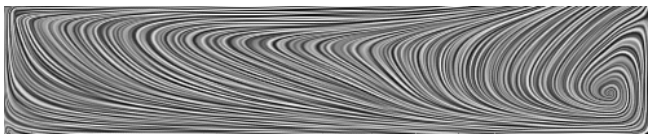

(b) Time mean streamlines in x-y plane at $z/W = 0.1$

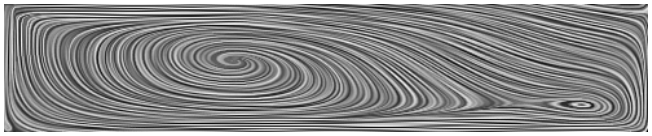

(c) Time mean streamlines in x-y plane at $z/W = 0.2$

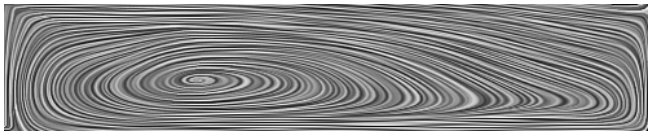

(d) Time mean streamlines in x-y plane at $z/W = 0.3$

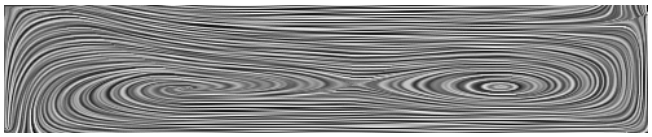

(e) Time mean streamlines in x-y plane at $z/W = 0.4$

Figure 4.26: Mean flow map for cavity with one missile, $L/D = 5$, $W/D = 2.5$ *and* $M_\infty = 0.85$.

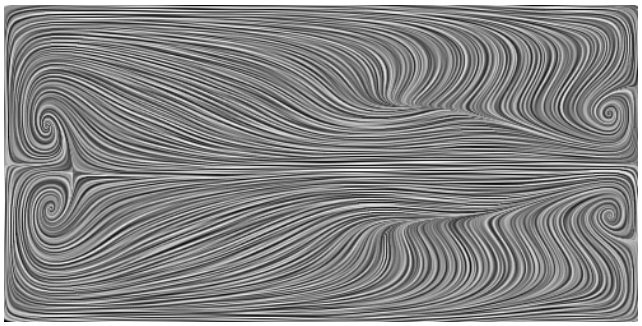

(a) Time mean streamlines in x-z plane at $y/D = 0.25$

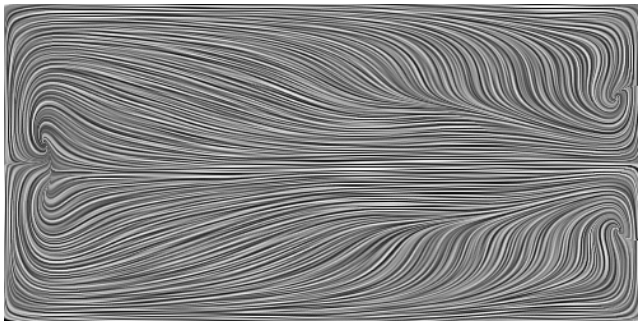

(b) Time mean streamlines in x-z plane at $y/D = 0.20$

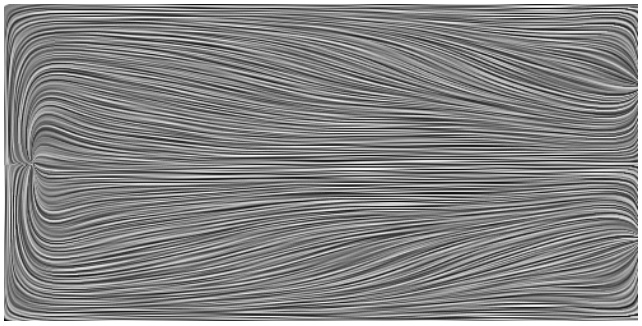

(c) Time mean streamlines in x-z plane at $y/D = 0.10$

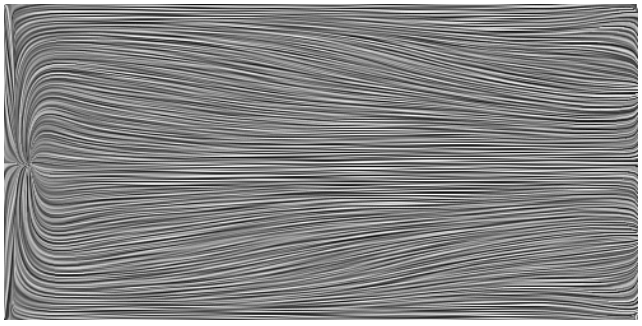

(d) Cavity Floor.

Figure 4.27: Mean flow map for cavity with one missile, $L/D = 5$, $W/D = 2.5$ and $M_\infty = 0.85$.

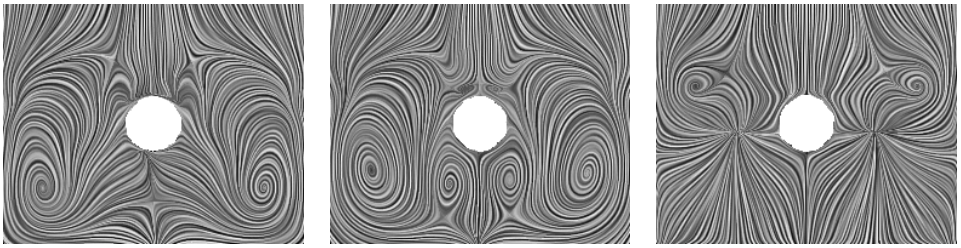

(a) $x/L = 0.50$ (b) $x/L = 0.75$ (c) $x/L = 0.99$

Figure 4.28: Mean flow maps at various streamwise sections for cavity with one missile, $L/D = 5$*,* $W/D = 2.5$ *and* $M_\infty = 0.85$*.*

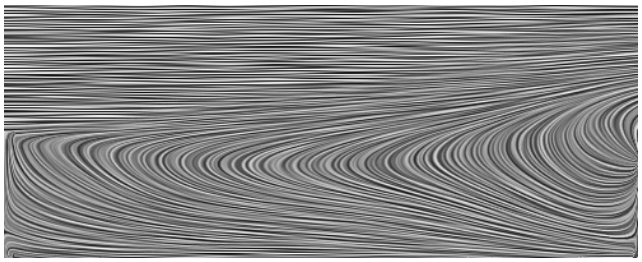

(a) Time mean streamlines at side wall

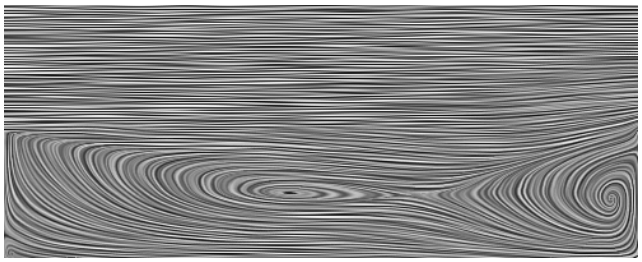

(b) Time mean streamlines in x-y plane at $z/W = 0.1$

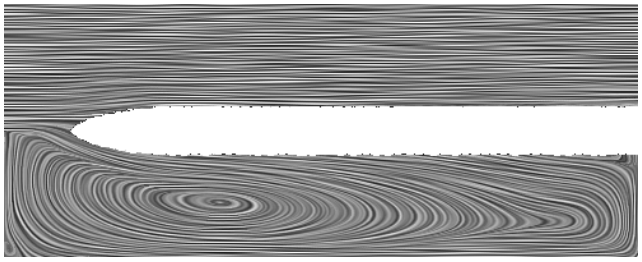

(c) Time mean streamlines in x-y plane at $z/W = 0.2$

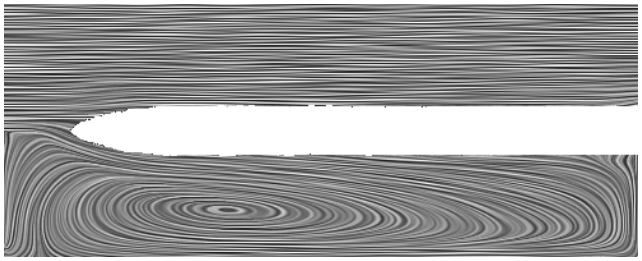

(d) Time mean streamlines in x-y plane at $z/W = 0.3$

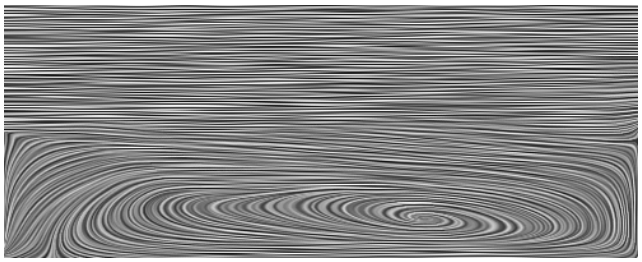

(e) Time mean streamlines in x-y plane at $z/W = 0.4$

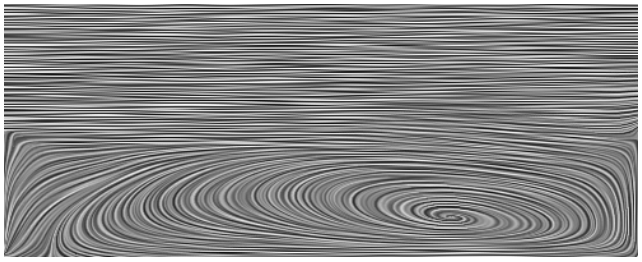

(f) Time mean streamlines in x-z plane at $z/W = 0.5$

Figure 4.29: Mean flow map for cavity with two missiles, $L/D = 5$, $W/D = 2.5$ and $M_\infty = 0.85$.

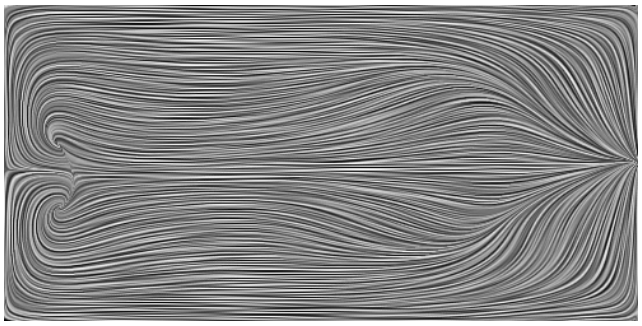

(a) Time mean streamlines in x-z plane at $y/D = 0.20$

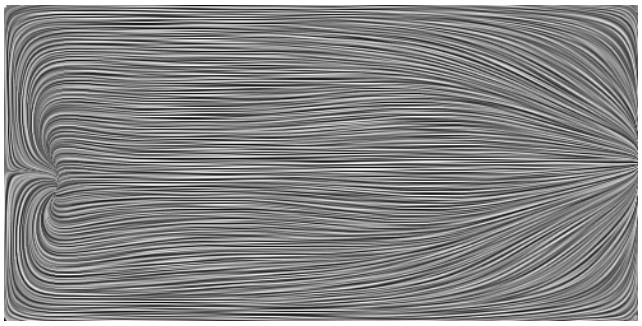

(b) Time mean streamlines in x-z plane at $y/D = 0.10$

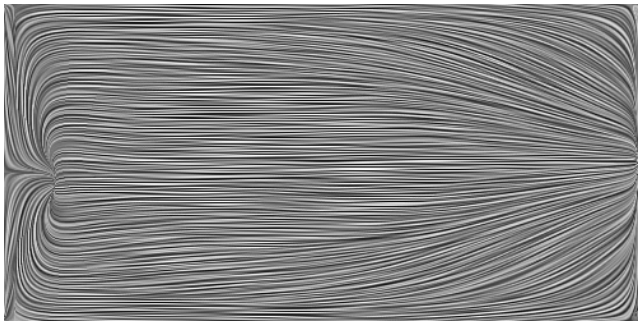

(c) Cavity Floor.

Figure 4.30: Mean flow map for cavity with two missiles, $L/D = 5$, $W/D = 2.5$ and $M_\infty = 0.85$.

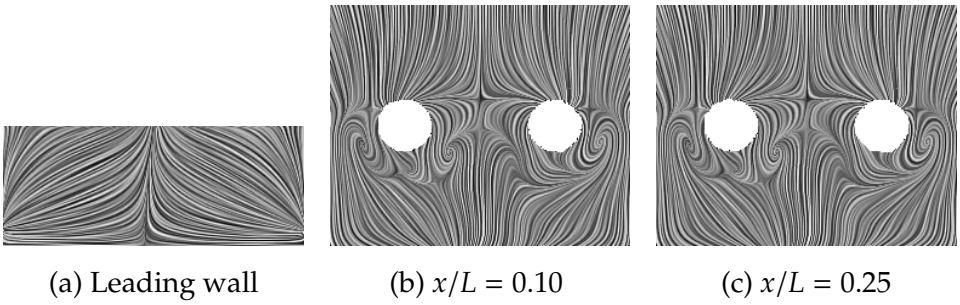

(a) Leading wall (b) $x/L = 0.10$ (c) $x/L = 0.25$

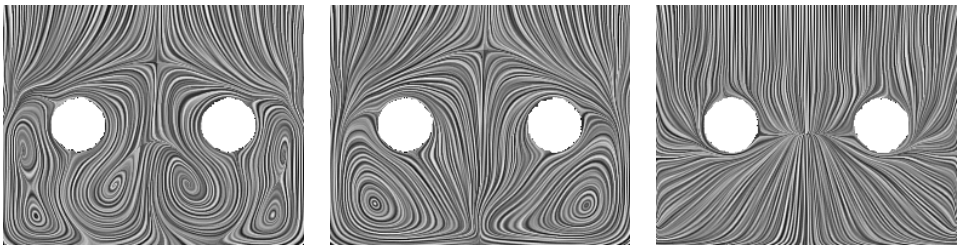

(a) $x/L = 0.50$ (b) $x/L = 0.75$ (c) $x/L = 0.99$

Figure 4.31: Mean flow map at various streamwise sections for cavity with two missile, $L/D = 5$*,* $W/D = 2.5$ *and* $M_\infty = 0.85$*.*

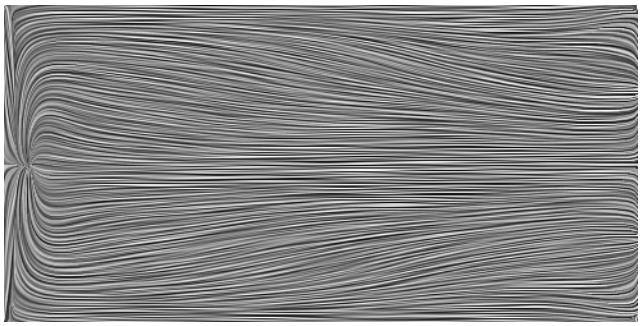

(a) Cavity with one missile, CFD.

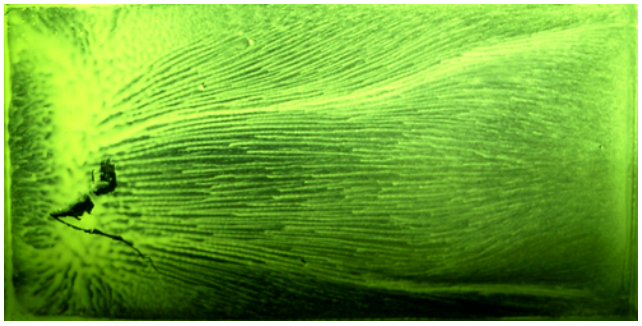

(b) Cavity with one missile, Experiment.

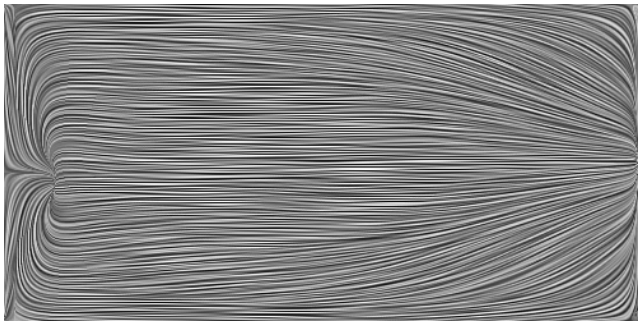

(c) Cavity with two missiles, CFD.

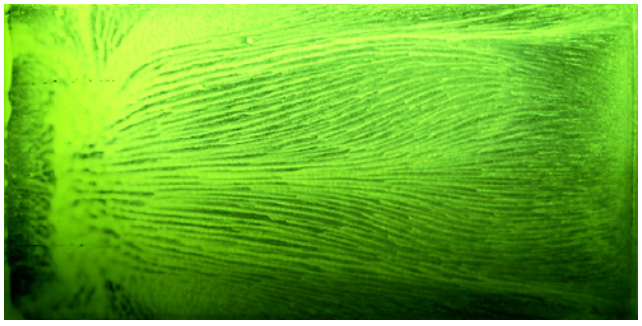

(d) Cavity with two missiles, Experiment.

Figure 4.32: Floor mean flow map comparison, $L/D = 5$, $W/D = 2.5$ and $M_\infty = 0.85$.

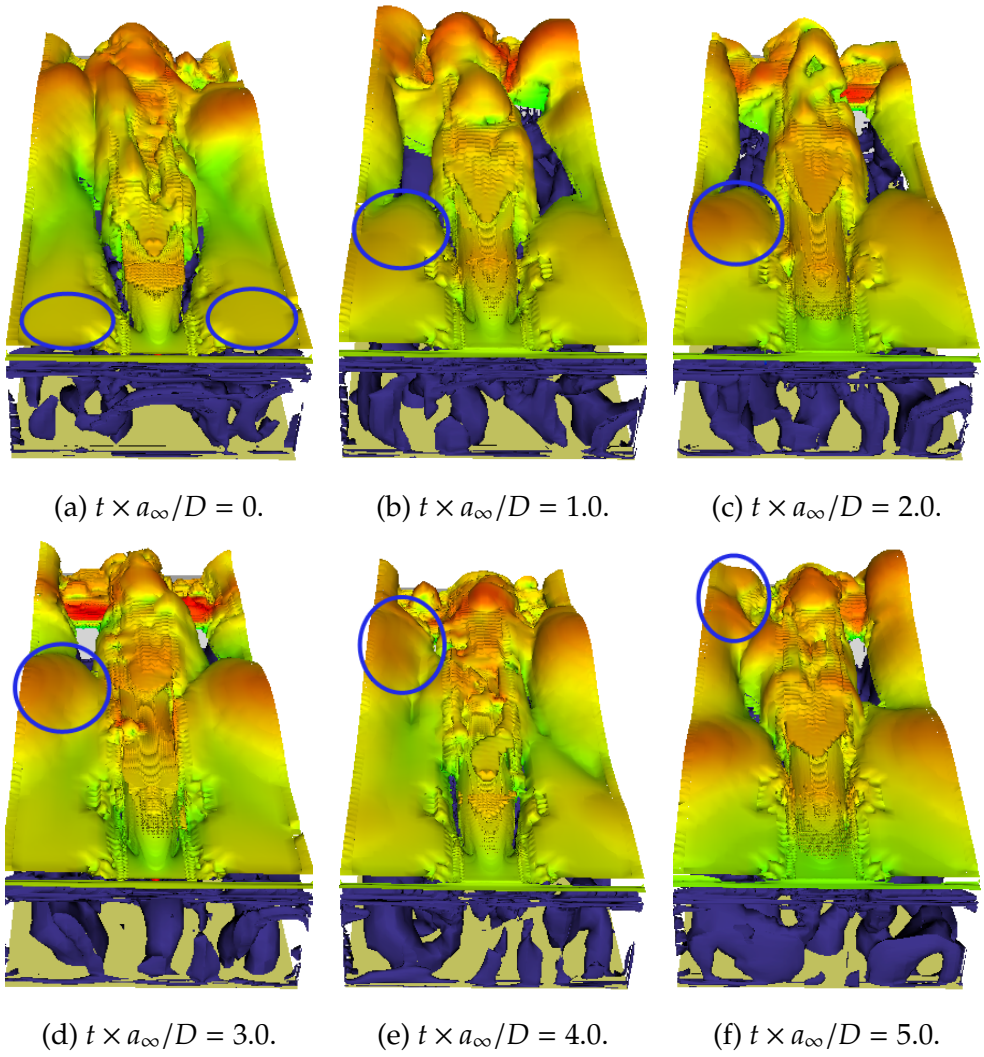

(a) $t \times a_\infty/D = 0.$ (b) $t \times a_\infty/D = 1.0.$ (c) $t \times a_\infty/D = 2.0.$

(d) $t \times a_\infty/D = 3.0.$ (e) $t \times a_\infty/D = 4.0.$ (f) $t \times a_\infty/D = 5.0.$

Figure 4.33: Shear layer vortex evolution over one cycle of oscillation: iso-contours of the Q-criterion and vorticity sheet, $L/D = 5$ *and* $W/D = 2.5$*;* $M_\infty = 0.85$.

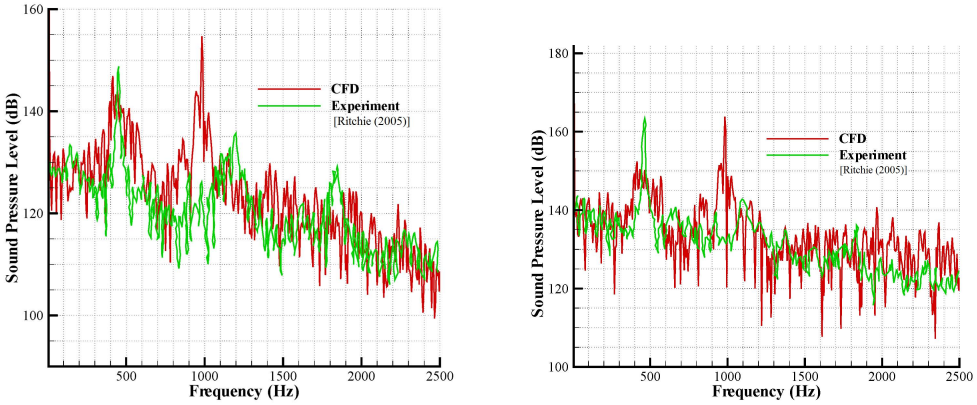

(a) Floor at x/L=0.10.

(b) Floor at x/L=0.90.

Figure 4.34: Cavity with one missile pressure spectra at floor centreline, $L/D = 5$*,* $W/D = 2.5$ *and* $M_\infty = 0.85$*.*

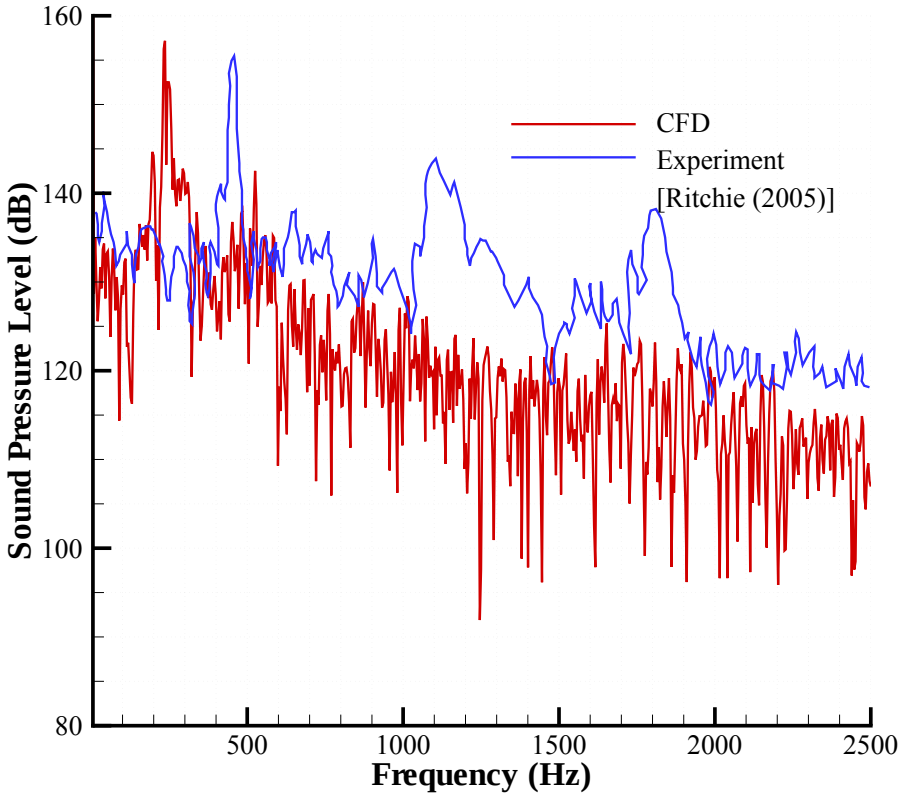

Figure 4.35: Cavity with two missiles pressure spectra at floor centreline, $L/D = 5$, $W/D = 2.5$ *and* $M_\infty = 0.85$.

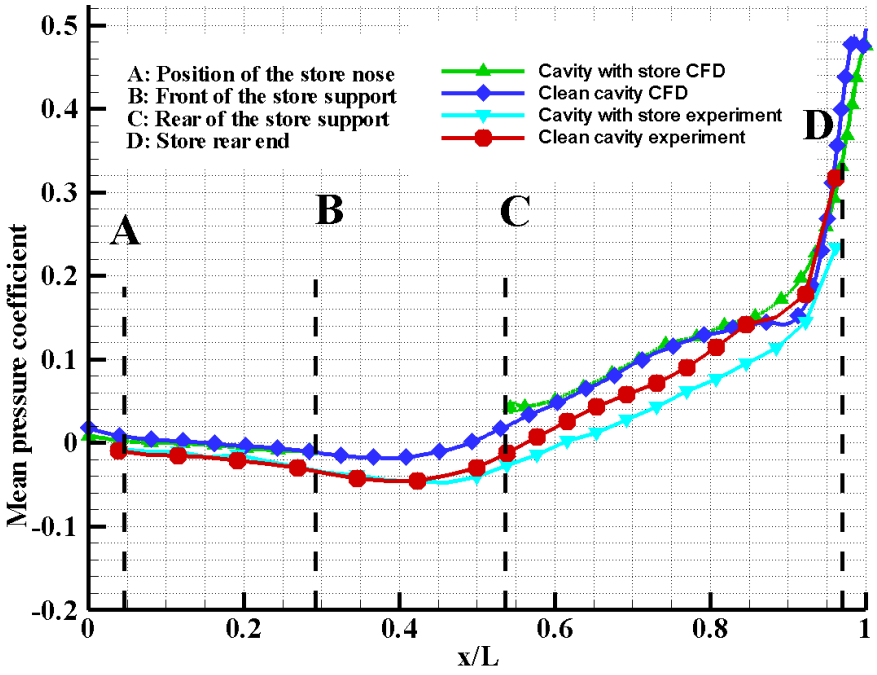

Figure 4.36: Mean C_p variations for clean cavity and cavity-with-store cases, L/D = 5.42 and W/D = 2.

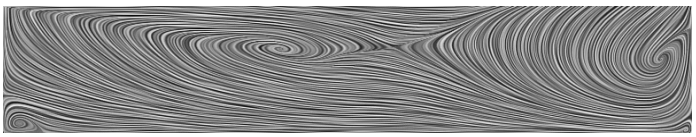

(a) Streamlines in x-y plane at $z/W = 0.01$

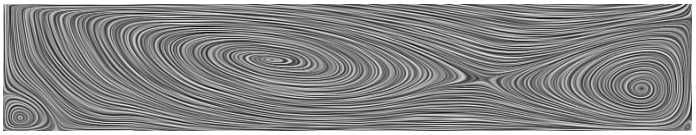

(b) Streamlines in x-y plane at $z/W = 0.2$

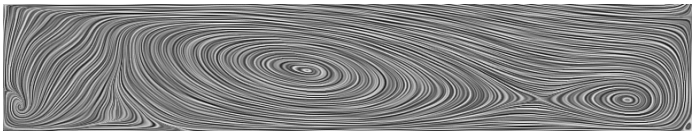

(c) Streamlines in x-y plane at $z/W = 0.3$

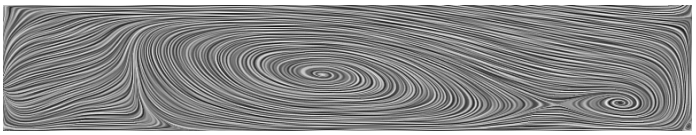

(d) Streamlines in x-y plane at $z/W = 0.4$

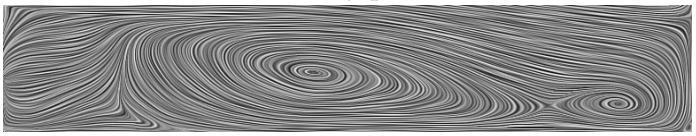

(e) Streamlines in x-y plane at $z/W = 0.5$

(f) Upstream wall.

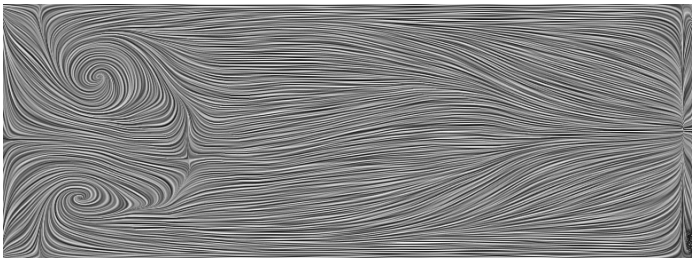

(g) Cavity Floor.

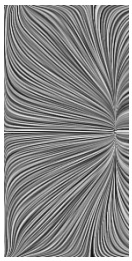

(h) Downstream wall.

Figure 4.37: Mean flow map in cavity using LIC, $L/D = 5.42$, $W/D = 2$ and $M_\infty = 0.80$.

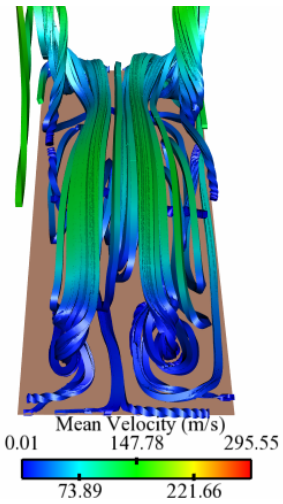

(a) 'Tornado-like' vortices in the cavity.

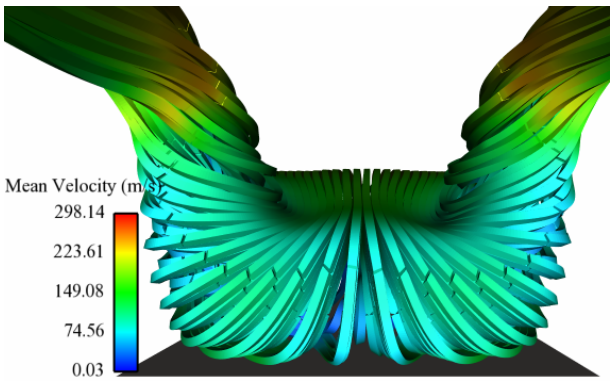

(b) View from the cavity rear wall.

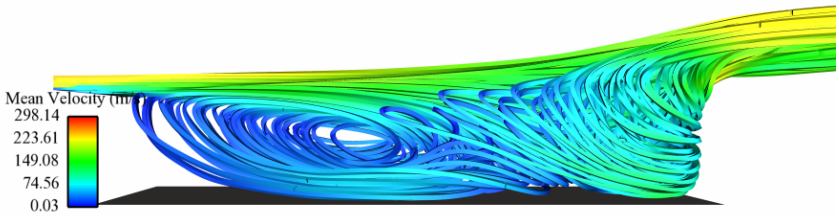

(c) View from the cavity side wall.

Figure 4.38: Time-mean streamlines for 3D cavity, $L/D = 5.42$, $W/D = 2$ and $M_\infty = 0.80$.

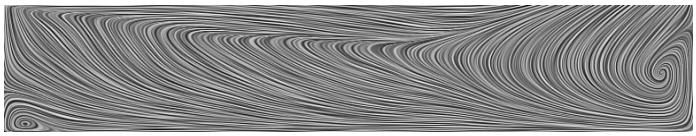

(a) Streamlines in x-y plane at $z/W = 0.01$

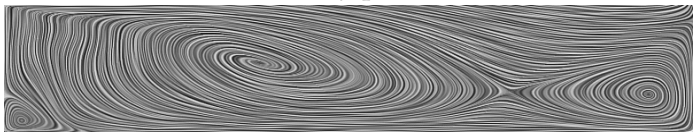

(b) Streamlines in x-y plane at $z/W = 0.2$

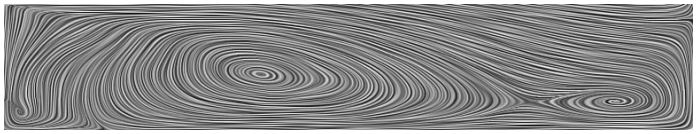

(c) Streamlines in x-y plane at $z/W = 0.3$

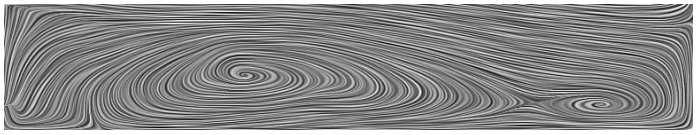

(d) Streamlines in x-y plane at $z/W = 0.4$

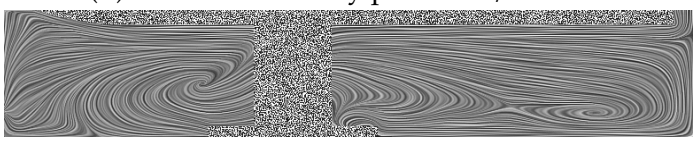

(e) Streamlines in x-y plane at $z/W = 0.5$

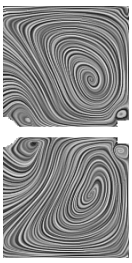

(f) Strut section.

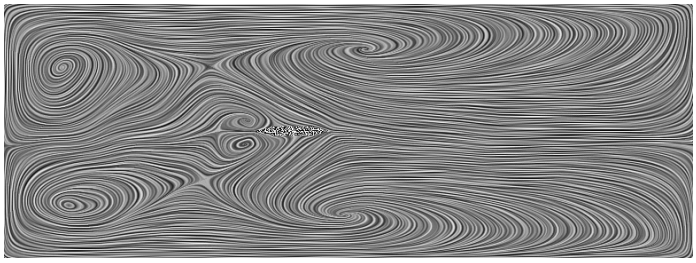

(g) Mid-depth plane.

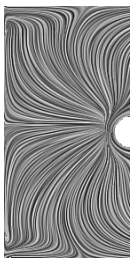

(h) Rear of store.

(i) Upstream wall.

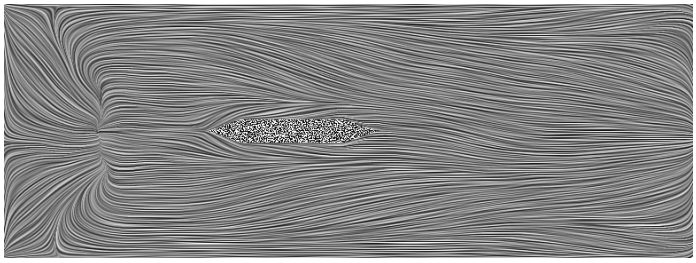

(j) Cavity Floor.

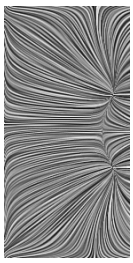

(k) Downstream wall.

Figure 4.39: Mean flow map for cavity-with-store case using LIC, $L/D = 5.42$, $W/D = 2$ and $M_\infty = 0.80$.

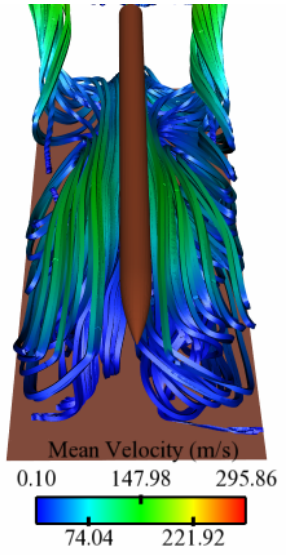

(a) Flow structure in the cavity.

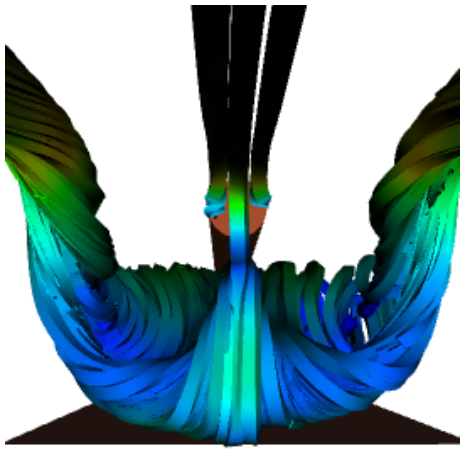

(b) View from the cavity rear wall.

Streamlines released from vortex cores inside the cavity.

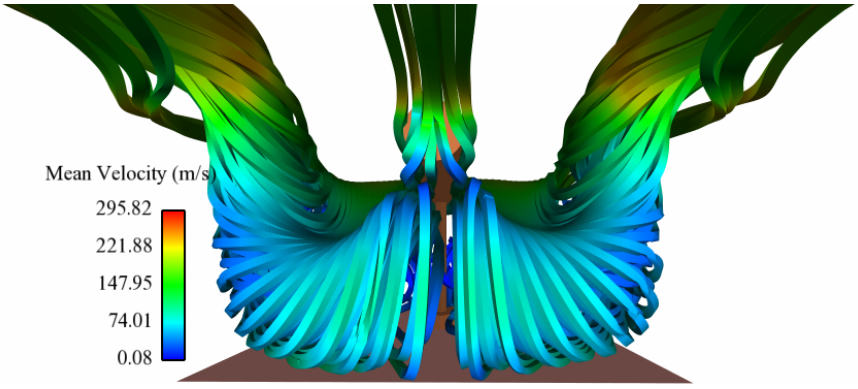

(c) View from the cavity rear wall.

Figure 4.40: Time-mean streamlines for 3D cavity-with-store, $L/D = 5.42$, $W/D = 2$ *and* $M_\infty = 0.80$.

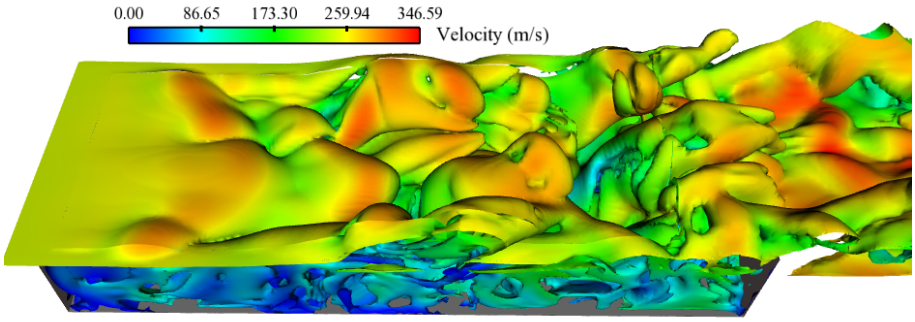

(a) Iso-surface of vorticity magnitude, clean cavity.

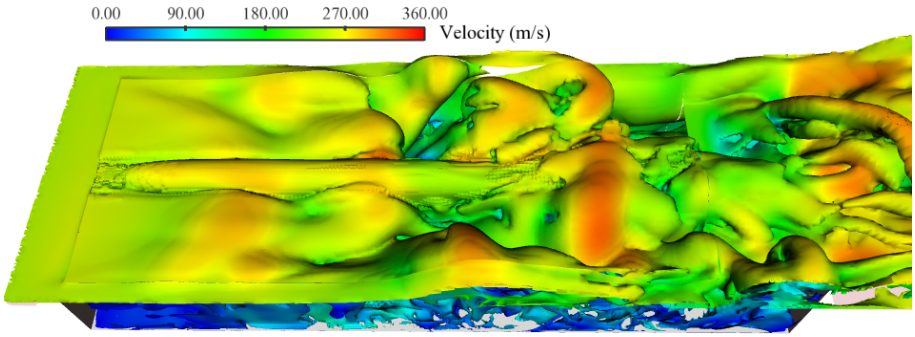

(b) Iso-surface of vorticity magnitude, cavity-with-store.

Figure 4.41: Instantaneous vorticity iso-surfaces showing shear layer warping, $L/D = 5.42$*,* $W/D = 2$ *and* $M_\infty = 0.80$*.*

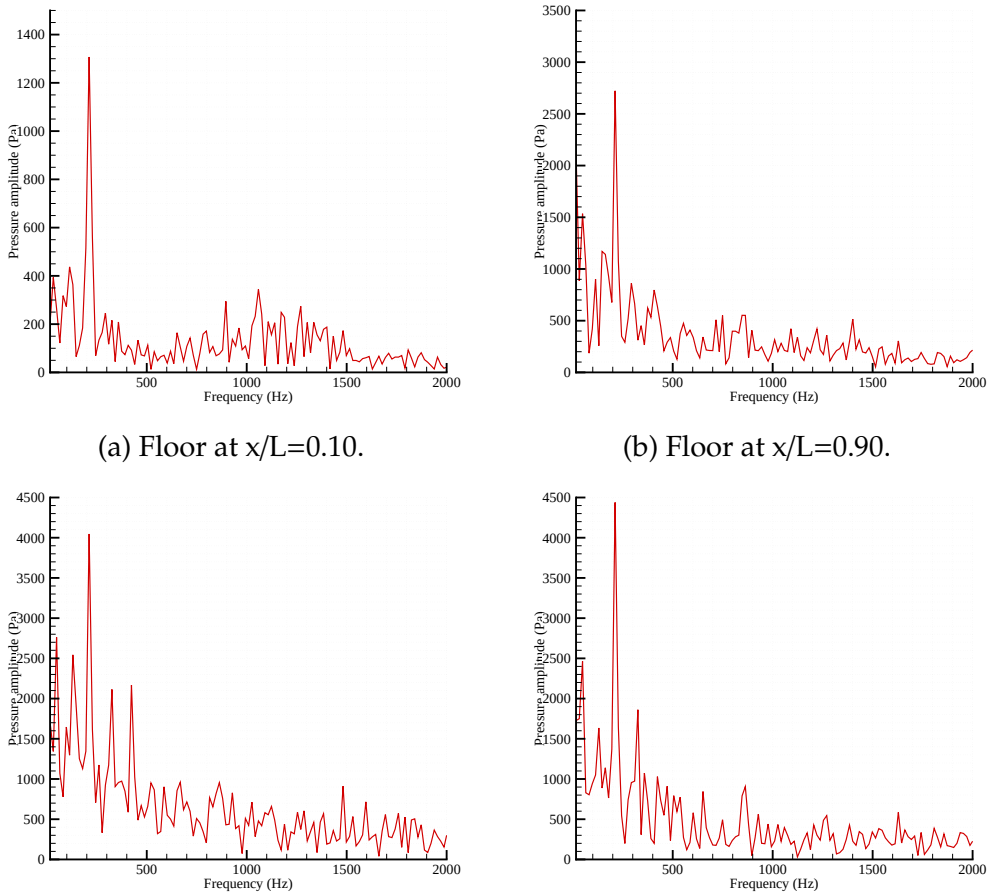

(a) Floor at x/L=0.10.

(b) Floor at x/L=0.90.

(c) Rear cavity wall at y/D=0.25.

(d) Rear cavity wall at y/D=0.50.

Figure 4.42: Empty cavity pressure spectra at floor and rear wall centreline, $L/D = 5.42$*,* $W/D = 2$ *and* $M_\infty = 0.80$*.*

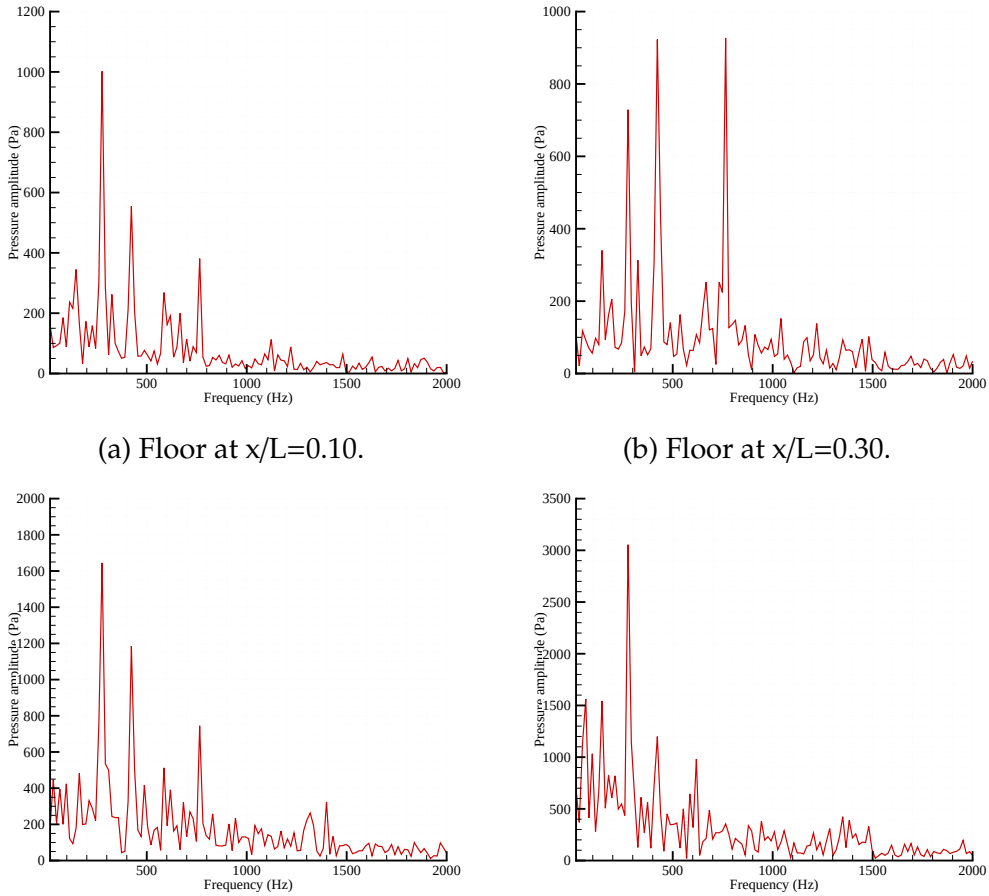

(a) Floor at x/L=0.10.

(b) Floor at x/L=0.30.

(c) Floor at x/L=0.667.

(d) Floor at x/L=0.90.

Figure 4.43: Cavity-with-store pressure spectra at floor, $L/D = 5.42$*,* $W/D = 2$ *and* $M_\infty = 0.80$*.*

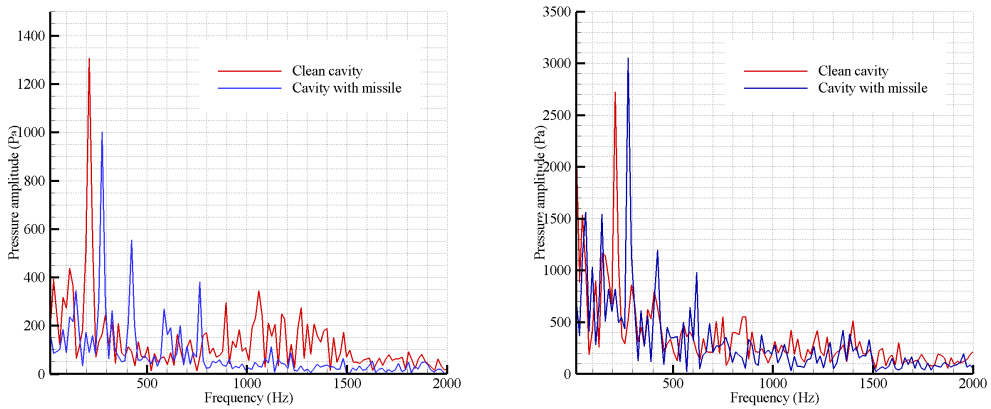

(a) Floor at x/L=0.10.

(b) Floor at x/L=0.90.

Figure 4.44: Floor centreline pressure spectra comparison for clean cavity and cavity with store, L/D = 5.42, W/D = 2 and M_∞ = 0.80.

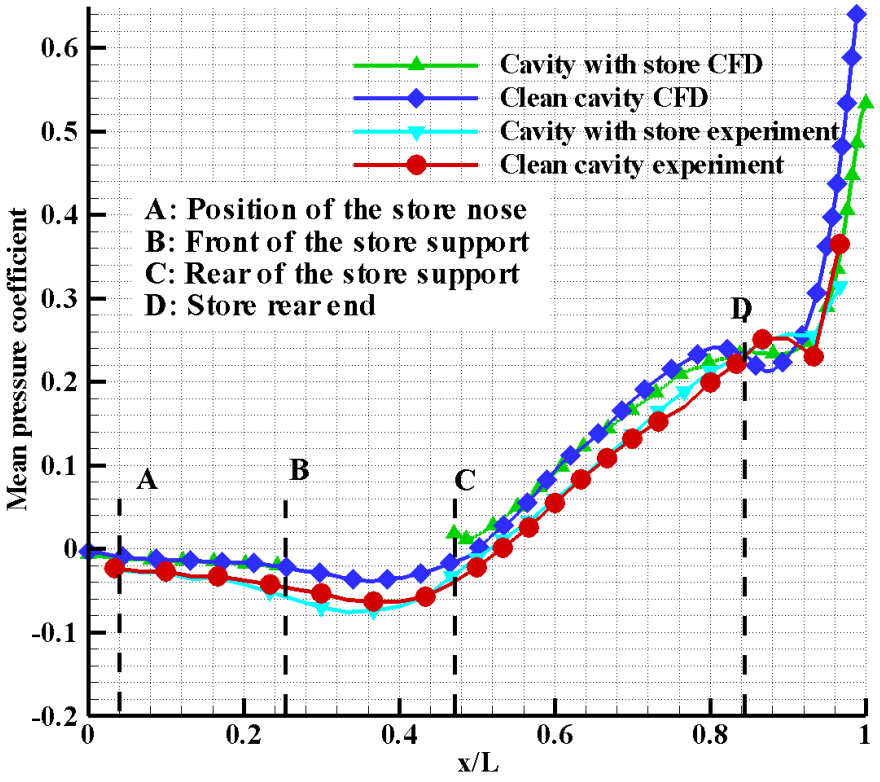

Figure 4.45: Mean C_p variations for clean cavity and cavity-with-store cases, L/D = 6.25 and W/D = 2.

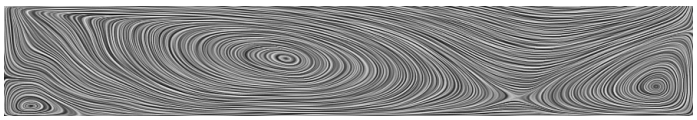

(a) Streamlines in x-y plane at $z/W = 0.2$

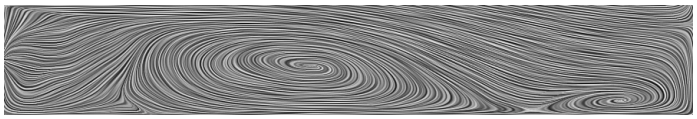

(b) Streamlines in x-y plane at $z/W = 0.4$

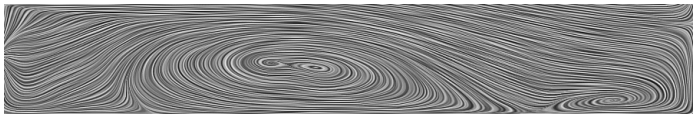

(c) Streamlines in x-y plane at $z/W = 0.5$

(d) Upstream wall.

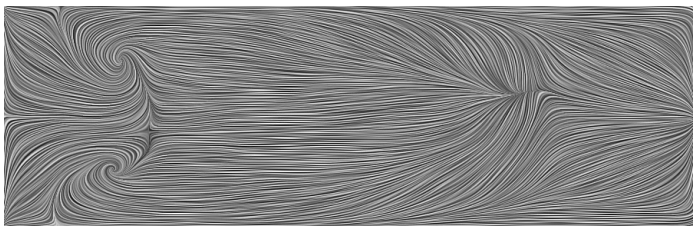

(e) Cavity Floor.

(f) Downstream wall.

Surface mean flow maps, clean cavity .

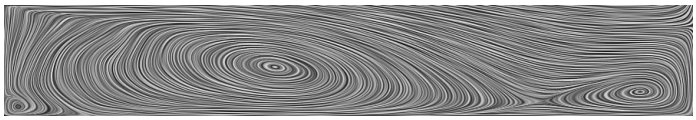

(g) Streamlines in x-y plane at $z/W = 0.3$

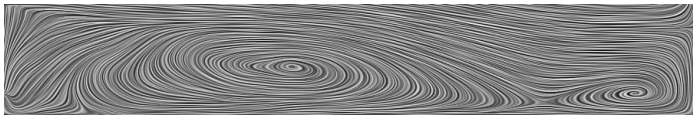

(h) Streamlines in x-y plane at $z/W = 0.4$

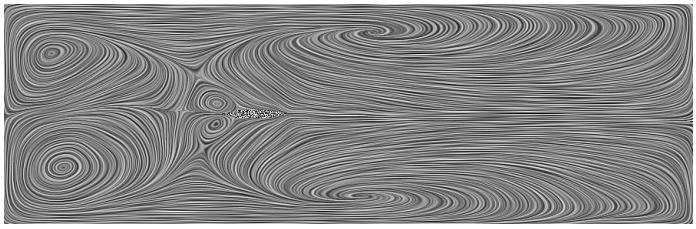

(i) Mid-depth (x-z) plane

(j) Upstream wall.

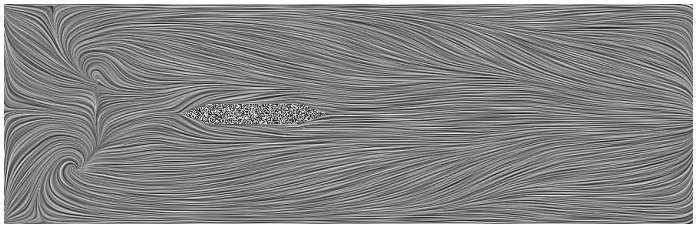

(k) Cavity Floor.

(l) Downstream wall.

Surface mean flow maps, cavity with store.

Figure 4.46: Mean flow maps using LIC, $L/D = 6.25$, $W/D = 2$ and $M_\infty = 0.80$.

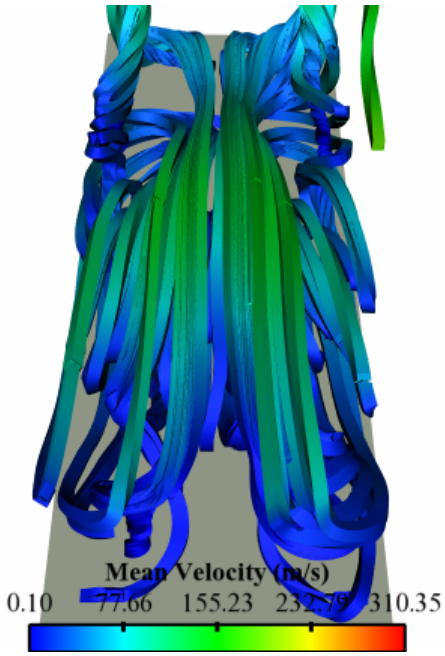

(a) Clean cavity.

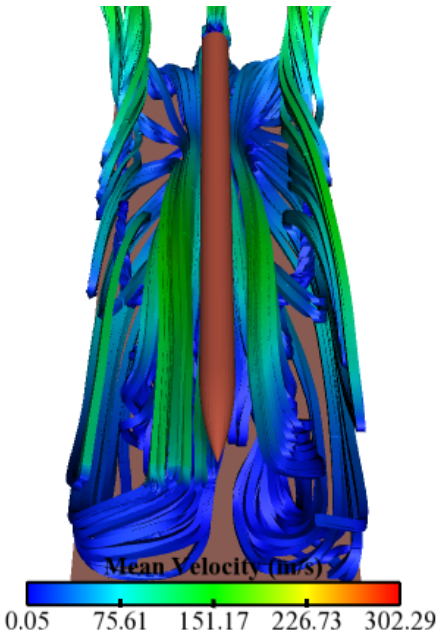

(b) Cavity with store.

Streamlines released from vortex cores inside the cavity.

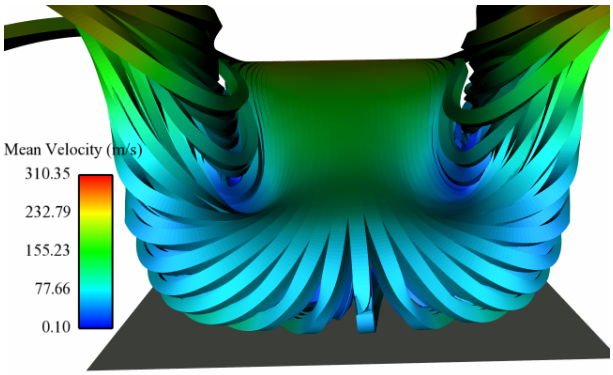

(c) View from the cavity rear wall, clean cavity.

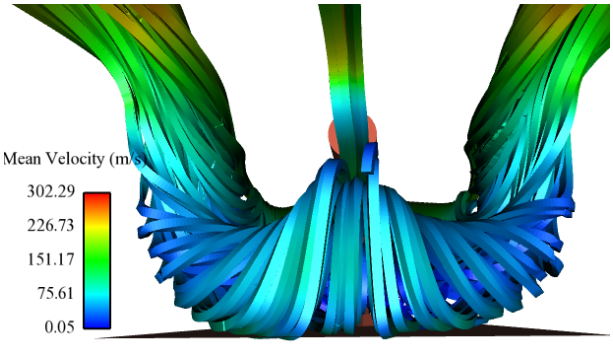

(d) View from the cavity rear wall, cavity with store.

Figure 4.47: Time-mean streamlines, $L/D = 6.25$, $W/D = 2$ and $M_\infty = 0.80$.

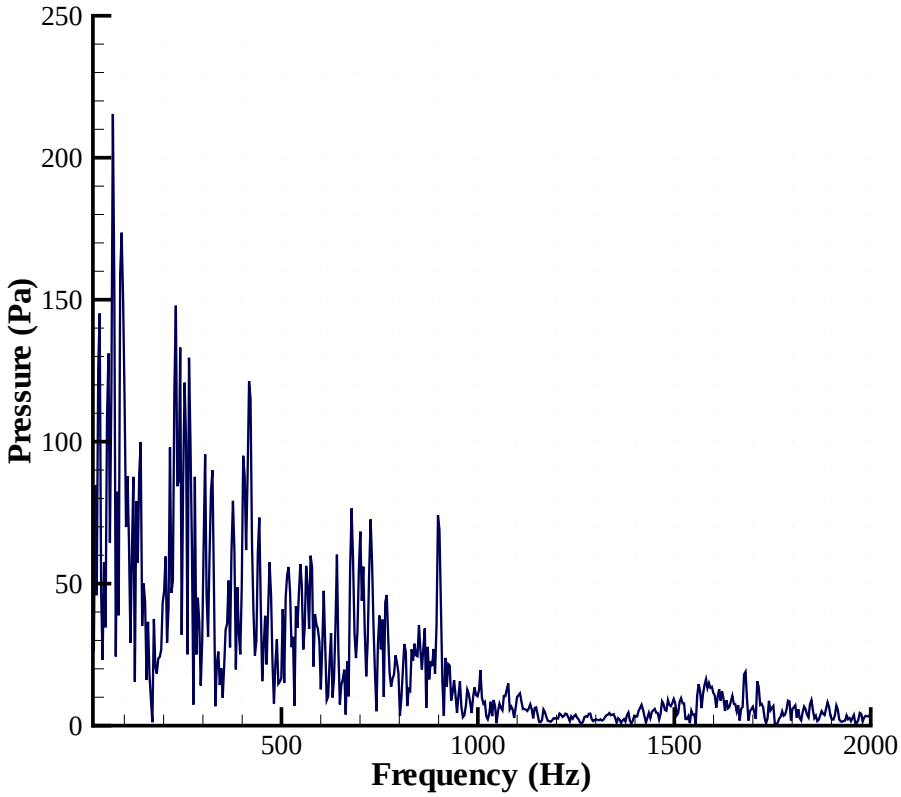

(a) Clean cavity.

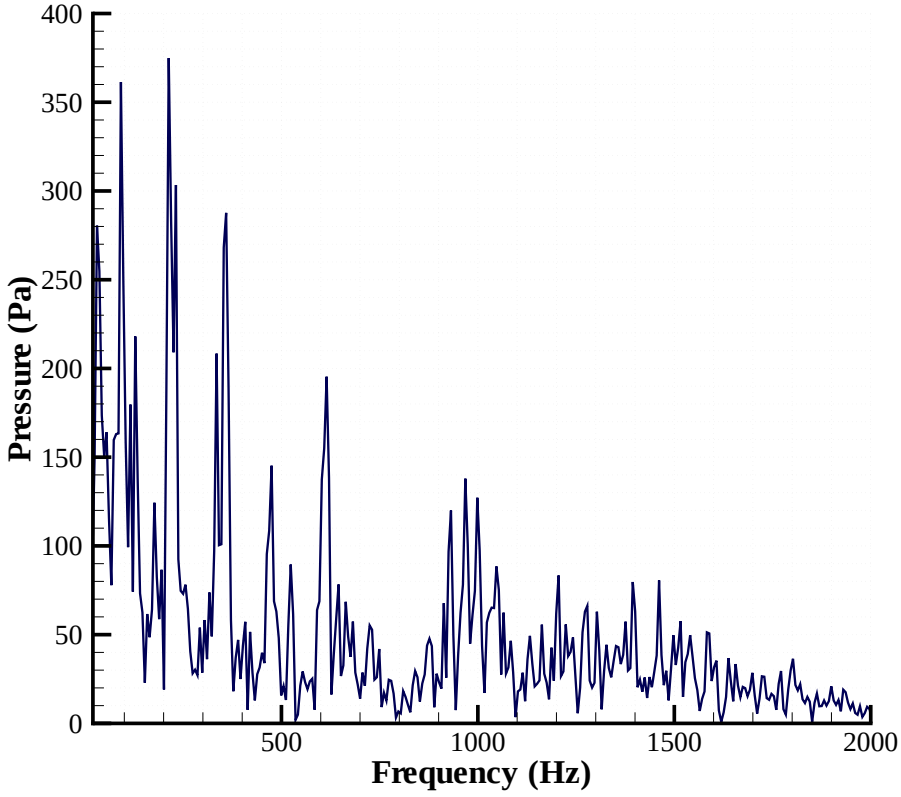

(b) Cavity with store.

Figure 4.48: Floor centreline pressure spectra at x/L=0.10, L/D = 6.25, W/D = 2 and M_∞ = 0.80.

(a) Experiment.

(b) CFD.

Figure 4.49: Spoiler geometry.

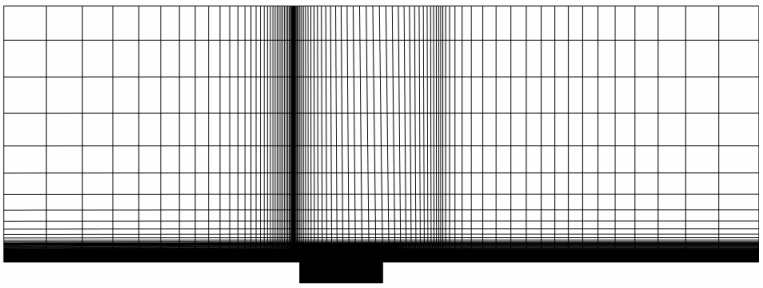

(a) Section view of grid in empty cavity.

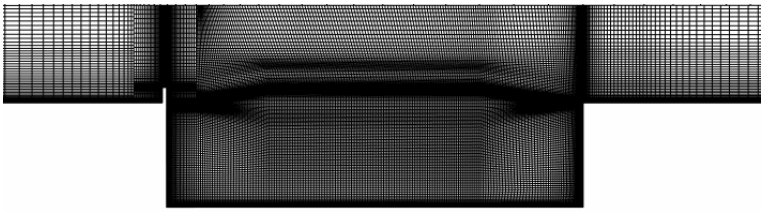

(b) Section view of grid (zoomed in).

Figure 4.50: Structured grid distribution across XY-plane.

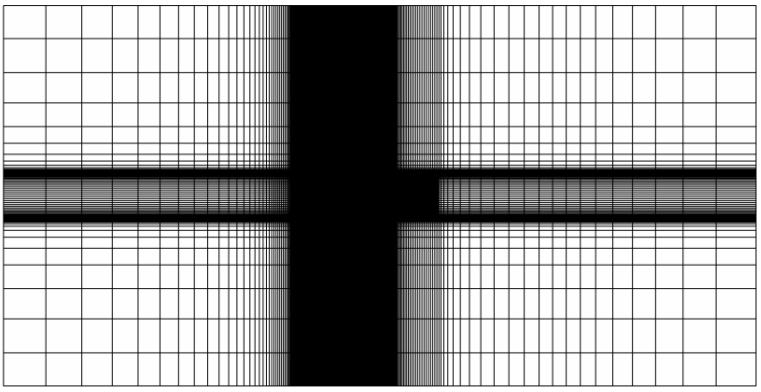

(a) Section view of grid in empty cavity.

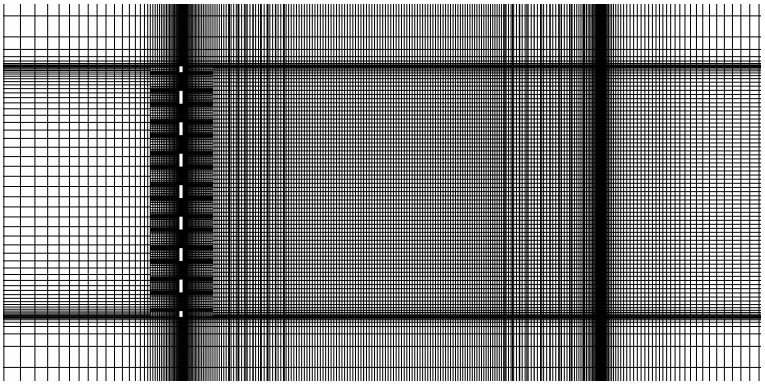

(b) Section view of grid (zoomed in).

Figure 4.51: Structured grid distribution across XZ-plane.

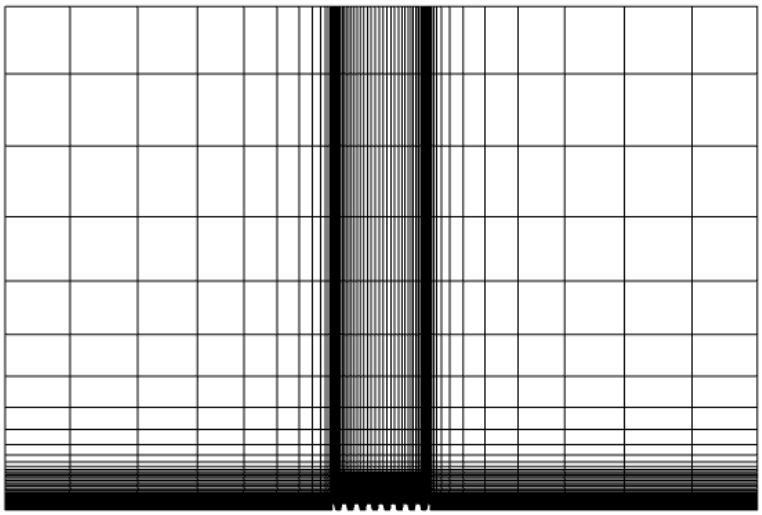

(c) Section view of grid in empty cavity.

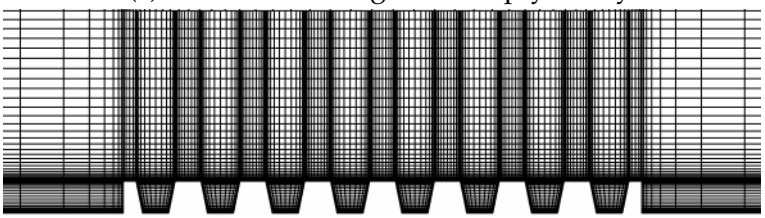

(d) Section view of grid (zoomed in).

Figure 4.52: Structured grid distribution across YZ-plane.

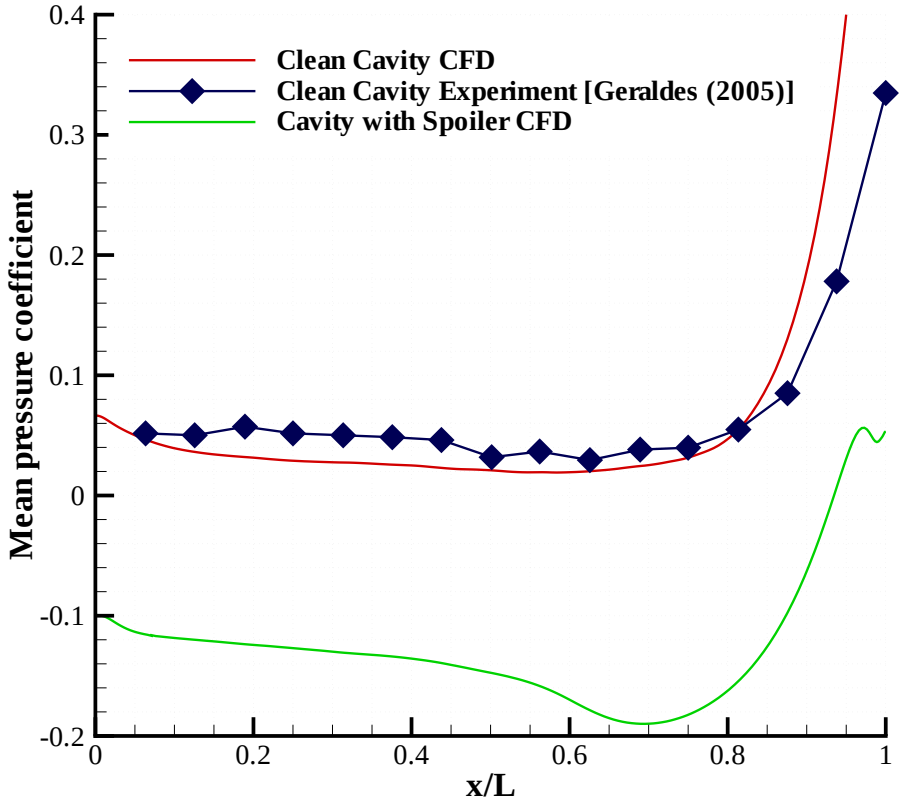

Figure 4.53: Centre line mean C_p along the cavity floor, $L/D = 4$ and $W/D = 2.4$.

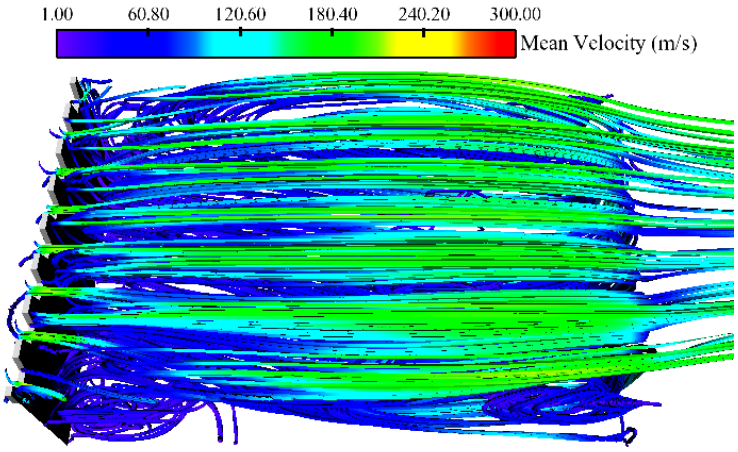

(a) Streamwise streamlines without tornado vortices.

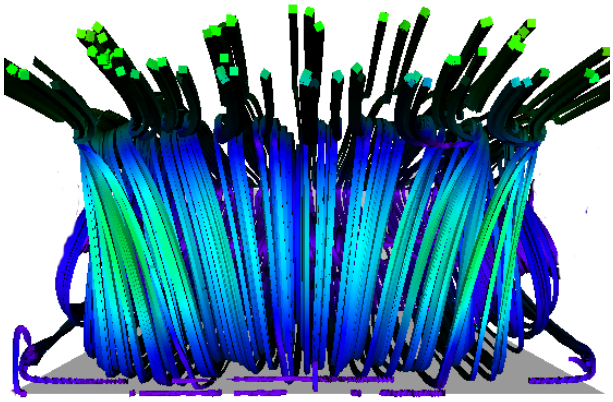

(b) View from the cavity rear wall.

Figure 4.54: Time-mean streamlines for cavity-with-spoiler, $L/D = 4$, $W/D = 2.4$ and $M_\infty = 0.85$.

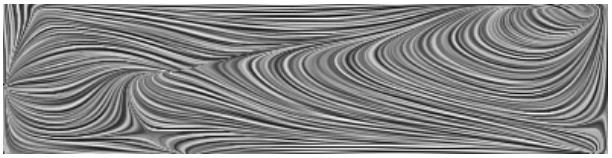

(a) Time mean streamlines at side wall

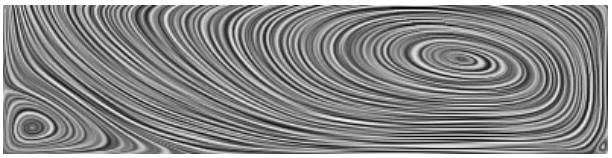

(b) Time mean streamlines in x-y plane at $z/W = 0.1$

(c) Time mean streamlines in x-y plane at $z/W = 0.2$

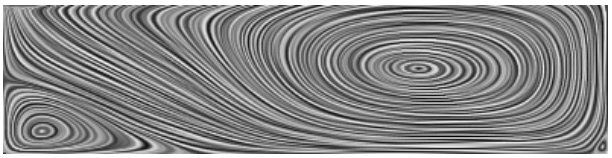

(d) Time mean streamlines in x-y plane at $z/W = 0.3$

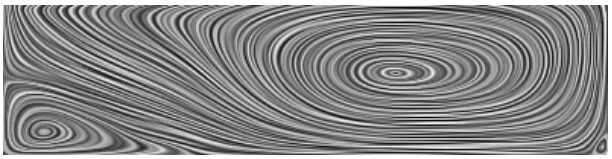

(e) Time mean streamlines in x-y plane at $z/W = 0.4$

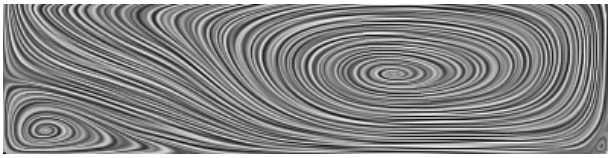

(f) Time mean streamlines in x-y plane at $z/W = 0.5$

(g) Upstream wall.

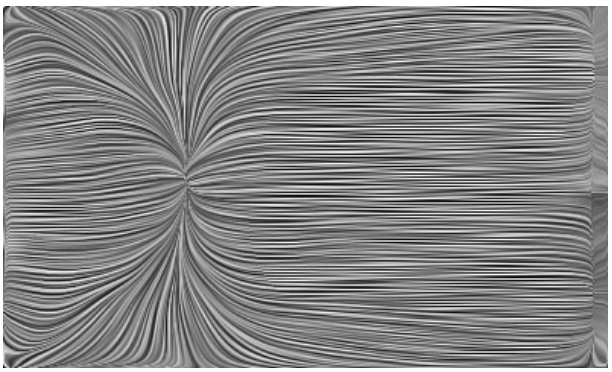

(h) Cavity Floor.

(i) Downstream wall.

Figure 4.55: Mean flow map for cavity-with-spoiler using LIC, $L/D = 4$, $W/D = 2.4$ and $M_\infty = 0.85$.

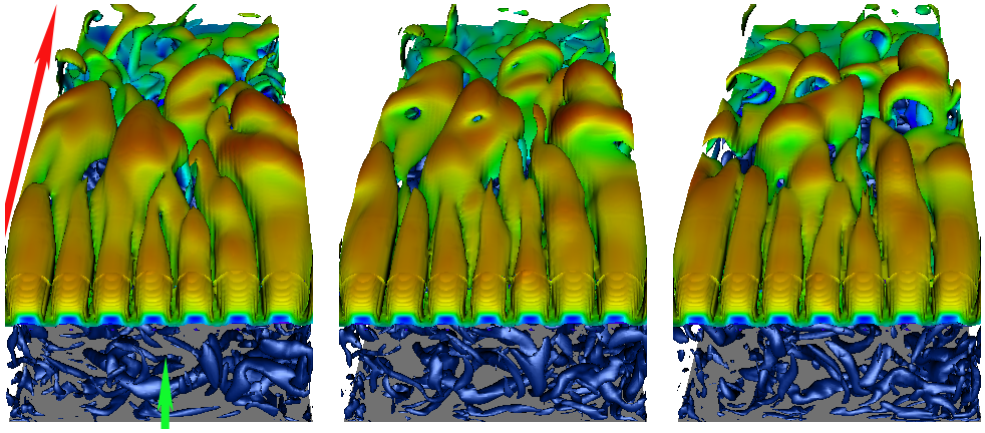

(a) $t \times a_\infty/D = 0.$ (b) $t \times a_\infty/D = 1.4.$ (c) $t \times a_\infty/D = 2.8.$

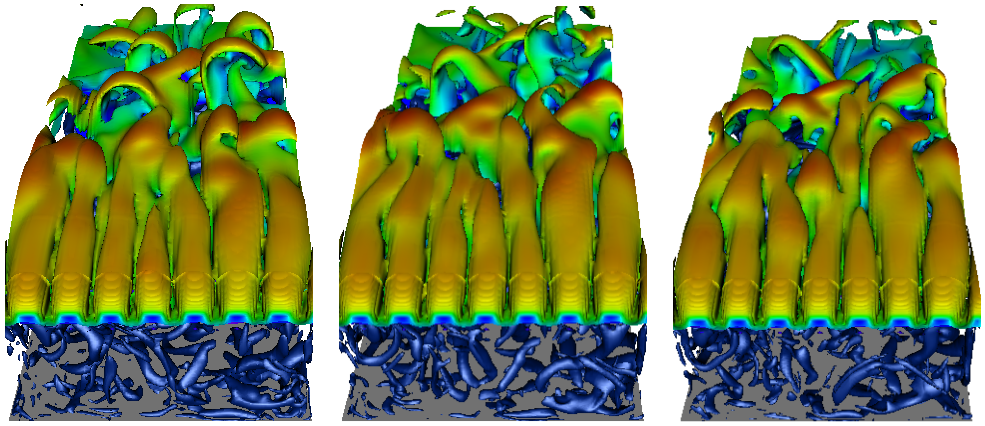

(c) $t \times a_\infty/D = 4.2.$ (c) $t \times a_\infty/D = 5.6.$ (c) $t \times a_\infty/D = 7.0.$

Figure 4.56: Shear layer vortex evolution over one cycle of oscillation: iso-contours of the Q-criterion and vorticity sheet, $L/D = 4$ and $W/D = 2.4$; $M_\infty = 0.85$.

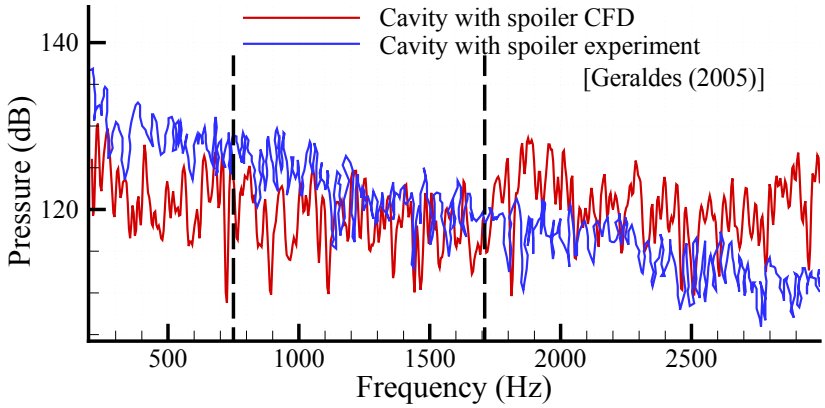

Figure 4.57: Pressure spectra at floor centreline, $x/L = 0.9$.

Chapter 5

Conclusions and Future Work

A summary of the main conclusions and the future work plan are now presented.

5.1 Concluding Remarks

The main aims of this research were to develop a computational research programme capable of resolving cavity flowfields accurately, investigate and describe the cavity flowfields for a range of truly three-dimensional (3D) cavity geometries which fall into the open flow category. In addition, investigation of the effects of missile bodies in the cavity and flow control using passive devices were also part of the research aim.

5.1.1 CAA Solver Results

The first part of this thesis was devoted to the development of a computational solver capable of resolving aeroacoustic phenomena. Central to this work was the need to develop efficient numerical tools to compute accurately the generation and farfield radiation of noise from turbulent flows. To fulfill this requirement, a hybrid strategy has been developed. The approach combines nearfield numerical simulations with a farfield radiation model. To complement the radiation solver, a family of optimized high-order accurate finite-difference compact schemes have been adopted in the CAA code developed in this thesis. An extensive set of two-dimensional numerical simulations were performed to validate the solver. In addition a rectangular cavity with a lip was also simulated which showed the cavity to behave as a Helmholtz resonator, with the fluid volume inside the cavity directly affecting the frequency of oscillation. The sound spectrum was found to be dominated by a single tonal component. Results for the plane rectangular cavity geometries showed greater complexity, with the cavity oscillations often characterized by the presence of multiple modes with similar strength. All the computed results from the CAA solver were found to agree well with experiments. Both the frequency and the magnitude of acoustic pressure were in good agreement with the available experimental data. The solver was also used to study a 3D landing gear geometry to test its robustness and stability for 3D generic curvilinear grids. The result showed the solver to be robust and stable for geometries involving complex structured grids.

5.1.2 CFD Solver Results

Wider cavities had significant spanwise flow compared to a narrow cavity (i.e. $W/D = 1$) and the effect of the side walls is thought to have significance in limiting the spanwise flow in a narrow cavity. Study of the time-mean flowfields inside the empty cavities has, in general, indicated the presence of three dimensionality in the time-averaged flows. The clean cavity and the cavity with a missile have negligible differences in C_p distribution, especially on the front half of the cavity, whereas the difference was more pronounced over the rear half. The presence of a missile in the cavity was found to limit the spanwise flow in the cavity.

Unsteady flow results were also analysed for various configurations. Analysis of the clean cavity unsteady flowfields found that the computed mode frequencies were in good agreement with the experiments although the CFD was found generally to under-predict the magnitude of the first resonant mode. However, CFD was found to record the second mode as dominant whereas the reverse is true in the experiment. A strong oscillation feedback mechanism was found to be present in all the empty cavity cases studied. Pressure peaks were also found to exist at frequencies which were not close to Rossiter modes for the clean cavity cases. This is thought to be the result of the coupling between the spanwise and the streamwise flow fluctuations. Spanwise flow, however, is less evident in cavity-with-missile cases and it had multiple Rossiter modes co-existing without coupling (or any amplitude modulations). The blockage effect of the missile on the spanwise flow is thought to be the reason which limits the interaction of spanwise and streamwise flow fluctuations undergoing non-linear coupling to result in amplitude modulations. Also in the cavity-with-missile cases, the separated shear layer was found to undergo warping in two parts due to the presence of the missile (i.e. the missile is seen to act as a central wall which promotes warping of the vortices on either side). As the vortical structures in these regions reach the trailing edge, the vortex axis is aligned with the streamwise direction. Then the 3D flow in the end wall regions leads to the formation of streamwise vortices. The overall effect on the flowfield is that the missile in the cavity divides the cavity flow such that the resulting flowfield behaves similar to two narrow cavity flowfields.

5.1.3 Flow Control Results

The tone suppression effectiveness of using a serrated spoiler on the upstream cavity edge was also studied computationally. To understand the flow physics behind the tone suppression effects of passive devices (spoiler in this case) detailed analysis of time-averaged

as well as unsteady flowfields were performed. The mean flow study indicated the heavy pressure loss due to the presence of the spoiler. The dissipation (at Kolmogorov scale) and self-regeneration of turbulent kinetic energy all takes place in the boundary layer and the spoiler acts as an external device that extracts energy from the flow, resulting in the heavy pressure loss. The computed unsteady result showed complete suppression of resonant modes, consistent with the experiment. Based on the CFD results a mechanism by which the spoiler suppresses the cavity resonant modes has been suggested in this thesis. It is seen that the spoiler acts as an energy-extracting device, thus dissipating the turbulent energy from the approaching boundary layer. This then reduces the widely-occurring phenomenon (in empty cavities) of cross-stream warping of transverse vortical structures in the free shear layer. Unsteady flow within the cavity, therefore, has insufficient energy to excite flapping of this free shear layer to cause resonance.

5.2 Future Work

The computational studies presented in this research thesis have developed a high-order CAA solver capable of resolving aerodynamically generated noise. The solver in its current state requires a structured grid domain (and one-to-one matching at block interfaces while generating multi-block grids). However, one-to-one matching at block interfaces in multi-block grids can cause significant difficulty for complex geometrical configurations. Also, an attempt to create a structured grid for a complex geometry causes highly-skewed cells which, in turn, results in inaccurate calculations. The grid-generation issue mentioned above can be improved by the use of a zonal, or patched, grid method. Hence addition of the overset and overlapping grid capabilities in the solver is suggested. The solver currently uses an explicit time-marching method which restricts the time step sizes to excessively small values determined by the stability condition that the *CFL* number should be less than 1. This results in very long and expensive computing times. An implicit time-stepping with sub-iterations (to maintain the high-order accuracy in time) is, therefore, suggested for implementation in the solver.

A final recommendation is to explore other flow control methods based on active control techniques to suppress the high acoustic fluctuations seen in the computational results. Such an approach would overcome the high pressure loss seen with the spoiler, which is a disadvantage of this simple passive approach.

References

(2005). *FLUENT 6.2 User Guide*. Fluent Inc.

Ahuja, K. K. & Mendoza, J. (1995). Effects of cavity dimensions, boundary layer and temperature on cavity noise with emphasis on bench mark data to validate computational aeroacoustic codes. Technical Report NASA–CR–4653, NASA.

Arunajatesan, S. & Sinha, N. (2003). Hybrid rans-les modeling for cavity aeroacoutics predictions. *International Journal of Computational Aeroacoustics*, *2*(1), 65–93.

Ashcroft, G. & Zhang, X. (2003). Optimized prefactored compact schemes. *Journal of computational physics*, *190*, 459–477.

Atvars, K., Knowles, K., Ritchie, S. A., & Lawson, N. J. (2009). Experimental and computational investigation of an ŚopenŠ transonic cavity flow. *Proceedings of the Institution of Mechanical Engineers, Part G: Journal of Aerospace Engineering*, *23*(4), 357–368.

Benkenida, A., Bohbot, J., & Jouhaud, J. C. (2002). Patched grid and adaptive mesh refinement strategies for the calculation of the transport vortices. *International Journal of Numerical Methods in Fluids*, *40*, 855–873.

Brentner, K. S. (1986). Prediction of helicopter discrete frequency rotor noise - a computer program incorporating realistic blade motions and advanced formulations. (NASA–TM–87721).

Brentner, K. S. & Farassat, F. (1998). Analytical comparison of the acoustic analogy and kirchhoff formulation for moving surfaces. *AIAA Journal*, *36*(8), 1379–1386.

Cattafesta, L., Shukla, D., Garg, S., & Ross, J. (1999). Development of an adaptive weapons-bay suppression system. Number AIAA–99–1901, Bellevue, Washington, USA. 5^{th} AIAA/CEAS Aeroacoustics Conference and Exhibit.

Cattafesta, L., Song, Q., Williams, D., Rowley, C., & Alvi, F. (2008). Active control of flow-induced cavity oscillations. *Progress in Aerospace Sciences*, *44*(7-8), 479–502.

Cattafesta, L., Williams, D., Rowley, C., & Alvi, F. (2003). Review of active control of flow-induced cavity resonance. Number AIAA–2003–3567, Orlando, Florida, USA. 33^{rd} AIAA Fluid Dynamics Conference.

Charwat, A. F., Roos, J. N., Dewey, F. C., & Hitz, J. A. (1961a). An investigation of separated flows Part 1 : The Pressure Field. *Journal of Aerospace Sciences*, *28*(6), 457–470.

Charwat, A. F., Roos, J. N., Dewey, F. C., & Hitz, J. A. (1961b). An investigation of separated flows Part 2 : Flow in the Cavity and Heat Transfer. *Journal of Aerospace Sciences*, *28*(7), 513–527.

Chen, X. & Zha, G.-C. (2006). Implicit application of non-reflective boundary conditions for NavierŰStokes equations in generalized coordinates. *International Journal of Numerical Methods in Fluids*, *50*, 767–793.

Chung, Y. M. & Tucker, P. G. (2003). Accuracy of higher-order finite difference schemes on non-uniform grids. *AIAA Journal*, *41*(8).

Colonius, T. (2001). An overview of simulation, modeling, and active control of flow/acoustic resonance in open cavities. Number AIAA–2001–0076.

Crighton, D. G., Dowling, A. P., Williams, F. J. E., Heckl, M., & Leppington, F. G. (1992). *Modern Methods in Analytical Acoustics, Lecture Notes*, chapter 11, (pp. 334–342). Springer-Verlag.

Curle, N. (1955). The influence of solid boundaries upon aerodynamic sound. *Proceedings of Royal Society*, *A*(231), 505–514.

DeBonis, J. R. & Scott, J. N. (2002). Study of the error and efficiency of numerical schemes for computational aeroacoustics. *AIAA Journal*, *40*(2), 227–234.

Dix, R. E. & Bauer, R. C. (2000). Experimental and predicted acoustic amplitudes in a rectangular cavity. Number AIAA–2002–0472.

East, L. F. (1966). Aerodynamically induced resonance in rectangular cavities. *Journal of Sound and Vibration*, *3*, 277–287.

ESDU (2004). *Aerodynamics and aero-acoustics of rectangular planform cavities. Part I: Time-averaged flow*. IHS ESDU, London, UK. ESDU Data Item 02008.

Farassat, F. (1994). Introduction to generalized functions with applications in aerodynamics and aeroacoustics. Technical Report 1994–3428, NASA Langley Research Center.

Farassat, F. & Succi, G. P. (1983). The prediction of helicopter discrete frequency noise. *Vertica*, *7*, 309–320.

Ffowcs-Williams, J. E. & Hawkings, D. L. (1969). Sound generation by turbulence and surfaces in arbitrary motion. *Philosophical Transactions of Royal Soccietу*, *A*(264), 321–342.

Francescantonio, P. D. (1997). A new boundary integral formulation for the prediciton of sound radiation. *Journal of Sound and Vibration*, *202*(4), 491–509.

Gaitonde, D. V. & Visbal, M. R. (1999). Further development of a navier-stokes solution procedure based on higher-order formulas. Number AIAA–1999–0557. AIAA.

Geraldes, P. (2005). *Instabilities in Transonic Cavity Flows*. PhD thesis, Cranfield University.

Gharib, M. & Roshko, A. (1991). The effect of flow oscillation on cavity drag. *Journal of Fluid Engineering*, *113*, 369–376.

Grace, S. M. (2001). An overview of computational aeroacoustic techniques applied to cavity noise prediction. Number AIAA–2001–0510, Reno, Nevada, USA. 39^{th} AIAA Aerospace Sciences Meeting and Exhibit.

Guo, Y. (2008). A study on local flow variations for landing gear noise research. Number AIAA–2008–2915, Vancouver, British Columbia. 14^{th} AIAA/CEAS Aeroacoustics Conference.

Hedges, L. S., Travin, A. K., & Spalart, P. R. (2002). Detached-eddy simulation over a simplified landing gear. *ASME Journal of Fluid Engineering*, *124*(2), 413Ű–423.

Heller, H., Holmes, D., & Covert, E. (1971). Flow-induced pressure oscillations in shallow cavities. *Journal of Sound and Vibration*, *18*, 545–553.

Helmholtz, H. (1875). *On the sensations of tone as a physiological basis for the theory of music*. Thoemmes Press, London.

Henderson, B. (2000). Category 6 - automobile noise involving feedback. Ohio Aerospace Institute. Third Computational Aeroacoustics Workshop. Published in **?**.

Henderson, J., Badcock, K. J., & Richards, B. E. (2000). Understanding subsonic and transonic open cavity flows and suppression of cavity tones. Number AIAA–2000–0658, Reno, Nevada, USA. 38^{th} AIAA Aerospace Sciences Meeting and Exhibit.

Hixon, R. (2000). Prefactored small-stencil compact schemes. *Journal of Computational Physics*, *165*, 522–541.

Hu, F. Q., Hussaini, M. Y., & Manthey, J. (1996). Low-dissipation and -dispersion runge-kutta schemes for computational acoustics. *Journal of Computational Physics*, *124*, 177–191.

Huang, X. & Weaver, D. (1991). Active control of shear layer oscillations across a cavity in the presence of pipeline acoustic resonance. *Journal of Fluids and Structures*, *5*(2), 207–219.

Joeng, J. & Hussain, F. (1995). On the identification of a vortex. *Journal of Fluid Mechanics*, *285*, 69–94.

Jovic, S. & Driver, D. M. (1994). Backward-facing step measurements at low Reynolds number, Re_h = 5000. Technical Report TM–1994–108807, NASA Ames Research Center.

Jr., R. L. S., Plentovich, E. B., Tracey, M. B., & Hemsch, M. J. (2002). Measurements of store forces and moments and cavity pressures for a generic store in and near a box cavity at subsonic and transonic speeds. Technical Report NASA–TM–4611, NASA.

Kasper, J. H., Lockard, D. P., Khorrami, M. R., & Streett, C. L. (2004). Investigation of volumetric sources in airframe noise simulations. Number AIAA–paper–2004–2805, Manchester, United Kingdom. 10^{th} AIAA/CEAS Aeroacoustics Conference.

Kim, J. W. (2007). Optimised boundary compact finite difference schemes for computational aeroacoustics. *Journal of Computational Physics*, *225*(1), 995–1019.

Kim, J. W. & Lee, D. J. (1996). Optimised compact finite difference schemes with maximum resolution. *AIAA Journal*, *34*(5), 887–893.

Kim, J. W. & Lee, D. J. (2000a). Adaptive nonlinear artificial dissipation model for computational aeroacoustics. Number AIAA–2000–1978, Lahaina, HI, USA. 21st AIAA Aeroacoustics Conference.

Kim, J. W. & Lee, D. J. (2000b). Generalized characteristic boundary conditions for computational aeroacoustics. *AIAA Journal*, *38*(11), 2040–2049.

Kim, J. W. & Lee, D. J. (2003). Characteristic interface conditions for multiblock high-order computation on singular structured grid. *AIAA Journal*, *41*(12), 2341–2348.

Kim, J. W. & Lee, D. J. (2004). Generalized characteristic boundary conditions for computational aeroacoustics, part 2. *AIAA Journal*, *42*(1), 47–55.

Kim, S., Dai, Y., Koutsavdis, E. K., Sovani, S., Kadam, N. A., & Ravuri, K. M. R. (2003). A versatile implementation of acoustic analogy based noise prediction method in a general-purpose cfd code. Number AIAA–2003–3202, Hilton Head,South Carolina, USA. 9^{th} AIAA/CEAS Aeroacoustics Conference and Exhibit.

Knowles, R. D., Finnis, M. V., Saddington, A. J., & Knowles, K. (2006). Planar visualization of vortical flows. *Proceedings of IMechE Part G: Journal of Aerospace Engineering*, *220*(G6), 619–627. Special Issue on Integrating CFD and Experiments in Aerodynamics.

Krishnamurty, K. (1955). Acoustic radiation from two-dimensional rectangular cutouts in aerodynamic surfaces. Technical Report TN–3487, NACA.

Krist, S. L., Biedron, R. T., & Romsey, C. L. (1998). CFL3D User manual (version 5.0). Technical Report TM–1998–208444, NASA.

Kurbatskii, K. A. & Mankbadi, R. R. (2004). Review of computational aeroacoustics algorithms. *International Journal of Computational Fluid Dynamics*, *18*(6), 533–546.

Lawson, S. J. & Barakos, G. N. (2009). Assessment of passive flow control for transonic cavity flow using detached-eddy simulation. *Journal of Aircraft*, *46*(3), 1009–1029.

Lele, S. K. (1992). Compact finite difference schemes with spectral-like resolution. *Journal of Computational Physics*, *103*(16), 16–42.

Lerat, A. & Wu, C. Z. N. (1996). Stable conservative multidomain treatments for implicit Euler solvers. *Journal of computational physics*, *123*, 45–64.

Lighthill, M. J. (1952). On sound generated aerodynamically. i. general theory. *Proceedings of Royal Society*, *A*(211), 564–587.

Manoha, E., Herrero, C., Sagaut, P., & Redonnet, S. (2002). Numerical prediction of airfoil aerodynamic noise. Number AIAA–paper–2002–2573, Breckenridge, Colorado, USA. 8^{th} AIAA/CEAS Aeroacoustics Conference.

Mathey, F., Morin, O., Caruelle, B., & Debatin, K. (2006). Simulation of aeroacoustic sources in aircraft climate control systems. Number AIAA–2006–2493, Cambridge, Massachusetts, USA. 12^{th} AIAA/CEAS Aeroacoustics Conference and Exhibit.

Norton, D. A. (1952). Investigation of b47 bomb bay buffet. Technical Report DN–D12675, Boeing Airplane Co.

Owen, T. W. (1958). Techniques of pressure-fluctuation measurements employed in the rae low speed wind tunnels. Technical Report A.R.C.–20780, AGARD.

Plentovich, E. (1992). Three-dimensional cavity flow fields at subsonic and transonic speeds. Technical Report NASA–TM–4209, NASA Langley Research Center.

Plumblee, H., Gibson, J. S., & Lassiter, L. (1962). A theoretical and experimental investigation of the acoustic response of cavities in aerodynamic flow. Technical Report TR–61–75, WADD.

Poinsot, T. J. & Lele, S. K. (1992). Boundary conditions for direct simulations of compressible viscous flow. *Journal of Computational Physics*, *101*(1), 104–129.

Powell, A. (1953). On edge tone and associated phenomena. *Acoustica*, *3*(12), 233–243.

Pulliam, T. H. & Steger, J. L. (1980). Implicit finite difference simulation of three dimensional compressible flows. *AIAA Journal*, *18*(2), 159–167.

Rai, M. M. (1986a). A conservative treatment of zonal boundaries for euler equation calculations. *Journal of Computational Physics*, *62*, 472–503.

Rai, M. M. (1986b). An implicit, conservative, zonal-boundary scheme for euler equation calculations. *Computers and Fluids*, *14*, 295–319.

Raman, G. & McLaughlin, D. K. (2000). Recent aeroacoustics research in the United States. *Noise and Vibration Worldwide*, *31*(10), 15–20.

Raman, G., Raghu, S., & Bencic, T. (1999). Cavity resonance suppression using miniature fluidic oscillators. Number AIAA–1999–1900, Seattle, Washington, USA. 5^{th} AIAA Aeroacoustics Conference.

Rayleigh, J. (1896). *The theory of sound*. Macmillan Company Ltd, London.

Renaut, V. L. & Rosemary, A. (1997). Computing aerodynamically generated noise. *Annual Review of Fluid Mechanics*, *29*, 161–199.

Ringshia, A., Ravetta, P., Ng, W., & Burdisso, R. (2006). Aerodynamic measurements of the 777 main landing gear model. Number AIAA–2006–2625, Cambridge, Massachusetts. 12^{th} AIAA/CEAS Aeroacoustics Conference.

Ritchie, S. A. (2005). *Non-Intrusive Measurements and Computations of Transonic Cavity Flows with Applications to Aircraft Stores Release*. PhD thesis, Cranfield University.

Rizzetta, D. P. & Visbal, M. R. (2003). Large-eddy simulation of supersonic cavity flowfields including flow control. *AIAA Journal*, *41*(8), 1452–1462.

Rockwell, D. & Naudascher, E. (1978). Review-self sustaining oscillations of flow past cavities. *Journal of Fluids Engineering*, *100*, 152–165.

Rockwell, D. & Naudascher, E. (1979). Self-sustained oscillations of impinging free shear layers. *Annual Review Fluid Mechanics*, *11*, 67–94.

Rossiter, J. (1966). Wind-tunnel experiments on the flow over rectangular cavities at subsonic and transonic speeds. Technical Report 3438, Aeronautical Research Council Reports and Memoranda.

Schlichting, H. (1979). *Boundary-Layer Theory* (7^{th} ed.). McGraw Hill.

Singer, B. A. & Guo, Y. (2004). Development of computational aeroacoustic tools for airframe noise calculations. *International Journal of Computational Fluid Dynamics*, *18*(6), 455–469.

Spalart, P. R. & Allmaras, S. R. (1992). A one-equation turbulence model for aerodynamic flows. Number AIAA–1992–0439, Reno, Nevada, USA. 30^{th} AIAA Aerospace Sciences Meeting and Exhibit.

Spalart, P. R. & Allmaras, S. R. (1997). Comments on the feasibility of LES for wings and on a hybrid RANS/LES approach. Ruston, Louisiana, USA. Proceedings of first AFOSR international conference on DNS/LES.

Spalart, P. R., Deck, S., Shur, M. L., Squires, K. D., Strelets, M. K., & Travin, A. (2006). A new version of detached-eddy simulation, resistant to ambiguous grid densities. *Theoritical and Computational Fluid Dynamics*, *20*, 181–195.

Srinivisan, S. & Baysal, O. (1991). Navier-Stokes calculations of transonic flow past cavities. *Journal of Fluid Engineering*, *113*, 369–376.

Stallings, R. & Wilcox, F. (1987). Experimental cavity pressure distributions at supersonic speeds. Technical Report NASA–TP–2683, NASA.

Sumi, T. & Kurotaki, T. (2006). Generalized characteristic interface conditions for accurate multi-block computations. Number AIAA–2006–1272, Reno, Nevada, USA. 44^{th} AIAA Aerospace Sciences Meeting and Exhibit.

Sumi, T., Kurotaki, T., & Hiyama, J. (2007). Practical multi-block computations with generalized characteristic interface conditions around complex geometry. Number AIAA–2007–4471, Miami, Florida, USA. 18^{th} AIAA Computational Fluid Dynamics Conference.

Sunderland, J. C. & Kennedy, C. A. (2003). Improved boundary conditions for viscous, reacting, compressible flows. *Journal of Computational Physics*, *191*, 502–524.

Taborda, N. M., Bray, D., & Knowles, K. (2001). Visualisation of three-dimensional cavity flows. Number ExHFT5, Thessaloniki, Greece. In 5th World Conference on Experimental Heat Transfer, Fluid Mechanics and Thermodynamics.

Takeda, K. & Shieh, C. (2004). Cavity tones by computational aeroacoustics. *International Journal of Computational Fluid Dynamics*, *18*(6), 439–454.

Tam, C. K. W. (2002). Computational aeroacoustics examples showing the failure of the acoustic analogy theory to identify the correct sources. *Journal of Computational Acoustics*, *10*(4), 387Ű–405.

Tam, C. K. W. & Block, P. J. W. (1978). On the tones and pressure oscillations induced by flow over rectangular cavities. *Journal of Fluid Mechanics*, *89*, 373–399.

Tam, C. K. W., Hardin, J. C., & (Eds.) (1997). Second computational aeroacoustics workshop on benchmark problems. Technical Report CP–1997–3352, NASA Langley Research Center.

Tam, C. K. W. & Webb, J. C. (1993). Dispersion-relation-perserving finite difference schemes for computational acoustics. *Journal of Computational Physics*, *107*, 262–281.

Thomas, P. D. & Lombard, C. K. (1979). Geometric conservation law and its application to flow computations on moving grids. *AIAA Journal*, *17*(10), 1030–1058.

Thompson, K. W. (1987). Time dependent boundary conditions for hyperbolic systems. *Journal of Computational Physics*, *68*(1), 1–24.

Thompson, K. W. (1990). Time dependent boundary conditions for hyperbolic systems ii. *Journal of Computational Physics*, *89*(2), 439–461.

Tracy, M. B. & Plentovich, E. (1992). Measurements of fluctuating pressure in a rectangular cavity in transonic flow at high Reynolds number. Technical Report NASA–TM–4363, NASA Langley Research Center.

Tracy, M. B. & Plentovich, E. (1993). Characterization of cavity pressure flow fields data obtained in Langley 0.3m transonic cryogenic tunnel. Technical Report NASA–TM–4436, NASA Langley Research Center.

Tracy, M. B. & Plentovich, E. B. (1997). Cavity unsteady-pressure measurements at subsonic and transonic speeds. Technical Report NASA–TP–3669, NASA Langley Research Center.

Vakili, A. & Gauthier, C. (1994). Control of cavity flow by upstream mass-injection. *Journal of Aircraft*, *31*(1), 90–96.

Visbal, M. R. & Gaitonde, D. V. (2000). Pade-type higher-order boundary filters for the navier-stokes equations. *AIAA Journal*, *11*, 2103Ű–2112.

Visbal, M. R. & Gaitonde, D. V. (2001). Very high-order spatially implicit schemes for computational acoustics on curvilinear meshes. *Journal of Computational Acoustics*, *9*(4), 1259Ű–1286.

Visbal, M. R. & Gaitonde, D. V. (2002). On the use of higher-order finite-difference schemes on curvilinear and deforming meshes. *Journal of Computational Physics*, *181*(1), 155–185.

Whitham, G. B. (1974). *Linear and Nonlinear Waves*. Wiley, New York, 1974 (Page no. 124).

Wilcox, D. C. (2006). *Turbulence Modeling for CFD* (3^{rd} Edition. ed.). DCW Industries.

Xiao, X., Edwards, J. R., & Hassan, H. A. (2003). Inflow boundary conditions for hybrid large eddy/reynolds averaged navierŰstokes simulations. *AIAA Journal*, *41*(8), 1481–1489.

Xiao, X., Edwards, J. R., & Hassan, H. A. (2004). Blending functions in hybrid large-eddy/reynolds-averaged navierŰstokes simulations. *AIAA Journal*, *42*(12), 2508–2515.

Yoo, C. S. & Im, H. G. (2007). Characteristic boundary conditions for simulations of compressible reacting flows with multi-dimensional, viscous and reaction effects. *Combustion Theory and Modelling*, *11*(2), 259–286.

Yoo, C. S., Wang, Y., Trouve, A., & Im, H. G. (2005). Characteristic boundary conditions for direct simulations of turbulent counterflow flames. *Combustion Theory and Modelling*, *9*(4), 617–646.

Yu, Y. H. (1977). Measurements of sound radiation from cavities at subsonic speeds. *Journal of Aircraft*, *14*, 838–843.

Appendices

Appendix A

Derivation of Characteristic Boundary Conditions

Characteristic interface boundary treatments have been well documented [e.g. Kim & Lee (2003); Sumi & Kurotaki (2006); Sumi et al. (2007)] although these methods are only valid for inviscid and laminar flows. As far as the author knows, all the existing interface treatments based on the method of characteristics lack a satisfactory interface matching of turbulence quantities. This work proposes a characteristic interface condition for complex geometries which addresses these issues and also ensures multi-dimensionality. The method does not neglect any transverse terms during characteristic wave amplitude calculations and all the viscous source terms are also taken into account in the derivation. For turbulent flow problems, a simple and robust technique is proposed to match turbulence quantities at the multi-block interface.

A.1 Navier-Stokes Equations in Characteristic form

The time-dependent, three-dimensional Navier-Stokes equations can be expressed, in Cartesian coordinates as:

$$\frac{\partial \mathbf{Q}}{\partial t} + \frac{\partial \mathbf{E}}{\partial x} + \frac{\partial \mathbf{F}}{\partial y} + \frac{\partial \mathbf{G}}{\partial z} = \mathbf{S}_v. \tag{A.1}$$

Where the conservative variables and the inviscid flux variables are represented as

$$\mathbf{Q} = \begin{bmatrix} \rho \\ \rho u \\ \rho v \\ \rho w \\ \rho e_t \end{bmatrix}, \quad \mathbf{E} = \begin{bmatrix} \rho u \\ \rho u^2 + p \\ \rho uv \\ \rho uw \\ (\rho e_t + p)u \end{bmatrix}, \quad \mathbf{F} = \begin{bmatrix} \rho v \\ \rho uv \\ \rho v^2 + p \\ \rho vw \\ (\rho e_t + p)v \end{bmatrix},$$

$$\mathbf{G} = \begin{bmatrix} \rho w \\ \rho uw \\ \rho vw \\ \rho w^2 + p \\ (\rho e_t + p)w \end{bmatrix}$$

and $\mathbf{S}_v$ is the source term containing the viscous flux derivatives represented as

$$\mathbf{S}_v = \frac{\partial \mathbf{E}_v}{\partial x} + \frac{\partial \mathbf{F}_v}{\partial y} + \frac{\partial \mathbf{G}_v}{\partial z}.$$

$$\mathbf{E}_v = \begin{bmatrix} 0 \\ \tau_{xx} \\ \tau_{xy} \\ \tau_{xz} \\ u\tau_{xx} + v\tau_{xy} + w\tau_{xz} + q_x \end{bmatrix}, \quad \mathbf{F}_v = \begin{bmatrix} 0 \\ \tau_{yx} \\ \tau_{yy} \\ \tau_{yz} \\ u\tau_{yx} + v\tau_{yy} + w\tau_{yz} + q_y \end{bmatrix}$$

$$\text{and } \mathbf{G}_v = \begin{bmatrix} 0 \\ \tau_{zx} \\ \tau_{zy} \\ \tau_{zz} \\ u\tau_{zx} + v\tau_{zy} + w\tau_{zz} + q_z \end{bmatrix}$$

These equations can also be written, in quasi-linear form, as:

$$\frac{\partial \mathbf{Q}}{\partial t} + \mathbf{A}\frac{\partial \mathbf{Q}}{\partial x} + \mathbf{B}\frac{\partial \mathbf{Q}}{\partial y} + \mathbf{C}\frac{\partial \mathbf{Q}}{\partial z} = \mathbf{S}_v \tag{A.2}$$

where $\mathbf{A} = \frac{\partial \mathbf{E}}{\partial \mathbf{Q}}$, $\mathbf{B} = \frac{\partial \mathbf{F}}{\partial \mathbf{Q}}$ and $\mathbf{C} = \frac{\partial \mathbf{G}}{\partial \mathbf{Q}}$ are Jacobian matrices. Eq. A.2 can also be written in terms of primitive variables, with $\mathbf{U}$ being the primitive variables vector, as:

$$\frac{\partial \mathbf{U}}{\partial t} + \mathbf{a}\frac{\partial \mathbf{U}}{\partial x} + \mathbf{b}\frac{\partial \mathbf{U}}{\partial y} + \mathbf{c}\frac{\partial \mathbf{U}}{\partial z} = \mathbf{S}_p \tag{A.3}$$

where $\mathbf{S}_p$ is the viscous flux vector and $\mathbf{a}$, $\mathbf{b}$ and $\mathbf{c}$ are the respective Jacobian matrices in primitive variables form. The relation between the Jacobian matrices in Eqns A.2 and A.3 can be written as:

$\mathbf{A} = \mathbf{M}\mathbf{a}\mathbf{M}^{-1}$ and so on.

where $\mathbf{M}$ is the transformation matrix between the conservative variables and the primitive variables and $\mathbf{M}^{-1}$ is its inverse. Note here that $\mathbf{a}$ and $\mathbf{A}$ have the same eigenvalues. In

order to express these in characteristic form, the above sets of equations are transformed to the non-conservative form in the generalized coordinate system (ξ, η, ζ):

$$\frac{\partial \mathbf{Q}}{\partial t} + \mathbf{N}_\xi \frac{\partial \mathbf{Q}}{\partial \xi} + \mathbf{N}_\eta \frac{\partial \mathbf{Q}}{\partial \eta} + \mathbf{N}_\zeta \frac{\partial \mathbf{Q}}{\partial \zeta} = \mathbf{S}_v \tag{A.4}$$

$$\frac{\partial \mathbf{U}}{\partial t} + \mathbf{n}_\xi \frac{\partial \mathbf{U}}{\partial \xi} + \mathbf{n}_\eta \frac{\partial \mathbf{U}}{\partial \eta} + \mathbf{n}_\zeta \frac{\partial \mathbf{U}}{\partial \zeta} = \mathbf{S}_p \tag{A.5}$$

where $\mathbf{N}_\kappa = \kappa_x \mathbf{A} + \kappa_y \mathbf{B} + \kappa_z \mathbf{C}$ and $\mathbf{n}_\kappa = \kappa_x \mathbf{a} + \kappa_y \mathbf{b} + \kappa_z \mathbf{c}$ (with $\kappa = \xi$, η or ζ) are flux Jacobian matrices and are interrelated by $\mathbf{N}_\kappa = \mathbf{M}\mathbf{n}_\kappa\mathbf{M}^{-1}$.

The flux Jacobian matrix $\mathbf{n}_\kappa$ can be diagonalized by its left eigenvector matrix $\mathbf{S}^{-1}$ as:

$$\mathbf{n}_\kappa = \mathbf{S}\mathbf{\Lambda}_\kappa\mathbf{S}^{-1} \tag{A.6}$$

Here $\mathbf{\Lambda}_\kappa$ is the eigenvalue matrix of $\mathbf{n}_\kappa$. Similarly, the flux Jacobian matrix $\mathbf{N}_\kappa$ can also be diagonalized by its left eigenvector matrix $\mathbf{P}^{-1}$ and has the same eigenvalue matrix as that of $\mathbf{n}_\kappa$ i.e.,

$$\mathbf{N}_\kappa = \mathbf{P}\mathbf{\Lambda}_\kappa\mathbf{P}^{-1} \tag{A.7}$$

where $\mathbf{P} = \mathbf{MS}$ and $\mathbf{P}^{-1} = \mathbf{S}^{-1}\mathbf{M}^{-1}$. All the transformation matrices $\mathbf{M}$, $\mathbf{M}^{-1}$, $\mathbf{S}$ and $\mathbf{S}^{-1}$ are given in Section A.6.

The eigenvalue matrix in Eqns A.6 and A.7 is a diagonal matrix and is given by:

$$\mathbf{\Lambda}_\kappa = \begin{pmatrix} \mathbf{V}_\kappa & 0 & 0 & 0 & 0 \\ 0 & \mathbf{V}_\kappa & 0 & 0 & 0 \\ 0 & 0 & \mathbf{V}_\kappa & 0 & 0 \\ 0 & 0 & 0 & \mathbf{V}_\kappa + \mathbf{C}_\kappa & 0 \\ 0 & 0 & 0 & 0 & \mathbf{V}_\kappa - \mathbf{C}_\kappa \end{pmatrix} \tag{A.8}$$

Where $\mathbf{V}_\kappa = \mathbf{u} \cdot \kappa$, $\mathbf{C}_\kappa = c\,|\kappa|$ and $\kappa = (\kappa_x, \kappa_y, \kappa_z)$ with $\kappa_x = \partial\kappa/\partial x$ (metrics of coordinate transformation) etc. Here κ is an index to represent the generalized coordinate axis direction.

In order to analyse and derive the boundary conditions, the Navier-Stokes equations represented by Eqns A.4 and A.5 are transformed into characteristics form. In the following, only the derivations for the ξ direction will be presented but those for the other directions are similar. Representing the total spatial derivative terms (including viscous source terms but excluding the inviscid spatial derivatives in the ξ direction) by vectors $\mathbf{S}_c$ and $\mathbf{S}_d$ respectively for Equations A.6 and A.7, the Eqns A.6 and A.7 can be written as:

$$\frac{\partial \mathbf{Q}}{\partial t} + \mathbf{N}_\xi \frac{\partial \mathbf{Q}}{\partial \xi} + \mathbf{S}_c = 0 \tag{A.9}$$

$$\frac{\partial \mathbf{U}}{\partial t} + \mathbf{n}_\xi \frac{\partial \mathbf{U}}{\partial \xi} + \mathbf{S}_d = 0 \tag{A.10}$$

The source terms in Eqns A.9 and A.10 are related by the relation:

$$\mathbf{S}_d = \begin{bmatrix} S_{c1} \\ \dfrac{S_{c2} - uS_{c1}}{\rho} \\ \dfrac{S_{c3} - vS_{c1}}{\rho} \\ \dfrac{S_{c4} - wS_{c1}}{\rho} \\ (\gamma - 1)\left[0.5\mathbf{u}^2 S_{c1} - uS_{c2} - vS_{c3} - wS_{c4} + S_{c5}\right] \end{bmatrix}$$

where $\mathbf{u}^2 = (u^2 + v^2 + w^2)$.
Eqns A.9 and A.10 can be converted into characteristic form by multiplying them by left eigenvector matrices $\mathbf{P}^{-1}$ and $\mathbf{S}^{-1}$ respectively i.e. at a boundary with constant ξ,

$$\mathbf{P}_\xi^{-1} \frac{\partial \mathbf{Q}}{\partial t} + \mathbf{L}_\xi + \mathbf{P}_\xi^{-1} \mathbf{S}_c = 0 \tag{A.11}$$

$$\mathbf{S}_\xi^{-1} \frac{\partial \mathbf{U}}{\partial t} + \mathbf{L}_\xi + \mathbf{S}_\xi^{-1} \mathbf{S}_d = 0 \tag{A.12}$$

where

$$\mathbf{L}_\xi = \mathbf{\Lambda}_\xi \mathbf{P}_\xi^{-1} \frac{\partial \mathbf{Q}}{\partial \xi} = \mathbf{\Lambda}_\xi \mathbf{S}_\xi^{-1} \frac{\partial \mathbf{U}}{\partial \xi} \tag{A.13}$$

As discussed in section 2.2.2 of Chapter 2, the characteristic equations in Eqns A.11 and A.12 do not satisfy Pfaff's condition for the integrability of differential forms. For the first term in the left side of Eqn A.11 [or A.12] to exist, the matrix $\mathbf{P}_{\xi}^{-1}$ (or $\mathbf{S}_{\xi}^{-1}$ in Eqn A.12) needs to either satisfy Pfaff's condition for the integrability of differential forms [Whitham (1974)] or be constant, a condition not possible for the fluid equations. Hence, the matrix $\mathbf{P}_{\xi}^{-1}$ cannot be absorbed into the partial derivatives as represented in Eqn A.11. To avoid this and restore the mathematical consistency, Eqns A.11 and A.12 are rewritten as:

$$\frac{\partial \mathbf{Q}}{\partial t} + \mathbf{P}_{\xi}\mathbf{L}_{\xi} + \mathbf{S}_{c} = 0 \tag{A.14}$$

$$\frac{\partial \mathbf{U}}{\partial t} + \mathbf{S}_{\xi}\mathbf{L}_{\xi} + \mathbf{S}_{d} = 0 \tag{A.15}$$

The left eigenvector matrix for the Navier-Stokes equations expressed in primitive variable form (Equation A.5) is simpler than the corresponding left eigenvector matrix for the Navier-Stokes equations in terms of conserved variables (Equation A.4). Hence, Equation A.15 is used hereafter for all the analysis and the derivation of boundary conditions. Multiplying matrices $\mathbf{S}_{\xi}$ and $\mathbf{L}_{\xi}$, and after some algebraic manipulation, the time derivatives of the primitive variables can be expressed as:

$$\begin{aligned}
\frac{\partial \rho}{\partial t} &= -\hat{\xi}_x L_1 - \hat{\xi}_y L_2 - \hat{\xi}_z L_3 - \frac{(L_4 + L_5)}{2} - S_{d1} \\
\frac{\rho}{c}\frac{\partial u}{\partial t} &= \hat{\xi}_z L_2 - \hat{\xi}_y L_3 - \frac{\hat{\xi}_x (L_4 - L_5)}{2} - \frac{S_{d2}}{c} \\
\frac{\rho}{c}\frac{\partial v}{\partial t} &= -\hat{\xi}_z L_1 + \hat{\xi}_x L_3 - \frac{\hat{\xi}_y (L_4 - L_5)}{2} - \frac{S_{d3}}{c} \\
\frac{\rho}{c}\frac{\partial w}{\partial t} &= \hat{\xi}_y L_1 - \hat{\xi}_x L_2 - \frac{\hat{\xi}_z (L_4 - L_5)}{2} - \frac{S_{d4}}{c} \\
\frac{1}{c^2}\frac{\partial p}{\partial t} &= -\frac{(L_4 + L_5)}{2} - \frac{S_{d5}}{c^2}
\end{aligned} \tag{A.16}$$

The relations represented by Eq. A.16 form the main basis of deriving characteristic wall, interface and inflow/outflow boundary conditions. Figure A.1 shows a simple, structured grid consisting of two blocks. The derivation of accurate interface conditions is based on the fact that time developments of the primitive variables at the upstream limit (left side) and those at the downstream limit (right side) on the block interface are strictly matched. Based on this simple logic, it can be said that the right hand sides in the system of equations in A.16 need to be exactly matched at the block interface i.e.

$$\hat{\xi}_x L_1 + \hat{\xi}_y L_2 + \xi_z L_3 + \frac{(L_4 + L_5)}{2} + S_{d1}\Big|_{\text{left}} = \hat{\xi}_x L_1 + \hat{\xi}_y L_2 + \hat{\xi}_z L_3 + \frac{(L_4 + L_5)}{2} + S_{d1}\Big|_{\text{right}} \quad \text{(A.17)}$$

$$-\hat{\xi}_z L_2 + \hat{\xi}_y L_3 + \frac{\hat{\xi}_x (L_4 - L_5)}{2} + \frac{S_{d2}}{c}\Big|_{\text{left}} = -\hat{\xi}_z L_2 + \hat{\xi}_y L_3 + \frac{\hat{\xi}_x (L_4 - L_5)}{2} + \frac{S_{d2}}{c}\Big|_{\text{right}} \quad \text{(A.18)}$$

$$\hat{\xi}_z L_1 - \hat{\xi}_x L_3 + \frac{\hat{\xi}_y (L_4 - L_5)}{2} + \frac{S_{d3}}{c}\Big|_{\text{left}} = \hat{\xi}_z L_1 - \hat{\xi}_x L_3 + \frac{\hat{\xi}_y (L_4 - L_5)}{2} + \frac{S_{d3}}{c}\Big|_{\text{right}} \quad \text{(A.19)}$$

$$-\hat{\xi}_y L_1 + \hat{\xi}_x L_2 + \frac{\hat{\xi}_z (L_4 - L_5)}{2} + \frac{S_{d4}}{c}\Big|_{\text{left}} = -\hat{\xi}_y L_1 + \hat{\xi}_x L_2 + \frac{\hat{\xi}_z (L_4 - L_5)}{2} + \frac{S_{d4}}{c}\Big|_{\text{right}} \quad \text{(A.20)}$$

$$\frac{(L_4 + L_5)}{2} + \frac{S_{d5}}{c^2}\Big|_{\text{left}} = \frac{(L_4 + L_5)}{2} + \frac{S_{d5}}{c^2}\Big|_{\text{right}} \quad \text{(A.21)}$$

Now subtracting Eq. A.21 from Eq. A.17:

$$\hat{\xi}_x L_1 + \hat{\xi}_y L_2 + \xi_z L_3 + S_{d1} - \frac{S_{d5}}{c^2}\Big|_{\text{left}} = +\hat{\xi}_x L_1 + \hat{\xi}_y L_2 + \hat{\xi}_z L_3 + S_{d1} - \frac{S_{d5}}{c^2}\Big|_{\text{right}} \quad \text{(A.22)}$$

Hereafter, a superscript of 'l' refers to the variable at the left side of the interface and that of 'r' refers to the variable at the right side of the interface. Now $\hat{\xi}_x\times$ Eq. A.22 + $\hat{\xi}_z\times$ Eq. A.19 - $\xi_y\times$ Eq. A.20 gives:

$$L_1 + \frac{\hat{\xi}_z S_{d3}}{c} - \frac{\hat{\xi}_y S_{d4}}{c} + \hat{\xi}_x \left(S_{d4} - \frac{S_{d5}}{c^2} \right) \Bigg|_{\text{left}} = \left(\hat{\xi}_l . \hat{\xi}_r \right) L_1^r + \frac{\hat{\xi}_z^l S_{d3}^r}{c} - \frac{\hat{\xi}_y^l S_{d4}^r}{c} + \hat{\xi}_x^l \left(S_{d1}^r - \frac{S_{d5}^r}{c^2} \right) \quad \text{(A.23)}$$

Hence Eq. A.23 can be written as:

$$L_1 + S_{r1}|_{\text{left}} = \left(\hat{\xi}_l . \hat{\xi}_r \right) L_1^r + S_{r1}\,|_{\text{right}} \quad \text{(A.24)}$$

where

$$S_{r1}|_{\text{left}} = \frac{\hat{\xi}_z S_{d3}}{c} - \frac{\hat{\xi}_y S_{d4}}{c} + \hat{\xi}_x \left(S_{d4} - \frac{S_{d5}}{c^2} \right) |_{\text{left}}$$

and

$$S_{r1}|_{\text{right}} = \frac{\hat{\xi}_z^l S_{d3}^r}{c} - \frac{\hat{\xi}_y^l S_{d4}^r}{c} + \hat{\xi}_x^l \left(S_{d1}^r - \frac{S_{d5}^r}{c^2} \right)$$

.

Similar mathematical manipulation leads to,

$$L_2 + S_{r2}|_{\text{left}} = \left(\hat{\xi}_l . \hat{\xi}_r \right) L_2^r + S_{r2}\,|_{\text{right}} \quad \text{(A.25)}$$

$$L_3 + S_{r3}|_{\text{left}} = \left(\hat{\xi}_l . \hat{\xi}_r \right) L_3^r + S_{r3}\,|_{\text{right}} \quad \text{(A.26)}$$

where

$$
\begin{aligned}
S_{r2}|_{\text{left}} &= -\frac{\hat{\xi}_z S_{d2}}{c} + \frac{\hat{\xi}_x S_{d4}}{c} + \hat{\xi}_y \left(S_{d4} - \frac{S_{d5}}{c^2} \right) |_{\text{left}} \\
S_{r3}|_{\text{left}} &= -\frac{\hat{\xi}_x S_{d3}}{c} + \frac{\hat{\xi}_y S_{d2}}{c} + \hat{\xi}_z \left(S_{d4} - \frac{S_{d5}}{c^2} \right) |_{\text{left}} \\
S_{r2}|_{\text{right}} &= -\frac{\hat{\xi}^l_z S^r_{d2}}{c} + \frac{\hat{\xi}^l_x S^r_{d4}}{c} + \hat{\xi}^l_y \left(S^r_{d1} - \frac{S^r_{d5}}{c^2} \right) \\
S_{r3}|_{\text{right}} &= -\frac{\hat{\xi}^l_x S^r_{d3}}{c} + \frac{\hat{\xi}^l_y S^r_{d2}}{c} + \hat{\xi}^l_z \left(S^r_{d1} - \frac{S^r_{d5}}{c^2} \right)
\end{aligned}
$$

Again, $\hat{\xi}_x\times$ Eq. A.18 + $\hat{\xi}_y\times$ Eq. A.19 + $\hat{\xi}_z\times$ Eq. A.20 gives:

$$
\begin{aligned}
L_4 - L_5 + \frac{2}{c} \left(\hat{\xi}_x S_{d2} + \hat{\xi}_y S_{d3} + \hat{\xi}_z S_{d4} \right) \Big|_{\text{left}} \\
= \left(\hat{\xi}_l . \hat{\xi}_r \right) \left(L^r_4 - L^r_5 \right) + \frac{2}{c} \left(\hat{\xi}^l_x S^r_{d2} + \hat{\xi}^l_y S^r_{d3} + \hat{\xi}^l_z S^r_{d4} \right)
\end{aligned} \tag{A.27}
$$

Now Eqns A.27 and A.21 can be rewritten as:

$$
L_4 - L_5 + S_{r4}|_{\text{left}} = \left(\hat{\xi}_l . \hat{\xi}_r \right) \left(L^r_4 - L^r_5 \right) + S_{r4}|_{\text{right}} \tag{A.28}
$$

$$
L_4 + L_5 + S_{r5}|_{\text{left}} = L^r_4 + L^r_5 + S_{r5}|_{\text{right}} \tag{A.29}
$$

where

$$
\begin{aligned}
S_{r4}|_{\text{left}} &= \frac{2}{c} \left(\hat{\xi}_x S_{d2} + \hat{\xi}_y S_{d3} + \hat{\xi}_z S_{d4} \right) |_{\text{left}} \\
S_{r4}|_{\text{right}} &= \frac{2}{c} \left(\hat{\xi}^l_x S^r_{d2} + \hat{\xi}^l_y S^r_{d3} + \hat{\xi}^l_z S^r_{d4} \right) \\
S_{r5}|_{\text{left}} &= \frac{2 S_{d4}}{c^2} |_{\text{left}} \\
S_{r5}|_{\text{right}} &= \frac{2 S_{d4}}{c^2} |_{\text{right}}
\end{aligned}
$$

Equations A.24, A.25, A.26, A.28 and A.29 form the main basis of characteristic matching at the block interface. The usual convention in which either the left or the right hand convection terms are corrected by the other one according to Eqns A.26 and A.28 is decided based on the sign of the convection speed (i.e. the incoming convection term is corrected while the outgoing term is left unchanged). In this way, accurate interface conditions are maintained at the block interfaces.

A.2 Characteristic relations for conservative equations

In general, compressible viscous flows are solved in conservation form of the Navier-Stokes equations and so it is inconvenient to use the non-conservative form of the governing equations as depicted in Eq. A.4 or Eq. A.5. Hence for practical purposes, the conservative form of the Navier-Stokes equations in generalised coordinates is used:

$$\frac{\partial \hat{\mathbf{Q}}}{\partial t} + \frac{\partial \hat{\mathbf{E}}}{\partial \xi} + \frac{\partial \hat{\mathbf{F}}}{\partial \eta} + \frac{\partial \hat{\mathbf{G}}}{\partial \zeta} = \hat{\mathbf{S}}_v \tag{A.30}$$

where the caret represents the transformed variables in the generalised coordinates. The conserved variables, inviscid fluxes and the viscous fluxes in the generalized coordinates can be represented as:

$$\begin{aligned}
\hat{\mathbf{Q}} &= \mathbf{Q}/J \\
\hat{\mathbf{E}} &= (\xi_x \mathbf{E} + \xi_y \mathbf{F} + \xi_z \mathbf{G})/J \\
\hat{\mathbf{F}} &= (\eta_x \mathbf{E} + \eta_y \mathbf{F} + \eta_z \mathbf{G})/J \\
\hat{\mathbf{G}} &= (\zeta_x \mathbf{E} + \zeta_y \mathbf{F} + \zeta_z \mathbf{G})/J \\
\hat{\mathbf{S}}_v &= \frac{\partial \hat{\mathbf{E}}_v}{\partial \xi} + \frac{\partial \hat{\mathbf{F}}_v}{\partial \eta} + \frac{\partial \hat{\mathbf{G}}_v}{\partial \zeta}
\end{aligned} \tag{A.31}$$

with,

$$\begin{aligned}
\hat{\mathbf{E}}_v &= (\xi_x \mathbf{E}_v + \xi_y \mathbf{F}_v + \xi_z \mathbf{G}_v)/J \\
\hat{\mathbf{F}}_v &= (\eta_x \mathbf{E}_v + \eta_y \mathbf{F}_v + \eta_z \mathbf{G}_v)/J \\
\hat{\mathbf{G}}_v &= (\zeta_x \mathbf{E}_v + \zeta_y \mathbf{F}_v + \zeta_z \mathbf{G}_v)/J
\end{aligned}$$

The Jacobian of the transformation, J, and the grid metrics in the system of equations (A.31) is given by:

$$J = \left[\frac{\partial x}{\partial \xi}\left(\frac{\partial y}{\partial \eta}\frac{\partial z}{\partial \zeta} - \frac{\partial y}{\partial \zeta}\frac{\partial z}{\partial \eta}\right) - \frac{\partial x}{\partial \eta}\left(\frac{\partial y}{\partial \xi}\frac{\partial z}{\partial \zeta} - \frac{\partial y}{\partial \zeta}\frac{\partial z}{\partial \xi}\right) + \frac{\partial x}{\partial \zeta}\left(\frac{\partial y}{\partial \xi}\frac{\partial z}{\partial \eta} - \frac{\partial y}{\partial \xi}\frac{\partial z}{\partial \eta}\right)\right]^{-1}.$$

$$\begin{aligned}
\xi_x &= \frac{\partial \xi}{\partial x} = J\left(\frac{\partial y}{\partial \eta}\frac{\partial z}{\partial \zeta} - \frac{\partial y}{\partial \zeta}\frac{\partial z}{\partial \eta}\right), \quad \xi_y = \frac{\partial \xi}{\partial y} = J\left(\frac{\partial x}{\partial \zeta}\frac{\partial z}{\partial \eta} - \frac{\partial x}{\partial \eta}\frac{\partial z}{\partial \zeta}\right), \quad \xi_z = \frac{\partial \xi}{\partial z} = J\left(\frac{\partial x}{\partial \eta}\frac{\partial y}{\partial \zeta} - \frac{\partial x}{\partial \zeta}\frac{\partial y}{\partial \eta}\right) \\
\eta_x &= \frac{\partial \eta}{\partial x} = J\left(\frac{\partial y}{\partial \zeta}\frac{\partial z}{\partial \xi} - \frac{\partial y}{\partial \xi}\frac{\partial z}{\partial \zeta}\right), \quad \eta_y = \frac{\partial \eta}{\partial y} = J\left(\frac{\partial x}{\partial \xi}\frac{\partial z}{\partial \zeta} - \frac{\partial x}{\partial \zeta}\frac{\partial z}{\partial \xi}\right), \quad \eta_z = \frac{\partial \eta}{\partial z} = J\left(\frac{\partial x}{\partial \zeta}\frac{\partial y}{\partial \xi} - \frac{\partial x}{\partial \xi}\frac{\partial y}{\partial \zeta}\right) \\
\zeta_x &= \frac{\partial \zeta}{\partial x} = J\left(\frac{\partial y}{\partial \xi}\frac{\partial z}{\partial \eta} - \frac{\partial y}{\partial \eta}\frac{\partial z}{\partial \xi}\right), \quad \zeta_y = \frac{\partial \zeta}{\partial y} = J\left(\frac{\partial x}{\partial \eta}\frac{\partial z}{\partial \xi} - \frac{\partial x}{\partial \xi}\frac{\partial z}{\partial \eta}\right), \quad \zeta_z = \frac{\partial \zeta}{\partial z} = J\left(\frac{\partial x}{\partial \xi}\frac{\partial y}{\partial \eta} - \frac{\partial x}{\partial \eta}\frac{\partial y}{\partial \xi}\right)
\end{aligned} \tag{A.32}$$

Comparing Eq. A.4, A.14 and A.30, the source term and the characteristic wave amplitudes corresponding to Eq. A.30 can be written as:

$$\mathbf{S}_c = J\left[\left\{\mathbf{E}\frac{\partial}{\partial\xi}\left(\frac{\xi_x}{J}\right)+\mathbf{F}\frac{\partial}{\partial\xi}\left(\frac{\xi_y}{J}\right)+\mathbf{G}\frac{\partial}{\partial\xi}\left(\frac{\xi_z}{J}\right)\right\}+\frac{\partial\hat{\mathbf{F}}}{\partial\eta}+\frac{\partial\hat{\mathbf{G}}}{\partial\zeta}-\hat{\mathbf{S}}_v\right]$$

$$L_\xi = \begin{bmatrix} L_1 \\ L_2 \\ L_3 \\ L_4 \\ L_5 \end{bmatrix} = \begin{bmatrix} U\left\{\hat{\xi}_x\left(\frac{\partial\rho}{\partial\xi}-\frac{1}{c^2}\frac{\partial p}{\partial\xi}\right)+\frac{\rho}{c}\left(\hat{\xi}_z\frac{\partial v}{\partial\xi}-\hat{\xi}_y\frac{\partial w}{\partial\xi}\right)\right\} \\ U\left\{\hat{\xi}_y\left(\frac{\partial\rho}{\partial\xi}-\frac{1}{c^2}\frac{\partial p}{\partial\xi}\right)+\frac{\rho}{c}\left(\hat{\xi}_x\frac{\partial w}{\partial\xi}-\hat{\xi}_z\frac{\partial u}{\partial\xi}\right)\right\} \\ U\left\{\hat{\xi}_z\left(\frac{\partial\rho}{\partial\xi}-\frac{1}{c^2}\frac{\partial p}{\partial\xi}\right)+\frac{\rho}{c}\left(\hat{\xi}_y\frac{\partial u}{\partial\xi}-\hat{\xi}_x\frac{\partial v}{\partial\xi}\right)\right\} \\ (U+C)\frac{\rho}{c}\left\{\frac{1}{\rho c}\frac{\partial p}{\partial\xi}+\left(\hat{\xi}_x\frac{\partial u}{\partial\xi}+\hat{\xi}_y\frac{\partial v}{\partial\xi}+\hat{\xi}_z\frac{\partial w}{\partial\xi}\right)\right\} \\ (U-C)\frac{\rho}{c}\left\{\frac{1}{\rho c}\frac{\partial p}{\partial\xi}-\left(\hat{\xi}_x\frac{\partial u}{\partial\xi}+\hat{\xi}_y\frac{\partial v}{\partial\xi}+\hat{\xi}_z\frac{\partial w}{\partial\xi}\right)\right\} \end{bmatrix} \tag{A.33}$$

A.3 Interface matching

In this section, the interface matching process is described. As shown in Figure A.1, the domain is decomposed into two blocks along a common face, and the characteristic-based interface conditions are imposed on the block interface. As explained in Section A.1, the generalized characteristic interface conditions are based on the simple fact that time development of the flow variables at the upstream limit and those at the downstream limit at the block interface are strictly matched. Using equations A.24, A.25, A.26, A.28 and A.29 these conditions are replaced by the spatial relations.

The transfer direction of a characteristic wave component L_i is determined by the eigenvalue λ_i given by Eq. A.8. Under subsonic conditions, four eigenvalues have a positive sign, and one eigenvalue has a negative sign. Thus, four characteristic waves are travelling from the upstream to the downstream side and one wave is travelling in the opposite direction. The decision over which wave amplitude needs to be corrected is dependent on whether the convection speed at the interface is larger or smaller than the sound speed. Based on the signs of the contravariant velocities at the block interface four possible combinations of wave directions can be found, which are shown in Figure A.2. The characteristic wave components, denoted by solid arrows, are the known ones and those with a hollow arrow are unknown ones, which are corrected by the characteristic interface treatment. In all cases a total of five unknown and five known vectors exist at the interface.

A.4 Interface matching of turbulence quantities

Turbulence is of great technological importance because of the large effects it has on the flows in which it occurs. Turbulence results in increased energy dissipation, mixing, and heat transfer in the flow. The prediction of these effects in a flow of interest is one of the primary concerns of applied fluid dynamicists, and it is often the case that the uncertainties in a fluid dynamic calculation are dominated by uncertainties in the turbulence models. Hence it is vital for any characteristic-based computational solvers which use a multi-block grid to have an accurate matching method for turbulence properties at block interfaces. An efficient matching approach is derived for turbulence quantities in this work. For illustrative purposes, the one-equation turbulence model of Spalart & Allmaras (1992) is used. The turbulent transport equation solved by the model is given by,

$$\frac{\partial}{\partial t}\left(\rho\tilde{\nu}\right) + \frac{\partial}{\partial x_i}\left(\rho\tilde{\nu}u_i\right) = G_\nu + \frac{1}{\sigma_\nu}\left[\frac{\partial}{\partial x_j}\left\{\left(\mu + \rho\tilde{\nu}\right)\frac{\partial\tilde{\nu}}{\partial x_j}\right\} + C_{b2}\rho\left(\frac{\partial\tilde{\nu}}{\partial x_j}\right)^2\right] - Y_v \tag{A.34}$$

where G_ν is the production term of turbulent viscosity and Y_ν is the turbulent viscosity dissipation term. σ_ν and C_{b2} are constants. The system of partial differential equations in Eq. A.34 is solved for the transport variable $\tilde{\nu}$ to calculate μ_t using the relation, $\mu_t = \rho\tilde{\nu}f_{\nu 1}$. The turbulent viscosity term (μ_t) is required to close the system of equations in Eq. A.1. $f_{\nu 1}$ is the viscous damping function. Additional details of the turbulence model can be found in the literatures [Spalart & Allmaras (1992); flu (2005); Krist et al. (1998)]. Now, Eq. A.34 is reorganized as:

$$\frac{\partial}{\partial t}\left(\rho\widetilde{\nu}\right) = G_v - Y_v + T_s \tag{A.35}$$

where

$$T_s = \frac{1}{\sigma_v}\left[\frac{\partial}{\partial x_j}\left\{\left(\mu + \rho\widetilde{\nu}\right)\frac{\partial\widetilde{\nu}}{\partial x_j}\right\} + C_{b2}\rho\left(\frac{\partial\widetilde{\nu}}{\partial x_j}\right)^2\right] - \frac{\partial}{\partial x_j}\left(\rho\widetilde{\nu}u_i\right)$$

The interface matching of turbulence quantities is based on the simple fact that time developments of the turbulent variables at the upstream limit and those at the downstream limit on the block interface are strictly matched. Also the production and dissipation terms need to be the same at the block interface. Based on this simple logic, the matching condition for turbulence quantities can be written as:

$$G_v - Y_v + T_s|_{\text{left}} = G_v - Y_v + T_s|_{\text{right}} \tag{A.36}$$

Eq. A.36 can be rewritten as:

$$(G_v - Y_v)|_{\text{left}} = (G_v - Y_v)|_{\text{right}} + T_s^r - T_s^l \tag{A.37}$$

Using Eq. A.37, net production and dissipation effects are strictly matched at the interface at each time step.

A.5 Characteristic wall boundary conditions

The system of equations (A.16) is used as a starting point to deduce relations for the wall boundary conditions. Considering the viscous wall condition, all the velocity terms become zero and also the first three convection terms disappear at the wall. Hence, the system of equations (A.16) can be written as:

$$\frac{\partial \rho}{\partial t} = -\frac{(L_4 + L_5)}{2} - S_{d1} \tag{A.38}$$

$$\frac{\hat{\xi}_x\,(L_4 - L_5)}{2} + \frac{S_{d2}}{c} = 0 \tag{A.39}$$

$$\frac{\hat{\xi}_y\,(L_4 - L_5)}{2} + \frac{S_{d3}}{c} = 0 \tag{A.40}$$

$$\frac{\hat{\xi}_z\,(L_4 - L_5)}{2} + \frac{S_{d4}}{c} = 0 \tag{A.41}$$

$$\frac{\partial p}{\partial t} = -\frac{c^2\,(L_4 + L_5)}{2} - S_{d5} \tag{A.42}$$

Now, $\hat{\xi}_x\times$ Eq. A.39 + $\hat{\xi}_y\times$ Eq. A.40 + $\hat{\xi}_z\times$ Eq. A.41 and some algebraic manipulations leads to:

$$L_4 - L_5 + \frac{1}{c}\left(\hat{\xi}_x S_{d2} + \hat{\xi}_y S_{d3} + \hat{\xi}_z S_{d4}\right) = 0 \tag{A.43}$$

The characteristic wave amplitudes L_1, L_2 and L_3 are all set to zero at the wall as all the velocity terms are zero. Also Eq. A.43 is used to correct the incoming characteristic waves (at ξ_{min} boundary, the characteristic wave L_4 is entering the domain whereas L_5 is entering the domain at ξ_{max} boundary) at the wall boundary. In addition, the normal heat flux is set to zero at the boundary when an adiabatic wall is considered.

A.6 Characteristic Transformation Matrices

The matrices $\mathbf{M}, \mathbf{M}^{-1}$ transform the conservative variables to primitive variables and vise versa. These matrices along with $\mathbf{S}$ and $\mathbf{S}^{-1}$ are given as:

$$\mathbf{M} = \begin{bmatrix} 1 & 0 & 0 & 0 & 0 \\ u & \rho & 0 & 0 & 0 \\ v & 0 & \rho & 0 & 0 \\ w & 0 & 0 & \rho & 0 \\ \frac{u^2}{2} & \rho u & \rho v & \rho w & \frac{1}{\gamma} \end{bmatrix}$$

$$\mathbf{M^{-1}} = \begin{bmatrix} 1 & 0 & 0 & 0 & 0 \\ -\frac{u}{\rho} & \frac{1}{\rho} & 0 & 0 & 0 \\ -\frac{v}{\rho} & 0 & \frac{1}{\rho} & 0 & 0 \\ -\frac{w}{\rho} & 0 & 0 & \frac{1}{\rho} & 0 \\ \frac{(\gamma-1)u^2}{2} & u(1-\gamma) & v(1-\gamma) & w(1-\gamma) & (\gamma-1) \end{bmatrix}$$

$$\mathbf{S} = \begin{bmatrix} \hat{\xi}_x & \hat{\xi}_y & \hat{\xi}_z & \frac{1}{2} & \frac{1}{2} \\ 0 & -\frac{c\hat{\xi}_z}{\rho} & \frac{c\hat{\xi}_y}{\rho} & \frac{c\hat{\xi}_x}{2\rho} & -\frac{c\hat{\xi}_x}{2\rho} \\ \frac{c\hat{\xi}_z}{\rho} & 0 & -\frac{c\hat{\xi}_x}{\rho} & \frac{c\hat{\xi}_y}{2\rho} & -\frac{c\hat{\xi}_y}{2\rho} \\ -\frac{c\hat{\xi}_y}{\rho} & \frac{c\hat{\xi}_x}{\rho} & 0 & \frac{c\hat{\xi}_z}{2\rho} & -\frac{c\hat{\xi}_z}{2\rho} \\ 0 & 0 & 0 & \frac{c^2}{2} & \frac{c^2}{2} \end{bmatrix}, \quad \mathbf{S^{-1}} = \begin{bmatrix} \hat{\xi}_x & 0 & \frac{\rho\hat{\xi}_z}{c} & -\frac{\rho\hat{\xi}_y}{c} & -\frac{\hat{\xi}_x}{c^2} \\ \hat{\xi}_y & -\frac{\rho\hat{\xi}_z}{c} & 0 & \frac{\rho\hat{\xi}_x}{c} & -\frac{\hat{\xi}_y}{c^2} \\ \hat{\xi}_z & \frac{\rho\hat{\xi}_y}{c} & -\frac{\rho\hat{\xi}_x}{c} & 0 & -\frac{\hat{\xi}_z}{c^2} \\ 0 & \frac{\rho\hat{\xi}_x}{c} & \frac{\rho\hat{\xi}_y}{c} & \frac{\rho\hat{\xi}_z}{c} & \frac{1}{c^2} \\ 0 & -\frac{\rho\hat{\xi}_x}{c} & -\frac{\rho\hat{\xi}_y}{c} & -\frac{\rho\hat{\xi}_z}{c} & \frac{1}{c^2} \end{bmatrix}$$

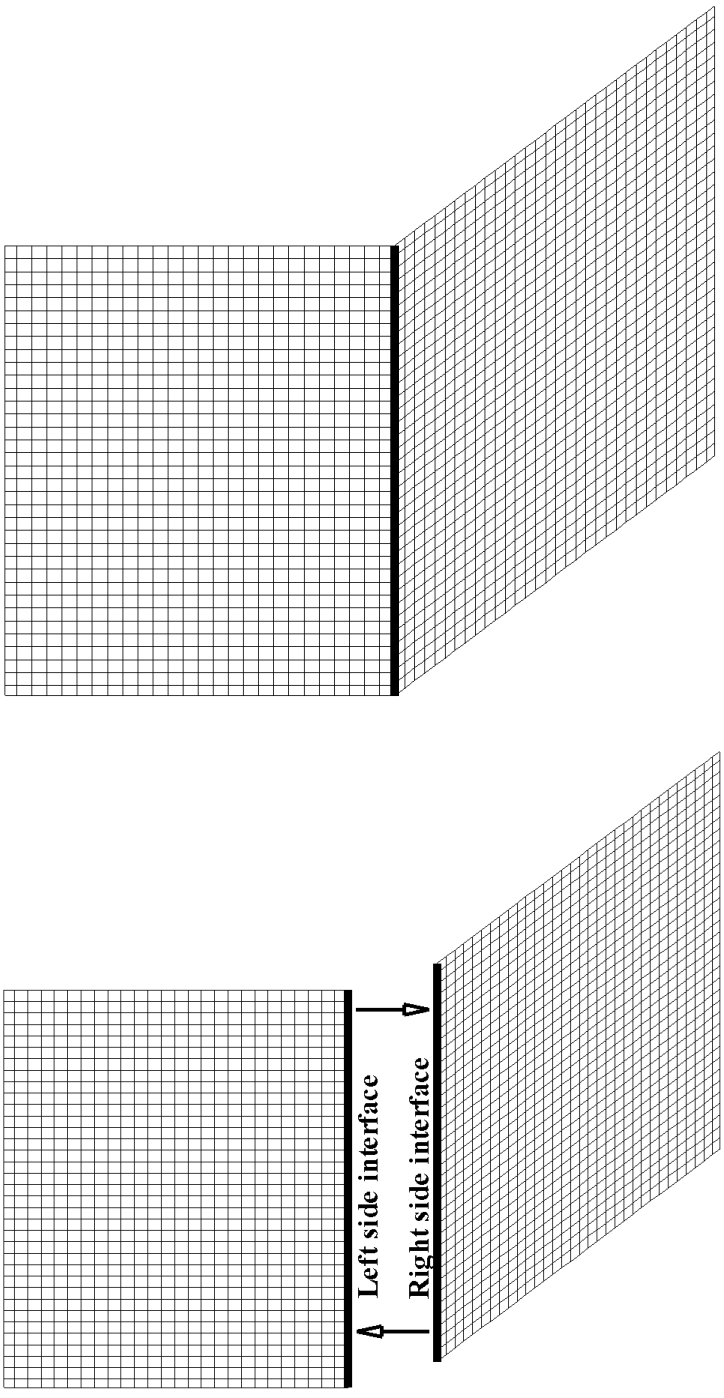

Figure A.1: Two-block domain with single interface (top) and block decomposition for interface treatment (bottom)

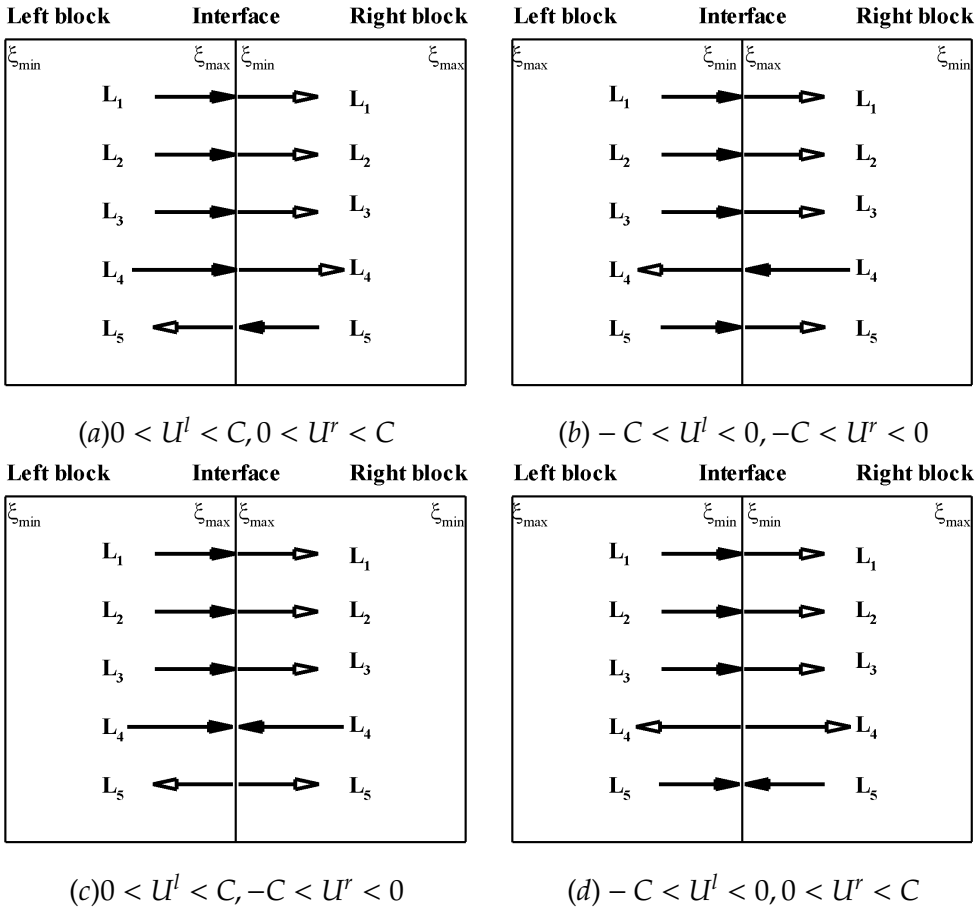

Figure A.2: Various block grid orientations and the direction of characteristic waves at the interface

Appendix B

Derivation and Solution of the FW-H Equation

The Ffowcs Williams and Hawkings (FW-H) equation [Ffowcs-Williams & Hawkings (1969)] is the most general form of Lighthill's acoustic analogy [Lighthill (1952)]. It is an exact rearrangement of the Navier-Stokes equations and is appropriate for computing the acoustic field when there are solid boundaries present in the flow field. The FW-H equation can be used to predict the acoustic signal at far-field observer locations based solely upon information of the near-field flow, provided by computation or experiment. Its solution is obtained in terms of volume and surface integrals and can be applied either by having the integration surface coincide with solid boundaries, or off the body as a permeable surface. It is even valid if the integration surface lies in the non-linear region making it a very flexible technique. In the following sections the derivation of the FW-H equation and its solution is given beginning with the Navier-Stokes equations.

B.1 Lighthill's acoustic analogy

In 1952 Lighthill (1952) published a pioneering paper, establishing the theory of sound generated aerodynamically. Lighthill's theory was based upon the rearrangement of the Navier-Stokes equations showing how the source of aerodynamic noise could be obtained from exact time-accurate calculations or experiment. The result is a wave equation including a source term. Lighthill's inhomogeneous wave equation is expressed as:

$$\left[\frac{\partial^2}{\partial t^2} - c_0^2 \nabla^2\right] \rho' = \frac{\partial^2 T_{ij}}{\partial x_i \partial x_j} \tag{B.1}$$

The left-hand side is the linear wave equation and the right-hand side represents a quadrupole distribution. T_{ij} is the Lighthill stress tensor ...

$$T_{ij} = \rho u_i u_j + P_{ij} - c_0^2 \rho' \delta_{ij} \tag{B.2}$$

Where P_{ij} is the compressive stress tensor ...

$$P_{ij} = p\delta_{ij} + \mu\left\{-\frac{\partial u_i}{\partial x_j} - \frac{\partial u_j}{\partial x_i} + \frac{2}{3}\left(\frac{\partial u_k}{\partial x_k}\right)\delta_{ij}\right\} \tag{B.3}$$

The limitation of Lighthill's formulation is that it assumes the absence of solid boundaries in the flow field. In real applications this is often impractical and consequently the FW-H equation is derived to include the presence of solid boundaries in arbitrary motion.

B.2 A body in arbitrary motion and the Heavyside function

The FW-H equation may be derived by considering a body in arbitrary motion with surface S, described by the equation $f(\mathbf{x}, t) = 0$, and immersed in a fluid such as air. The function $f(\mathbf{x}, t)$ is a function of time so that it always surrounds the volume or surface of interest, and is defined to be positive everywhere outside the surface S and negative in the interior of S. Therefore ...

$$\begin{aligned} f > 0 \quad & \text{inside} \quad S \\ f < 0 \quad & \text{outside} \quad S \end{aligned} \tag{B.4}$$

If the body submerged in the fluid is replaced by fluid at rest ($p = p_0$, $\rho = \rho_0$, and $u_i = 0$) and the flow variables are regarded as generalized functions, the validity of the equations of fluid motion may be extended to all space through the use of the Heavyside fuction $H(f)$ where:

$$H(f) = \begin{Bmatrix} 1 & f < 0 \\ 0 & f > 0 \end{Bmatrix} \tag{B.5}$$

The Heavyside function can then be applied to the governing equations of the fluid.

B.2.1 Governing Equations

Outside the body the continuity and momentum conservation equations hold true. In tensor notation these are expressed as:

$$\frac{\partial}{\partial t}\Big(\rho - \rho_0\Big) + \frac{\partial}{\partial x_i}\Big(\rho u_i\Big) = 0 \tag{B.6}$$

$$\frac{\partial}{\partial t}\Big(\rho u_i\Big) + \frac{\partial}{\partial x_i}\Big(P_{ij} + \rho u_i u_j\Big) = 0 \tag{B.7}$$

Where P_{ij} is the compressive stress tensor, $P_{ij} = p\delta_{ij} - \tau_{ij}$, and τ_{ij} is the viscous stress tensor. Multiplying the continuity equation, equation B.6, by $H(f)$ gives:

$$H(f)\frac{\partial}{\partial t}\Big(\rho - \rho_0\Big) + H(f)\frac{\partial}{\partial x_i}\Big(\rho u_i\Big) = 0 \tag{B.8}$$

The next step is to express equation B.8 with $H(f)$ inside the differential operators. For this we need to perform some algerbra. We can write:

$$\frac{\partial f(\mathbf{x},t)}{\partial t} + \frac{\partial f(\mathbf{x},t)}{\partial x_i}\frac{\partial x_i}{\partial t} = 0 \tag{B.9}$$

$$\Rightarrow \frac{\partial f(\mathbf{x},t)}{\partial t} = -v_i\frac{\partial f(\mathbf{x},t)}{\partial x_i} \qquad \text{where} \quad v_i = \frac{\partial x_i}{\partial t} \tag{B.10}$$

also,

$$\frac{\partial}{\partial t}\Big\{\Big(\rho - \rho_0\Big)H(f)\Big\} = H(f)\frac{\partial}{\partial t}\Big(\rho - \rho_0\Big) + \Big(\rho - \rho_0\Big)\frac{\partial H(f)}{\partial t} \tag{B.11}$$

and,

$$\frac{\partial H(f)}{\partial t} = \frac{\partial H(f)}{\partial f}\frac{\partial f}{\partial t} = \frac{\partial H(f)}{\partial t}\Big(-v_i\frac{\partial f}{\partial x_i}\Big) \tag{B.12}$$

$$\Rightarrow \frac{\partial H(f)}{\partial t} = -v_i \frac{\partial H(f)}{\partial x_i} \tag{B.13}$$

Applying these relationships we have:

$$\frac{\partial}{\partial t}\Big\{\big(\rho - \rho_0\big)H(f)\Big\} = H(f)\frac{\partial}{\partial t}\big(\rho - \rho_0\big) - \big(\rho - \rho_0\big)v_i \frac{\partial H(f)}{\partial x_i} \tag{B.14}$$

and we can also write,

$$\frac{\partial}{\partial x_i}\big(\rho u_i H(f)\big) = H(f)\frac{(\partial \rho u_i)}{\partial x_i} + (\rho u_i)\frac{\partial H(f)}{\partial x_i} \tag{B.15}$$

Finally, subtracting equation B.14 from B.15 gives the result:

$$\frac{\partial}{\partial t}\Big\{\left(\rho - \rho_0\right)H(f)\Big\} + \frac{\partial}{\partial x_i}\Big\{\rho u_i H(f)\Big\} = \rho_0 v_i \frac{\partial H(f)}{\partial x_i} + \rho\left(u_i - u_i\right)\frac{\partial H(f)}{\partial x_i} \tag{B.16}$$

Multiplying the momentum equation, equation B.7 by $H(f)$ gives:

$$H(f)\frac{\partial}{\partial t}\big(\rho u_i\big) + H(f)\frac{\partial}{\partial x_i}\big(P_{ij} + \rho u_i u_j\big) = 0 \tag{B.17}$$

Now,

$$\frac{\partial}{\partial t}\Big\{\rho u_i H(f)\Big\} = H(f)\frac{\partial}{\partial t}\big(\rho u_i\big) - \big(v_i \rho u_i\big)\frac{\partial H(f)}{\partial x_j} \tag{B.18}$$

and,

$$\frac{\partial}{\partial x_j}\Big\{\big(P_{ij} - \rho u_i u_j\big)H(f)\Big\} = H(f)\frac{\partial}{\partial x_j} + \big(P_{ij} + \rho u_i\big(u_j - v_j\big)\big)\frac{\partial H(f)}{\partial x_i} \tag{B.19}$$

Adding equations B.18 and B.19 yields the following:

$$\frac{\partial}{\partial t}\Big\{\rho u_i H(f)\Big\} + \frac{\partial}{\partial x_j}\Big\{\big(P_{ij} + \rho u_i u_j\big)H(f)\Big\} = \Big\{P_{ij} + \rho u_i\big(u_j - v_j\big)\Big\}\frac{\partial H(f)}{\partial x_j} \tag{B.20}$$

We have now multiplied the equations of continuity and momentum by $H(f)$ and expressed the result with $H(f)$ inside the differential operators. Taking the time derivative of equation B.16 and the space derivative of equation B.20, then subtracting one from the other gives:

$$\frac{\partial^2}{\partial t^2}\Big\{(\rho-\rho_0)H(f)\Big\} - \frac{\partial^2}{\partial x_i \partial x_j}\Big\{\Big(P_{ij}+\rho u_i u_j\Big)H(f)\Big\} = \frac{\partial}{\partial t}\Big\{\rho_0 v_i + \rho\,(u_i - v_i)\,\frac{\partial H(f)}{\partial x_i}\Big\} - \frac{\partial}{\partial x_i}\Big[\Big(P_{ij}+\rho u_i\Big(u_j - v_j\Big)\Big)\frac{\partial H(f)}{\partial x_j}\Big] \tag{B.21}$$

Adding then subtracting $c_0^2\,\frac{\partial}{\partial x_0^2}\Big\{(\rho-\rho_0)H(f)\Big\}$ from the LHS of equation B.21 gives:

$$\begin{aligned}\Big\{\frac{\partial^2}{\partial t^2} - c_0^2\nabla^2\Big\}\Big((\rho-\rho_0)H(f)\Big) &= \frac{\partial^2}{\partial x_i \partial x_j}\Big[\Big(\rho u_i u_j + P_{ij} - c_0^2\,(\rho-\rho_0)\,\delta_{ij}\Big)H(f)\Big] \\ &- \frac{\partial}{\partial x_i}\Big[\Big\{P_{ij}+\rho u_i\Big(u_j - v_j\Big)\Big\}\frac{\partial H(f)}{\partial x_j}\Big] \\ &+ \frac{\partial}{\partial t}\Big[\Big\{\rho_0 v_i + \rho\,(u_i - v_i)\Big\}\frac{\partial H(f)}{\partial x_j}\Big]\end{aligned} \tag{B.22}$$

We can now make use of the relation:

$$\frac{\partial H(f)}{\partial x_j} = \frac{\partial H(f)}{\partial f}\frac{\partial f}{\partial x_j} = \delta(f)\frac{\partial f}{\partial x_j} \qquad \Rightarrow \delta(f) = \frac{\partial H(f)}{\partial f} \tag{B.23}$$

. . . which leads to the FW-H equation:

$$\Big(\frac{\partial^2}{\partial t^2} - c_0^2\frac{\partial^2}{\partial x_i \partial x_j}\Big)\Big(H(f)\rho'\Big) = \frac{\partial^2}{\partial x_i \partial x_j}\Big(T_{ij}H(f)\Big) + \frac{\partial}{\partial x_i}\Big(F_i\delta(f)\Big) + \frac{\partial}{\partial t}\Big(Q\delta(f)\Big) \tag{B.24}$$

where . . .

$$T_{ij} = \rho u_i u_j + P_{ij} - c_0^2 \rho' \delta_{ij} \tag{B.25}$$

$$L_i = -\Big(P_{ij} + \rho u_i \left(u_j - v_j\right)\Big)\frac{\partial f}{\partial x_j} \tag{B.26}$$

$$U_n = \Big(\rho_0 v_i + \rho \left(u_i - v_j\right)\Big)\frac{\partial f}{\partial x_i} \tag{B.27}$$

The contribution of the Lighthill stess tensor, T_{ij}, to the right-hand side of equation B.24 is known as the quadrupole term. This is followed by the dipole term F_i, involving an unsteady force, and Q represents a monopole-type term.

B.2.2 Retarded Time Formulation

The FW-H equation is typically solved using a Green's function technique. Retarded time formulation involves the calculation of acoustic signals by summing all the signals received by an observer at the same time t. Depending on the location and the velocity of both source and observer, these signals are emitted at different times and travel different distance to reach the observer at the same time t. Hence, it can be regarded as the signal analysed from the point of view of the observer. In this formulation the computational time is the reception (or observer) time.

Let,

$$\frac{\partial^2}{\partial t^2} - c_0^2 \nabla^2 = L$$

Where L is a linear differential operator. This immediately suggests that equation B.24 is of the form,

$L\phi = P$,

where ϕ is any source variable and P is a source term. If we assume initially that ϕ and P are functions of x only in volumetric space V, then

$$L_x \phi = P \tag{B.28}$$

Now we choose a function $G(x, y)$ such that following equation holds.

$$L_x G(x, y) = \delta(x - y) \tag{B.29}$$

Where G is the Greens function and δ, the Dirac delta function. Now multiplying both sides of equation B.29 with the value of source term at y and integrating over whole volume V, we get:

$$\int_{V(y)} L_x G(x,y) P(y) dy = \int_{V(y)} \delta(x-y) P(y) dy = P(x) \tag{B.30}$$

In deriving above relation, the sifting property of delta functions has been used, i.e. $\int f(x)\delta(x)dx = f(0)$.

The linear differential operator L_x in equation B.30 can be taken out of the integral because it is independent of variable y. Hence equation B.30 becomes,

$$L_x \int_{V(y)} G(x,y) P(y) dy = P(x) \tag{B.31}$$

Comparing equation B.31 with equation B.28, it immediately follows that,

$$\phi = \int_{V(y)} G(x,y) P(y) dy \tag{B.32}$$

Exactly the same principle will be used to solve equation B.24.

Now consider a Green's function which satisfies following equation:

$$\left(\frac{\partial^2}{\partial t^2} - c_0^2 \nabla^2 \right) G(x,y;t,\tau) = \delta(x-y)\delta(t-\tau) \tag{B.33}$$

Now, as before, multiplying equation B.33 by right hand side of equation B.24 (Here use right hand side of equation B.24 evaluated at position y and time τ) and integrating over all space and time, we get:

$$\left(\frac{\partial^2}{\partial t^2} - c_0^2 \frac{\partial^2}{\partial x_i^2} \right) \int_{(V,\tau)} G(x,y;t,\tau) M dV(y) d\tau \quad = \int_{(V,\tau)} \delta(x-y)\delta(t-\tau) M dV(y) d\tau \tag{B.34}$$

where,

$$M = \frac{\partial^2 T_{ij}}{\partial y_i \partial y_j} H(f) + \frac{\partial F_i}{\partial y_i}\delta(f) + \frac{\partial Q}{\partial \tau}\delta(f)$$

Use of the sifting property of delta functions immediately results in:

$$\int_{(V,\tau)} \delta(x-y)\delta(t-\tau) M dV(y) d\tau = \frac{\partial^2 T_{ij}}{\partial x_i \partial x_j} H(f) + \frac{\partial F_i}{\partial x_i}\delta(f) + \frac{\partial Q}{\partial t}\delta(f) \tag{B.35}$$

Comparing equations B.34 and B.35 above, we can write,

$$\begin{aligned}\left(\frac{\partial^2}{\partial t^2} - c_0^2 \frac{\partial^2}{\partial x_i^2}\right) \int_{(V,\tau)} G(x,y;t,\tau) M dV(y) d\tau &= \frac{\partial^2 T_{ij}}{\partial x_i \partial x_j} H(f) \\ &+ \frac{\partial F_i}{\partial x_i}\delta(f) + \frac{\partial Q}{\partial t}\delta(f)\end{aligned} \tag{B.36}$$

Finally, comparing equations B.24 and B.36 it can be seen that:

$$c_0^2(\rho - \rho_0) H(f) = \int_{(V,\tau)} G(x,y;t,\tau) \left[\frac{\partial^2 T_{ij}}{\partial y_i \partial y_j} H(f) + \frac{\partial F_i}{\partial y_i}\delta(f) + \frac{\partial Q}{\partial \tau}\delta(f)\right] dV(y) d\tau$$

i.e.

$$\begin{aligned}c_0^2(\rho - \rho_0) H(f) &= \int_{(V,\tau)} G \frac{\partial^2 (T_{ij} H(f))}{\partial y_i \partial y_j} dV(y) d\tau \\ &+ \int_{(V,\tau)} \left[G \frac{\partial (F \delta(f)_i)}{\partial y_i} + G \frac{\partial (Q\delta(f))}{\partial \tau}\right] dV(y) d\tau\end{aligned} \tag{B.37}$$

Assuming the volume sources are limited to a finite region of space and using the sifting property of delta functions, we get:

$$c_0^2(\rho-\rho_0)H(f) = \int_{(V,\tau)} T_{ij}\frac{\partial^2 G}{\partial y_i \partial y_j}dV(y)d\tau + \int_{(S,\tau)} F_i\frac{\partial G}{\partial y_i}dS(y)d\tau + \int_{(S,\tau)} Q\frac{\partial G}{\partial \tau}dS(y)d\tau \tag{B.38}$$

Hence, this is the required solution for the wave equation representing sound propagation expressed in terms of any Green's function G which satisfies:

$$\left(\frac{\partial^2}{\partial t^2} - c_0^2\nabla^2\right)G(x,y;t,\tau) = \delta(x-y)\delta(t-\tau)$$

Also three dimensional free space Green's function is given by,

$$G(x,y;t,\tau) = \frac{\delta(g)}{4\pi r} \quad \text{where,} \quad g = \tau - t + \frac{|\mathbf{x}-\mathbf{y}|}{c_0}, \quad \text{and} \quad r = \left|\mathbf{x}-\mathbf{y}\right| \tag{B.39}$$

Also, symmetric properties of Green's functions tell us that,

$$\frac{\partial G}{\partial t} = -\frac{\partial G}{\partial \tau}, \quad \text{and} \quad \frac{\partial G}{\partial x_i} = -\frac{\partial G}{\partial y_i}.$$

Using these properties, we can write,

$$c_0^2(\rho-\rho_0)H(f) = \frac{\partial^2}{\partial x_i \partial x_j}\int_{(V,\tau)} T_{ij}\frac{\delta(g)}{4\pi r}dV(y)d\tau - \int_{(S,\tau)} F_i\frac{\partial G}{\partial x_i}dS(y)d\tau - \int_{(S,\tau)} Q\frac{\partial G}{\partial t}dS(y)d\tau \tag{B.40}$$

Also using the conversion relationship for spatial to temporal derivatives in the form,

$$\frac{\partial}{\partial x_i}\left(\frac{\delta(g)}{4\pi r}\right) = \frac{1}{c_0}\frac{\partial}{\partial t}\left(\frac{\hat{r}_i\delta(g)}{4\pi r}\right) - \frac{\hat{r}_i\delta(g)}{4\pi r^2} \tag{B.41}$$

This gives finally,

$$\begin{aligned} c_0^2(\rho-\rho_0)H(f) &= \frac{\partial^2}{\partial x_i \partial x_j}\int\limits_{(V,\tau)} T_{ij}\frac{\delta(g)}{4\pi r}dV(y)d\tau - \frac{1}{c_0}\frac{\partial}{\partial t}\int\limits_{(S,\tau)} F_i\frac{\hat{r}_i\delta(g)}{4\pi r}dS(y)d\tau \\ &+ \int\limits_{(S,\tau)} F_i\frac{\hat{r}_i\delta(g)}{4\pi r^2}dS(y)d\tau - \frac{\partial}{\partial t}\int\limits_{(S,\tau)} Q\frac{\delta(g)}{4\pi r}dS(y)d\tau \end{aligned} \tag{B.42}$$

To integrate the above equation with respect to τ, following property of delta function in relation to variable change is required:

$$\int Q(t)\delta\Big\{f(\tau)\Big\}\mathrm{d}\tau = \sum_{n=1}^{N}\left(\frac{Q(\tau_n^*)}{\left|\frac{\partial f}{\partial\tau}\right|_{\tau=\tau^*}}\right) \tag{B.43}$$

Where τ^* is the value of τ for which $f(\tau) = 0$. Also in this case, $f(\tau) = t - \tau - \frac{|\mathbf{x}-\mathbf{y}|}{c_0}$. To account for the effect of the source motion in the solution represented by equation B.42, consider a source at position $x_s(t)$ at time t. Then the acoustic perturbation satisfies,

$$\left(\frac{\partial^2}{\partial t^2} - c_0^2\frac{\partial^2}{\partial x_i^2}\right)(\rho-\rho_0)c_0^2 = \frac{\partial}{\partial t}\left(Q(t)\delta(\mathbf{x}-\mathbf{x}_s(t))\right) \tag{B.44}$$

The above equation B.44 has the solution of the form,

$$c_0^2(\rho-\rho_0)=\int\limits_{(V,\tau)}\frac{Q(t)\delta(\mathbf{x}-\mathbf{x}_s(t))\delta\left(t-\tau-\frac{|\mathbf{x}-\mathbf{x}_s(t)|}{c_0}\right)}{4\pi\,|\mathbf{x}-\mathbf{x}_s(t)|}dV(y)d\tau \tag{B.45}$$

Where $f(\tau)=t-\tau-\frac{|\mathbf{x}-\mathbf{x}_s(t)|}{c_0}$ for source motion. Hence,

$$\frac{\partial f}{\partial\tau}=-1-\frac{1}{c_0}\frac{\partial\,|\mathbf{x}-\mathbf{x}_s(t)|}{\partial\tau} \tag{B.46}$$

and,

$$\frac{\partial\,|\mathbf{x}-\mathbf{x}_s(t)|}{\partial\tau}=-\frac{\partial\mathbf{x}_s(t)}{\partial\tau}.\frac{(\mathbf{x}-\mathbf{x}_s(t))}{|\mathbf{x}-\mathbf{x}_s(t)|},\quad \frac{1}{c_0}\frac{\partial\mathbf{x}_s(t)}{\partial\tau}=\mathbf{M},\quad M_r=-\mathbf{M}.\frac{(\mathbf{x}-\mathbf{x}_s(t))}{|\mathbf{x}-\mathbf{x}_s(t)|}.$$

Using these results equation B.46 becomes,

$$\frac{\partial f}{\partial\tau}=-1+M_r \tag{B.47}$$

Using equation B.47, and the result of equation B.43, equation B.45 becomes,

$$c_0^2\,(\rho-\rho_0)=\sum_{n=1}^{N}\frac{\partial}{\partial t}\left\{\frac{Q(\tau_n^*)}{4\pi r\,(1-M_r)}\right\} \tag{B.48}$$

This results enables us to straight away right the solution for the moving surface in this exercise which is,

$$\begin{aligned}4\pi c_0^2\,(\rho-\rho_0)\,H(f) &= \frac{\partial^2}{\partial x_i\partial x_j}\int\limits_V\left[\frac{T_{ij}}{r\,|1-M_r|}\right]_{\tau^*}\mathrm{d}V\\ &+ \int\limits_S\left[\frac{F_r}{r^2\,(1-M_r)}\right]_{\tau^*}\mathrm{d}S\;+\;\frac{1}{c_0}\frac{\partial}{\partial t}\int\limits_S\left[\frac{F_r-Qc_0}{r\,|1-M_r|}\right]_{\tau^*}\mathrm{d}S\end{aligned} \tag{B.49}$$

τ^* is an emission time of sound heard by the observer at time 't'. At this time,

$$c_0\,(t-\tau^*) = |x - x_s(\tau^*)| = r \tag{B.50}$$

i.e.

$$c_0\left(1 - \frac{\partial\tau^*}{\partial t}\right) = -\frac{(x_i - x_{si})}{|x - x_s|}\frac{\partial x_{si}}{\partial\tau^*}\frac{\partial\tau^*}{\partial t} \tag{B.51}$$

i.e

$$\frac{\partial\tau^*}{\partial t} = \frac{1}{1-M_r}, \quad \text{and} \qquad \frac{\partial}{\partial t}\bigg|_x = \left[\frac{1}{1-M_r}\frac{\partial}{\partial\tau^*}\bigg|_x\right] \tag{B.52}$$

This relation can now be used to present the final solution in the following form,

$$\begin{aligned} c_0^2\,(\rho-\rho_0)\,H(f) &= \frac{\partial^2}{\partial x_i \partial x_j}\int_V \left[\frac{T_{ij}}{r\,|1-M_r|}\right]_{\tau^*} \mathrm{d}V \;+\; \int_S \left[\frac{Q_r \dot{+} Q_r}{r\,(1-M_r)^2}\right]_{\tau^*} \mathrm{d}S \\ &+ \frac{1}{c_0}\int_S \left[\frac{F_r}{r\,(1-M_r)^2}\right]_{\tau^*} \mathrm{d}S \;+\; \int_S \left[\frac{F_r + F_m}{r^2\,(1-M_r)^2}\right]_{\tau^*} \mathrm{d}S \\ &+ \frac{1}{c_0}\int_S \left[\frac{F_r\left(rM_r \dot{+} c_0 M_r - c_0 M^2\right)}{r^2\,(1-M_r)^2}\right]_{\tau^*} \mathrm{d}S \\ &+ \int_S \left[\frac{Q_r\left(rM_r \dot{+} c_0 M_r - c_0 M^2\right)}{r^2\,(1-M_r)^3}\right]_{\tau^*} \mathrm{d}S \end{aligned} \tag{B.53}$$

Equation B.53, with the volume quadrupole term neglected, is known as formulation 1A of Farassat **?**. Solvers which are based on this formulation are known as 'retarded time methods'. The computation of retarded time becomes intense because in the equation for retarded time;

$$\tau_{ret} = t - \frac{\left|\mathbf{x} - \mathbf{y}(\tau_{ret})\right|}{c_0}$$

the relation for retarded time is implicit and so it requires a suitable root finding techniques to find the value of retarded time.

B.2.3 Advanced Time Formulation

This is effectively retarded time formulation, but from the view point of source. In advanced time, computational time is the emission time. Hence at a given time the contributions from the integration domain are calculated based on the current aerodynamic data and the current kinematics of the domain. At each computational time and for each source element, the time at which the corresponding disturbance will reach the observer is calculated and referred to as advanced time. The advantage of this formulation is that the expression for the advanced time is in explicit form. The retarded time formulation was interpreted by Casalino as an advanced time formulation **?** from the view point of the source:

$$t_{adv} = t + \frac{1}{c_0}\left|x\left(t_{adv}\right) - y\left(t\right)\right| = t + \frac{r\left(t\right)}{c_0}\left[\frac{M_{or} + \sqrt{M_{or}^2\left(t\right) + 1 - M_0^2}}{1 - M_o^2}\right] \tag{B.54}$$

where for each panel $r_i = x_i(t) - y_i(t)$ is the radiation vector and $M_{or} = \widehat{r_i} M_{oi}$ is the observer Mach number vector in the radiation direction.

Appendix C

Fourier Optimization

Interpolations are extensively used in numerical methods and Lagrange method is the most common and widely used method. Although Lagrange method is very popular, it can incur instabilities in large scale computing and the cases where high accuracy is desired (i.e. schemes used for acoustic simulations especially in high wave number band). Here an attempt is made to develop optimized interpolation scheme using Fourier analysis. Consider a function $f(x)$ (which is to be approximated using interpolation) having a fourier transform, $f(\alpha)$.

Therefore,

$$f(x) = \int_{-\infty}^{\infty} f(\alpha) e^{i\alpha x} d\alpha \tag{C.1}$$

Assume that $f(\alpha)$ can be represented by, $f(\alpha) = A(\alpha)\angle\phi(\alpha)$

where, $A = |f(\alpha)|$ and $\phi(\alpha) = \arg[f(\alpha)]$.

Then

$$f(x) = \int_{\infty}^{\infty} A(\alpha) e^{i(\alpha x+\phi)} d\alpha \tag{C.2}$$

Now let us consider a unit magnitude simple wave of wave number α such that

$$f_\alpha(x) = e^{i(\alpha x+\phi)} \tag{C.3}$$

Consider that $f(x)$ is to be approximated by interpolation at stencil point 'm' using 'N' point stencil such that

$$f_m(x) = \sum_{n=1}^{N} c_n f_n \tag{C.4}$$

For the stencil shown in Figure C.1, the value of the function can be written as

$$f\Big(x_1 + \big((m-1)+\eta\big)\Delta x\Big) = \sum_{n=1}^{N} c_n f_n \tag{C.5}$$

Now if we define the error as the square of difference between the left and right of above equation, it can be written as

$$E_{local} = \left| f\Big(x_1 + \big((m-1)+\eta\big)\Delta x\Big) - \sum_{n=1}^{N} c_n f(x_1 + (n-1)\Delta x) \right|^2 \tag{C.6}$$

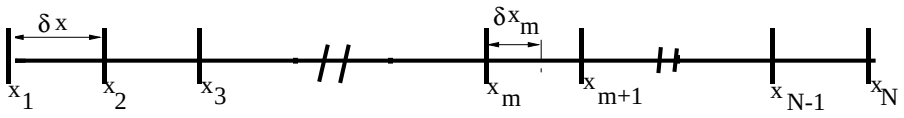

Figure C.1: Interpolation grid in one dimension

Substituting for $f(x)$ from equation C.3, the local error in equation C.8 becomes

$$E_{local} = \left| e^{i\left[\alpha\left(x_1+\left((m-1)+\eta\right)\Delta x\right)+\phi\right]} - \sum_{n=1}^{N} c_n e^{i\left(\alpha\left(x_1+(n-1)\Delta x\right)+\phi\right)} \right|^2 \tag{C.7}$$

With some algebraic manipulation, it simplifies to:

$$E_{local} = \left| e^{i\alpha\left(m+\eta-1\right)\Delta x} - \sum_{n=1}^{N} c_n e^{i\alpha(n-1)\Delta x} \right|^2 \tag{C.8}$$

Now the integrated error over a range of wave numbers from 0 to κ can be expressed as:

$$E = \int_0^{\kappa} \left| e^{i\alpha(m+\eta-1)\Delta x} - \sum_{n=1}^{N} c_n\, e^{i\alpha(n-1)\Delta x} \right|^2 d\left(\alpha\Delta x\right) \tag{C.9}$$

For $\alpha\Delta x = 0$, $E_{local} = 0$. This results in Equation C.10 from C.8.

$$\sum_{n=1}^{N} c_n - 1 = 0 \tag{C.10}$$

Equations C.10 and C.9 are used to derrive a Lagrange function which can be differenciated to evaluate the condition for the minimum overall error.

$$L = \int_0^{\kappa} \left| e^{i\alpha(m+\eta-1)\Delta x} - \sum_{n=1}^{N} c_n\, e^{i\alpha(n-1)\Delta x} \right|^2 d\left(\alpha\Delta x\right) + \lambda\left(\sum_{n=1}^{N} c_n - 1\right) \tag{C.11}$$

Conditions for the minimum error can now be expressed as,

$$\frac{\partial L}{\partial c_n} = 0 \tag{C.12}$$

and

$$\frac{\partial L}{\partial \lambda} = 0 \tag{C.13}$$

Equation C.12 leads to,

$$\mathrm{Re}\left[\int_0^{\kappa} -e^{i(n-1)k}\left(e^{i(m+\eta-1)k} - \sum_{p=1}^{N} c_p e^{i(p-1)k}\right)dk\right] + \frac{\lambda}{2} = 0 \tag{C.14}$$

$$\mathrm{Re}\left[-\frac{e^{i(m+n+\eta-2)k}}{i(m+n+\eta-2)} + \sum_{p=1}^{N} c_p \frac{e^{i(p+n-2)k}}{i(p+n-2)}\right]_0^{\kappa} + \frac{\lambda}{2} = 0$$

i.e.

$$\sum_{p=1}^{N} c_p \frac{\sin(p+n-2)\kappa}{p+n-2} + \frac{\lambda}{2} = \frac{\sin(m+n+\eta-2)\kappa}{m+n+\eta-2} \tag{C.15}$$

Similarly, Equation C.13 leads to:

$$\sum_{n=1}^{N} c_n - 1 = 0 \tag{C.16}$$

Now the systems of linear equations C.15 and C.16 are solved simultaneously to find the interpolating coefficients c_n (for $n = 1, 2, 3, ...$).

Appendix D

Grid Convergence Studies

D.1 Introduction

In this section the results from initial studies to establish grid convergence on two-dimensional cavity geometry are presented and analyzed.

D.2 2D cavity simulation using CAA solver

The first study was conducted using the CAA solver to simulate a 2D cavity geometry which is shown in Figure D.1(a). This computation was performed to establish an optimum computational grid domain for 3D cavity simulation performed in Chapter 3. The cavity has a (L/D) ratio of 4, Mach number of the flow = 0.8 and corresponds to one of the cases in the experimental investigation by Tracy and Plentovich Tracy & Plentovich (1997). For this case, three different computational domains were generated with the same basic grid topology, but with varying number of grid cells. The coarse grid had approx. 21500 cells, the intermediate and the fine grids had 32300 and 51400 cells respectively. The zoomed in views of 2D coarse and fine meshes (the intermediate mesh is identical to that shown in Figure 3.25(c)) is shown in Figure D.2 and grid boundaries are shown in Figure **??**(b). The results of the grid convergence study are shown in Figure D.3. The data correspond to sampling points located at $x/L = 0.9$ on the floor of the cavity. From the figure, the agreement between the fine and intermediate grid densities is good. Only the higher harmonics of the dominant mode show difference. However, higher modes generally carry less energy and are not of principle interest in this work. Also Any attempts to capture these higher modes by refining the grid makes the three dimensional simulation becomes prohibitively expensive. The coarse grid result is found to suffer from the dissipation due to the grid coarsening. Therefore the intermediate mesh was chosen for the distribution of grid cells in XY-plane.

D.3 2D cavity simulation in Fluent

As in Section D.2, 2D grid convergence studies were also performed to establish an optimum computational grid domain for 3D cavity simulation performed in Chapter

4. The first cavity case had a (L/D) ratio of 4, Mach number of the flow = 0.85 and corresponds to one of the cases in the experimental investigation by Geraldes (2005). This investigation was carried out to establish an optimum computational grid domain for the 3D simulation in Section 4.2. For this study, three different computational domains were generated with the same basic grid topology, but with varying number of grid cells. The grid topology is based on a structured meshing strategy which utilizes non-matching grid interfacing techniques to reduce the number of grid cells significantly (see also Section 4.2). The coarse grid had approx. 21300 cells, the intermediate and the fine grids had 31100 and 49200 cells respectively. The computational grid boundaries are shown in Figure D.4 and the zoomed in views of 2D meshes (the intermediate mesh is identical to that shown in Figure 4.3(b)) are shown in Figure D.5. The results of the grid convergence study are shown in Figure D.6. The data correspond to sampling points located at $x/L = 0.9$ on the floor of the cavity. From the figure, the fine and intermediate grid results are similar. The coarse grid, however, suffers from excessive dissipation due to the large grid sizes. The intermediate grid, therefore, was chosen as the basis for 3D grid generation. Similar study was also performed for another cavity which had a (L/D) ratio of 5, Mach number of the flow = 0.85 and corresponds to the 3D case studied in Sections 4.3 and 4.4. The result for this case is shown in Figure D.7, and again medium grid was used for the subsequent 3D study based the result.

Similar studies were performed to establish the optimum number of grid cells for other 3D clean cavities simulated in Chapter 4. For the cavity-with-store cases, The grid cell sizes inside the cavity were maintained similar to the equivalent clean cavity geometry (for the DES, simulation, the 3D grid cells are ideally required to be isotropic. Hence all clean cavity meshes had near isotropic cells inside the cavity with minimum stretching. These cells sizes were used while generating the grid for the cavity-with store cases).

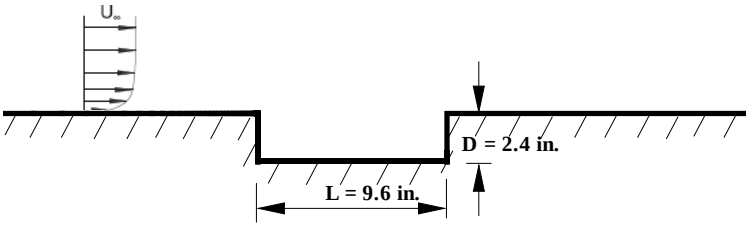

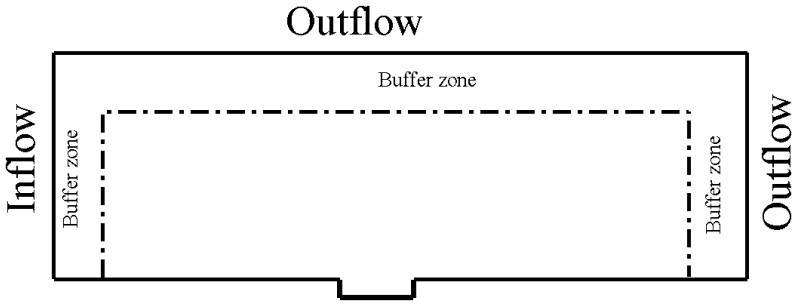

(a) 2D cavity geometry.

(b) Computational domain boundary for CAA simulation.

Figure D.1: Cavity geometry and computational domain extent.

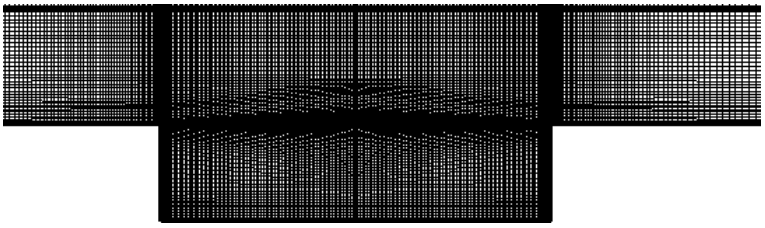

(a) Coarse grid domain.

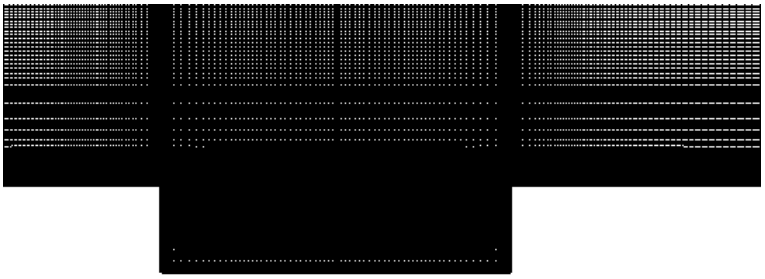

(b) Fine grid domain.

Figure D.2: Structured grids used in 2D CAA simulation.

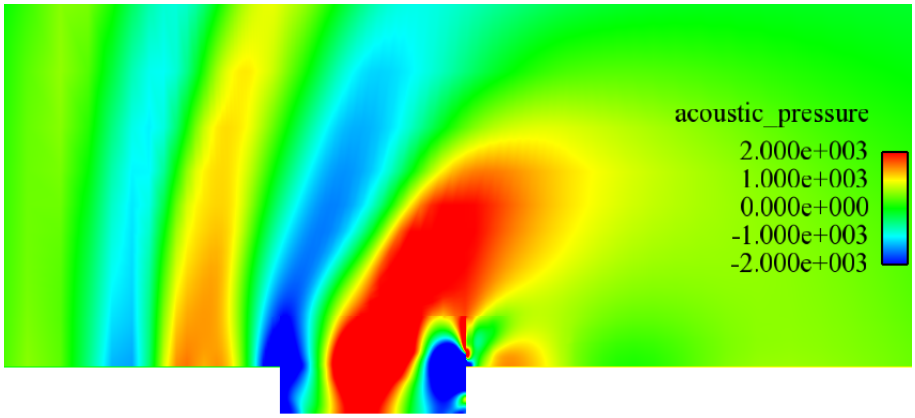

(a) Acoustic pressure contours, intermediate grid.

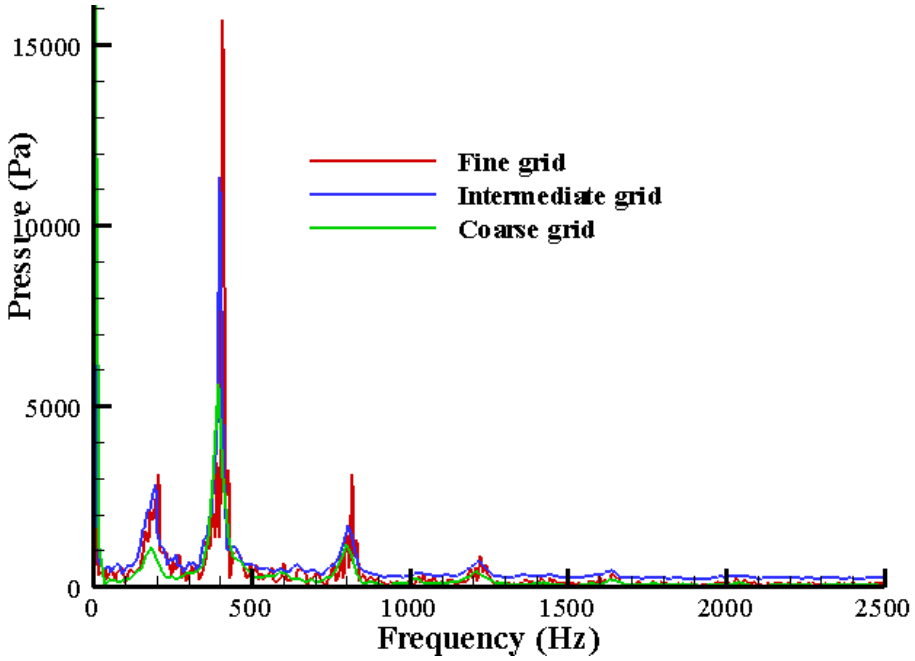

(b) Pressure spectra at $x/L = 0.9$.

Figure D.3: Result from CAA grid convergence study.

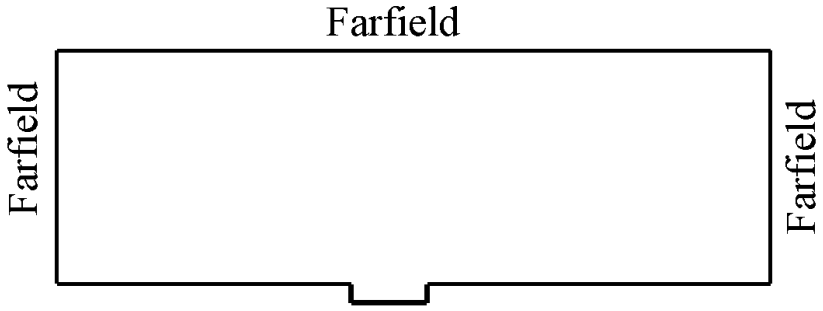

(a) Computational domain boundary for Fluent simulation.

Figure D.4: grid boundaries for Fluent and CAA study.

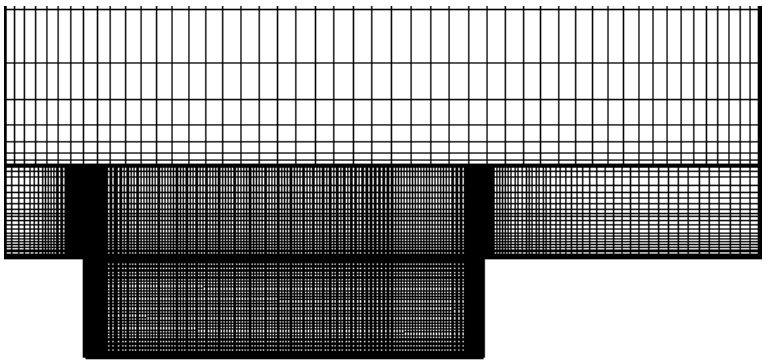

(a) Coarse grid domain.

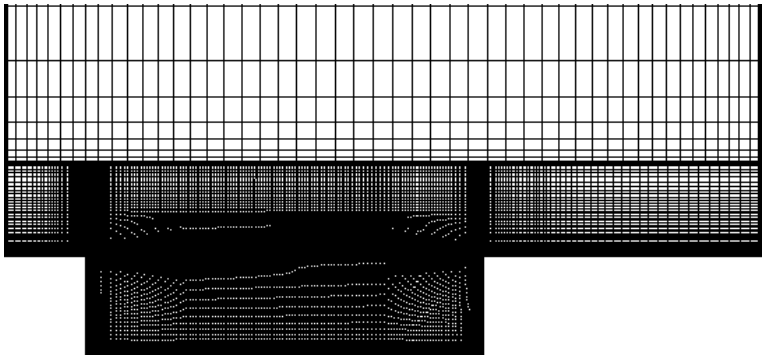

(b) Intermediate grid domain.

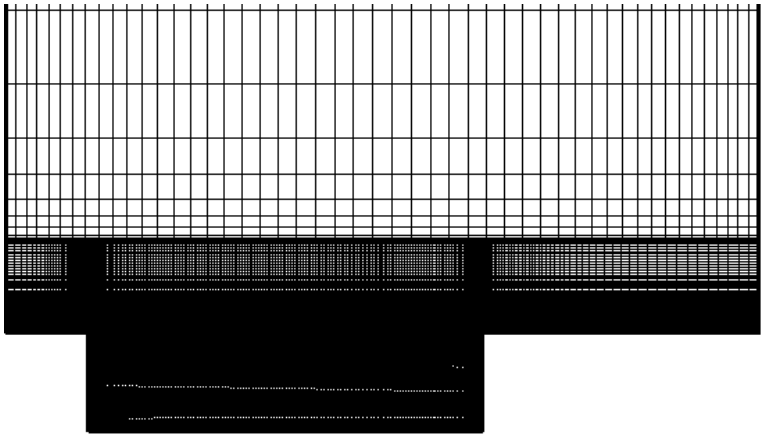

(c) Fine grid domain.

Figure D.5: Structured grids used in 2D cavity simulation, $L/D = 4$ and $M_\infty = 0.85$.

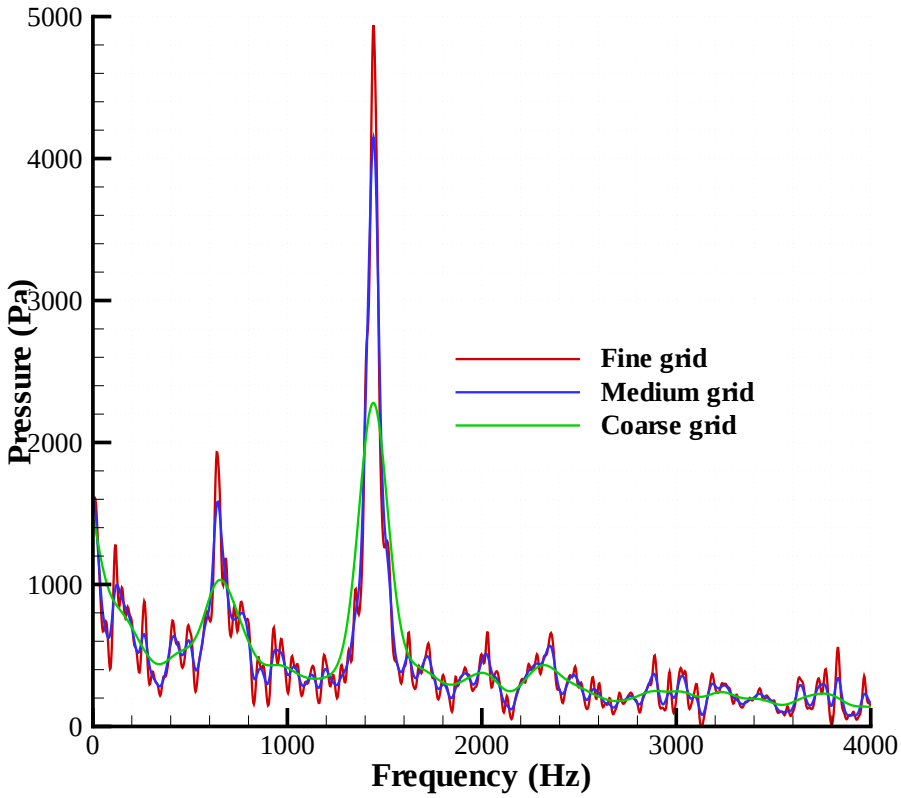

Pressure spectra at $x/L = 0.9$.

Figure D.6: Result from grid convergence study, $L/D = 4$ and $M_\infty = 0.85$.

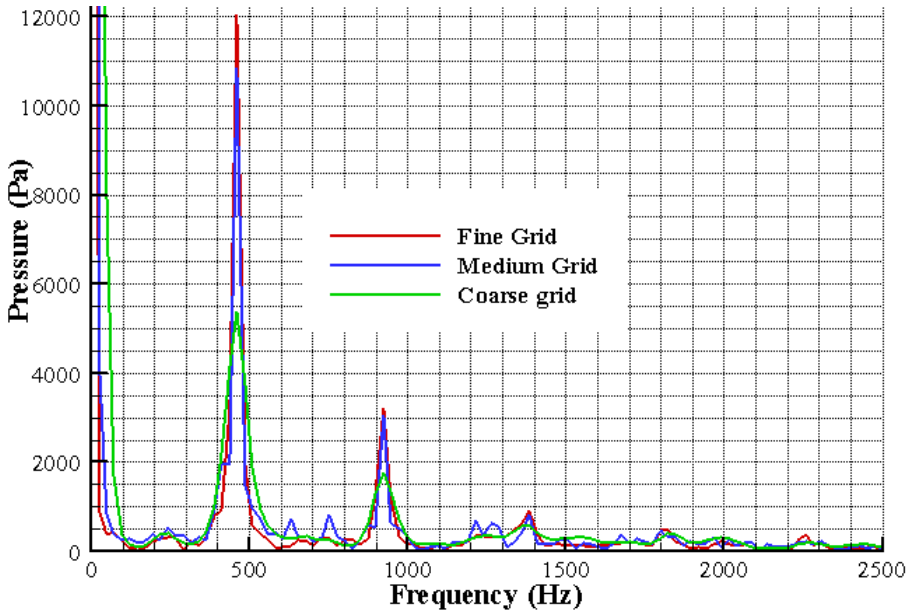

Pressure spectra at $x/L = 0.9$.

Figure D.7: Result from grid convergence study, $L/D = 5$ and $M_\infty = 0.85$.